Development and Machine Learning-Based Optimisation of a Microfluidic Bone-on Chip Model



Brian Collins, MSc

Submitted for the Award of Doctor of Philosophy (PhD)

School of Mechanical & Manufacturing Engineering

Dublin City University

Supervised by:

[1] Dr Tanya Levingstone

[2] Dr Malika Bendechache

[1] Professor Nicholas Dunne

[1] School of Mechanical & Manufacturing Engineering

Dublin City University

[2] Adapt Centre, School of Computer Science, University of Galway

July 2026

Declaration

I hereby certify that this material, which I now submit for assessment on the programme of study leading to the award of Doctor of Philosophy is entirely my own work, and that I have exercised reasonable care to ensure that the work is original and have conformed to the regulations on the use and declaration of Generative AI, and does not to the best of my knowledge breach any law of copyright, and has not been taken from the work of others save and to the extent that such work has been cited and acknowledged within the text of my work..

Signed: Brian Collins Date: 02/07/2026

Student ID: 20216634

Reporting of Gen AI Tool Use in Research Thesis

Tools: Clearly indicate the tool name and model (or version) you used and the date(s) of use. If you used a tool multiple times, provide the range of dates over which the tool was used and the model/versions used.	**Grammarly Pro Write Full Assist for Microsoft Office (version 6)** Used between March 2025 and December 2025 for spelling, grammar checking, and clarity suggestions during thesis drafting. **ChatGPT *GPT-4 model*, *GPT-5 model*** Used between March 2025 and December 2025 to support the literature review process**.**
Outputs: Specify what tool outputs were generated and used by you and for what purpose.	**Grammarly Pro -** Automated grammar, spelling, punctuation, and clarity suggestions. These outputs were used solely to improve readability and correctness of the written text. No Grammarly-generated content was inserted into the thesis. **ChatGPT -** High-level summaries of academic literature, and thematic outlines. These outputs were used only as thinking aids to support early-stage literature review work. All text appearing in the thesis was written by the researcher.
Prompts: Provide a record of the prompts you used here or link to an appendix where the prompts used are listed.	**ChatGPT prompts** **-** Requests for summaries of primary academic sources
Iterations: Provide some commentary on the number and type of iterations. This can be linked to your report on prompts and outputs above.	**Grammarly Pro -** Used iteratively throughout drafting the thesis involving multiple rounds of revision per chapter. **ChatGPT** — Iterative use occurred mainly during the literature review phase. The primary academic source was maintained as the main source of information.
Critical Reflection: If Gen AI tools have been used minimally, a very brief critical reflection on its role in the research submitted for examination can be included here. Otherwise, specify the parts of the thesis where critical reflection on the use and role of Gen AI tools is included.	GenAI tools played a limited and supportive role in this research. Grammarly Pro contributed to improving the clarity and readability of the thesis but did not influence its intellectual content. ChatGPT was used only to aid thinking during the literature review phase. No ChatGPT-generated text appears in the thesis and all text was produced independently by the researcher. Full engagement with all primary academic sources used maintained throughout the research process.

Acknowledgements

This research was funded by the SFI Centre for Research Training in Artificial Intelligence (CRT-AI) with Science Foundation Ireland Grant No. 18/CRT/6223.

Undertaking this PhD journey has been both challenging and rewarding, marking a significant stage in my personal growth and self-actualisation, as well as a major academic achievement. I would like to thank my partner and family for the support they have offered during often challenging and tumultuous periods; the world has moved on and changed quite a bit since starting this programme in the midst of Covid where many workarounds were required for this. Fortunately, those work-arounds gave ground to opportunities, and I would like to first thank Coventry University for offering a traineeship for cell culturing. This also allowed additional experimental facilities for formal testing and feedback from publications (a thank you shout out to Derek & Mark). In addition to this, I'd like to thank Keele University, particularly the relevant researchers at Keele's Guy Hilton Research Facility for offering me a formal CRT-AI placement, suggestions and advice for publications, additional training for various equipment and preparing hydrogels (thanks to Pooya, Arjun & Ali). Between these two places I was able to carry out and complete my formal experiments, essential for my thesis. I would also like to thank my co-supervisor Malika and her excellent researcher Dost at the University of Galway for their invaluable help, advice, and mentorship during the Machine Learning modelling stage of my project. I'm most grateful for their experience during this crucial stage of development.

I would also like to thank John, Srishti, Tina and Ali within my research group at DCU for their help and advice on carrying out required preparation work in the early days, in preparation for the transfer and carrying out initial viability tests (a shout out to John & Srishti there). I also want to thank Dr David Kinahan, a lecturer within our department, for stepping in for supervision during a maternity leave offering invaluable advice on microfluidics along with Nicholas Dunne. Within DCU, I would also like to express my gratitude and best wishes to Liam Domican and Michael May with their team of colleagues for giving me access to the required laser cutting and other equipment or tools at the MME and NRF facilities for producing the required bone-on-chips and their protocols. Their assistance has been important for this research investigation. I would like to thank Tanya my primary supervisor, for her general advice on coordinating experiments and all the writings from my literature review, transfer report, abstracts, papers and of course this thesis.

I would like to sincerely thank and wish my best wishes going forward to the CRT-AI group for offering the required funding, networking, training and co-ordination of this PhD programme. I want to give particular thanks to Barry O'Sullivan, Janet Choi, Angela Lally and Vicky Flannagan for the best advice and wishes during the various stages and challenges of my PhD and for their words of wisdom during this. It was pivotal in providing funds, access, and opportunity of placement for completing this comprehensive PhD study.

Table of Contents

Declaration ii
Acknowledgements iii
List of Figures x
List of Tables xi
List of Equations xii
Nomenclature xiii
Table of Symbols and Units xiv
Research Publications xv
Abstract xvii
1 Introduction 2
1.1 Overview 2
1.2 Thesis Outline 3
2 Literature Review 5
2.1 Bone Biology 5
2.1.1 Bone Structure and Function 5
2.1.2 Bone Pathologies 6
2.1.3 Current standard *ex/in vivo* models 7
2.1.4 Cell Stimulation and Mechanotransduction 9
2.2 BoC Technology 13
2.2.1 Evolution of Organ-on-Chip and BoC Systems 13
2.2.2 Microfluidic Design Considerations for BoC 14
2.2.3 Materials 14
2.2.4 Mechanical Stimulation 15
2.2.5 Flow Stimulation 20
2.2.6 Chip Sterilisation and Re-usability 23
2.2.7 Cell Source 23
2.2.8 Cell Culture Conditions 24
2.3 Hydrogel-based Substrates for Bone Tissue Engineering 24
2.3.1 Properties of Hydrogels for Bone Tissue Engineering 24
2.3.2 Hydrogels for 3D culture models 25
2.4 Data Generation for BoC Models 26
2.4.1 Imaging Modalities 26
2.4.2 Assay Detection and Fluorescence 27
2.5 Machine Learning Models 28
2.5.1 ML Modelling and Bio-analysis 28

2.5.2 Model Optimisation Techniques 30
2.5.3 Application of ML in OoC 30
2.6 Critical Limitation and Gaps in Current Research 31
2.6.1 3D Culture Optimisation Challenges 31
2.6.2 Combined Mechanical and Flow Stimulation 31
2.6.3 Machine Learning Modelling Gaps 31
2.7 Research Aim and Objectives 32
3 BoC Platform with Physiologically Relevant Loading and a Tuneable GelMA/HAMA Hydrogel Microenvironment 34
3.1 Introduction 34
3.2 Methodology 36
3.2.1 BoC Platform Materials and Fabrication 36
3.2.2 BoC Platform Design and Verification 36
3.2.3 BoC Platform Verification 41
3.2.4 Sterilisation 42
3.2.5 Assessment of Indirect and Direct Biocompatibility 42
3.2.6 GelMA and HAMA Synthesis 43
3.2.7 Hydrogel Characterisation 44
3.2.8 Hydrogel Biological Assessment 45
3.2.9 Optimisation of Hydrogel Thickness 46
3.2.10 Direct Chip Testing –Longitudinal Study 47
3.2.11 Investigation of the Effect of Hypoxia on Cellular Response 47
3.2.12 Statistical Analysis 48
3.3 Results 49
3.3.1 Verification of the BoC Platform 49
3.3.2 Assessment of Indirect and Direct Biocompatibility 49
3.3.3 Hydrogel Characterisation 50
3.3.4 Hydrogel Biological Assessment 53
3.3.5 Optimisation of Hydrogel Thickness and Longitudinal Study 55
3.3.6 Investigation of the Effect of Hypoxia on Cellular Response 57
3.4 Discussion 59
3.5 Conclusion 62
4 Investigation of Centrifuge and Flow Stimulation Effects on Osteoblast Response 64
4.1 Introduction 64
4.2 Methodology 65
4.2.1 Microfluidic Chip Preparation 65

4.2.2 Application of Mechanical Stimuli 65
4.2.3 Monitoring and Assays 66
4.2.4 Data Analysis 66
4.3 Results 67
4.3.1 Centrifuge-Only Stimulation 67
4.3.2 Flow-Only Stimulation 70
4.3.3 Combined Centrifuge and Flow Stimulation 74
4.4 Discussion 78
4.5 Conclusion 81
5 Investigation of the effect of Centrifuge and Flow Stimulation on Osteoblast Response with Cell Protectant Media 83
5.1 Introduction - Media Optimisation 83
5.2 Methodology of Centrifuge and Flow Tests with Varied Media 84
5.2.1 CellShip Media Optimisation and Testing Method 84
5.2.2 Flow & Mechanical Experimentation 84
5.2.3 Data Analysis 85
5.3 Results – CellShip media supplemented stimulated BoCs 86
5.3.1 CellShip Media Optimisation 86
5.3.2 Comparative Impact of CellShip under Centrifugation Conditions 87
5.3.3 Comparative Impact of CellShip under Varying Flow Rates 90
5.3.4 Quantitative Observations & Combined Stimuli: CellShip vs. Non-CellShip 93
5.4 Discussion 96
5.5 Conclusion 98
6 Development of Machine Learning-based Models of Cell Responses within the BoC Platform 100
6.1 Introduction 100
6.2 Classical Machine Learning Methods: Data and Processing 102
6.2.1 Experimental Design Rationale 102
6.2.2 Data Acquisition and Processing 102
6.2.3 Dataset Detailed Description 104
6.3 Machine Learning Descriptive Analysis 105
6.3.1 Dataset Statistical Summary, Distribution and Correlation 105
6.3.2 Summary of PCA: Input Features Impact on Flow Centrifuge Outputs 108
6.3.3 Predictive Regression Model Overview 110
6.4 Deep Learning Methodology 111
6.4.1. Implementation Environment 111
6.4.2. Dataset 111

6.4.3. Data Preprocessing 113
6.4.4. Proposed Randomised-Based Deep Neural Network (Randomised NN) 113
6.4.5. Benchmark Approaches 114
6.4.6. Evaluation Metrics 116
6.4.7. Training Time 117
6.4.8. Explainable Artificial Intelligence (XAI) 117
6.5 Results 119
6.5.1 Classical Machine Learning Results 119
6.5.2 Deep Learning Results 121
6.5.3 Explainable AI Results 123
6.6 Discussion 129
6.6.1 Classical Machine Learning Discussion 129
6.6.2 Deep Learning Discussion 130
6.7 Conclusions 132
7 Overall Discussion, Concluding Remarks and Future Perspectives 134
7.1 Overall Discussion 134
7.1.1 BoC and Gel Development 134
7.1.2 Impact of Mechanical Stimulation: Centrifugation & Perfusion Flow 135
7.1.3 Machine Learning Applications and Modelling Opportunities 138
7.2 Concluding Remarks 140
7.3 Future Research Directions 141
References 143
Appendices 185
Appendix A1: All Design Revisions 185
Appendix A2: Raw Metrology Width & Roughness Data 187
Appendix A3: Detailed Flow Testing RGB Data 190
Appendix A4: Centrifuge Disk Setup & Testing 193
Appendix A5: SPSS T-Test Compare Alpha-Mem 10 % CellShip vs Alpha-Mem 195
Appendix A6: Compared effects of Centrifugation vs Non-Centrifugation on biomarker outputs 197
Appendix A7: One-Way ANOVA Comparison of Flow Rate Effects on Cellular Biomarkers 203
Appendix A8: Multiway ANOVA: Combined Effects of Flow rate, Centrifugation & CellShip Media 209
Appendix A9: Additional Mechanical Stimulation Assay Output Charts 216

List of Figures

Figure 2.1 Anatomy of the cartilage and subchondral bone structure 6
Figure 2.2 Arthritis and degeneration of joint subchondral bone tissue 7
Figure 2.3 Schematic representation of the differentiation of osteoblast lineage cells 9
Figure 2.4 Schematic showing mechanical forces on in vivo bone cells..... 10
Figure 2.5 Schematic components of the bone mechanosensory system 12
Figure 2.6 Brief history of background microfluidic technology development 13
Figure 2.7 Mechanical force modulation methods 16
Figure 2.8 Gait cycle dynamic loading pattern 19
Figure 2.9 A range of flow shear stimulation in bone cell studies compared..... 21
Figure 2.10 Synovial JoC..... 26
Figure 3.1 BoC platform configurations. 37
Figure 3.2 Centrifuge disk layout 38
Figure 3.3 Schematic of controlled input angular velocity by spin frequency (shown). 41
Figure 3.4 Cell viability at 1 Day..... 49
Figure 3.5 Cell viability at Day 3, 7, 2nd use and 3rd use on PLL coated BoC. 50
Figure 3.6 A): NMR 400 MHz material characterisation of GelMA 51
Figure 3.7 Mechanical properties of GelMA/HAMA hydrogels..... 52
Figure 3.8 ViaFluor cell proliferation by hydrogel composition..... 53
Figure 3.9 Shows Day 28 ALP abs. readings for different gel formulations..... 54
Figure 3.10 ALP and alamarBlue™ abs. readings for various bone cell gel thicknesses **A)** ALP absorption assay values and **B)** 55
Figure 3.11 Gel in chip alizarin red fluorescence at 5 weeks for various gel thicknesses.. 56
Figure 3.12 Long term culture of MC3T3 pre-osteoblast cells on the optimal hydrogel composition..... 57
Figure 3.13 Normoxic and hypoxic incubation effects on bone cell samples 58
Figure 4.1 Optimisation of centrifuge duration. 67
Figure 4.2 Centrifuge cyclic loading by g-level 69
Figure 4.3 Cell metabolic activity and proliferation for flow stimulated samples 70
Figure 4.4 ALP absorption by flow stimulated vs static cell samples 71
Figure 4.5 Cell metabolic activity and proliferation by flow rate treatment 72
Figure 4.6 Comparison of ALP absorption (osteogenesis) by flow rate treatment 73
Figure 4.7 alamarBlue™ absorption by flow and centrifuge 74
Figure 4.8 ViaFluor Fluorescence (normalised abs.) proliferation by flow and centrifuge 75

Figure 4.9 Alkaline Phosphatase absorption (osteogenesis) by flow and centrifuge stimulation. 76
Figure 4.10 Visual Brightfield microscope flow comparison of surface bone cell 77
Figure 4.11 Visual Brightfield microscope comparison of bone samples centrifuged..... 77
Figure 5.1 Compared varied media : CellShip ratios effect on cell viability 86
Figure 5.2 Compared distribution of Alpha-Mem media (Std. media) vs Alpha-Mem media +10 % CS 87
Figure 5.3 Comparative illustration of Day 3 Trypan Blue Viability..... 88
Figure 5.4 Centrifuged with 10 % CS..... 89
Figure 5.5 ALP absorption (osteogenesis) by BoC coating/treatment 89
Figure 5.6 Comparison of Alpha-Mem and Alpha-Mem 10 % CS media by flow rate 90
Figure 5.7 ViaFluor fluorescence compared by media type 91
Figure 5.8 ALP absorption compared by media type 92
Figure 5.9 Result Summary – Full culture period (all weeks) comparative distribution.... 93
Figure 5.10 Cell proliferation (ViaFluor normalised abs.) compared by centrifuge and flow treatments, and media 94
Figure 5.11 ALP abs. compared by centrifuge and flow treatments, and media..... 95
Figure 6.1 ALP, ViaFluor Output data probability density 106
Figure 6.2 Correlation Matrix Heatmap..... 107
Figure 6.3 PCA comparison of different input features effect size..... 109
Figure 6.4 Classical ML Regression Models R^2 fit for all outputs, with MAPE error rate. 119
Figure 6.5 Regression Models R^2 fit for each output. 119
Figure 6.6 Model Performance - R^2 vs Error Metrics by regression model type 120
Figure 6.7 LIME explanation for $405nm_alkP$ prediction instance..... 124
Figure 6.8 SHAP feature importance summary for 405nm_alkP. 124
Figure 6.9 LIME explanation for $488nm_VFz_abs$ prediction instance 125
Figure 6.10 SHAP summary plot for $488nm_VFz_abs$ 126
Figure 6.11 LIME explanation for 560nm_alamB prediction instance. 127
Figure 6.12 SHAP summary plot for 560nm_alamB..... 127
Figure 6.13 LIME explanation for $488nm - VF - FL$ prediction instance. 128
Figure 6.14 SHAP summary plot for $488nm - VF - FL$. 128

List of Tables

Table 2.1 2D vs 3D in vitro cell culture systems, versus animal models 8
Table 2.2 Comparison of cellular sources of mechanical force modulation in cells 11

Table 2.3 Compared advantages and disadvantages of microfluidic channel materials 15
Table 2.4 Various joint-on-chip force modulation methods and forces induced 17
Table 2.5 Flow shear profiles by advantages and drawbacks 22
Table 6.1 Descriptive statistics of core flow/centrifugation data 105
Table 6.2 Performance comparison for target 405nm_alkP 121
Table 6.3 Performance comparison for target 488nm_VFz_abs. 122
Table 6.4 Performance comparison for target 560nm_alamB. 122
Table 6.5 Performance comparison for target 488nm_VF_FL. 123

List of Equations

Equation 3.1: Centripetal acceleration in terms of angular velocity in RPM units 39
Equation 3.2: Flow shear force for microfluidic channels 39
Equation 3.3: Adjusted Flow shear force for microfluidic channels 39
Equation 3.4: Gel Porosity in terms of gel volume and absorbed media volume 39
Equation 3.5: Cell Viability (alamarBlue^{TM} assay based) channels 42
Equation 6.1: Stats normalisation z-score, to infer distribution probability 113
Equation 6.2: Functional mapping from input vector for neural network 114
Equation 6.3: Mean Square Error (MSE) 114
Equation 6.4: Artificial Neural Network (ANN) for forward pass transformation 115
Equation 6.5: Deep Neural Network (DNN) transformation equation 115
Equation 6.6: Simple Neural Network (NN) transformation equation 115
Equation 6.7: Coefficient of Determination (R^2) 116
Equation 6.8: Root Mean Squared Error (RMSE) 116
Equation 6.9: Mean Absolute Error (MAE) 117
Equation 6.10: Local Interpretable Model-Agnostic Explanations (LIME) 118
Equation 6.11: SHapley Additive explanations (SHAP) 118
Equation 6.12: Randomised NN dropout probability p from uniform distributions 130
Equation 6.13: Randomised learning stochastic model space 130
Equation 6.14: DNN forward pass transformation equation 130
Equation 6.15: Total number of trainable parameters in a conventional DNN 130

Nomenclature

Acronym	Full term:		Acronym	Full term:
abs.	Absorption / absorbanace		LR	Learning Rate
AI	Artificial Intelligence		ML	Machine Learning
ANN	Artificial Neural Network		MSC	Mesenchymal Stem Cells
ANOVA	Analysis of Variance		MSE	Mean Square Error
ALP	Alkaline Phosphatase		MAE	Mean Absolute Error
ARS	Alizarin Red Staining		MAPE	Mean Absolute % Error
avg.	average		NN	Neural Network
BoC	Bone-on-Chip		NS	Not Significant
CS	CellShip		OA	Osteo-arthritis
CNN	Convolutional Neural Network		OoC	Organ-on-chip
DMOAD	Disease modifying drugs(s)		PCA	Principal Component Analysis
DL	Deep Learning		PLL	Poly-L-Lysine
DNN	Deep Neural Network		PMMA	Polymethyl-methacrylate
DT	Decision Tree		PSA	Pressure Sensitive Adhesion
ECM	Extracellular Matrix		R^2	Co-efficient of determination
FGF	Fibroblast Growth Factor		RA	Rheumatoid Arthritis
GelMA	Gelatin Methacryloyl		ReLU	Rectified Linear Unit
HA	Hyaluronic Acid		RF	Random Forest
HSD	Honestly significantly different		RGB	Red Green Blue
HEPES	N-2-hydroxyethylpiperazine-N-2-ethane sulfonic acid cell buffer		RGD	Arginine-Glycine-Aspartic acid (motif peptide), cell binding site
HAp	Hydroxyapatite		RMSE	Root Mean Square Error
HAMA	Hyaluronic Acid Methacrylate		RPM	Revolutions Per Minute
iPSC	induced Pluripotent Stem Cells		Std. dev	Standard Deviation
IGF	Insulin-like growth factor		SVM	Standard Vector Machine
iPSC	induced Pluripotent Stem Cells		SVR	Standard Vector Regression
JoC	Joint-on-chip		TGF-β	Transforming growth factor- β
LGBM	Light Gradient Boost Machine		VF	ViaFluor
LoC	Lab-on-chip		XG	Extreme Gradient

Table of Symbols and Units

Symbol	Term	Unit
*	Statistical significance	unity
A	area	cm^2
a_c	Centrifugal acceleration	m/s^2
b	Vector bias (for AI NN models)	Co-efficient
D	distance/width	µm
f	frequency	Hz
F	micro-flow rate	µL/min
Fs	Flow Shear	kPA
g	Gravitational acceleration	m/s^2
GF	Gel Fraction	%
h	height	µm, mm
p	p-value significance	significance
p	porosity	%
P	Pressure	Pa or N/cm^2
Q	Flow rate	m^3/s
R^2	Co-efficient of determination	Co-efficient
V	micro-volume	µL or mL
w	width	µm, mm
W	Vector Weights (for AI NN model)	Co-efficient
x_i	Sample z-score normalisation	Co-efficient
η^2	Effect size	Co-efficient
λ	wavelength	nm
λ	wavelength	nm
μ	viscosity (dynamic)	kg/ms
μ_i	Mean of sample i	value
ρ	density	kg/m^3
σ	Std. deviation	Co-efficient
ω	Angular	Radians / s
$\mathcal{L}$	Model loss	Co-efficient

Research Publications

Journal Articles

(1) B. Collins, D.Muhammed, M. Bendecache, T. J. Levingstone, and N. Dunne,

"*Curated Datasets for Machine Learning-Based Modelling of Stimulated Osteoblasts-on-chip*" (2025), Journal Proceedings of the 27th Irish Machine Vision and Image Processing Conference IMVIP 2025 Page 227 – 234

The datasets for this paper used to train the model sets fitting python scripts (derived from experiment cell culture data assay readings) is available on Github: https://github.com/Collib29/Collib29. Corresponding python coding scripts can be made available on this online repository.

Publications in Preparation

(1) B. Collins, P.Davoodi, D.Kinahan N. Dunne, and T. J. Levingstone

"*Development of a Bone-on-Chip Platform with Physiologically Relevant Loading and a tuneable Microenvironment*"

In preparation for submission to Lab on chip journal

(2) B.Collins, M.Turner, D.Renshaw, N.Dunne and T.J. Levingstone

"*Investigation of the effect of Flow and Centrifuge stimulation on osteoblast response in Bone-on-Chip with Media Protectant"*

In preparation for submission to Lab on chip journal

(3) B. Collins, D.Muhammed, M.Bendechache, N. Dunne and T. J. Levingstone,

"*Dual-Stimulation Bone-on-Chip Dataset and Explainable Randomised Deep Learning Framework for Osteogenic Mechanobiology*"

In preparation for submission to journal of Computer Methods and Programs in Biomedicine

Conference Presentations

(1) B. Collins, N. Dunne, and T. J. Levingstone "*Development of A Microfluidic-Based Joint-on-A-chip Platform for Cartilage tissue engineering applications*" 29th Annual Conference of the Chapter of Bioengineering of Royal Academy of Medicine in Ireland (RAMI), January 2023, Enfield, Oral Presentation

(2) B. Collins, D. Kinahan N. Dunne, and T. J. Levingstone "*Development of a Microfluidic-based Joint-on-a-Chip Platform for Tissue Engineering and Testing Applications*" Biomedical Round Table - Tissue Engineering and Drug Testing, 2024 FPSS National Conference, (Cork, Ireland, 7th February 2024). Oral dissemination and discussion at FPSS Feb 2024.

(3) B. Collins, D. Kinahan N. Dunne, and T. J. Levingstone, "*Development of A Microfluidic-Based Joint-on-A-chip Platform for Bone and Cartilage tissue engineering applications*" 31st Annual Conference of the Chapter of Bioengineering of Royal Academy of Medicine in Ireland (RAMI), January 2025, Athlone, Oral Presentation

(4) B. Collins, N. Dunne, M.Bendechache, and T. J. Levingstone "*Generation of Flow Centrifuged Bone in Gel Cell Culture Optimising Data with ML models*" Irish Machine Vision Image Processing (IMVIP) Conference Derry UK, Sep 2025. Oral Presentation

Poster Presentations

(1) Collins B, Levingstone TJ, Bendechache M, Kinihan D, Dunne NJ. "*Applied machine learning: Microfluidic Joint-on-chip*" Faculty of Engineering Research Day 2023. (Dublin City University, Dublin, Ireland, 20th April 2023).

(2) Collins B, Levingstone TJ, Bendechache M, Kinihan D, Dunne NJ "*Applied Machine Learning: Microfluidic Joint*", 2024 Particular Science QSense & Amp; QCM-D seminar (Dublin City University, Dublin, Ireland, June 19th 2024)

Development and Machine Learning-Based Optimisation of a Microfluidic Bone-on Chip Model

Brian Collins

Abstract

Traditional cell culture and animal models cannot reproduce the dynamic mechanical and biochemical environment of human bone, limiting studies of remodelling, osteogenesis and diseases such as osteoporosis. This PhD develops a microfluidic bone-on-chip (BoC) platform that combines an optimised hydrogel to create a 3D culture environment, combined with mechanical stimulation to promote osteoblast proliferation and differentiation. The aim of this research was to refine the BoC environment by systematically analysing cell responses to flow shear, cyclic loading, and incubation conditions. A prototype was designed, fabricated and validated for long-term use by leak and flow tests. MC3T3 pre-osteoblast cells were seeded and their responses were measured under varying conditions. Optimisation targeted a hydrogel coating with suitable composition and stiffness and adjusted oxygen and media (including a cell protectant supplement) to maximise viability, proliferation and long-term development under mechanical stimulation. The optimal setup used a 1 mm hydrogel of 10 % GelMA and 1 % HAMA under normoxia (19 % O2), with 10 % (w/v) cell protectant.

Multi-stage experiments evaluated combinations of centrifuge-based cyclic loading and flow shear, with and without cell protectant. Stimulated and supplemented cultures maintained higher levels of cell viability and proliferation than static controls. Flow stimulation had the strongest effect, increasing proliferation and differentiation by 60 to 100 % at 4 to 5 weeks, followed by interaction effects of cell protectant (30 to 45 %) and centrifugation (25 to 35 %) at later stages (5 to 7 weeks).

Machine learning (ML) models were then trained on experimental data for data-driven optimisation of in-chip bone tissue culture. Bayesian-optimised Random Forest models performed best (R2 = 0.93). Deep learning and neural networks were trained on extended data, of which Randomised deep learning was the best (R2 = 0.77 with the best output). PCA and Explainable AI methods (LIME and SHAP) clarified model behaviour and data. This work presents a novel BoC platform that integrates multimode dual mechanical stimulation with data-driven modelling, advancing strategies for bone tissue regeneration.

Chapter 1: Introduction

1 Introduction

1.1 Overview

Bone-related conditions such as osteoporosis [1], osteogenesis imperfecta [2], and Paget's disease [3] increase morbidity through impaired bone remodelling and higher fracture risk. One in three women and at least one in six men will experience an osteoporotic fracture in their lifetime [1], and 1 to 5 % of people over 50 years, depending on region and ethnicity, develop Paget's disease [3]. Other musculoskeletal diseases, including osteoarthritis (OA) and rheumatoid arthritis (RA), involve cartilage degradation and pathological changes in subchondral bone that critically drive disease progression [4]. OA, the most prevalent form of arthritis, impacts approximately 595 million individuals worldwide as of 2020, with incidence continuing to rise [5]. RA, an autoimmune condition affecting around 18 million people as of 2019 [6], is characterised by inflammatory joint destruction and systemic bone loss. In Europe, bone fragility and fragility fractures are the fourth leading cause of chronic diseases [7]. Symptoms often remain undetected until a fracture occurs [7]. Despite the prevalence of these musculoskeletal diseases, current treatment options remain inadequate, hindered by a limited understanding of joint tissue degeneration and insufficiently predictive preclinical models [8] [9].

Traditional two-dimensional (2D) and three-dimensional (3D) culture systems oversimplify the joint microenvironment and lack key physiological cues such as mechanical forces [10] [11]. Animal models, though informative, are costly, time-consuming, and often translate poorly to human disease outcomes [12]. Microfluidic lab-on-chip (LoC) technologies have enabled organ-on-chip (OoC) platforms that recapitulate organ-level functions *in vitro* under controlled conditions, offering a promising alternative for disease modelling and therapeutic testing [12]. Within this field, joint-on-chip (JoC) and bone-on-chip (BoC) devices mimic the mechanical and biochemical milieu of musculoskeletal tissues, enabling long-term cell culture, precise mechanical stimulation, and real-time monitoring [13].

Integrating artificial intelligence (AI), machine learning (ML), and microfluidic OoC data can improve the predictive modelling of complex multivariate biological systems [14]. Adaptive ML models can detect intricate interactions between culture conditions and tissue responses [15], optimising parameters to accelerate tissue growth and disease modelling. However, BoC platforms with multimodal mechanical stimulation and robust data-driven modelling remain underdeveloped.

This thesis develops a BoC platform with accessible multimodal force stimulation, enabling bone cell culture under diverse mechanical and incubation conditions while producing data for advanced ML models. The platform will provide a more physiologically relevant *in vitro* model for studying musculoskeletal diseases and screening therapeutics.

1.2 Thesis Outline

This thesis aims to develop a BoC microfluidic platform for sustained osteoblast culture under physiologically relevant multimodal mechanical stimulation, integrated with ML modelling for predictive analysis and optimisation. It is structured by the following chapters:

Chapter 1 introduces musculoskeletal diseases, the limitations of existing *in vitro* and animal models, and the rationale for advancing BoC platforms enhanced by ML.

Chapter 2 reviews the biology of bone tissue and current models used in musculoskeletal research, including OoC technologies and ML applications. It identifies gaps in BoC device development and modelling approaches, with emphasis on mechanical stimulation and support matrices.

Chapter 3 describes the design, fabrication, and validation of the BoC device incorporating tuneable GelMA/HAMA hydrogels optimised for osteoblast viability and differentiation. Details include microfluidic fabrication methods, hydrogel composition and thickness optimisation, mechanical characterisation and *in vitro* assessment.

Chapter 4 reports results from flow shear experiments, centrifuge-based cyclic compression, and combined multimodal mechanical stimulations on osteoblast-laden BoC cultures. Effects on cell metabolic activity, proliferation, and osteogenic differentiation are quantified.

Chapter 5 evaluates the impact of a cell protectant media on bone tissue development under mechanical stimulation, elaborating on optimal supplementation concentration and its effect on cell proliferation and mineralisation.

Chapter 6 evaluates the output from the mechanical stimulation experiments (Chapters 4 and 5), develops, optimises, and compares classical machine learning and deep learning regression models and explainable AI techniques for predicting BoC cell responses.

Chapter 7 provides an overall discussion, summarises findings, addresses data volume and model generalisability, and proposes future directions – including greater chip complexity, co-culture studies, and improved predictive models to advance translational musculoskeletal disease modelling and therapies.

Chapter 2: Literature Review

2 Literature Review

2.1 Bone Biology

Bone is an essential tissue that protects vital organs and stores minerals such as calcium and phosphate [16]. It is a highly specialised connective tissue containing osteoblasts, osteoclasts, and osteocytes, which continuously remodel bone [17]. This dynamic activity allows bone to adapt to mechanical stresses and repair microdamage [18]. Beyond its mechanical role, bone regulates mineral metabolism and acts as an endocrine organ by secreting signalling molecules [19]. Understanding bone biology is crucial for managing osteoporosis, osteoarthritis, and fracture healing, as the interaction between structure and function underpins skeletal integrity [20].

2.1.1 Bone Structure and Function

Bone consists of two primary structural types: cortical and cancellous. Cortical bone forms the dense outer layer of the skeleton, providing strength and resistance to bending and torsional forces through its tightly packed osteons [21]. In contrast, cancellous bone, located mainly at the ends of long bones and within vertebrae, has a porous trabecular architecture that optimises load distribution and facilitates metabolic functions such as mineral exchange and haematopoiesis [21] [22]. Within synovial joints, the subchondral bone, positioned directly beneath the articular cartilage in joints, plays a critical role in load transmission and joint stability [23]. The subchondral bone plate, a thin layer of dense cortical bone is located just under calcified cartilage (Figure 2.1) [24].

The entire structure functions as an effective shock absorber, transferring forces from the cartilage to the underlying bone (including cancellous bone) [24]. The osteochondral junction is the interface where load is transferred between the articular cartilage and the subchondral bone, and where the diffusion of nutrients occurs [25]. While subchondral bone is better vascularised, articular cartilage remains avascular, relying instead on diffusion from synovial fluid for nutrition [26]. Given the structural and functional role of bone tissue in joints, its degeneration plays a key role in arthritic diseases [27].

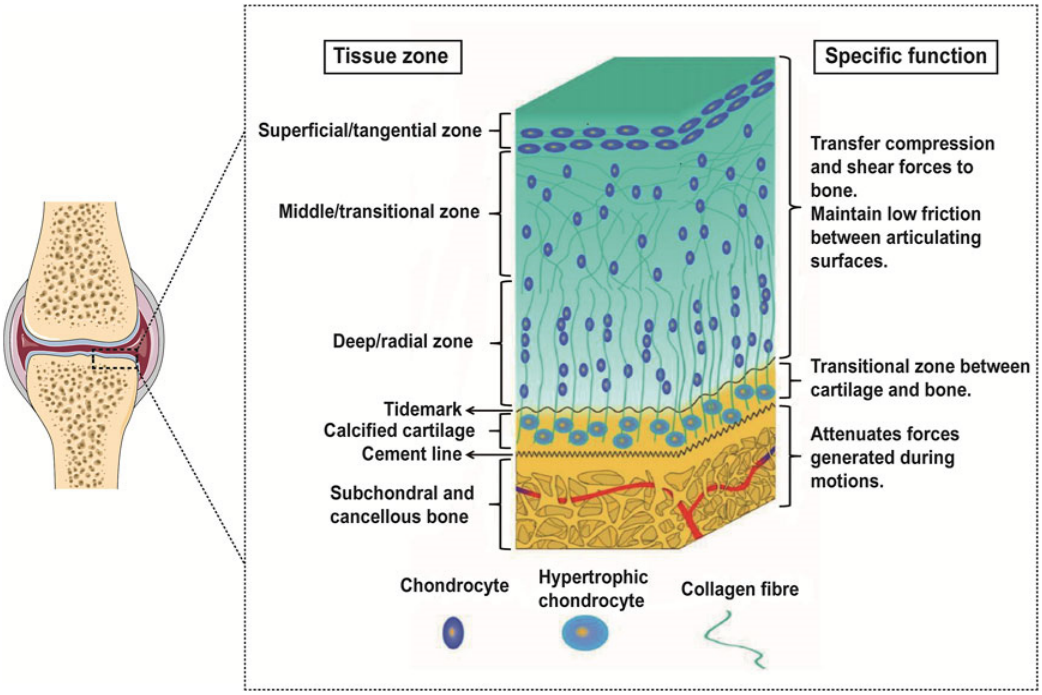


Figure 2.1 Anatomy of the cartilage and subchondral bone structure [24]

2.1.2 Bone Pathologies

Osteoporosis, one of the most common bone diseases, involves reduced bone mass and microarchitectural deterioration, greatly increasing fracture risk in the spine, hip, and wrist [28]. In contrast, osteopetrosis, a rare genetic disorder, causes abnormally dense but brittle bones due to defective osteoclasts [4]. Paget's disease of bone disrupts normal remodelling, producing enlarged, deformed bones with impaired mechanical strength [4]. Other bone conditions include osteogenesis imperfecta, a genetic disorder causing brittle bones [2], and osteomyelitis, an infection that can cause bone destruction and systemic complications [29]. Bone cancers, such as osteosarcoma [30], and metabolic disorders like hypophosphatasia further illustrate the complexity of skeletal pathologies.

Joint diseases such as OA cause cartilage degradation and subchondral bone remodelling, creating a reinforcing cycle of mechanical stress, inflammation, and structural failure [31]. Understanding these processes is critical for developing new therapies [31]. Bone-based pathology in OA is shown in Figure 2.2 [32]. OA can transform subchondral bone from a dynamic, load-adaptive structure into stiff, sclerotic, disorganised tissue with cysts, marrow lesions, and increased vascular or synovial infusion [31]. Key changes include subchondral sclerosis—thickening and hardening of the subchondral plate due to increased osteoblast activity and excessive bone formation [32] —and trabecular bone remodelling, with thinning, fragmentation, and loss of trabeculae, increased porosity, and higher susceptibility to microfractures and shear stress [33].

Additional alterations include bone marrow lesions and subchondral bone cysts, fluid-filled cavities within the subchondral or trabecular bone. [32].

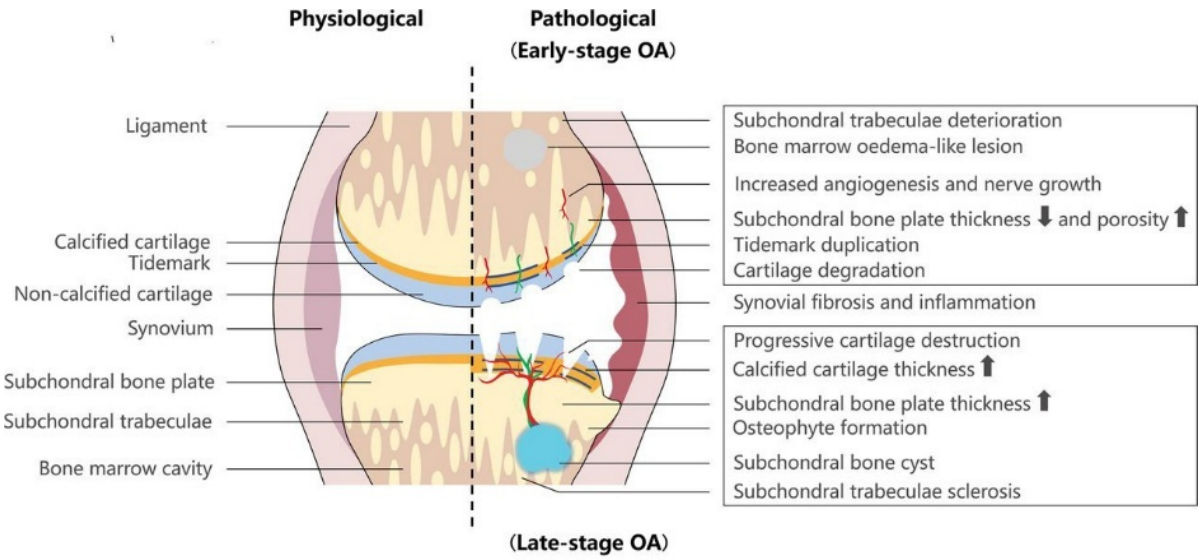


Figure 2.2 Arthritis and degeneration of joint subchondral bone tissue [32]

Beyond OA bone damage, pro-inflammatory cytokines and enzymes from the synovium and deeper bone further injure cartilage–bone junctions, amplifying inflammation, joint disruption, and ongoing tissue damage [34]. New strategies to slow this aspect of OA progression include targeting subchondral bone remodelling to prevent bone loss [31] and applying rejuvenation or regenerative approaches to affected bone [35]. RA, another common form of arthritis, is an autoimmune disease in which the immune system attacks the joint lining, causing inflammatory joint damage and systemic bone loss with similar degeneration to OA [6] [36].

2.1.3 Current standard *ex/in vivo* models

Cell culture is a widely used *in vitro* tool for studying cell biology, disease mechanisms, drug action, protein production, and tissue engineering [38]. Most bone biology and bone disease research uses cells grown in 2D on tissue culture plastic, but there is an increasing shift toward 3D cultures [37]. 3D models provide an environment that more closely mimics the complexity of living human tissue [37]. 2D cultures also do not adequately replicate the mechanical cues of surrounding cells and the extracellular matrix (ECM) [38], [39]. These issues are especially important in tissues where mechanical cues from neighbouring cells and the ECM are critical such as for bone or cartilage. These limitations have led to models that better mimic *in vivo* conditions, including 3D cultures, *in vivo* (animal or human)

models, and organ-on-a-chip (OoC) systems [12][37]. The pros and cons of 2D and 3D culture models and animal models are summarised in Table 2.1.

Table 2.1 2D vs 3D *in vitro* cell culture systems, versus animal models [37]

Model	Advantages	Disadvantages
2D	- Cost effective - Easy to use - Convenient - Easy downstream processing	- Less biologically relevant models - Reduced cell to cell interactions
3D	- More accurate representation of *in vivo* tissue - Increasingly relevant cell-to-cell and cell to ECM signalling - More applicable drug resistance models	- Added expense - More complex culture system & downstream processing
Animal	- Most accurate replication of *in vivo* tissue modelling - Can examine effect of connected organs or systems e.g. immune system	- High costs - Long experimental timeframe - Translatability from animal to human studies

3D cell cultures represent the biological environment more realistically, enabling better understanding of complex cellular biology and the analysis of biomarkers or targeted therapies [37]. However, their greater complexity increases the demands for culture maintenance and monitoring. Recent 3D models include spheroids, scaffold-based systems, bioreactor-based systems and organoids [40]. Spheroids are simple 3D extensions of 2D cultures, grown as small aggregates [41]. Scaffold-based systems culture cells on 3D porous or skeletal scaffolds made from materials such as hydrogels, porous gelatin, agarose, or composite fibres [42]. Bioreactors enable closed-loop 3D culture with improved environmental regulation and control [43]. Organoids are more advanced, multicellular (often heterogeneous) structures that can mimic tissue organisation [40], [43]. Despite these advances, 3D cultures still differ significantly from *in vivo* tissues, for example in their inability to reproduce relevant dynamic forces [11]. Developing physiologically accurate tissue models is crucial for improving disease and drug research, especially early safety and toxicity testing [44]. In contrast, organ-on-chip (OoC) models address these limitations via microfluidic platforms that replicate key human tissue functions in a controlled, dynamic environment [11]. Combining mechanical, biochemical and structural cues, OoC systems offer a sealed, fluidically controlled setting for precise, reproducible assays and are a promising alternative to static 3D and animal models. [45].

2.1.4 Cell Stimulation and Mechanotransduction

The underlying mechanisms for cell response to mechanical stimulation/modulation have been reported in detail by Polacheck *et al*. [46]. Fundamental characteristics of bone tissue development include bone cell lineage commitment, differentiation and functional evolution. A detailed review of osteogenesis, the process and stages of bone development and formation is provided by Liu *et al.* [47]. During osteogenesis, a sequential differentiation occurs in osteoblast lineage cells, progressing through four distinct sequential stages [47]:

1. Commitment: Mesenchymal Stem Cells (MSCs) commit to the osteoblast lineage
2. Proliferation: Committed cells proliferate and begin expressing early markers
3. Maturation: Cells mature and express additional bone-specific proteins
4. Mineralisation: Matrix mineralisation occurs, completing bone formation

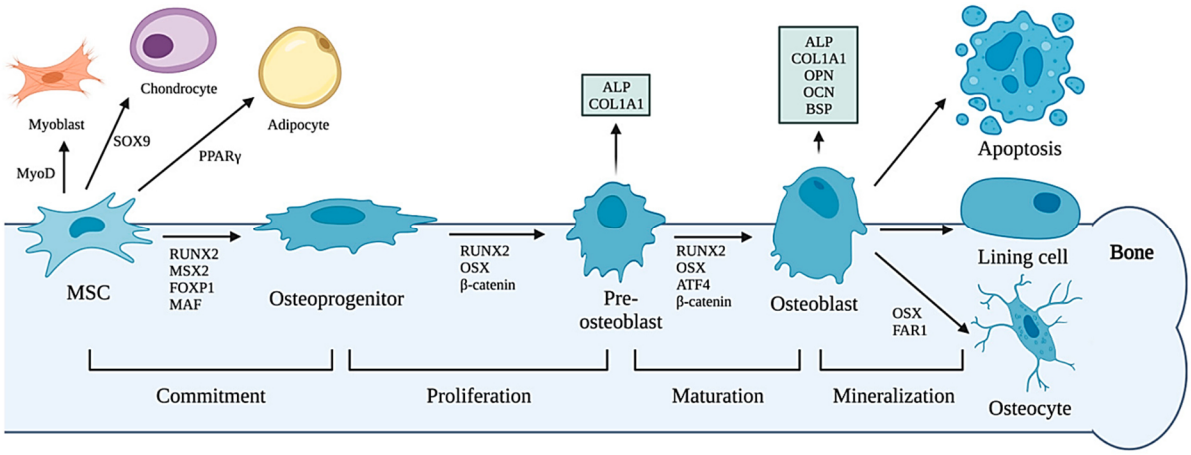


Figure 2.3 Schematic representation of the differentiation of osteoblast lineage cells and four corresponding differentiation stages to mature developed bone tissue [47]

Mesenchymal stem cells (MSCs) can differentiate into joint tissue cell types (osteoblasts, fibroblasts, adipocytes, chondrocytes), a process regulated by specific transcription factors [47]. Increased RUNX2 expression in progenitor cells drives differentiation into pre-osteoblasts and the osteogenic lineage [47]. At this stage, cells typically express Collagen type I alpha 1 (COL1A1) [47], and alkaline phosphatase (ALP) activity rises in parallel with bone development [47] [48]. During osteoblast maturation and mineralisation, expression of Bone sialoprotein (BSP), Osteocalcin (OCN), ALP and COL1A1 increases. Some markers have functional roles: ALP hydrolyses the mineralisation inhibitor pyrophosphate into phosphate, promoting mineral deposition [47] [48]; OCN maintains bone crystal structure, mineral density and strength; BSP promotes crystal formation; and OPN inhibits hydroxyapatite (HAp) formation and modulates MSC differentiation into

osteoblasts, helping balance osteoblasts and bone-resorbing osteoclasts [49]. Osteoblasts are anabolic and help build bone while osteoclasts are catabolic and break down unnecessary bone tissue or damaged/inflamed bone tissue as part of bone remodelling. The RANKL/OPG gene expression ratio controls the extent of bone break-down or remodelling [50]. The majority of mature osteoblasts embedded in mineralised matrix become osteocytes, the main mechanosensitive bone cells, forming the lacunar-canalicular mechanotransduction system. [50]. A small portion of osteoblast cells become lining cells or otherwise undergo apoptosis or break down from osteoclasts if further bone remodelling is needed. This mechanism between these cell types provides a balance for the amount of bone tissue grown or more mature bone a balance of the amount of bone tissue repaired or maintained [50].

The adaptive sensory system transmits mechanical signals to osteoblasts and other cells by releasing molecules such as ATP, prostaglandin E2, nitric oxide, and growth factors, enabling adaptive maturation of cells and tissues [51]. Figure 2.4 by Zuela-Sopilniak & Lammerding [51] illustrates the range of mechanical forces on *in vivo* bone cells.

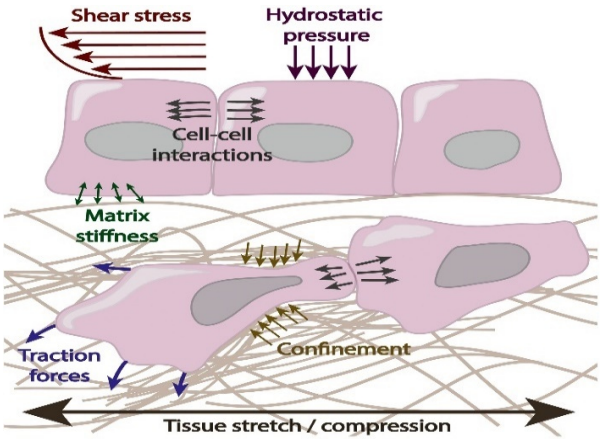


Figure 2.4 Schematic showing mechanical forces on *in vivo* bone cells: flow shear stress, hydrostatic (compressive) pressure and cell or ECM interactions cause confinement (compression) and traction (tensile) forces (reproduced) [51]. These net forces initiate mechano-transduction.

Figure 2.4 shows the range of static and cyclic forces (with varying frequencies and timescales) experienced by bone cells. Shear stress, pressure, and cyclic compression/confinement are the most relevant to bone cell loading and mechanical degradation of tissue in OA [52]. Many cell membrane receptors and ligands exist in all cell types, especially in joint cells such as bone and cartilage, which experience these mechanotransduction forces more intensely and frequently than most other cells [53]. Mechanical stimuli directly influence MSC differentiation, and as noted, osteoblasts and osteocytes are the main mechanosensitive cells in bone, with the lacunar–canalicular system being the key substructure for mechanosensing [47] [51].

Cells respond to mechanical signals (including physical forces such as flow shear, ultrasonic waves [54], and electromagnetic waves [55]) through various mechanisms (Table 2.2). There are additional receptor types that also sense the listed mechanical forces enacted on bone cells [50]. Cilia membrane tubules can sense flow shear across cell surfaces [50]. Examples include caveolae that interact with integrins to sense mechanical forces from the ECM; cadherins, which are not connexin gap junctions but sense and transmit mechanical forces at cell boundaries; and pannexin channels, membrane-based reactive channels that balance ATP [50]. Figure 2.5 elaborated by Choi *et al*. [50] gives a detailed schematic layout of such typical cell surface features of such mechanically stimulated cells. Stuart *et al.* [56] give a more specific discussion of various bone cell receptors (illustrated Figure. 2.5) with their associated expression pathways and their role in mechano-transduction.

Table 2.2 Comparison of cellular sources of mechanical force modulation in cells [50]

Cell Feature	Composition & Function	Force Response
Integrins	Transmembrane proteins with non-covalently linked α & β subunits	Tensile Force, Fluid Shear
Piezo Channels	Mechanosensitive calcium channels	Tensile, compressive forces, pressure
Primary Cilia	Protruding membrane tubules	Fluid shear
Connexins	Transmembrane proteins assembled in groups of six to form a gap junction or hemichannel (connexon)	Tensile, compressive forces
Connexins - Gap Junctions	Mechanical stimuli switch gap junctions between cells to open	Force transmission
Connexins - Hemi-channels	Similar to gap junctions but for mechanical sensing / transmission	Force transmission
Cadherins	Cell-cell adhesion proteins that directly sense intercellular mechanical tension / forces. Required as part of cell adhesion and bone surface building.	Force sensing and transmission (allow adhesion with ECM peptides)
Pannexins	Membrane ion channels that emit chemical signalling to the ECM and more distant cells for mechanical force transmission	Force transmission

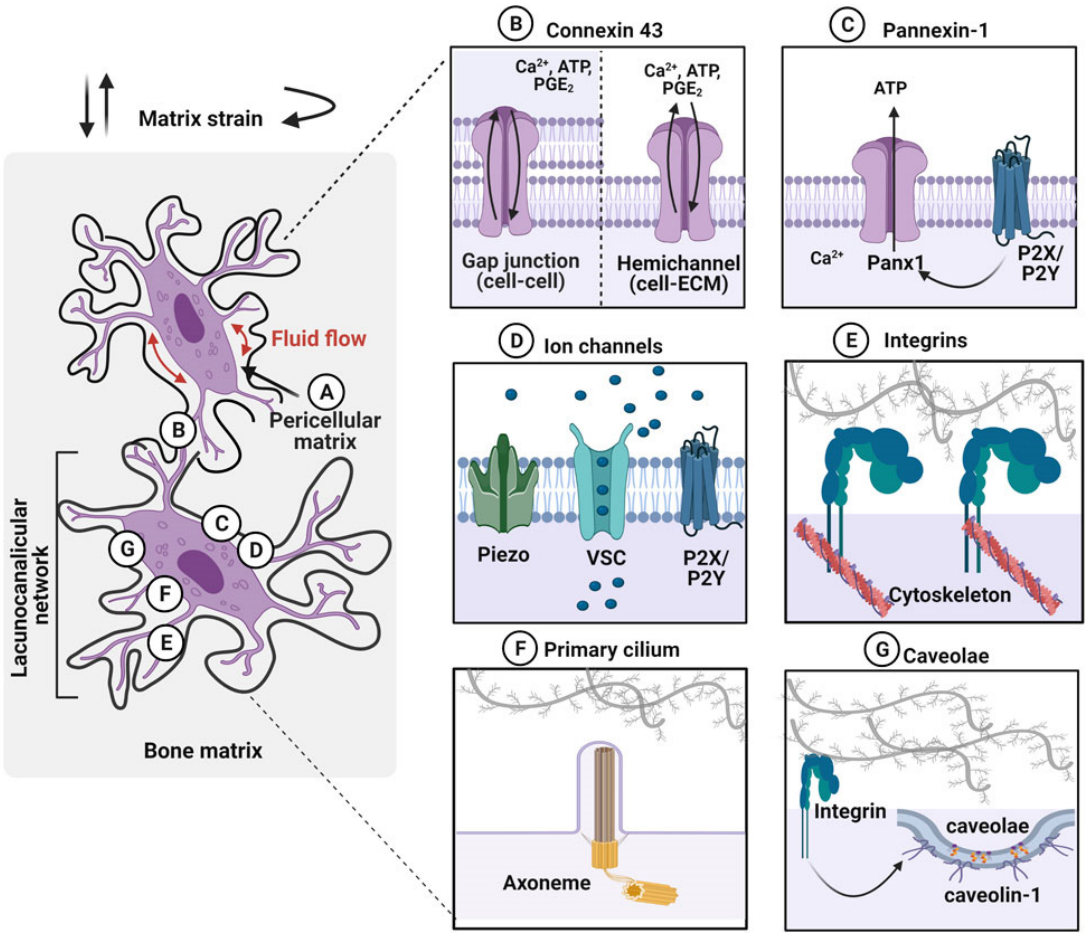


Figure 2.5 Schematic components of the bone mechanosensory system, illustrates connexins or pannexins for force transmission, ion channels and integrins for force sensing and cilium for fluid shear sensing [50]

In cell mechanotransduction studies, 3-day cultures are typical for short experiments, whereas up to 14 days is common for promoting MSC differentiation or culturing reprogrammed cells [57]. Post-differentiation mineralisation studies often last 4 to 5 weeks [58]. In OoC devices, the optimal duration of culture depends on the microfluidic well size, the number of cells, the growth methods, the medium, and any added therapeutics. Studies longer than 5 weeks may extend the testing window to examine bone remodelling or bone breakdown with support material, depending on support material durability, but risks of longer term contamination need to be considered.

2.2 BoC Technology

2.2.1 Evolution of Organ-on-Chip and BoC Systems

OoC systems are microfluidic platforms that contain engineered or natural miniature tissues, designed to control cell microenvironments and mimic human physiology [59]. OoC technology integrates four core components: (1) microfluidics and microfabrication, (2) sensors and micro-control systems, (3) biomaterials, and (4) cell culture techniques [60]. Microfluidics enables the manipulation of liquid volumes as small as 10^{-9} L, allowing precise control of flow dynamics and concentration gradients for the delivery of nutrients or drugs. Microfabrication methods include photolithography, replica moulding, micro-contact printing, micro-CNC and 3D printing technologies [60] [61]. Figure 2.6 presents a brief high-level history of OoC technology development.

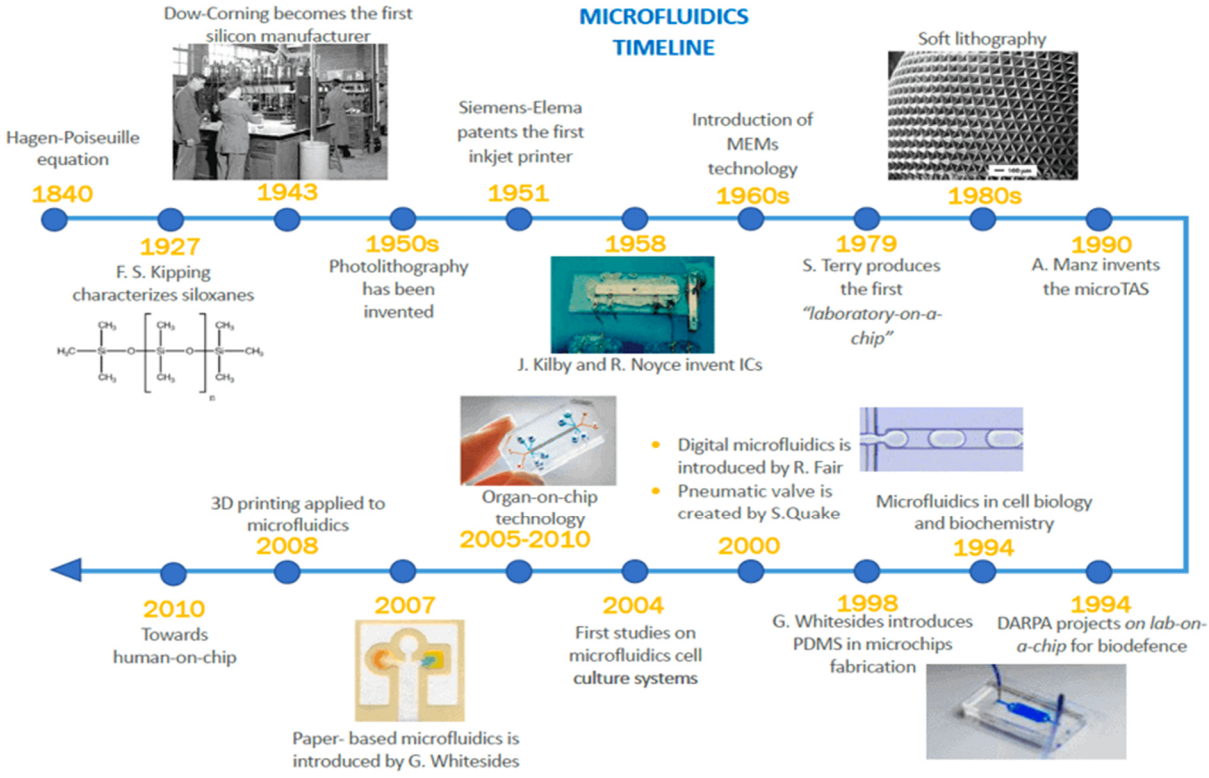


Figure 2.6 Brief history of background microfluidic technology development until 2010s OoC [62]

2.2.2 Microfluidic Design Considerations for BoC

OoCs are highly multidisciplinary and require many integrated design considerations for effective products. This section focuses on design considerations for bone and cartilage tissues. Key application-specific challenges in modelling and testing include:

- **Simplified design** and **scale reduction** requiring less material/agents, optimally uses low-cost materials and techniques.
- Appropriate choice of biocompatible **materials and structure for cell environment**
- Accurate re-creation of the synovial or blood flow **fluidic system**
- Accurate and reliable longer term **force actuation**
- Accurately recreate **cell nutrient signalling** for **cell differentiation/proliferation**
- Reliable and precise OoC biochemical-fluidic **monitoring and imaging**

2.2.3 Materials

Key advances in microfluidic technology in recent years have resulted from the development and introduction of new materials. Conventional OoC platforms use glass or silicon surfaces, which offer excellent optical clarity and chemical stability but require specialised high-cost equipment for fabrication and offer poor physiological relevance. New polymer-based materials, such as polydimethylsiloxne (PDMS), polymethyl methacrylate (PMMA), polycarbonate (PC), and poly-vinyl (PVC), enable easier fabrication, surface modification, and scalable high-throughput use. PDMS is widely used due to its low prototype cost, flexibility, transparency and biocompatibility but it does not scale well for larger volume production or batch consistency [63]. PMMA is a competitive low-cost alternative for OoC applications [64]. PMMA retains good transparency for OoC imaging with sufficient cut quality for features such as mid-scale microfluidic channel sizes [65] (around 500 μm in scale or width).

Key challenges in the fabrication of OoC platforms with small scale features e.g. channel cross sections below 100 μm, is sourcing low-cost, high quality microfluidic components, and machining such features with low-cost, accessible cutting tools [66]. This can be particularly challenging without access to advanced soft lithography, relying instead on common methods like laser cutting and micro-milling [67]. Table 2.3 outlines their advantages and disadvantages and providing a detailed comparison of OoC materials [68].

Table 2.3 Compared advantages and disadvantages of microfluidic channel materials [68]

Materials	Advantages	Disadvantages	Typical Use
PDMS	- Low Cost - Optical transparency - Elasticity - Biocompatibility	- Absorption small molecules - Difficult for mass production - Swells or degrades in many organic solvents	- High volume manufacturing of microfluidic chips
Thermoplastics e.g. PMMA	- Optical transparency - Mass production - Cost-effective - Mechanical stability	- Limited solvent resistance (crazing) - Low gas permeability	- Rapid Prototyping of cell culture devices
Glass	- Optical transparency - Chemically resistant - Biocompatibility	- Complex fabrication - Not gas permeable - Brittle	- Analytical chemistry chips and devices

Despite the successful application of the polymer materials discussed above, direct cell culture on these polymers often results in poor adhesion and limited biocompatibility. To overcome this, coatings such as collagen, gelatin and poly-L-lysine have been applied to improve cell adhesion and proliferation [69], [70]. Despite these improvements, models with 2D coatings remain inadequate for replicating the complex 3D architecture of *in vivo* tissues or longer cell culture experiments [71].

2.2.4 Mechanical Stimulation

The application of dynamic loading to bone cells can be achieved in various ways, including fluid flow stimulation, external mechanical actuation, pneumatic/hydrostatic loading, centrifugal loading and non-contact methods such as ultrasound or electromagnetic stimulation. Hodgkinson *et al.* reviewed multiple approaches to modulating force on bone or cartilage samples in microfluidic systems including vacuum-expanded elastic supports for axial strain, hydrostatic loading for compression, and microfluidic pumping or cone viscometers for fluid shear (Figure 2.7) [52]. Most mechanical force stimulation methods require custom equipment or specialised expertise. In addition to the mechanical and perfusion flow device methods described in Figure 2.7, several other alternative non-contact

mechanical stimulation methods have been investigated *in vitro, in vivo* and in clinical studies.

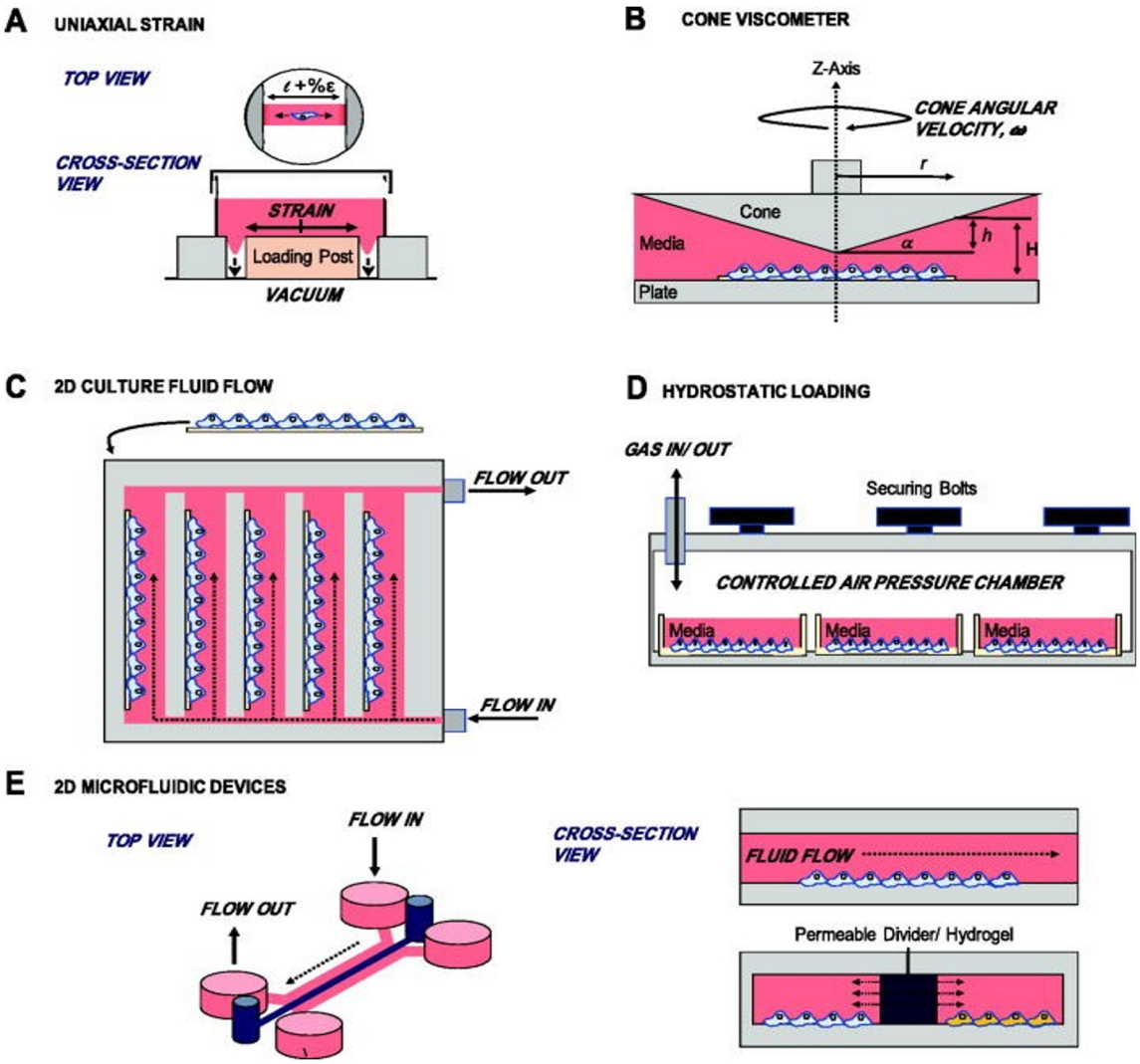


Figure 2.7 Mechanical force modulation methods include strain (vacuum-strained elastic support), compression (hydrostatic loading), and fluid shear (microfluidic devices or cone viscometer) [52]

A desirable practical alternative to method to apply cyclic loading for compression (cyclic compressive forces) are centrifuge based systems that is a simpler method with minimal instrumentation, efficient, scalable and easy to automate with precise control [72] [73]. Non-contact Low-intensity pulsed ultrasound (LIPUS) is a clinically validated approach [54]. Using this technique with microbubbles Aliabouzar *et al.* reported a 40 % increase in human bone mesenchymal stem cells proliferation *in vitro* and 78 %- increases in collagen type II expression compared to static controls [74] . Electromagnetic field stimulation is another method to modulate bone cell growth [75], where Lin *et al.* reported a 24 % increase in osteoblast cell proliferation and 34 % increase in cell viability after applied low frequency magnetic field stimulation for 9 h [76]. Piezoelectric actuator-based systems can deliver

precisely controlled cyclic compression or tension at frequencies of 0.1-10 Hz through direct contact loading, achieving effects comparable to fluid shear [77]. Hydrostatic pressure systems demonstrated larger effect sizes (1.5-2-fold osteogenic marker increase) and have been shown to be useful for early differentiation [78]. However, piezo-electric actuators or hydrostatic systems require more specialised equipment or customised devices and are highly contact based which poses a sterility risk.

A further summary of typically used force modulating techniques on cartilage or bone has been reported by Bahn *et al*. (Table 2.4) [69]. To the authors knowledge, the only multi-modal stimulation OoC study that used combined compressive and bulk shear stimulation was conducted by Paggi *et al.* [79] was conducted only on chondrocyte cells. Thus, it is important to investigate and understand combined stimuli for bone mechanotransduction [69][80].

Table 2.4 Various joint-on-chip force modulation methods and forces induced. Modified from [69]

Mechanical & Fluidic Integration	Compressive	Bulk Shear	Hemodynamic Shear Stress	Cell Type
Lee *et al.* [81] Pneumatic deflection of a PDMS membrane for static / dynamic unconfined compression	Yes	No	No	Chondrocyte
Occhetta *et al.* [82] Pneumatic deflection of a PDMS membrane for defined 10 or 30 % confined compression	Yes	No	No	Chondrocyte
Paggi et al. [79] Pressure – controlled inflation chambers for lateral compression or shear stress	Yes	Yes	No	Chondrocyte
Lin *et al.* [83] [84] [85] Microfluidic base, bioreactor insert, mechano-activated lid assembly	Yes	No	No	Osteoblast, Chondrocyte, Fibroblast
Mondadori *et al.* [86] Fluid flow-driven shear stress on endothelial monolayer	No	No	Yes	Chondrocyte, Fibroblast

Other studies used either compressive force–based or fluid shear stimulation, but not both. The closest studies to combining stimulation modes for bone tissue included a study by Kim *et al*. [87] and reviewed by Middelton *et al*. [88], applied non-focal hydrostatic pressure via a fluidic chamber or applied flow-induced shear on 3D cultured trabecular bone cells. This study did not apply both modes of stimulation together, just compared them individually and

lacked a dedicated compact microfluidic BoC platform for long term culture. It was found that fluid shear stress had a greater effect on alkaline phosphatase activity and osteogenic expression than compressive strain. Another study by Lovecchio *et. al* that used dual stimulation on human bone MSC on chitosan coated graphene templates was also within a compact standalone bioreactor rather than an OoC with low shear from larger channels [89]. The study increased ECM mineralisation 3-fold compared to static samples after 1 week of stimulation (1 % compression at 1 Hz for 30 min twice daily plus low-shear 1 ml/min continuous perfusion). As discussed in Section 2.1.4., bone cells have multiple cell receptor types (e.g. primary cilia, ion channels, and integrins) that respond in different ways to mechanical stimulation. Further study of combined mechanical stimuli is thus critical to better understand osteogenic responses. While previous studies have focussed on static or single-mode stimulation only, a combined bone cell stimulation study for BoC could provide greater insight into optimal approaches for bone cell stimulation.

In addition to considering force stimulation methods and combinations, the loading pattern and the general regimen for loading or flow shear should be considered [90]. The loading duration, frequency and timing have been considered in research studies by various authors. These considerations are critical for accurately modelling *in vivo* forces on bone or joint tissue during walking. Stavenschi *et al.* applied oscillatory fluid flow of different magnitudes (1 Pa, 2 Pa and 5 Pa from base level), frequencies (0.5 Hz, 1 Hz and 2 Hz), and durations (1 h, 2 h and 4 h) to bone MSCs cultured on a 2D fibronectin coat and found that physiological shear cycle at 2 Hz (with 2 Pa for 2 h) most significantly increased osteogenic markers such as RUNX2, COX-2 and ALP expression compared static controls [90]. Carriero *et al.* investigated the gait cycle (the repeated pattern of forces acting on a joint from walking) and modelled the ranges of knee force magnitude, variation, pattern per stride cycle for healthy adults and adults with cerebral palsy (Figure 2.9) [91]. The study used a finite element model that predicted altered forces during walking in children with cerebral palsy affect hip bone growth, resulting in increased twisting and a more upright femoral shape [91]. A study review by Crowell *et al.* then found that a frequency range of the gait cycle from various studies is about 0.8 to 2.1 Hz per single stride [92]. These force magnitudes, patterns and frequencies have been explored through various mechanical stimulation methods including varied spin rate centrifuges or oscillating flow shear systems [90]. Centrifuging cell media on adhesive cells with a flow or load spin cycle on the order of 1 Hz mimics this frequency and is also consistent with a Rindt *et al*. [93] study that tested compressive loading at 1 Hz for a 3D bone bioreactor system for 3 weeks.

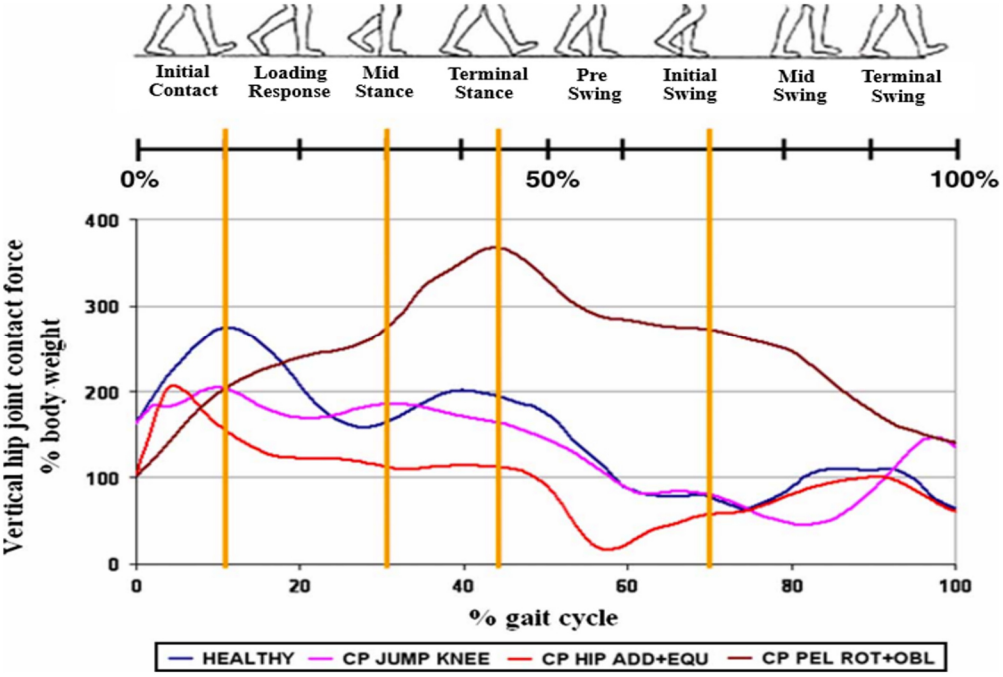


Figure 2.8 Gait cycle dynamic loading pattern, a variety of knee and hip joint based forces as a percentage of human body weight (average), with distinguished chart series of healthy joints and cerebral palsy effected joints (CP JUMP KNEE), (CP HIP ADD+EQU) and (CP PEL ROT+OBL) CP=Cerebral Palsy, HIP ADD + EQU = Hip Adduction & Equinus, PEL ROT + OBL = Pelvic rotation & obliquity [91]

Various mechanical stimulation methods replicate the loading frequency of walking, including centrifuge, hydrostatic, and actuator-based loading [52]. A centrifuge with a set spin rate can conveniently and minimally invasively load samples using standard lab equipment [94], and can apply GAIT like cyclic loading. This low-cost method offers an adjustable force amplitude and frequency for a wide range of test conditions [94], [95], and its setup, programming, and configuration are generally simpler than many actuator systems [94]. Given the limited centrifuge testing and optimisation on BoC samples to date, there is an opportunity to further investigate this with a suitable BoC platform.

Another issue to consider is that body weight, torque or compressive loads can vary on joints depending on the subject (demography, size or BMI and disease state) and can also vary depending on joint type as well as joint region [91] [92]. This can pose a challenge when making direct comparisons to other studies when this set of factors are not considered. A more closely universal metric that measures what an entire joint experiences, that varies less by subject but varies more by subject action (e.g. walking or running) is needed. Lafortune *et al.* resolve this by comparing tests and studies by joint bulk acceleration that will have similar values for a given joint type and have a similar consistent range for a given action such walking or running [241], and guides acceleration ranges for BoC centrifuge systems.

2.2.5 Flow Stimulation

A well-designed microfluidic system is crucial to replicate the cellular shear flow and provide nutrients [96]. In BoC platforms, it can provide constant, oscillatory, pulsatile, or adaptive flow with adjustable frequency and duration [90], and the required regimen dictates the choice of flow supply method. Pumping systems (injection, pump, control and tubing) typically operate at 10^{-6} to 10^{-12} L/s with defined pressure ranges, flow durations, and high-precision control [97]. Syringe pumps are widely used in LoC and OoC applications [98], enabling precise, time-controlled flow. Biocompatible PTFE micro-tubing with a 0.5 mm internal diameter is commonly used for fluid delivery [99], smaller diameters are available but are more expensive and may increase capillary-related flow losses [99]. At the microscale, connecting 0.1 to 1 mm tubing to PMMA or PDMS chips requires air- and fluid-tight biocompatible polymer luer sealants [99].

A range of long-duration flow rates has been examined for chip validation. Vereshchagina *et al.* [100] tested HL60 cells (human promyelocytic leukemia cell line derived from peripheral blood) and chip stability at 5 to 500 µL/min. Bancroft *et al.* quantified calcium deposition by osteoblast cells within mineralised matrices under flow conditions of up to 3000 µL/min for 16 days [101], though the maximum usable flow depends on adhesion type, support material, and tissue maturity. Longer bone cell cultures (over 21 days) use lower flow rates for proliferation, with more than 0.01 mL/min favouring proliferation and 0.2 mL/min promoting differentiation [102]. A meta-study by Wittkowse *et al.* reviewed osteocyte and osteoblast responses to 0.01 to 3 Pa fluid shear that covers the full range of in-vivo flow shear experienced and found effects depended on shear level [103]. Low shear (less than 0.1 Pa) increased proliferation, mid-range shear promoted calcium mineralisation and differentiation, and high shear enhanced osteogenic gene expression [103]. Fluid shear stress promotes osteogenic gene expression in bone progenitor cells, but the relationship between flow shear magnitude and mineral deposition is non-linear, moderate physiological magnitudes (e.g., 0.5 Pa) can maximise both gene expression and mineralisation [104]. Although higher shear magnitudes do not further increase this and can even disrupt and reduce mineralisation despite continued mechanotransductive signalling [104] [105]. Although most studies use 0.5 to 1.5 Pa, fewer examine low to mid-range shear (Figure 2.7). Limraksasin *et al.* subjected a 6-day old murine iPSC 2D cell cultured to 2 days of continuous steady flow shear (0.15, 0.5 and 1.5 Pa) and showed 0.5 Pa was optimal for osteogenesis with a 50 % increase in ARS detected matrix mineralisation compared to static controls, or a 20 % increase from 1.5 Pa shear stimulated samples [104]. More recently,

Leclerc *et al.* used a fibronectin-coated PDMS microfluidic chip with 0.05 to 0.35 Pa shear for up to 2 weeks and found the highest viability at the lowest shear [106].

Spatz *et al.* found that mechanical loading via fluid shear stress (0.05 to 0.2 Pa for 2 h to 3 days) decreased SOST (bone formation inhibition) expression by 75 to 100 % in osteocytes on 2D ligand coats to allow bone formation, [107]. Kreke *et al.* [108] examined osteogenic gene expression of BMSCs cultured on 2D collagen surfaces over 3 weeks with continuous and intermittent steady flow shear (5 mins on/off) of 0.23 Pa applied for 24h, reporting similar increased expression of osteopontin (OPN), bone sialoprotein (BSP), and osteocalcin (OCN). Intermittent flow increased PGE_2 (bone differentiation and formation signal) compared to continuous flow. Vis *et al.* [109] explored the influence of 0.01 to 0.045 Pa average. surface shear stress on the osteogenic response of human BMSCs cultured on a fibronectin-coated microfluidic BoC over a 5-week timeframe. This corresponded to strains of 4.7×10^{-4} to 6.7×10^{-3}, comparable to the 1×10^{-4} to 1×10^{-3} range optimal for bone healing [110]. Flow stimulated samples showed increased expression of RUNX2 (x1.5) and OPN (x1.9) at 21 days compared to static controls. Few studies have investigated osteoblast response at mid-shear (0.1 to 0.5 Pa), especially for long-term or 3D cultures (Fig 2.9).

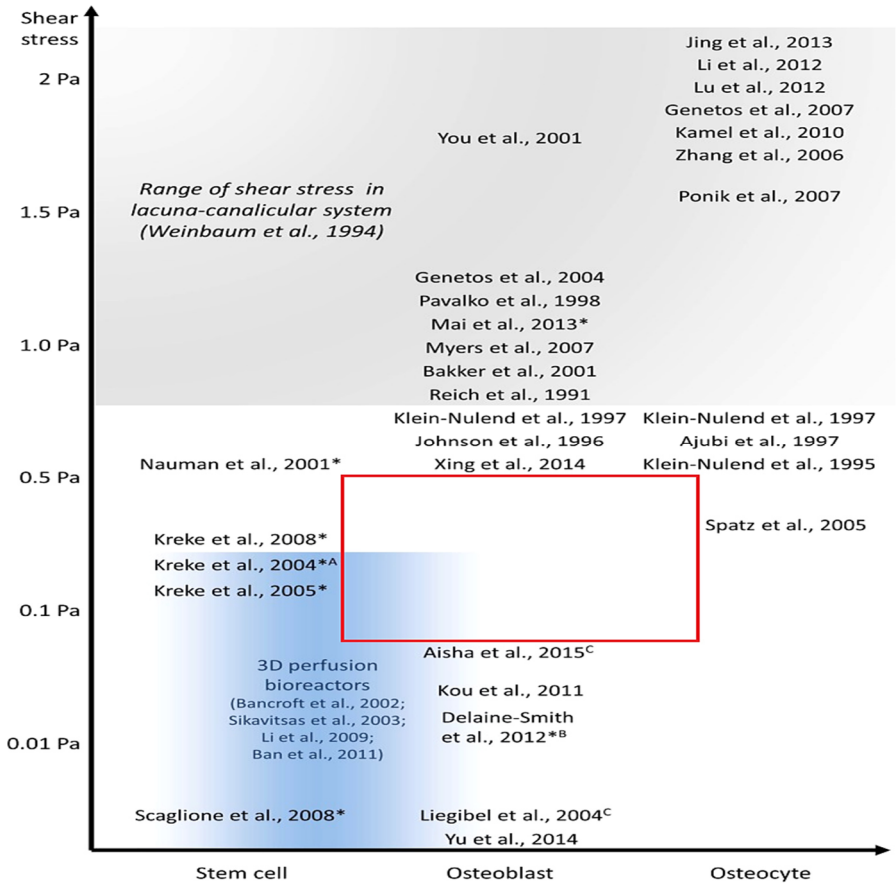


Figure 2.9 A range of flow shear stimulation in bone cell studies compared, low shear stress studies are in lower blue section, high shear stress studies are in upper grey section while intermediate shear stress studies are in mid white area. Osteoblast study gap in flow shear range highlighted in red [103]

A further flow shear study by Jaasma *et al.* [111] examined how flow type and frequency affect the osteogenic response of osteoblasts, finding that pulsatile flow produced the strongest response and that a 1 Hz flow frequency increased cell responsiveness. Osteoclasts were more sensitive to flow stimulation than osteoblasts. They also reported that increasing shear stress to 0.75 Pa elevated osteoblast COX-2 expression 1.2 to 3-fold that of the no-flow condition [111]. Dynamic flow patterns, such as oscillatory and pulsatile flow, are potent stimulators of bone cells *in vitro*, often more effective than continuous flow [111]. Both steady and oscillatory flow enhanced osteoblast differentiation and upregulates key bone formation markers OPN and OCN [109], with effects dependent on flow duration and pattern [103], [107]. Oscillatory and pulsatile flow optimally stimulate cells at 0.5 to 2 Hz [90] [111] [112], a range matching a brisk walk gait frequency [92] (Section 2.2.4), and can elicit the strongest osteogenic response in bone culture when combined with an appropriate pulse profile and frequency, but this requires specialised perfusion equipment [113][114].

Table 2.5 Flow shear profiles by advantages and drawbacks. Table adapted from [112] [113] [115]

Flow Type	Advantages	Drawbacks
Continuous (Steady) Bahmaee *et al.* [115]	• Easy to apply with syringe pump • Produces moderate ALP and PGE_2 increases, • nutrient transport support	• Rapid desensitisation of Ca^{2+} signalling over prolonged exposure • Less physiologically relevant
Intermittent (On/Off) Bahmaee *et al.* [115]	• Prevents mechanosensory fatigue; stronger Runx2/ALP response • Enhances long-term osteogenic differentiation, can use syringe pump	• Requires programmable pump/valve • Response depends on ON/OFF timing
Oscillatory (± Reversal) Jacobs *et al.* [112], You *et al.,* [116]	• Mimics lacunar–canalicular shear reversals • Activates COX-2, NO, and osteogenic genes	• Ca^{2+} signalling weaker than pulsatile • Minimal net mass transport • Sensitive to frequency/amplitude
Pulsatile Ajubi *et al.,*[114], Jin *et al.* [113]	• Strongest Ca^{2+} and PGE_2 signalling • Maximises osteogenic gene expression	• Requires precise pulsatile flow profile hardware • High peak shear can detach 2D cells

Frequency-dependent effects on cellular response have been reported (e.g., Stavenschi *et al.* [90]), and optimal oscillatory parameters such as magnitude and frequency must be tailored for cell types such as osteoblasts [117]. Intermittent steady flow is more effective for long-term MSC osteogenesis than continuous steady flow as shown by Bahmaee *et al*. [115]. This

study used intermittent flow (alternating between 1.5 h of 0.8 to 1.4 Pa flow shear and 4.5 h of 0.2 to 0.4 Pa flow shear daily for 3 weeks) and it increased ALP activity (DNA normalised) by 2.3-fold and calcium deposition by 1.8-fold compared to continuous flow (0.8 to 1.4 Pa flow shear for 24h daily for 3 weeks) for embryonic MSC-like bone cells in a 3D GelMA microfluidic BoC at 3 weeks [115]. Pulsatile and intermittent flow (e.g., from simple syringe pumps) generally outperform oscillatory or steady flow for promoting mechanotransduction and osteogenesis (Table 2.5). Flow duration is also important but reported culture periods have varied. Some *in vitro* studies have examined its effect on osteogenic responses, and it depended jointly on flow shear stress magnitude, frequency, and duration of the flow shear rather than on the duration alone [90] [108]. Bahmaee *et al.* recommended 1 to 2 h/day of active steady flow to be optimal, and that 3D cultures tolerate higher flow rates and longer durations [115]. Steady flow durations of 1 h/day have been deemed sufficient for osteogenic development [118]. Although there is some trade off with shear and duration, excess shear can damage or detach cells, whereas very low flow produces minimal changes in proliferation and osteogenic development [119].

2.2.6 Chip Sterilisation and Re-usability

Contamination can be problematic in small-scale microfluidics, so assembly should occur in a clean room [120], followed by pre-culture sterilisation. Because PMMA deforms at temperatures under 100 °C [121], non-thermal sterilisation is required, such as UV exposure or 70 % ethanol wipes [122]. Thin, non-annealed, additive-free PMMA films can become brittle and crack under prolonged exposure to ethanol and similar agents, and leaching can reduce biocompatibility [121]. In contrast, crosslink treated or annealed PMMA better tolerates such extended chemical exposure [123][124]. More thorough sterilisation can use low-concentration hydrogen peroxide (0.5 to 2 %), followed by repeated Phosphate Buffered Saline (PBS) rinsing [125], especially for reusable platforms. PMMA can typically withstand 3 to 5 reuse cycles without hazing or clouding [126], though this depends on chip design and culture type [127].

2.2.7 Cell Source

The choice of cell type for the BoC platform is critical. Primary cells, directly isolated from animal or human tissue, offer greater translational relevance but have a finite lifespan and limited expansion capacity, making them unsuitable for long-term studies [128], [129]. Cell lines are cheaper, easier to handle, provide an almost unlimited supply, and avoid ethical or safety issues associated with animal or human tissues, such as disease risk and confidential

medical data [130]. They also provide greater consistency and reproducibility, which is essential for experimental reliability [131]. In addition to this, cell lines are highly proliferative and easy to culture, making them well suited for proliferative 3D cultures [130]. Mouse osteocyte (IDG-SW3) and osteoblast (MC3T3-E1) cell lines are widely used in relevant BoC studies [132]. However, cell lines do not always accurately replicate primary cells, so the results must be interpreted cautiously [130]. Key experiments should ideally be repeated in primary cells to validate conclusions from cell lines.

2.2.8 Cell Culture Conditions

Varied O_2 levels during incubation are crucial for bone cell response [133]. Bone tissue naturally exists in a low O_2 (hypoxic) environment deep within bones and distant blood vessels [134] [135]. Bone and many other cells grow best at physiological O_2 levels of 2 to 6 % [135], whereas standard incubators use 19 % O_2 [136]. Binder *et al.* [133] showed that 3D cell culture requires physioxic conditions to accurately mimic *in vivo* tissue, especially for bone. Few studies have examined hypoxia in hydrogel bone cultures. Li *et al.* [134] reviewed hypoxic BoC methods, and Scheinpflug *et al*. [137] developed a hypoxic BoC, mechanically loaded for 1-week cultures. Further investigation of hypoxic 3D bone hydrogels is needed.

Cell Protectants: Cell protectants are an emerging area in cell culture. CellShip, a refrigerated shipping media supplement developed at Coventry University, preserves cells under shear, thermal and metabolic stress during transport or storage [138] [139]. It buffers thermal and metabolic changes at 4 to 8 °C for up to 5 days [138], enabling temporary metabolic flexibility when media supply is irregular or when samples are frequently outside standard incubation (37 °C, 5 % CO_2) [140], and experiment incubation space is limited. Its shear-protectant effects increase tolerance to mechanical stress, potentially extending mechanical stimulation tests outside incubators beyond the 1 h limit of standard HEPES buffer [141], which is beneficial for prolonged centrifugation or flow shear studies [142].

2.3 Hydrogel-based Substrates for Bone Tissue Engineering

2.3.1 Properties of Hydrogels for Bone Tissue Engineering

To better mimic native tissue, *in vitro* culture models have shifted from 2D to 3D. Hydrogels are widely used as 3D scaffolds because their tuneable stiffness, porosity, and biochemical properties enable long-term culture and improved cell viability in bone and cartilage tissue engineering [143]. Engler *et al.* [144] investigated the response of bone MSCs to substrate

stiffness on polyacrylamide hydrogels and found that a substrate stiffness of around 25 to 45 kPa is optimal for osteogenesis. An optimal cell substrate must be biocompatible (avoid immune reaction), degrade at a rate that enable new supported bone formation and mineralisation prior to gel scaffold degradation, and have interconnected pores that facilitate cell proliferation, nutrient diffusion, balanced oxygen transfer and waste removal [145][146] [147]. A wide variety of hydrogels have been developed to meet these criteria for bone and cartilage applications [147], differing in composition, cross-linking type (UV, thermal, chemical, magnetic), and cross-linking conditions (initiator amount, crosslinking time), yielding gels with distinct stiffness, density, and water absorption [148].

2.3.2 Hydrogels for 3D culture models

Hydrogels from natural polymers such as gelatin and hyaluronic acid (HA) are widely used in tissue engineering because they are biocompatible, tuneable, and resemble native ECM [149] [150] [151]. Gelatin is derived from collagen, and HA is an ECM component that supports tissue hydration and elasticity [152]. GelMA is produced by adding methacryloyl groups to gelatin, enabling photo-crosslinking under light to form a stable, tuneable 3D network for tissue engineering [152]. HA, a key component of bone ECM, maintains tissue hydration [149] and promotes cell proliferation and osteogenesis [153]. Adding HA to GelMA, as reported by Hwang *et al*. [152] and Camci-Unal *et al*. [149], allows tuning of pre-curing viscosity and post-curing stiffness. Velasco-Rodríguez *et al*. showed that 10 % (w/v) GelMA with 1 % (w/v) HAMA increased hydrogel stiffness to 30 kPa (by over 40%) while preserving gel fraction porosity up to 91 % [154]. High porosity supports bone cell infiltration, intercellular signalling and nutrient transport. [147].

Composite GelMA–HA hydrogels, as shown by Cao *et al.* [155], support co-cultures of bone and chondrocytes to study intercellular interactions at different GelMA concentrations. Alternatively, multicellular JoC constructs can be cultured in heterogeneous layers to better mimic native osteochondral junctions, as demonstrated by Zhang *et al*., who arranged bone and cartilage tissues in separate layers within JoC platforms [156]. Accurate mimicking of bone and cartilage tissue requires a 3D environment with permeability, porosity, microstructure, biochemical composition and bulk mechanical properties comparable to native ECM [157]. These features create a physiologically relevant, stable microenvironment that supports appropriate cell differentiation, proliferation and long-term survival in OoC systems [158]. Flow-based experiments of at least 3 days are usually needed to assess initial cell attachment and viability, while studies of 7 days or more are required to

evaluate proliferation and differentiation. Some OoC systems have been maintained for over 3 to 5 weeks [109] [159], with mineralisation observed after about 2 weeks [160].

Given these requirements, custom gelatin-based hydrogels provide a cost-effective; and adaptable option for long-term culture. Gels optimised for multiple cell types can also support heterogeneous layered osteochondral-on-chip models [156], as shown in Figure 2.10.

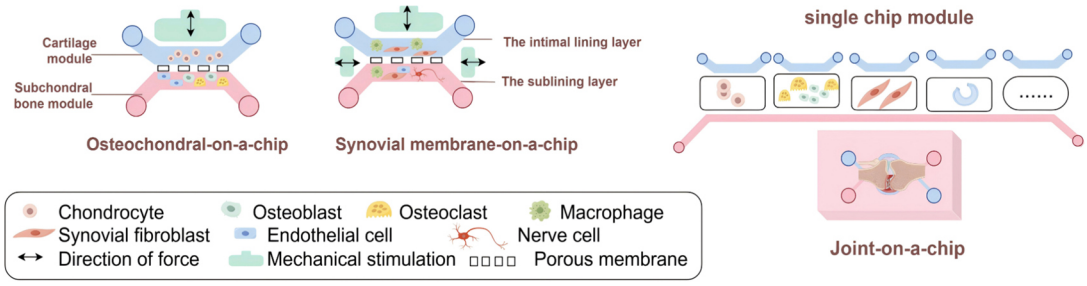


Figure 2.10 Synovial JoC. Multiple tissue types are needed for JoC models [156].

Various natural and synthetic hydrogels have been investigated for bone tissue engineering. Silk fibroin (SF) hydrogels show strong potential for bone regeneration due to their high strength and support of osteogenesis, especially with HAp [161], but their fabrication is complex and prone to batch variability, reducing reproducibility [162]. In contrast, poly(ethylene glycol) (PEG) hydrogels enable precise and flexible crosslinking. Although PEG is not inherently bioactive, it can support osteogenesis in the presence of osteo-inductive factors [163]. Hydrogels from decellularised bone ECM (dECM) provide native biochemical cues that enhance osteogenesis [164], but decellularisation protocols require extensive optimisation to ensure full removal of cellular components and avoid immunogenicity [165]. Thus, despite their promise, dECM hydrogels face challenges in standardisation, scalability, and immunogenicity that limit widespread use [166].

2.4 Data Generation for BoC Models

2.4.1 Imaging Modalities

Robust image data generation methods are critical for BoC models, particularly when integrated with quality assessment and ML approaches. Bright-field microscopes use transmitted visible light, sent through objects that attenuate (absorb / scatter) this light producing dark cellular structures against a bright background, suitable for bone imaging [167]. Bright-field microscopy is widely used to visualise stained tissue sections and cellular components such as osteoblasts, osteoclasts, and mineralised matrix, providing high-contrast bright-field images suitable for morphometric and qualitative analysis [168]. Typically, a 10× objective lens is used to capture images, sufficiently resolving individual cells and clusters over fields of view of about 0.3 mm^2 and resolve resolution of 1 µm [169].

2.4.2 Assay Detection and Fluorescence

Assays are essential in bone tissue engineering for quantitative and qualitative evaluation of cellular behaviour, tissue development, and mineralisation. They range from metabolic activity assays for cell viability and proliferation to mineralisation assays for calcium deposition and osteogenic differentiation [170][171], and high-throughput plate read assays can be applied to 3D samples with appropriate methods [172] [173].

Trypan blue is a standard method for cell viability assessment, as it selectively stains dead cells with compromised membranes while live cells exclude the dye, enabling accurate live/dead counts using a hemocytometer or automated cell counter [174] [175]. For non-invasive, continuous monitoring of metabolic activity, alamarBlue™ is widely used [176]. It acts as a redox indicator, metabolically active cells reduce resazurin (blue, weakly fluorescent) to resorufin (red, highly fluorescent), whose fluorescence intensity correlates with metabolic activity and viability [176]. alamarBlue™ is non-toxic, suitable for live-cell monitoring [170], and is typically measured by absorbance or fluorescence at specific wavelengths (e.g. 570 nm excitation, 600 nm emission) [177]. It can also be used for cell viability assessments with positive and negative controls according to ISO 10993.

Monitoring cumulative proliferation and aggregate structure provides useful metrics for tissue growth. Fluorescent molecular dyes such as ViaFluor enable non-invasive, longitudinal quantification of cell proliferation [178]. ViaFluor 488 is an amine-reactive dye that covalently labels the live cell cytoplasm and intracellular compartments, allowing live monitoring of cell division by flow cytometry or fluorescence microscopy [178]. Quantification is performed at 485 to 490 nm using a spectroscopic plate reader [179], [180].

Mineralisation assays assess osteogenesis by detecting calcium deposition [181], which typically becomes measurable around 10 to 14 days, reflecting late-stage osteogenic differentiation [182]. Early differentiation is marked by rising alkaline phosphatase (ALP) activity, which provides phosphate for initial calcium phosphate deposition, this deposition in the bone matrix correlates with bone formation and effectively indicates osteogenesis [183]. ALP as a bone dephosphorylating enzyme, rises due to this process and is detected by ALP assay kits [184] [185]. ALP colorimetric kits function similarly to alamarBlue™ assays but are read at 405 nm [185]. ALP can be used in live cultures or as a terminal assay on fixed samples to quantify final calcium levels [186]. Alizarin Red S staining is another common method; it chelates calcium ions in bone cultures, allowing visualisation of calcium-rich deposits and mineralisation assessment in fixed osteoblast cultures [187].

2.5 Machine Learning Models

ML uses statistical algorithms to enable human-like learning from large datasets without prior assumptions [188]. These algorithms are well suited to pattern recognition, including computer vision (CV) tasks that involve many variables. Integrating ML with LoC or OoC systems enables high-throughput, automated, intelligent monitoring and analysis [189]. ML applications include image-based tissue classification (e.g. diagnostics) and predictive regression models that estimate continuous cell or tissue responses (e.g. growth) rather than discrete states [188]. Such modelling gives the ability to model complex varied non-linear multivariable relationships that occur within cell or tissue based samples over time.

2.5.1 ML Modelling

Convolutional neural networks (CNNs) are now standard in computer vision for object recognition and classification on image datasets, sequential snapshots, or video streams—applications highly relevant to flow and cell imaging [189][190]. They excel at image classification [189][190] but are less suitable for regression on structured tabular data, especially with limited samples, due to requiring more training data and high computational resources [188][191]. Classical ML regression methods are often preferable for complex non-linear modelling with data limited tissue engineering applications [191]. Traditional methods such as Support Vector Machines (SVM), Decision Trees (DT), and Random Forests (RF) remain widely used for high-volume, rapid training time with lower computational cost and well-established tuning practices [191][192]. OoC systems produce heterogeneous data, a mix of continuous and discrete variables (time-series flow data, environmental parameters, device settings) that can feed classification or regression models. SVMs and RF work well for smaller datasets, while more complex time series can benefit from advanced architectures such as long adaptive CNNs [191][193].

XGBoost, another ensemble method, also relies on decision trees but builds them sequentially so each tree reduces the remaining loss of the previous ones; regularisation and bootstrapping further improve predictive accuracy [194] [192]. Time-series fluorescence or unstructured microscopy images are often well-suited to CNN-based analysis, but the associated computational cost and data requirements frequently make simpler methods like SVM, RF, and XGBoost more practical for datasets such as microplate assay readings [195] [196]. An overview of these algorithms is given in Figure 2.11. A related ensemble method, LightGBM, performs efficient gradient boosting by iteratively updating trees and splitting at leaves or nodes that maximise the reduction in regression loss [197].

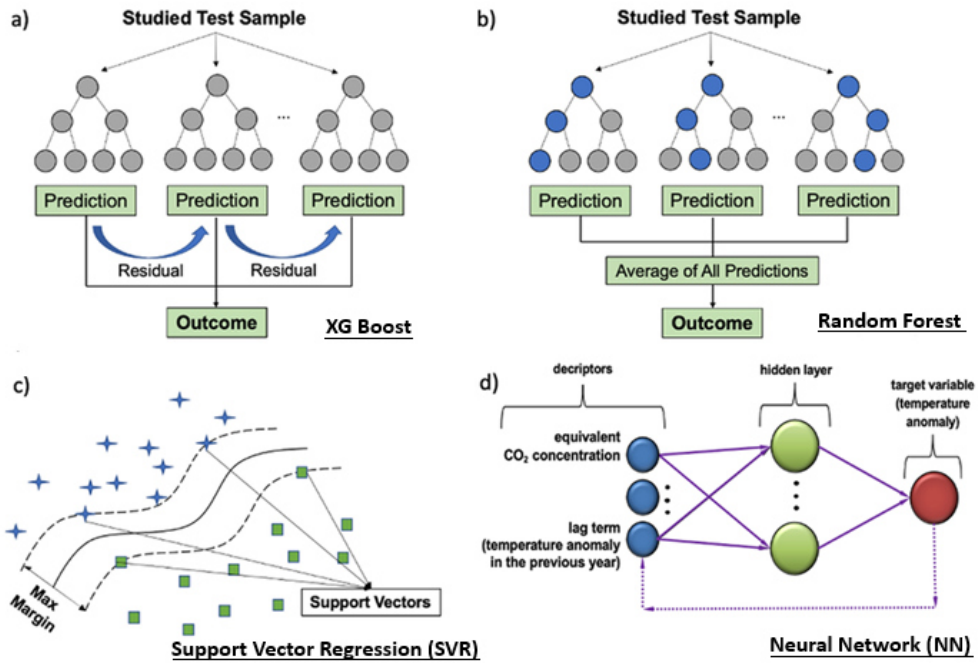


Figure 2.11 ML algorithms compared for predictive regression modelling [198].

Randomised Deep Learning reduces the size of the neural network by stochastically pruning connections, making it useful when large CNNs are impractical due to more parameters than training samples. Many connections are fixed, often randomly, and not trained [199], creating a "random-weights" architecture where learning focuses on a smaller subset of weights, improving efficiency over fully trained models [199] [200]. Structural randomness or dropout in deep randomised networks reduces training complexity and preserves expressive power at test time, with structural randomness in CNN paths [201] and random node dropout in deep networks [199][202] providing complementary mechanisms to improve accuracy, error and computational efficiency. Randomised architectures and sparsification strategies for layers or nodes have also been shown to improve generalisation by limiting overfitting with given data [201] [203]. Simpler single-layer networks, such as Extreme Learning Machines (ELMs), can further enhance generalisation through pre-training [199] [204]. These models can also alleviate issues such as vanishing gradients. Gallichio *et al.* [199] report that randomised neural systems achieve higher classification accuracy and better computational efficiency than basic CNNs with line, image and graph datasets, and the method applies to both regression and classification [199]. Its adaptive modelling is promising for limited datasets common in life sciences. Theoretically, randomised architectures also enable analysis of intrinsic network properties before training hidden layers, supporting more explainable AI and comparison of feature contributions [199], [205]. However, such frameworks have not yet been applied to bone tissue engineering, BoC or OoC datasets, highlighting a new research opportunity.

2.5.2 Model Optimisation Techniques

Several optimisation techniques can refine ML regression models and improve their data-fitting accuracy. Grid search tests predefined hyperparameter combinations to find the best model but scales poorly for complex models with many hyperparameters [206]. Random search instead samples hyperparameter configurations from a predefined distribution within a given computational budget and often explores the space more efficiently when only a few hyperparameters strongly affect performance [207]. However, its performance depends on the number of iterations and randomness, and it remains computationally expensive for large, complex models [208]. Bayesian optimisation instead uses a statistical surrogate model and past evaluations to search for promising hyperparameters, avoiding direct optimisation of the original model each time [209] [210]. It typically outperforms grid and random search by greatly reducing the number of evaluations needed [208]. Bayesian optimisation is especially useful for complex or large models with moderately high-dimensional spaces but its performance degrades in very high-dimensional settings (over 20 dimensions) [211].

2.5.3 Application of ML in OoC

To date, only one study by Paek *et al.* [132] has applied ML or deep learning directly to a BoC platform, using a CNN to classify the effects of osteoporosis drugs on cellular responses with over 96 % accuracy in distinguishing treated from untreated cells. No regression-based ML or deep learning models have yet been applied specifically to BoC, although various ML methods have been used in bone diagnostics, materials, and tissue engineering [212]. For example, Javaid *et al.* applied SVMs, decision trees and ANNs to classify biomaterials and rank bone scaffolds, and ANNs had the highest accuracy [213]. Shaikhina *et al.* used ANN regression to predict age-related trabecular bone properties in OA, using real human trabecular bone 3D specimens, achieving an R^2 of 0.96 with low errors, demonstrating the potential of ANNs and other ML models for bone tissue applications [214]. This was one of the few regression-based predictive models of bone tissue behaviour but not applied to a BoC. The majority of ML-based studies on bone tissues applications have focussed on classification tasks, often employing simpler ML models such as Random Forests, that are used to support data analysis or to optimise experimental design and material selection [212] [215]. Deep learning CNNs are typically used for large-scale image diagnosis, assessment, and screening tasks [215], such as image-based scaffold screening and bone mineral density prediction with histology and micro-CT data [216]. Similar ML and deep learning methods have been applied in LoC systems for other cell and tissue types [175], and show opportunity for BoC applications, where ML-driven models could enable new insights and advances.

2.6 Critical Limitation and Gaps in Current Research

2.6.1 3D Culture Optimisation Challenges

Despite advances in OoC technologies, physiologically relevant 3D culture environments for BoC models remain underdeveloped. Most systems still use simplified 2D or partially structured scaffolds that do not capture the spatial organisation, mechanics, or biochemical gradients of native bone. This limits accurate modelling of osteogenic differentiation, mineralisation dynamics, and cell–matrix interactions under physiological conditions. A key challenge is optimising hydrogels to achieve appropriate stiffness to support osteoblast growth and differentiation, particularly in long-term cultures. Overcoming these issues is essential to make BoC platforms predictive and clinically translatable for drug screening, disease modelling, and regenerative medicine.

2.6.2 Combined Mechanical and Flow Stimulation

A critical research gap in BoC development lies in the integration of combined mechanical and flow stimulation to replicate the dynamic *in vivo* environment of bone tissue. Although fluid shear stress and mechanical loading are known to influence osteoblast differentiation, mineralisation, and overall tissue maturation, current microfluidic systems often fail to deliver physiologically relevant combinations of these stimuli. Using centrifugal stimulation presents a novel approach to achieve cyclic mechanical loading at a frequency that replicates the natural gait cycle or physiological loading. Addressing this gap will achieve a more physiologically relevant platform for drug testing and regenerative medicine.

2.6.3 Machine Learning Modelling Gaps

ML shows promise in tissue engineering, but its use in BoC platforms is largely unexplored. Existing work focuses on image analysis and predictive modelling in conventional bone cultures or scaffold screening, with little attention to the specific challenges of microfluidic BoC systems. These systems produce complex multimodal data—imaging, flow dynamics, and biochemical markers—that require advanced ML for effective analysis. Addressing this gap could enable real-time monitoring, automated decision-making, and better design of physiologically relevant BoC systems, offering a major avenue for future research.

2.7 Research Aim and Objectives

This doctoral thesis aims to develop a BoC platform that supports long-term bone cell culture with integrated multimodal mechanical stimulation, specifically fluid shear and cyclic centrifugal compression loading that can also be used for sequential dual stimulation. The platform will allow systematic monitoring of bone cell behaviour under varied culture and stimulation conditions. Data will be analysed with optimised ML models to identify key factors driving bone cell growth and differentiation, improving predictive modelling. The specific research objectives are as follows:

Objective 1: To develop a microfluidic BoC platform capable of applying combined centrifugal and flow-induced shear forces sequentially (one after the other) to cells embedded within an optimised tuneable GelMA/HAMA hydrogel (Chapter 3).

Objective 2: To investigate the effects of varying cyclic centrifugal forces and flow shear on bone cell metabolic activity, proliferation, and osteogenesis (Chapter 4).

Objective 3: To assess the impact of a cell protectant media supplement on bone cell responses under static, centrifuge cyclic loading and flows shear conditions (Chapter 5). This would examine protectant media can enhance cell proliferative and osteogenesis for mechanically stimulated bone cells.

Objective 4: To develop, optimise and compare classical and deep regression models and explainable AI methods for predicting cell responses within the BoC platform (Chapter 6).

Chapter 3: BoC Platform with Physiologically Relevant Loading and a Tuneable GelMA/HAMA Hydrogel Microenvironment

3 BoC Platform with Physiologically Relevant Loading and a Tuneable GelMA/HAMA Hydrogel Microenvironment

3.1 Introduction

In the physiological environment, bone cells are routinely exposed to both the fluid shear stress from interstitial flow and compressive mechanical loading. These mechanical cues are critical regulators of osteoblast differentiation, signalling and matrix production during bone remodelling and regeneration [52]. Static 3D cell models can create more realistic 3D intercellular interactions [217] [10], but still lack the ability to fully mimic the mechanical loading environment present for *in vivo* tissues [217][52]. Microfluidic BoC platforms offer promising systems for mimicking such stimulated physiological environments and studying cellular behaviour *in vitro* [217], as an alternative to static 2D or 3D cell culture models.

To date, several approaches have been explored to apply mechanical stimulation in BoC platforms. For example, Scheinpflug *et al.* [137] developed a BoC platform where pneumatic compression induced compressive loading in a bioreactor, whereas Zhang *et al.* employed mechanical actuation for similar purposes [218]. Tsao et *al.* used a microfluidic BoC with injection of syringe to stimulate bone marrow stromal cells by flow shear, enhancing osteogenic differentiation *in vitro* [218]. To date, no known BoC platform has applied dual stimulation through combined flow shear and compressive loading. Paggi *et al.* developed a platform for the application of complex mechanical stimulation to 3D chondrocyte-laden hydrogels [79]. This system combined three independently controllable actuation chambers capable of applying specific pressure sequences, uniform compression and/or shear strain. This highlights a critical gap, whereby current BoC models lack the multi-modal stimulation present in the biological *in vivo* environment, thus limiting their physiological relevance.

Recent advances in mechanobiology have also demonstrated the role of the cellular microenvironment, particularly the stiffness and biochemical composition, in directing osteogenic responses [144][219]. In particular, the role of substrate stiffness in promoting osteogenic responses has been demonstrated by Engler *et al.*, with matrices of 25-40 kPa stiffness shown to promote osteogenesis [144]. The osteoblast response to a wide range of hydrogel types, including natural hydrogels (collagen, gelatin, fibrin, hyaluronic acid, alginate, chitosan) and synthetic hydrogels (PEG, PVA, PAA) [220] [221], and stiffnesses (elastic modulus of 1 to 100 kPa) has been examined [219]. Natural hydrogels offer distinct advantages for bone cell culturing in terms of cell adhesion and proliferation with more similar indigenous binding sites [221]. Babaliari *et al.* developed a microfluidic platform designed for shear stimulation that contains a viscoelastic collagen/fibrin-based hydrogel

[222]. The ideal hydrogel should provide the appropriate biochemical cues, custom mechanical stiffness and support to mimic cellular behaviour *in vivo* [223][224], while allowing longer duration cell culture [225].

Hydrogels based on natural polymers such as GelMA and HAMA are widely used as 3D models in tissue engineering applications due to their biocompatibility, tuneable properties, and similarity to the native ECM [149] [150] [151]. Specifically, gelatin is a natural polymer derived from collagen, whereas HA is a natural ECM component, contributing to tissue hydration and elasticity [152]. GelMA and HAMA hydrogels also provide specific binding sites through which bone cell receptors can interact. GelMA retains the arginine-glycine-aspartic acid (RGD) sequences of collagen [158]. These RGD sequences act as adhesion sites for cell surface receptors called integrins, promoting cell attachment, proliferation, and differentiation [226]. Cells interact with HAMA through the CD44 non-integrin binding site [152]. Combining GelMA and HAMA provides both RGD and non-integrin binding and increases gel stiffness and durability [158]. Adjusting the GelMA:HAMA ratio has been shown by Camci-Unal *et al.* to tune hydrogel degradation and prolong structural stability *in vitro* [149]. A suitable curing agent (photo-initiator) and curing regimen for this gel composition can also further modulate gel stiffness and degradation rate [227][228]. This optimal tuneability of gel composition is important for optimal strength, stiffness and durability requirements for BoC applications. Velasco-Rodriguez *et al*. [229] developed a detailed guide method to produce and characterise GelMA HAMA gels including a test for stiffness (Young's and storage modulus), porosity, swell ratio and enzymatic degradation resistance (to collagenase). The study showed 1 % (v/v) HAMA addition to 10 % (v/v) GelMA increased stiffness (storage modulus) by 28 %, swell ratio (water uptake) by 33 % and degradation resistance by 30 %. Various studies like Yu *et al.* have measured GelMA/HAMA gels degradation directly in PBS at 37 °C without added enzymes, that showed 15 % degradation at 3 weeks for 10 % GelMA 1 % HAMA gels [230] .

A further factor to consider in the BoC platform is the cell culture environment, as oxygen tension has been shown to influence the bone cell microenvironment. Spencer *et al.* reported that bone cells occupy a hypoxic niche with *in vivo* oxygen levels averaging 4 % (range 2 to 6 %), compared with other tissues averaging about 6.5 % (range 1 to 12 %) [231]. Comparing normoxic and hypoxic environments can give better insights into bone cell behaviour under such conditions [232]. Incorporating cells within GelMA/HAMA hydrogels with suitable arrangement can help recreate oxygen gradients closer to those found *in vivo*, thereby improving biomimicry [233].

This study will develop a reusable microfluidic BoC platform that applies combined centrifugal cyclic loading and flow-induced shear forces to cells embedded in GelMA/HAMA hydrogels. The integrated system is hypothesised to support long-term osteoblast viability and differentiation under conditions that closely mimic *in vivo* bone tissue mechanics, matrix environment, and oxygen gradients. The specific aims are: (i) to design and validate the dual-stimulation BoC platform, (ii) to optimise GelMA/HAMA composition and thickness for osteogenesis and long-term culture (4 or more weeks), and (iii) to evaluate cellular responses under normoxic and hypoxic conditions.

3.2 Methodology

3.2.1 BoC Platform Materials and Fabrication

The BoC platform was fabricated from annealed PMMA (Radionics, Dublin, Ireland) with sheet thicknesses of 0.5 to 1 mm. PMMA was chosen for its low cost, biocompatibility, optical transparency, machinability, sterilisation compatibility, and sufficient mechanical robustness to withstand cyclic and shear forces along flow directions [234] [68]. Pressure-sensitive adhesive (PSA) biocompatible sheets (Adhesives Research, Limerick, Ireland), approximately 0.1 mm thick with high adhesion strength (21.5 N/ 25 mm adhesion or 1 MPa tensile strength), validated in a study by Kratz *et al.,* were used to bond the cut PMMA layers [235] [236].

During fabrication, PMMA sheets were cut using the Epilog Zing CO_2 laser cutter (Golden Colorado, US) and examined, using a similar process to that outlined by Huang *et al.* [65]. Optimal laser cutting parameters (30 W power, 2500 Hz, 1000 dpi) were employed, achieving high-resolution microfluidic channel cuts at 0.5 mm width, within the laser cutters specified settings [237]. PSA adhesion layers were cut with a Graphtec CE-6000 precision cutter (MDP, Portadown, UK). Assembly was conducted under cleanroom conditions using alignment bases and a high-pressure mechanical roller (HL-100, Cheminstrument, US).

3.2.2 BoC Platform Design and Verification

BoC Platform Design

The design of the BoC platform would enable multi-modal stimulation to be induced on chip samples sequentially (flow shear followed by centrifuge stimulation or vice versa) rather than in parallel given constraints of centrifuge stimulation requiring disconnection of the chips flow shear inlet/outlet tubes. Two configurations of the BoC platform were developed: a single-channel device and a tri-channel device, each incorporating 1 cm^2 cell wells (Figure

3.1). The channel width was set at 0.5 mm to minimise excess capillary pressure [238]. In the tri-channel device, the wells were aligned in parallel and placed in the centrifuge to be at radial distances of 3, 4.5, and 6 cm to apply different centrifugal forces simultaneously. Figure 3.1 (A, B) shows the chip cross-section with PMMA/PSA layers, channels, and top-down views. Detailed chip and holder designs are in Appendix A1 with corresponding quality control metrology in Appendix A2. The detachable base layer enabled the removal of the hydrogel sample for further analysis. A KFT NE-1000 programmable syringe pump (KFT, Italy) with syringe, luer adapter (Darwin Microfluidics, Paris, France), and 0.5mm ID PTFE tubing was connected to a polymer rubber luer adapter (Microfluidic Chip Shop, Stockholder, Germany) at the BoC inlet (luer port) to generate flow shear (Figure 3.1 E). Cell media was injected at a programmed rate for controlled shear. A set flow rate of cell media (Q) would be applied to each chip well via the syringe pump and syringe of media to induce a specific bulk flow shear per channel/well as given in Equations 3.2 and 3.3.

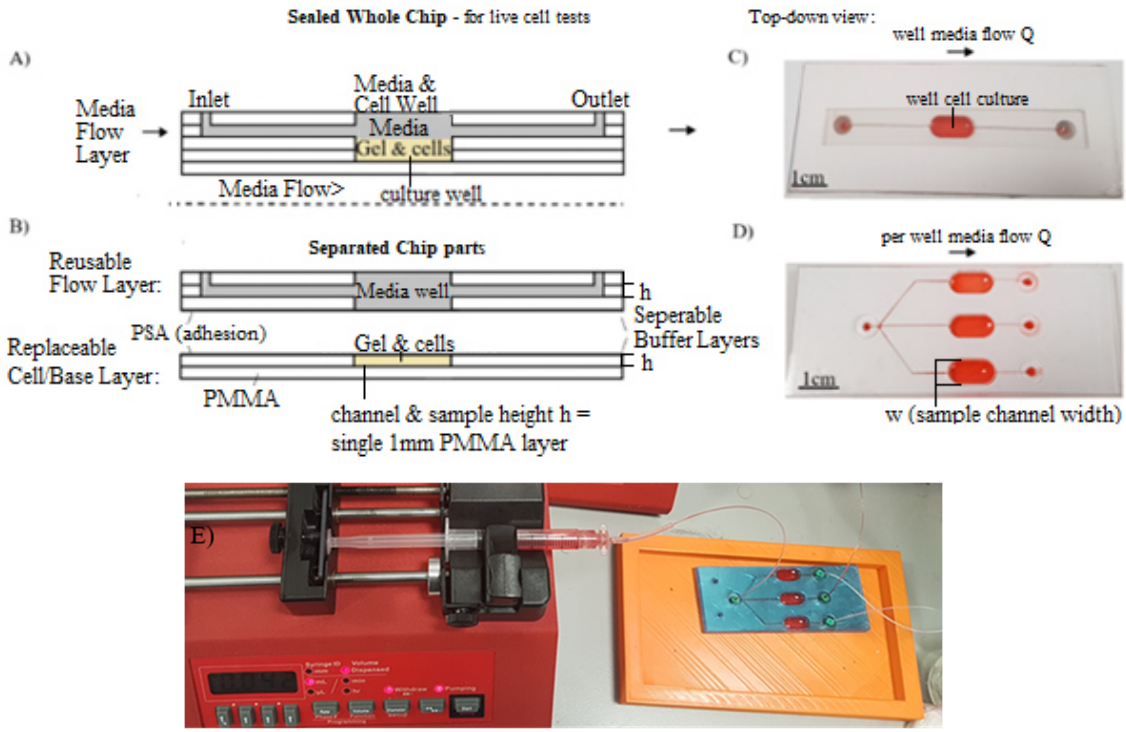


Figure 3.1 BoC platform configurations. **A)** Long-side cross-section schematic of the BoC platform. **B)** Side view showing the separated reusable top flow layer and the base hydrogel-loading layer (schematic, not to scale). **C)** Top-down view of a single-channel BoC with cell media. The outer frame fits a centrifuge disk holder; the inner chip fits 9 cm cell culture petri dishes. **D)** Top-down view of the principal tri-channel BoC with cell media. All chips have 0.5 mm-wide channels in 1 mm-thick PMMA layers and 1 cm^2 cell wells. A media flow rate of Q (50, 100 or 150 µL/min for main experiments) was applied per channel and well which induced the desired bulk flow shear per chip sample. **E)** Microfluidic syringe pump set-up for applying flow shear to the tri-channel chip.

Bi-directional media flow from a single syringe pump (with outlet tubes in a filled cylinder to reduce capillary effects) and a reciprocal synchronised dual syringe pump connected system filled and emptied the BoC cell wells repeatedly (for flow leak and validation tests). Single channel chips were used for simple leak and flow only tests. Blue transparent PSA adhesion was used for some chips (Figure. 3.1 E) as part of earlier flow and leak tests. This was done to visually demonstrate no internal leakage within the chips as part of chip production validation (Section 3.2.3). While white PSA chips (Figure. 3.1, C, D) were generally used for long-term direct cell on chip testing (Section 3.2.10) and later studies.

A custom-designed centrifuge holder compatible with standard laboratory centrifuges for mechanical testing was used to mount the BoC platform within the centrifuge during centrifugal stimulation (Figure. 3.2 A, B).

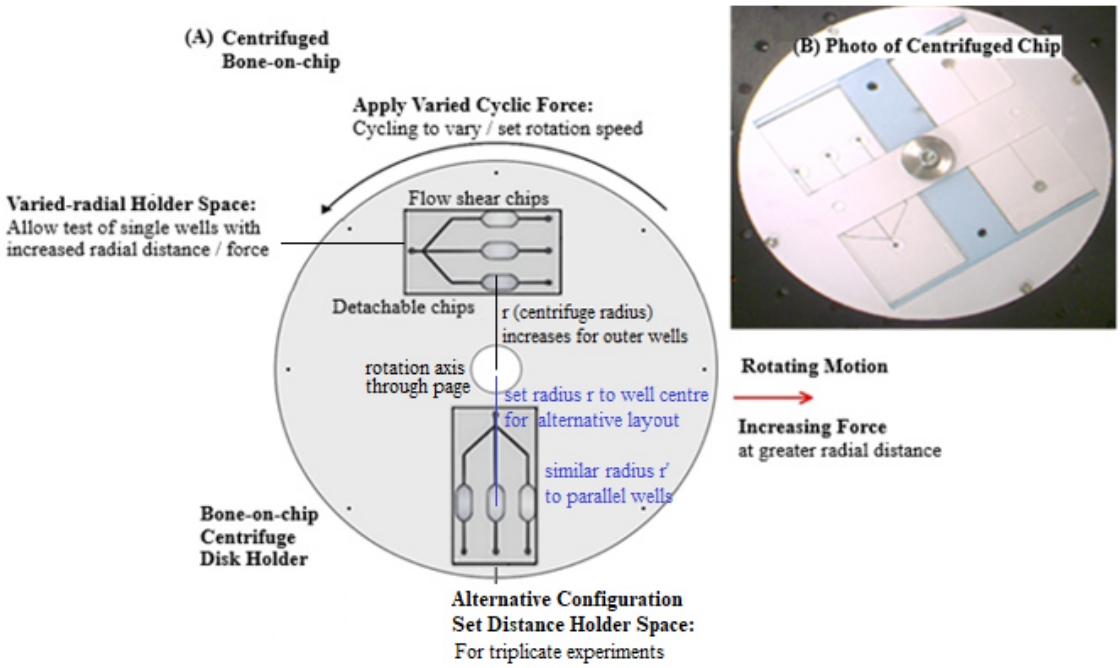


Figure 3.2 Centrifuge disk layout **A)** Schematic of main experiment tri-channel BoCs held in spinning centrifuge disk holder (not to scale), with 16 cm outer radius and 2 cm inner hub radius (schematic self-composed). Radial distance for cell wells measured from hub centre to outer cell well wall. **B)** Top-down image of BoCs sealed and covered in a holder under centrifuge operation for tests

Centrifugal and Flow-Induced Shear Force Calculations

The mechanical forces applied were calculated based on the fundamental principles of centripetal force magnitude and acceleration at a given radial distance from the disk centre (Equation 3.1) [239] [240]. Using the terms of centrifugal force magnitude and mass (m) to determine acceleration and convert the angular velocity to revolutions per minute (RPM) and the radius to centimetres, the equivalent expression of acceleration (a_c) was attained

(Equation 3.1) [239] [240]. Centripetal acceleration in terms of angular spin rate Ω_s is given as Equation 3.1 where the angular spin rate is measured directly by the calibrated centrifuge. In this equation that's expressed for custom units rather than SI units, a_c is the centrifugal acceleration, Ω_s is given in units of RPM (this being standard units for the centrifuge device) where RPM is the spin rate units (in revolutions per minute) and r is the radial distance from the centrifuge centre (in cm). The radius for varied centrifuge acceleration (and varied radial well distances) is measured from the centrifuge centre to the furthest vertical wall of the well as illustrated in Fig 3.2A. For the triplicate set with constant centrifuge acceleration configuration its measured as far as the well centres as also illustrated in Fig 3.2 A. This acceleration a_c is equivalent to joint acceleration that is universally experienced by all areas of a joint during motion and is given in terms of g acceleration (expressed as a factor of acceleration of earth's gravity g) for more direct comparisons of acceleration in other studies. It can be converted to m/s^2 units by multiplying by 9.81.

$$a_c = (1.118 / 10^5) (\Omega_s)^2 r \tag{3.1}$$

Compressive loading is proportional to sample acceleration divided by the chip well's outer wall area. The flow wall shear stress equation through a rectangular microfluidic chip channel is expressed by Equation 3.2 [103]. It assumes fully developed laminar steady flow for an incompressible Newtonian fluid (Poiseuille flow). The approximate average bulk wall shear stress on channels assuming infinitely deep parallel walls is given by:

$$F_s = \frac{6\mu Q}{h^2 w} \tag{3.2}$$

F_s is the wall shear stress on the channel or well walls assuming there is no channel expansion, otherwise it's an approximate average. Cell media is injected via the calibrated syringe pump at an inlet volumetric flow rate Q measured directly by the pump, developed flow is assumed not present in the channel to well expansion section. The cell media dynamic viscosity is given by μ, using a rectangular channel, h is the microfluidic well channel height, and w is the channel width (as illustrated in Fig 3.1 B, D). F_s is an approximate bulk average metric and considerable localised variation can still occur. Equation 3.2 can be updated to Equations 3.3 to be expressed in terms of a porosity adjusted wall shear stress ($F_{s\,adj}$), where the effective channel height (h_{adj}) and width (w_{adj}) are adjusted to account for hydrogel porosity in the BoC channel well.

$$F_{s\,adj} = \frac{6\mu Q}{h_{adj}^{\,2} (w_{adj})} \tag{3.3 a}$$

$$h_{adj} = hp \tag{3.3 b}$$

$$w_{adj} = wp \tag{3.3 c}$$

The channel height and width of the region of the BoC cell well containing the hydrogel were adjusted by multiplying by a porosity factor (p), due to restricted free flow space within the gels. It is expressed in terms of gel volume (Vg) and the maximum amount of media that the hydrogel can hold internally (Vgm) and is given by Equation 3.4 [154] [158].

$$p = \frac{Vgm}{Vg + Vgm} \tag{3.4}$$

To determine porosity, this equation uses the dry gel volume (excluding media) Vg in a chip well after UV curing and overnight hydration with swelling. Gel preparation (curing and hydro-swelling) is detailed in Section 3.2.6, and the method for quantifying gel and absorbed media volumes in Section 3.2.7 (Swelling Ratio and Porosity). Channel height and width in Equation 3.3 require adjustment by the porosity factor of 0.1 due to the gel being found to be 10% porous or having a 90 % gel fraction (see Section 3.3.3). A dynamic viscosity μ of 0.00195 was presumed for alpha-mem and similar media at 20 °C as it is more viscous during lower temperatures when out of incubation for flow shear or centrifuge stimulation [140].

Loading Regime Control

Centrifuge acceleration was controlled using a custom LabVIEW 2020 programme (National Instruments, Austin, Texas, US), which sets the motor direction and speed to apply mechanical loading at either a constant angular velocity or a variable spin-rate cycle mimicking joint loading in the gait cycle (Figure 3.2). In the tri-channel BoC platform, wells at 3.0, 4.5, and 6.0 cm from the disk spin centre produced accelerations of 0.24 g to 8.2 g at 60 to 350 RPM, as calculated by Equation 3.2. Using assay holders instead of disk holders increased the outer well radius to 7.5 cm, generating accelerations up to 10.3 g. This range of BoC accelerations (0.24 to 10.3 g) covers the range of tibial accelerations during walking and running reported by Lafortune *et al.* (walking peak: 2.7 g to 3.7 g; running peak: 10.6 g) [96] [241], with averages of around 1g for walking and 3.5 g for running.

Acceleration is a desirable metric to compare BoC behaviour and in vivo behaviour due to it being a more universal metric that occurs across an entire joint type without much localised variation and has more consistent ranges for actions like walking or running [92] [96]. The spin frequency, shown in Figure 3.3, indicates the spin rate of the centrifuge with +/- sign denoting clockwise/anticlockwise rotation and the simplified spin frequency magnitude denotes spin magnitude only relative to the highest rate anti-clockwise spin in the cycle, without specifying the clockwise/anticlockwise direction. The average spin frequency across the cycle is 2 Hz, which matches the optimal cyclic stimulation required to stimulate bone cell proliferation reported by Cullen *et al.* [242]. This is close to the frequency of the gait

cycle during walking for an average adult [243]. Similarly, Stavenschi *et al.* report that higher shear stress levels at a frequency of 2 Hz were optimal for promoting MSC cells [90].

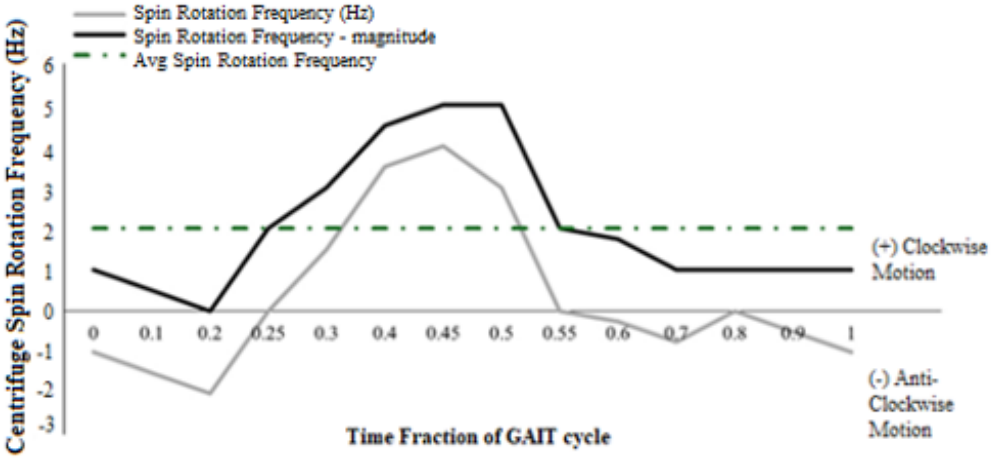


Figure 3.3 Schematic of controlled input angular velocity by spin frequency (shown). Rotational velocity variation implemented by centrifuge disk system with LabVIEW control software, with sample output rotation velocity and spin frequency readings required to mimic the gait cycle.

3.2.3 BoC Platform Verification

Chip verification was conducted to ensure consistent long-term function of the BoC platforms. The chip quality and consistency were assessed by measuring channel dimensions with a Keyence VHX2000 3D digital microscope (Keyence, UK) in triplicate (n=3) at the start, middle and end of inlet and outlet channels. Surface roughness was measured on the bottom of the inlet channel, well centre and outlet channel (n=3) using a ContourGT Profilometer (Bruker, Germany) with white-light interferometry.

Flow performance was evaluated by recording fill/empty times for 500 µL media at 5 to 1000 µL/min using a KFT NE-1000 syringe pump and 5, 10 and 20 mL glass syringes. Each test was repeated (n=3) to assess variance and leak-free operation via polymer luer ports connected by 500 µm ID PTFE tubing. Centrifuge validation was performed by spinning sealed, partially filled chips (buffer layers filled) up to 600 RPM (10 Hz) to stress test the system and simulate operational g-forces (60 to 350 RPM) and gait loading. Leak testing under variable acceleration profiles confirmed integrity under dynamic conditions.

Final perfusion rates of 50, 100 and 150 µL/min were selected for the main testing generated wall shear stress magnitudes of 0.15, 0.3 and 0.45 Pa (Equation. 3.4), based on the media flow and media viscosity, effective channel dimensions and porous gel adjustments, exceeding the threshold for osteogenic stimulation [103]. Chips were validated for flows up to 1 ml/min (Section 3.2.1), which gives 3 Pa flow shear that exceeds many high flow shear studies [103], showing the platform could mimic a wide range of physiologically relevant flow profiles. Details of flow leak tests and centrifuge test setup are in Appendix A3 and A4.

3.2.4 Sterilisation

The PMMA BoC platform was sterilised using a 1 % hydrogen peroxide solution for 30 min given the materials and microfluidic channel requirements [125]. This was followed by three sterile rinses in 1× PBS, and then given 30 minutes of UV sterilisation. This sterilisation technique is applied once per use and is done typically after chip assembly but prior to first cell culture, and then prior to any re-culture seeding in the case of re-use.

3.2.5 Assessment of Indirect and Direct Biocompatibility

Indirect testing: This testing was performed using alamarBlue™ (Merck, UK) according to the manufacturer's instructions and ISO 10993-5. A triplicate set BoC units (n=3) outside their holder were incubated in α-MEM (Gibco, Fisher Scientific, UK) supplemented with 10 % FBS (Sigma Aldrich, UK) and 1 % penicillin/streptomycin (Fisher Scientific, UK) for 24 h under standard conditions. The resulting media extract from each chip (n=3) was applied to six wells of MC3T3-E1 osteoblasts seeded at 10,000 cells/cm² in a 96-well plate.

Negative controls were another column of cells incubated in standard fresh media and positive controls were the same with 10 % dimethyl sulfoxide (DMSO) added. 10 % (v/v) alamarBlue™ was then added to the wells and incubated for 1 h followed by absorption plate readings at 570 nm and 600 nm using a VANTAstar Multi-Mode plate reader (BMG, Aylesbury, UK). Absorption values of samples were calibrated against controls to determine cell viability per sample (Equation 3.5). Viability of more than 70 % was considered as non-cytotoxic as per ISO 10993-5. Cell viability was calculated as:

$$Cell\ Viability\ (\%) = \frac{(\text{ES_abs}\ (570\text{nm}))}{\text{Avg.}(\text{NC_abs}\ (570\text{nm}))}\ 100 \qquad (3.5)$$

Where ES_abs is the experimental sample absorption, which is the viability assay absorption of the lab samples at 570 nm. It is expressed as a percentage of the average of the NC_abs(570nm) which is the negative control absorption at 570nm which is also the mean of the viability assay absorption of the negative control.

Direct testing: This test was performed on uncoated chips (triplicate, n=3) with cells grown directly on the incubated chips (excluding centrifuge chip holder). Cells were seeded at 10,000 cells/cm² and incubated under standard conditions (see Section 3.2.8). After 24 h, cells were detached using 0.25 % Trypsin-EDTA (Sigma Aldrich, Arklow, Ireland) with a 10 min incubation, then resuspended in fresh medium and transferred to Resazurin assay

wells at 10,000 cells/cm². Six wells per column per chip were seeded and assessed using alamarBlue™, with cell viability calculated using Equation 3.6.

The BoC platform was then coated with PLL (Sigma Aldrich, Arklow, Ireland). PLL is a biocompatible cationic polymer that improves cell adhesion and proliferation by providing positive charges that interact electrostatically with negatively charged cell membranes and proteins [244]. The 1 cm^2 area cell well was coated with a 0.1 mg/mL PLL solution and incubated for 1 h prior to analysis. Direct testing involved seeding cells on the BoC platform at a seeding density of 10,000 per cm^2 in triplicate (n=3). Cells were again cultured under standard incubation conditions (Section 3.2.8). Trypan Blue (Sigma Aldrich, UK) exclusion testing was used to assess cell viability [245]. Cells were trypsin detached and extracted as before, Trypan Blue stained as standard [245] and counted using a haemocytometer slide and automated cell counter (CytoSmart cell counter, Corning, Netherlands) to attain the average cell viability.

Following ISO 10993-5 guidelines, non-cytotoxicity is demonstrated by achieving greater than over 70 % cell viability after 72 h [246]. Afterwards, the BoC flow channel was rinsed with 1 % hydrogen peroxide solution, followed by 3 sterile PBS washes. A new chip base was attached using fresh adhesive and chips were then coated, cell cultured and viability tested in the same manner a 2nd and then 3rd time to demonstrate re-usability of the platform.

3.2.6 GelMA and HAMA Synthesis

To provide a more biomimetic 3D cell environment, GelMA and HAMA were added to BoCs wells. The hydrogels were synthesised as described by Velasco-Rodriguez *et al.* [154], that developed and systematically characterized UV-crosslinked hybrid hydrogel of varying GelMA/HAMA concentrations. This study showed that tuning the gelatin–hyaluronic acid composition can control gel stiffness, porosity, swelling, and degradation for various applications while demonstrating its own gel production protocol described below:

1) GelMA synthesis: Gelatin type A (porcine skin, Sigma Aldrich, Dorset, UK) was dissolved in PBS (pH 7.4) at 10 % (w/v) at 50 °C. Methacrylic anhydride (MA; Sigma Aldrich) was added dropwise (1.1 mL MA per 10 g gelatin), and the mixture was stirred at 50 °C for 3 h. The reaction was quenched by dilution with PBS, dialyzed against distilled water (12 to 14 kDa MWCO) at 40 °C for 7 days, lyophilised, and the resulting GelMA powder stored at −20 °C.

2) HAMA synthesis: Hyaluronic acid sodium salt (80 to 100 kDa) was dissolved in PBS (1 % w/v) at 4 °C. MA (1.1 mL per 1 g HA) was added dropwise and the mixture stirred at 4 °C for 24 h while maintaining pH 8 to 10 with 5 M NaOH. Completion was defined by stable pH. The solution was dialyzed against distilled water (12 to 14 kDa MWCO) at 4 °C for 4 days, lyophilised, and the HAMA powder stored at −20 °C.

3) GelMA/HAMA hydrogels: Lyophilised GelMA and HAMA were dissolved in PBS at 37 °C to prepare hydrogels containing 2.5 %, 5 %, 7.5 %, or 10 % (w/v) GelMA with or without 1 % or 2 % (w/v) HAMA. Irgacure 2959 (0.5 % w/v; Cellink, UK) was added as a photoinitiator. The pre-cured liquid gels were also visually compared for viscosity while applying to cell wells. Hydrogels were UV-cured (365 nm, 25 mW/cm²) for 1.5 min (equivalent to 4 mW/cm² for 10 min in a larger low-intensity sterile UV box). Cured gels in assay or chip wells were incubated overnight with distilled water or 1× PBS (at least twice the pre-cure gel volume) to allow hydration and swelling.

3.2.7 Hydrogel Characterisation

Chemical Characterisation

Material characterisation was conducted to understand the physical, chemical, and structural properties of the hydrogels. Nuclear Magnetic Resonance (NMR) was conducted using a Bruker Ascent 400 NMR scanner (Bruker, Ettlingen, Germany). The material spectra were acquired using a Ascend 400 MHz spectrometer (Bruker). Samples were lyophilised (both modified and unmodified polymers) and were dissolved in deuterium oxide (D_2O) at 25 mg/mL at room temperature (around 24 °C). The number of scans was increased from the usual 16 to 64 scans to give a better signal to noise ratio.

Mechanical Properties

The mechanical properties of acellular hydrogels with varying compositions (2.5 % GelMA, 5 % GelMA, 7.5 % GelMA, 10 % GelMA, 10 % GelMA 1 % HAMA, 10 % GelMA 2 % HAMA) were assessed using a Testometric X Series compression tester (Testometric, UK) (n=6). Cylindrical samples (78 mm² area, 4 mm thickness, 1 cm diameter) were UV-cured in custom moulds and PBS-hydrated to swell [142]. Hydrated gels underwent unconfined compression up to 75 % strain over 10 s or until failure, to determine compressive modulus (elastic linear range) and ultimate compressive strength.

Swelling Ratio and Porosity

Using an optimal gel (optimised for composition and thickness), the gel swelling ratio was determined from known pre-UV liquid gel volumes (n=3). Each gel was submerged in a water-filled graduated cylinder, and the displaced water was collected and weighed to obtain the swollen gel volume. The swelling ratio is the average of the displaced (swollen) volume divided by the original pre-cured volume. Gel porosity (Equation 3.5) for optimal gels was measured on triplicate samples (n=3) after overnight hydration using the same method to obtain pre-media volumes. Culture media was then pumped via a syringe pump at 50 µL/min until excess media was expelled from the gel, indicating saturation. The media volume used for this was recorded, and porosity was calculated as the average ratio of media volume to total volume using Equation 3.5 (Section 3.2.2). The mean, 95 % confidence intervals (CI) and std. deviations were determined for swell ratios and the porosity of optimised gels.

3.2.8 Hydrogel Biological Assessment

Cellular responses to 2.5 %, 5 %, 7.5 % and 10 % GelMA, with and without 1 % HAMA, were evaluated to identify the optimal hydrogel composition. MC3T3-E1 cells pre-labelled with ViaFluor (Section 3.2.8) were suspended at 10 % (v/v) in precured hydrogel solution at 1×10^6 cells/mL. Hydrogels (75 µL/well) were cast in a 48-well plate, cured and hydrated as 0.75 mm-thick hydrogel samples (Section 3.2.6). Triplicate samples and controls were cultured in 400 µL medium, replaced every 2 to 3 days. Over 4 weeks, alamarBlue™ and ALP assays were performed weekly and read directly on-plate (see following assay descriptions). At 4 weeks, CellCyte fluorescent imaging was used for visual comparison. The hydrogel formulation with the highest overall 4-week assay readings was considered optimal. Unless otherwise stated, cells were cultured in α-MEM with 10 % FBS and 1 % penicillin/streptomycin at standard incubation [140]: 37 °C, 19 % O_2, 5 % CO_2, pH 7.2 to 7.4, with media changed every 2 to 3 days.

Metabolic Activity (alamarBlue™) assay

alamarBlue™ assays (Fischer, UK) were used according to vendor instructions to assess cell viability, metabolic activity and activity distribution [247]. For the hydrogel optimisation study, 10 % (v/v) alamarBlue™ was added to each chip well, and incubated with cells for 1 h, and then read by microplate reader at 570 and 600 nm [247] [248]. For assessment of metabolic activity of cells cultured within the BoC platform, 10 % (v/v) alamarBlue™ was added to chip media. The BoC platform was then incubated for 1 h to allow hydrogel-

embedded cells to metabolise the reagent. From each chip, 50 µL media samples were collected in triplicate (n=3) and transferred into 96-well plates for these absorbance readings.

Cell Proliferation (ViaFluor)

ViaFluor (Biotium, Middlesex, UK) Green Cell Viability Stain is a membrane-permeant dye and is used to label live cells based on amine binding in the cell cytoplasm, allowing quantification and direct visualisation or quantification of cells in hydrogels [249]. ViaFluor was added in accordance with standard protocols [179] [250] and cell proliferation was measured on a microplate reader by fluorescence (excitation 488 to 493 nm, emission 525 nm). Fluorescence microscopy used a high-throughput Cellcyte assay fluorescence and brightfield scanner (Cytena GmbH, Germany) at 10× magnification. For direct chip validation and subsequent studies, whole chip wells in chip microscope slide holders were imaged. For microplate assays, 10 µL chip gel samples of image-verified average density were extracted weekly with alamarBlue^{TM} media into shared 96-well plates.

Early Osteogenic Differentiation (Alkaline Phosphatase)

Alkaline phosphatase (ALP) activity, an early marker of osteoblast differentiation detected via calcium mineralisation [181], was quantified using an Abcam ab83369 assay kit (Abcam, Cambridge, UK). Before adding other dyes/reagents to avoid interference, 50 µL media samples were collected from assay well gels or directly from gelled chips. Each sample was transferred to a 96-well plate in triplicate (n=3 per chip), with controls, and processed with dye and buffer according to the kit instructions [251]. For initial tests, standards were included as per the vendor protocol [251] to obtain absolute values. Colorimetric absorption was measured at 405 nm (and 415 nm for auxiliary parallel measurements), and microscopy was performed using Cellcyte assay and brightfield readers at 10× magnification.

3.2.9 Optimisation of Hydrogel Thickness

Using the optimal hydrogel composition (Sections 3.2.8, 3.3.4), the gel thickness was then optimised. MC3T3-E1 cells were cultured, and gels were prepared and cured as in Sections 3.2.4 (gel preparation) and 3.2.8 (cell culturing), using the same gel composition but varying thickness while keeping a constant seeding density per well. The cell number was adjusted for each gel volume to maintain around 50 K cells/well (50 K/cm^2), independent of gel thickness or volume. Three gel volumes were tested in a 48-well plate: 50 µL (0.5 mm thick), 75 µL (0.75 mm thick) and 100 µL (1 mm thick). Samples were tested in triplicate (n = 3), with blank cell-free hydrogels and 2D cultures as controls. Cell culture and monitoring was

carried out as per Sections 3.2.8. Hydrogels with the highest average assay readings at 4 weeks were deemed optimal due to cell proliferation and osteogenesis expected to peek around this stage.

3.2.10 Direct Chip Testing – Longitudinal Study

BoC platforms were coated with optimised gels (10 % GelMA, 1 % HAMA, 1 mm thickness (see results in Sections 3.3.4 to 3.3.5) in triplicate (n=3). ViaFluor stained suspended MC3T3-E1 cells [179] [250] were seeded at 0.5 × 10^6/mL in 100 µL pre-cured gel on the chip base/buffer layer. Hydrogels were then cured and hydrated (Section 3.2.6). Each well received 300 µL fresh α-MEM and was incubated under standard conditions (Section 3.2.8). Cell metabolic activity, proliferation, and ALP activity were monitored weekly for 5 weeks post-seeding as described in Section 3.2.8.

After validating cell viability, proliferation and ALP activity in the BoC platform, deposited mineralisation within the platform was assessed at the 5-week timepoint. Samples were fixed with 4 % formaldehyde (Thermo Scientific, UK) and transferred to an assay plate containing pre-stained 2D cell controls. A 1 % Alizarin Red S solution (Sigma Aldrich, Dorset, UK) was applied to detect calcium-based mineral deposition [187], in accordance with the manufacture's protocol [187]. Fluorescence imaging (500 nm excitation, 570 nm emission) was performed using a Cytena CellCyte fluorescence/brightfield microscope reader at 10× magnification.

3.2.11 Investigation of the Effect of Hypoxia on Cellular Response

The impact of altered O_2 on cells in GelMA/HAMA hydrogels was then assessed. Cells were seeded at 10 K/well in optimised gels (Section 3.3.4 to 3.3.5) and cultured under hypoxia (1 to 4 % O_2) or normoxia (19 % O_2), with other cell culture conditions unchanged (Section 3.2.8). As 2D controls, cells were seeded at 10 K/cm^2 in 48-well plates, with media-only and gel-only controls. An additional group included 10 % (w/v) CellShip (CS) (LSG, Bedford, UK) cell protectant in α-MEM under both O_2 conditions to assess the cell protectant properties in a hypoxic environment. All samples were first cultured for 2 days in normoxia and then cultured in hypoxic conditions (Galaxy 48R incubators, New Brunswick, Canada) for the remainder of the study. Cell metabolic activity (alamarBlue^{TM}) and proliferation (ViaFluor) were measured at 3, 7, and 14 days (Section 3.2.8).

3.2.12 Statistical Analysis

Statistical analyses were performed using GraphPad Prism 10 (GraphPad, San Diego, US) and equivalent Python SciPy.stats packages. Tukey HSD post-hoc tests were used for significant main effects between category pairs, and larger group comparisons were analysed with ANOVA. Two-way ANOVA assessed the effects of O_2 level and gel type on ViaFluor-normalised values. Coat type, gel composition, gel thickness, O_2 levels, and chip age/usage were treated as categorical variables. Parametric assumptions were checked with the Shapiro–Wilk test and visual inspection of distributions for normality, and Levene's test for homogeneity of variances. A p-value of less than 0.05 was considered statistically significant. Only significant differences with adjacent groups are indicated on the figures unless stated otherwise. Data is presented as mean ± standard deviation and statistical analysis done for triplicate sets of samples (n=3), unless stated otherwise.

3.3 Results

3.3.1 Verification of the BoC Platform

Measurements of laser-cut channels' width in the single- and tri-channel BoC platforms showed less than plus or minus 3 % variation across triplicate (n=3) measurements at multiple chip locations. The channel base and well base surface roughness across a triplicate (n=3) set of chips was approximately plus or minus 20 µm. Flow testing entailed filling covered chip wells with media to the top well level and then emptying the wells of media while timing fill time and empty time for each volumetric flow rate. Flow tests showed a variation of plus or minus 4% (or 8 % total variation) at 50 to 150 µL/min, indicating consistent flow, see Appendix A3 (Figure A3.5) for details of testing and test results. No leaks were observed during prolonged operation at both low and high flow rates, demonstrating robust, leak-free, sustained usage of the microfluidic system for perfusion tests.

3.3.2 Assessment of Indirect and Direct Biocompatibility

Average cell viability from cytotoxic testing was compared (Figure 3.4, 3.5). Viability averaged above 80 % for both indirect and direct chip testing, with viability comparable to the negative cytotoxic control (Figure 3.4). Direct biocompatibility testing of the Poly-L-Lysine coated BoC platform for enhanced adhesion and prolonged cell culturing indicated a viability of close to 80 %, with viability maintained over a 7-day period (Figure 3.5).

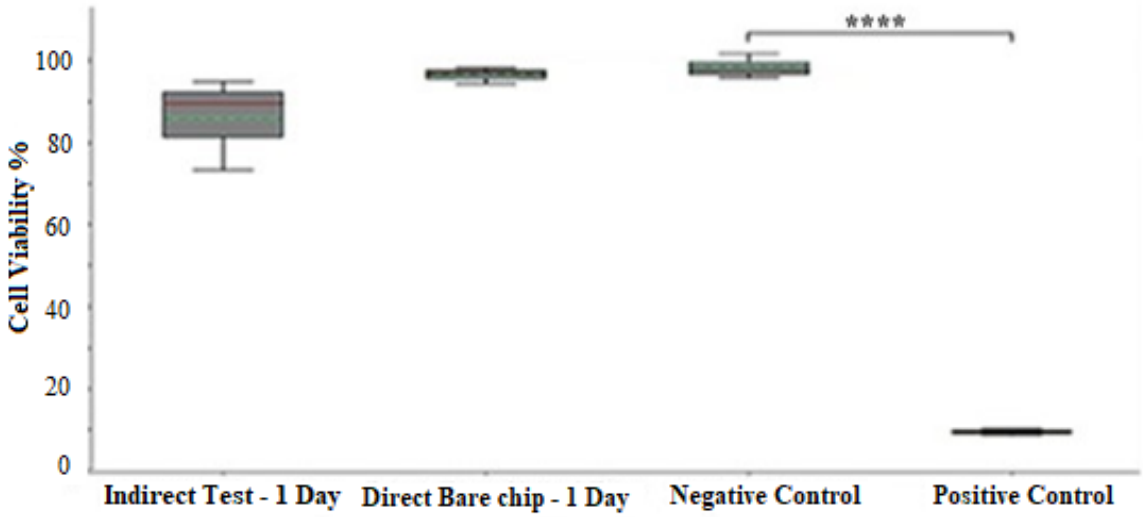


Figure 3.4 Cell viabilityResazurin Assay - Indirect and direct cell viability at Day 1 on the uncoated BoC platform vs negative (assay grown untreated cells) and positive controls (10 % DMSO terminated cells). Statistical significance between groups (by culture age) denoted by * ($p < 0.05$), **** ($p < 0.0001$), all tests performed in triplicate (n=3).

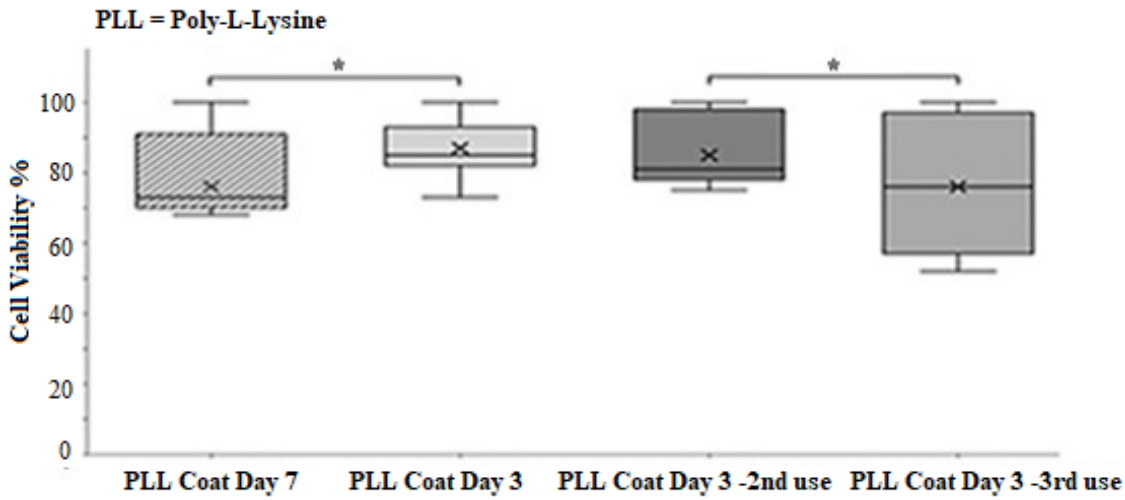


Figure 3.5 Cell viability at Day 3, 7, 2nd use and 3rd use on PLL coated BoC platform. Consistent viability of bone cells in the BoC platform with 2D PLL coating was confirmed up to 1 week. Statistical significance between groups (by number of uses) denoted by * ($p < 0.05$), all tests performed in triplicate (n=3).

Figure 3.5 also demonstrates the reusability of the microfluidic BoCs. First use at Day 3 showed the highest median viability (83 %), while the second use after cleaning had similar viability (80 %), and the third use showed a slight decrease (75 %). A similar trend was observed for chips used for 7 days, with viability remaining above 70 % during first use.

3.3.3 Hydrogel Characterisation

Chemical Characterisation

The peaks in Figure 3.6 confirm successful chemical modification, with degrees of modification of 58 % for GelMA and 17 % for HAMA. GelMA showed aromatic amino peaks at 6.8 to 7.6 ppm, methacrylate vinyl peaks at 5.2 to 5.8 ppm, and lysine amino peaks around 3 ppm, consistent with previous GelMA characterisation studies for process control, batch consistency, and general characterisation [252]. Similarly, HAMA showed methacrylate peaks at 5.6 to 6.2 ppm and methyl peaks around 2 ppm, consistent with reports of similar modification levels (about 20 %) [253]. This NMR characterisation confirmed that the GelMA and HAMA pre-polymers used in this gelled BoC study had molecular similarity and purity comparable to those previously reported, such as by V. Rodriguez *et al.* [154].

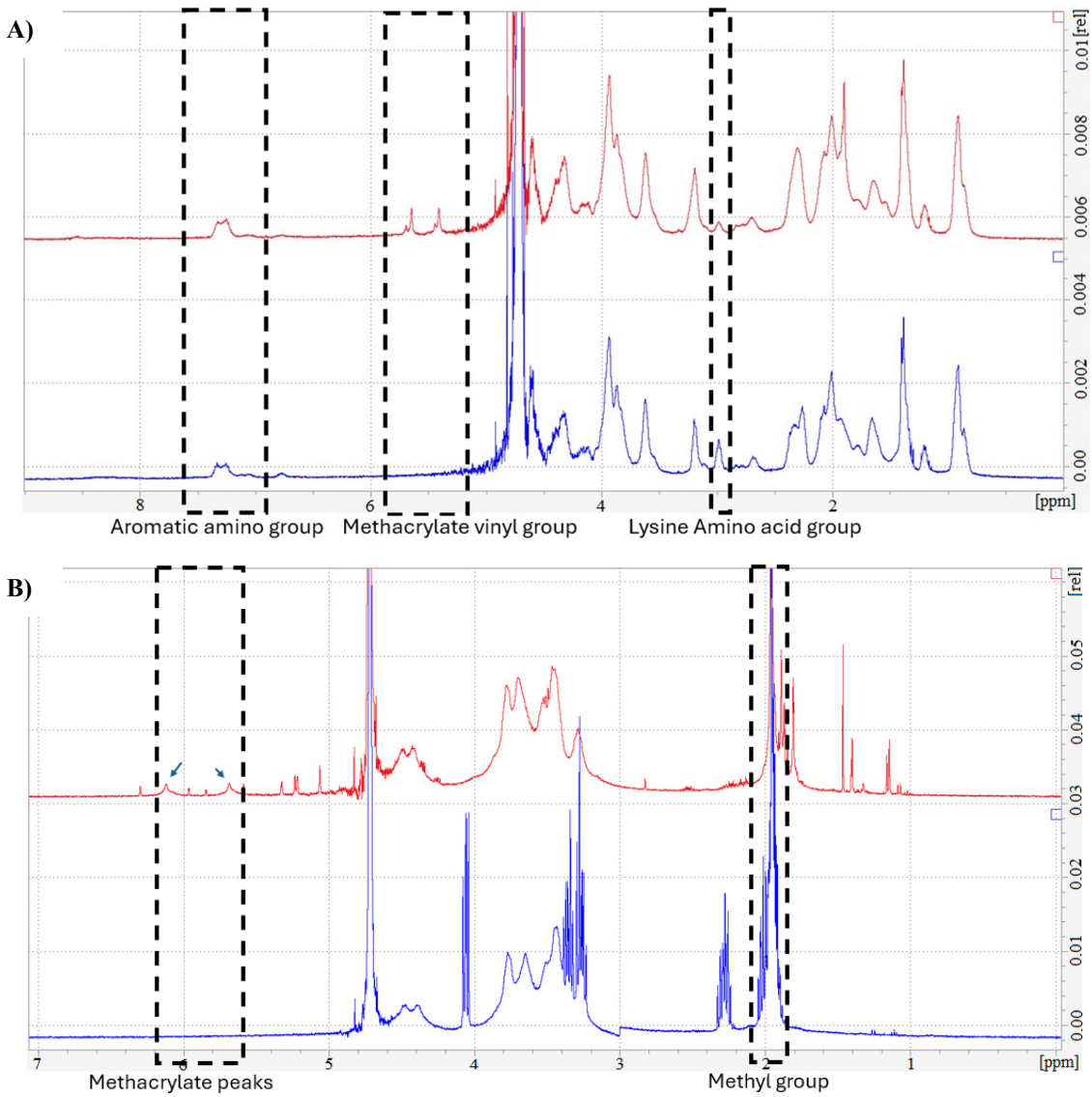


Figure 3.6 A): NMR 400 MHz material characterisation of GelMA (red) and Gelatin (blue) with expected red peaks at Aromatic amino, Methacrylate vinyl and Lysine amino acid groups. **B)** NMR 400 MHz material characterisation of HAMA (red) and Hyaluronic acid (blue) with expected peaks at Methacrylate peak and Methyl groups.

Mechanical Properties

Mechanical compression testing (Section 3.2.7 – Mechanical Characterisation) showed that both compressive strength and elastic modulus increased linearly as GelMA concentration rose from 2.5 % to 10 %, with further increases after adding 1 % or 2 % HAMA. The 10 % GelMA 2 % HAMA samples had the highest compressive strength and elastic modulus (Figure 3.7), while the 10 % GelMA 1 % HAMA group had a similar elastic modulus to 10 % GelMA 2 % HAMA, with no significant difference between the two. HAMA addition was observed to have a greater effect on the compressive strength than the elastic modulus.

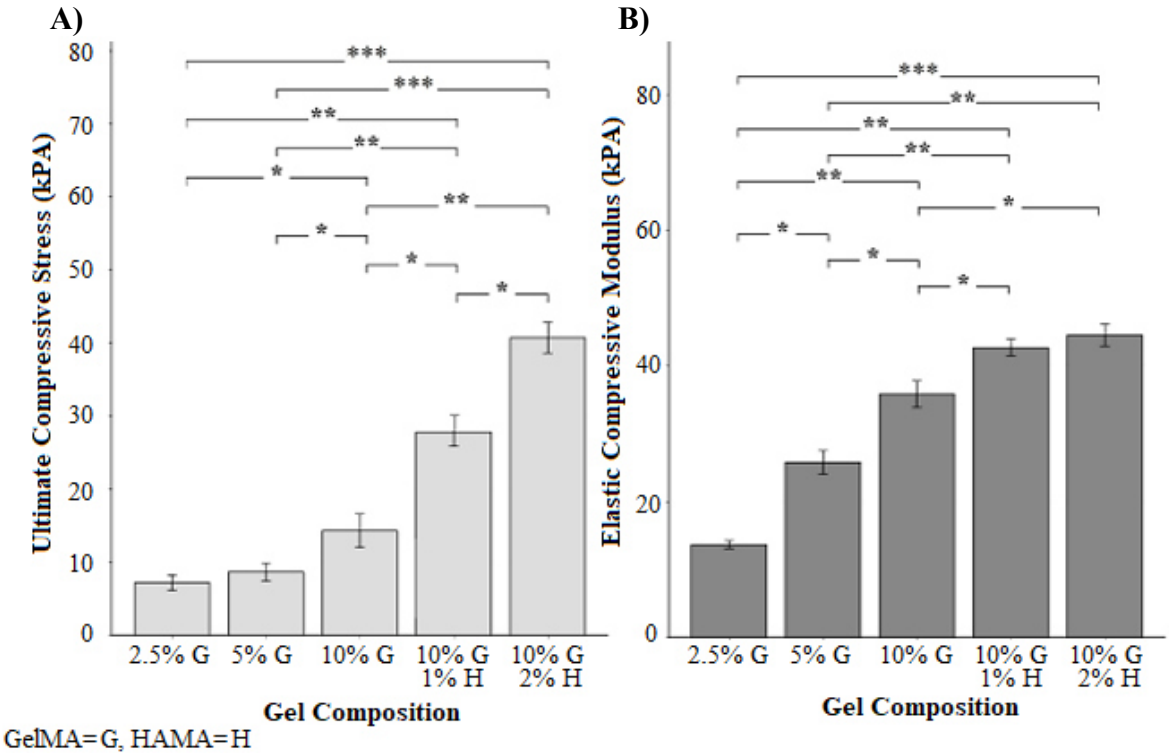


Figure 3.7 Mechanical properties of GelMA/HAMA hydrogels **A)** Compressive strength by GelMA HAMA mix. **B)** Elastic modulus by GelMA HAMA mix. Statistical significance of difference between gel types given by * $p < 0.05$, ** $p < 0.01$, *** $p < 0.001$ all tests done in double triplicate (n=6)

Addition of HAMA to GelMA hydrogels led to an observed increase in viscosity. Hydrogels with 2 % HAMA or higher concentrations were too viscous, preventing them for being more effectively incorporated into the BoC cell wells. Thus, 1 % HAMA with 10 % GelMA was selected as optimal, balancing mechanical stiffness and ease of application to chip wells. Photos and layout of flow and gel fill tests are in Appendix A3.

Swelling Ratio and Porosity

Using the optimal hydrogel (10 % GelMA, 1 % HAMA, 1 mm), the mean swelling ratio was 1.85 (95 % CI [1.71, 1.99]) and the std. deviation = 0.07. This swelling ratio corresponds to an average swelling degree of 54 %. The mean porosity of hydrogel (in bulk) was 10.3 % (95 % CI[7.7 % and 12.9 %]) and std. deviation = 1.3 %. This corresponds to an average 89.7 % gel fraction. For later flow shear calculations, the porosity adjustment factor could be approximated at 10 % or 0.1 for Equation 3.4 in Section 3.2.2.

3.3.4 Hydrogel Biological Assessment

Cell responses to different GelMA concentrations (5 %, 7.5 %, 10 % w/v), with or without 1 % (w/v) HAMA, were evaluated in the BoC platform using 75 µL gels. ViaFluor fluorescence imaging showed differences in cell distribution and proliferation among gel types at 4 weeks (Figure 3.8A). The 10 % GelMA formulations (10G and 10GH with 1 % HAMA) showed the highest amount of cell proliferation and even distribution.

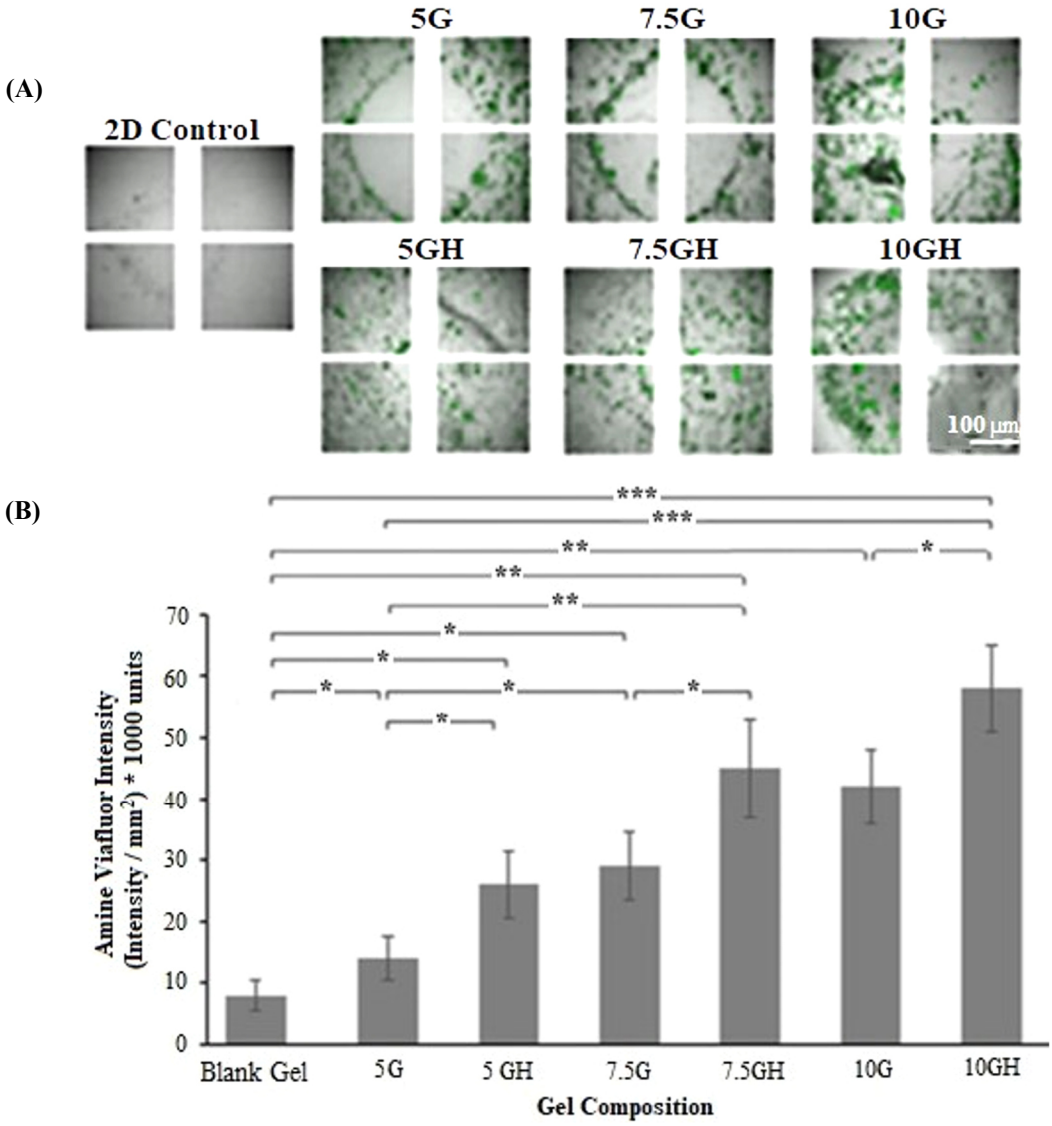


Figure 3.8 ViaFluor cell proliferation by hydrogel composition **A)** Grid of Cellcyte Scanner fluorescence microscopy images showing ViaFluor Green staining at 4 weeks for various gel compositions (5G, 5GH, 7.5G, 7.5GH, 10G, 10GH) in triplicate wells compared to blank gel (2D acellular) controls. 5 GH = 5 % GelMA + 1 % HAMA; 7.5G = 7.5 % GelMA; 7.5GH = 7.5 % GelMA + 1 % HAMA; 10G = 10 % GelMA; 10GH = 10 % GelMA + 1 % HAMA; Scale bar = 100 µm. **B)** Cell Amine Growth (ViaFluor intensity) compared by gel mix (0.75 mm thickness). Quantification of Cellcyte Scanner microscopy ViaFluor fluorescence by sample staining at 4 weeks. Statistical Significance of gel type difference given by * $p < 0.05$, ** $p < 0.01$, *** $p < 0.001$, all tests performed in triplicate (n=3). No significance not denoted. Group ANOVA comparison $p < 0.001$.

The Cellcyte ViaFluor imaging and quantification of the ViaFluor fluorescence (Figure 3.8 B) showed the highest proliferation on the 10 % GelMA hydrogels. ALP absorption (abs.) was then quantified to assess osteogenesis. Figure 3.9 shows average ALP absorbance (abs.) at 28 days for different gel compositions. Hydrogels containing 10 % GelMA 1 % HAMA and 7.5 % GelMA (without HAMA) had higher ALP absorbance than 7.5 % GelMA 1 % HAMA and 5 % GelMA 1 % HAMA hydrogels. The highest mean values occurred in 10 % GelMA and 10 % GelMA 1 % HAMA hydrogels, indicating greater osteogenic differentiation at 4 weeks. Adding 1 % HAMA to 7.5 % GelMA markedly reduced ALP absorbance, whereas 7.5 % GelMA alone remained relatively high. Overall, 10 % GelMA 1 % HAMA hydrogel showed the highest levels of ALP activity.

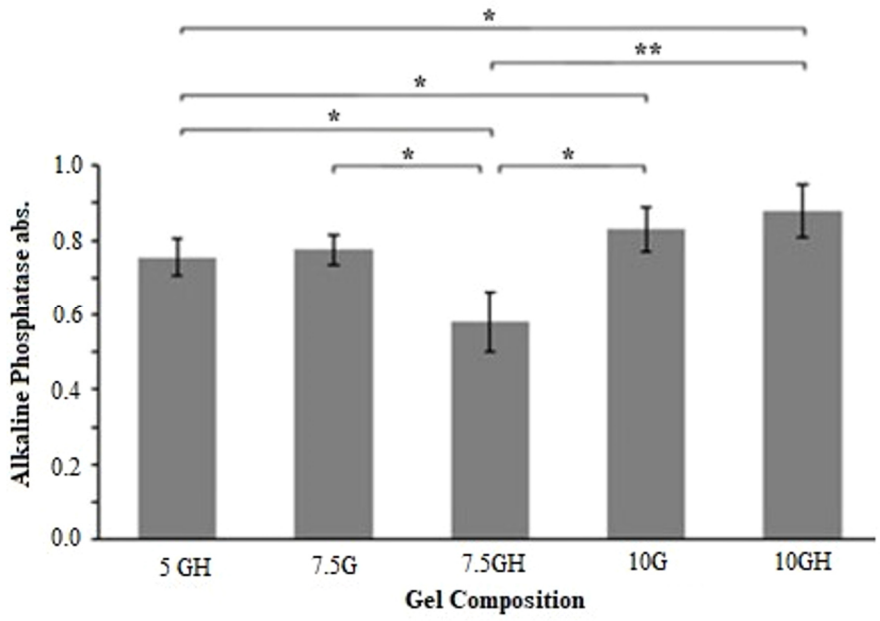


Figure 3.9 Shows Day 28 ALP abs. readings for different gel formulations: 5 GH = 5 % GelMA + 1 % HAMA; 7.5G = 7.5 % GelMA; 7.5GH = 7.5 % GelMA + 1 % HAMA; 10G = 10 % GelMA; 10GH = 10 % GelMA + 1 % HAMA; Statistical comparisons based on ALP activity (absorption) between different hydrogel composition types. Statistical significance of difference between groups given by * $p < 0.05$, ** $p < 0.01$, no significance not denoted. All tests were performed in triplicate (n=3).

Based on these combined assessments, visualised and quantified ViaFluor proliferation along with ALP activity, hydrogel samples composed of 10 % GelMA with the optional addition of 1 % HAMA were inferred as the optimal hydrogel formulation for supporting osteoblast function within the BoC platform.

3.3.5 Optimisation of Hydrogel Thickness and Longitudinal Study

Using the optimised composition (10 % GelMA 1 % HAMA), it was investigated how hydrogel thickness (0.5, 0.75, and 1 mm, corresponding to 50, 75, and 100 µl per well) affected cell activity and differentiation in the microfluidic chip. AlamarBlue™ activity and osteogenesis (ALP activity) were measured at 4 weeks (Figure 3.10). The maximum thickness of 1 mm was selected as hydrogels thicker than 1 mm were difficult to image clearly due to depth-of-field limits and hydrogel or chip base thickness.

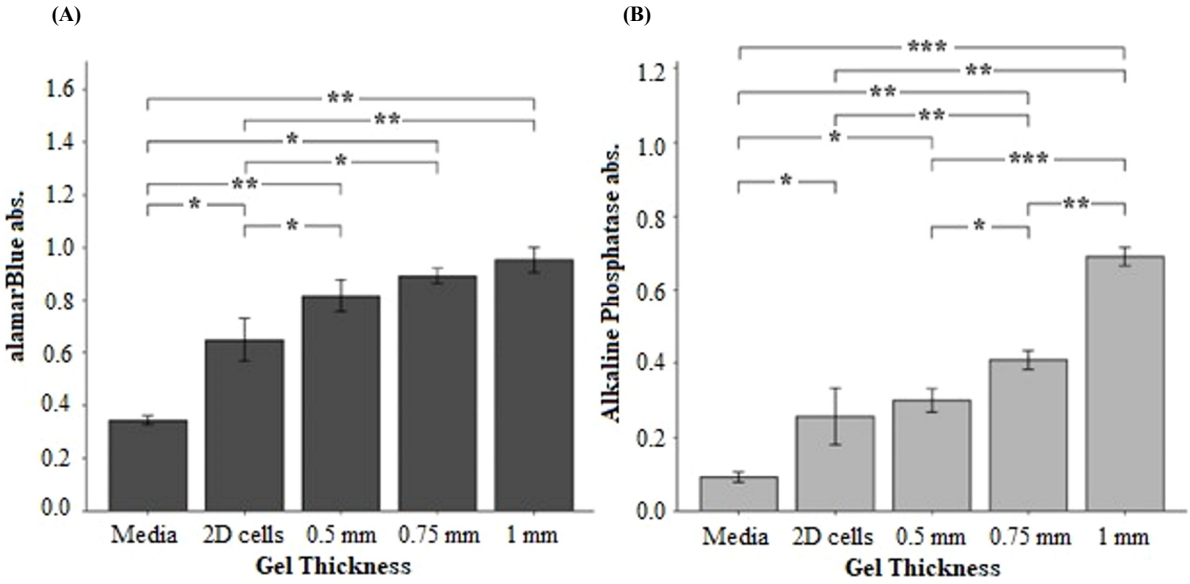


Figure 3.10 ALP and alamarBlue™ abs. readings for various bone cell gel thicknesses **A)** ALP absorption assay values and **B)** alamarBlue™ absorption assay values, measurements taken 4 weeks after cell seeding. Compared relative to 2D cell culture control. Statistical significance of difference between groups denoted by * $p < 0.05$, ** $p < 0.01$, *** $p < 0.001$ all tests performed in triplicate (n=3).

Thicker gels showed increased metabolic activity and ALP activity, most notably in the 1 mm and 0.75 mm samples, with 1 mm hydrogels giving the highest absorbance in both assays. Control wells ('2D Cells only' and 'media') showed much lower levels of ALP activity than 3D hydrogels, confirming enhanced metabolic activity and osteogenesis in 3D (Figure 3.10). Late-stage mineralisation, assessed after 5 weeks using Alizarin Red S fluorescence, (Figure 3.11), showed highest levels of mineralisation and best distribution in the 1 mm thickness hydrogel compared to the other control and other gel thicknesses (0.5 mm and 0.75 mm). Overall cellular activity, tissue development, and practical considerations for long-term culture and analysis in the microfluidic chip indicated that approximately 1 mm thickness was optimal for robust cell development.

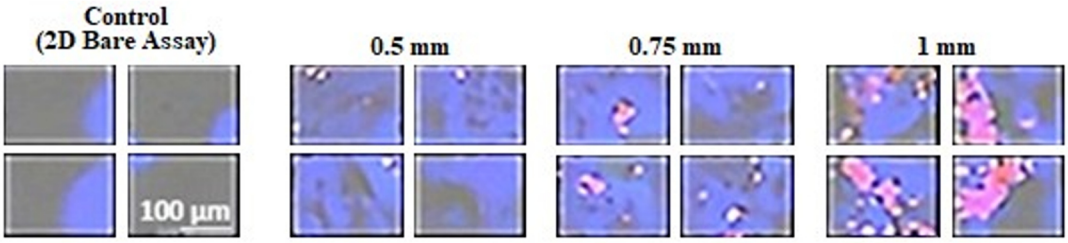


Figure 3.11 Gel in chip alizarin red fluorescence at 5 weeks for various gel thicknesses (0.5 mm, 0.75 mm, 1 mm) of 10 % GelMA and 1 % HAMA gel. Light pink colouring represents calcium mineral deposition clustering contrasted by Alizarin Red fluorescent staining. Scale bar 100 µm.

MC3T3 cells were then cultured in the BoC platform containing the optimised hydrogel (1 mm thick, 10 % GelMA, 1 % HAMA) for 5 weeks. Cell metabolic activity, proliferation and ALP activity were quantified each week. The results showed sustained metabolic activity, proliferation and osteogenesis across the 5-week timeframe demonstrating BoC culture feasibility for longitudinal studies beyond 1 month (Figure 3.12). The successful validation of culture of MC3T3-E1 cells directly in the BoC platform in static culture demonstrated the suitability of the platform for further studies employing mechanical stimulation. Viable cell culturing of at least 5 weeks was validated for longitudinal studies.

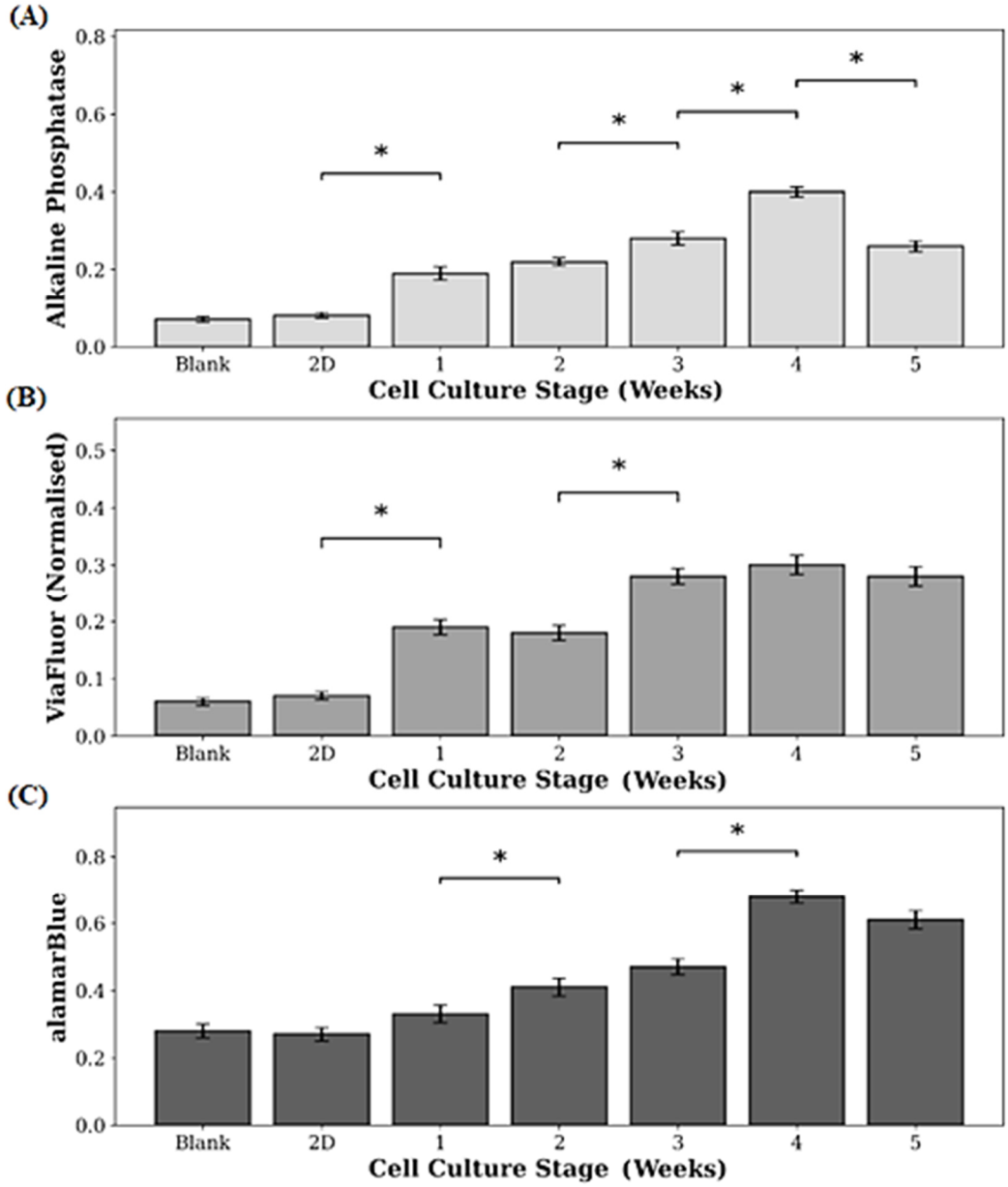


Figure 3.12 Long term culture of MC3T3 pre-osteoblast cells on the optimal hydrogel composition (1mm 10 % GelMA 1 % HAMA) in static culture within the BoC platform. **A)** Alkaline Phosphatase absorption values, **B)** ViaFluor (Normalised abs.) values **C)** alamarBlue^{TM} absorption values, Statistical significance of difference between adjacent groups indicated by * $p < 0.05$. Group ANOVA result for full period was *** $p < 0.001$ for all assays. All tests performed in triplicate (n=3).

3.3.6 Investigation of the Effect of Hypoxia on Cellular Response

Using optimised 10 % GelMA 1 % HAMA gels (1 mm thick), MC3T3 response to varied O_2 levels was examined. Normalised ViaFluor-based proliferation on different cell coatings under normoxia (19 % O_2) and hypoxia (1 to 4 % O_2) was compared after 1 week, at peak 2D control growth (Figure 3.13). Cells grown in 3D gels consistently showed higher proliferation than 2D samples. In 2D cultures, proliferation increased significantly under hypoxia compared to normoxia (0.14 to 0.37 units; 2.5-fold). In contrast, standard 3D gels

showed higher proliferation in normoxia than hypoxia, but with smaller differences. Thus, the hydrogel environment altered cellular responses to oxygen. Cells grown on gels with CellShip cell protectant showed no significant proliferation difference between normoxic and hypoxic conditions, indicating a buffering, cell protective effect at low O_2.

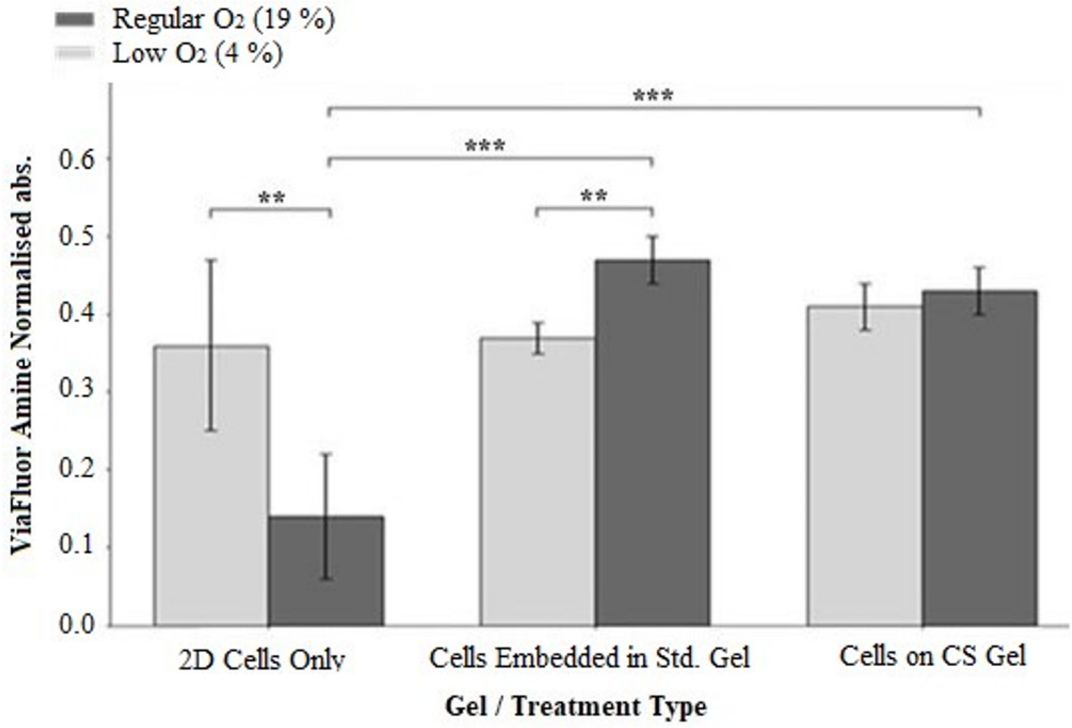


Figure 3.13 Normoxic and hypoxic incubation effects on bone cell samples . MC3T3 proliferation in optimal GelMA (10 % GelMA 1 % HAMA, 1 mm thick) was compared in normoxic (19 % O_2) vs hypoxic (4 % O_2) conditions with standard media and media supplemented with CellShip (CS) cell protectant at Day 7. Error bars indicate std. dev. Statistical significance between O_2 treatment and gel type indicated by * $p < 0.05$, ** $p < 0.01$, and *** $p < 0.001$. All tests were performed in triplicate (n=3).

Overall, bone cells in 3D gels in normoxia can mimic or exceed responses of bone cells in more physiological hypoxia, reducing the need for hypoxic incubation to achieve O_2 levels that mimic the native cell culture environment.

3.4 Discussion

This study developed and validated a BoC microfluidic platform for the investigation of MC3T3 bone cell responses to different mechanical stimuli. The platform uses optimised hydrogels as a biomimetic 3D culture environment to mimic the native bone ECM. The platform was initially validated by confirming leak-free operation under varying flow rates and then for up to 600 RPM non-contact centrifuge stimulation, confirming its suitability for dual stimulation osteoblast studies. Flow testing (Section 3.1) at 2 to 1000 µL/min showed accurate flow, with less than ± 5 % deviation (less than 10 % variance) for rates over 10 µL/min. All triplicate flow tests were leak-free, demonstrating microfluidic and mechanical reliability. The PMMA-based fabrication method with PSA bonding layers showed no cytotoxicity to MC3T3 cells, confirming the biocompatibility of the system [236] [254]. The indirect and direct viability tests (Section 3.2.2, 3.3.2) verified the biocompatibility of the platform (more than 80 % viability). Sustained cell viability (greater than 70 %) of PLL coated chips was confirmed at 7 days. BoC re-use tests validated the suitability of the design and cleaning protocols [125] [255], and successfully demonstrated the potential re-usability of the platform. Later tests of the chip with fully optimised gels (Section 3.3.5) with active cell cultures for over 4 weeks validated the BoC platform as viable for longitudinal studies. Overall, the BoC platform demonstrated combined transparency, sterility and biocompatibility, while being able to withstand required fluid flow and centrifugal forces.

A tuneable hydrogel was then optimised as a 3D culture environment to better mimic the native ECM environment and enable longer term culturing. GelMA HAMA hydrogels with varying compositions were investigated to identify a hydrogel with the required strength, toughness and durability. Camci-Unal *et al.* reported average stiffness values of 30 to 35 kPa for 10 % GelMA hydrogels and 62 to 84 kPa for 10 % GelMA 2 % HAMA hydrogels [149]. Similar stiffness values were obtained for the hydrogels produced in this study (10 % GelMA being around 36 kPa, 10 % GelMA 1 % HAMA being 43 kPa, Section 3.3.3). Other researchers have reported stiffnesses ranged from 10 kPa to 85 kPa for 10 % GelMA hydrogels from various bone tissue studies [149][256]. Mechanical testing showed 10 % GelMA 2 % HAMA samples had the highest elastic modulus (stiffness) of over 45 kPa. The 10 % GelMA 1 % HAMA samples had a similar elastic modulus (43 kPa), but showed lower pre-curing viscosity enabling easier handling, with less uneven swelling. This made them a more suitable choice for inclusion in the BoC platform. Overall, the stiffness of the hydrogels was in the 25 to 68 kPa combined range reported by Sun *et al.* [256] and Engler *et al*. [144] to promote osteogenic differentiation.

Long term (3 plus weeks) cell culture test results showed that MC3T3 cells cultured in hydrogels with higher % GelMA and HAMA demonstrated higher levels of cellular metabolic activity and proliferation. Such longer duration studies are needed to observe increased osteogenic differentiation and corresponding calcium mineralisation [257]. A study by Mullen *et al.* [258], showed the ALP activity which indicates osteogenesis, peaked on gels (polyacrylamide or cross-linked collagen) with stiffnesses around 38 kPa. This was close to the stiffness observed for the 10 % GelMA 1 % HAMA hydrogels investigated in this study. Regarding gel composition, 10 % GelMA 1 % HAMA hydrogels also showed the highest levels of cell proliferation and osteogenesis (Section 3.3.4). GelMA HAMA hydrogels (10 % GelMA 1 % HAMA) have also been successfully employed for bone tissue engineering by Lin *et al.* [227], where photo-initiator agents Irgacure 2959 and anthocyanidin were compared as photo-crosslinking agents. This study also showed that gels with 1 % HAMA addition significantly improved cell viability (plus 20 %), osteo-differentiation (plus 30 %) while slowing hydrogel degradation rates (minus 30 %) [227].

Longer duration cell culture experiments investigated the optimal hydrogel thicknesses within the BoC platform. The results demonstrated that the 1 mm thick gels performed best overall, they supported higher metabolic activity, proliferation, osteogenesis and mineralisation (detected via ALP absorption and Alizarin Red S) compared to thinner gels (0.5 mm, 0.75 mm) at 28 days (Section 3.3.5). This gel type and thickness had balanced depth for growth volume and thinness with porosity to allow diffusion while thicker hydrogels provide more space for cell proliferation and additional matrix deposition but have more imaging constraints. Additionally, media supply is more challenging for thicker gel with more cells and excessive nutrient gradients [259][260]. This was also the hydrogel sample thickness chosen by Lin *et al.* [227]. For the optimal conditions both porosity and nutrient diffusion should be considered. The average porosity results (10 %, or 90 % gel fraction) as well as swelling ratio (1.86, or 54 % swelling degree) in Section 3.3.3 aligned with the findings reported by Velasco-Rodriguez *et al.* [154] for 10 % GelMA 1 % HAMA hydrogels, further verifying the consistency of production methods for these hydrogels.

Exploring the influence of oxygen levels (Section 3.3.6) in the BoC platform showed that hypoxic 2D bone cell cultures had significantly higher proliferation than normoxic 2D cultures. In contrast, cells cultured in 3D hydrogels showed higher and less variable proliferation than 2D samples, with no added benefit observed from hypoxia. This suggests the hydrogel provides an O_2-buffering effect, closer to the conditions present in *in vivo* tissue [133] (Section 3.3.6). CellShip-supplemented 3D cultures showed a similar pattern, with CellShip further reducing variation and minimising differences between normoxic and

hypoxic proliferation. This is particularly relevant for joint or BoC platforms, indicating that an optimised hydrogel formulation can stabilise cellular responses under variable oxygen conditions in 3D gelled BoC samples [137]. In fact, with *in vivo* tissues hydrogels can retain media nutrients and water longer [261], while effectively releasing absorbed oxygen for tissue repair as observed by Yang *et al.* [262] and can explain why optimal 3D gels maintain conditions resembling more hypoxic *in vivo* bone environments.

Binder *et al.* [133] have also examined enhanced osteogenic growth under hypoxic culture. This study found that human MSCs cultured under hypoxic conditions (5 % O2) and reduced serum (1 % FBS) showed a 20 % increase in ALP activity at 21 days compared to cells cultured under normoxia (21 % O2) and higher serum (5 to 10 % FBS). Importantly, both hypoxia and reduced serum were required for enhanced osteogenic differentiation. Scheinpflug *et al.* [137], developed a 3D bone collagen culture stimulation platform with varied O_2 levels (7 % and 19.8 % O_2), with 10 % mechanical compressive strain at 1 Hz frequency implemented on human osteosarcoma reporter cell line samples. In this platform, unstimulated hypoxic samples showed early increased proliferation, but mechanically stimulated hypoxic samples showed inhibited osteogenesis, though only at the 1-week timepoint, with the study limited to 1 week. Combined with Section 3.3.6 hypoxia tests, this indicates that normoxic 3D hydrogels are more suitable for the promotion of osteogenesis than hypoxic settings for BoC MC3T3 cells, removing the need for hypoxic incubation in later studies.

Using multiple assays (alamarBlue^{TM}, ViaFluor, ALP, Alizarin Red S) provides a comprehensive assessment of cell viability, activity, proliferation, and mineralisation, enabling less invasive and diverse culture monitoring [176][178] [184]. Other studies have tracked in real-time cell growth or osteogenic development through gene expression analysis (e.g. ALP, COLA1) or bio-bioluminescence protein quantification [263]. Further BoC studies could compare alternative monitoring techniques with assay results and other studies. Optimal integration with assay or non-invasive methods could enable high-throughput, low-cost, minimally invasive, and frequent monitoring of 3D cell samples [263] [264] [265]. Adding HA with fine-tuned curing would allow the introduction of other cell types (e.g., chondrocytes) [227] [266]. Thus, future work could refine the hydrogels to support multiple cell types or create bi-hydrogels to establish a JoC model. This chapter has focused on the development and validation of the BoC platform. The following chapter explores dynamic stimulation with the BoC platform by applying flow-shear and centrifuge-based mechanical stimulation to evaluate the effect on osteogenesis.

3.5 Conclusion

This study presents a validated BoC microfluidic platform for long-term osteoblast culture, capable of applying controlled mechanical forces that mimic physiological loading. Tuneable GelMA HAMA hydrogels were investigated and the 10 % GelMA 1 % HAMA, 1 mm thick hydrogel was selected as the optimal for incorporation into the BoC platform. This hydrogel provided a longer-term stable, physiologically relevant 3D environment for MC3T3-E1 cell culture with a stiffness value within the required range for the promotion of osteogenesis. The integrated system combines precise mechanical control with an optimised culture environment to study customised mechanical stimulation of joint or bone tissue that can be used for longitudinal studies. This supports future research in tissue interaction modelling, drug testing, and mechanobiology. The following chapter investigates the combined effects of centrifuge cyclic loading and flow-induced shear stress stimulation on bone tissue.

Chapter 4: Investigation of Centrifuge and Flow Stimulation Effects on Osteoblast Response

4 Investigation of Centrifuge and Flow Stimulation Effects on Osteoblast Response

4.1 Introduction

Various BoC platforms have been developed to simulate the mechanical forces experienced by bone cells [52]. For instance, compressive forces have been delivered using cyclic compression bioreactors [137] and pneumatic compression systems [218]. Fluid shear stress has also been introduced via microfluidic platforms that control flow injection to stimulate stromal cells [267]. However, reviews note that relatively few investigations have focused on intermediate shear stress ranges (around 0.1 to 0.5 Pa), particularly in long-term three-dimensional cultures [103]. While no studies have yet applied dual stimulation (flow shear and compressive loading) in 3D BoC platforms, Paggi *et al.* developed a JoC platform that combined mechanical actuation system and perfusion flow to achieve compression and shear strain on chondrocyte-laden hydrogels [79]. This presents an opportunity to create a multi modal mechanical stimulation BoC platform, particularly for long-term 3D cultures.

Combining microfluidics and mechanical loading with a customised hydrogel for cells can better mimic the biological environment of bone tissue. Schuurman *et al.* [268], have developed GelMA–HAMA composite hydrogels to enable more controlled use of gel tissue constructs for JoC and disease modelling applications. GelMA and HAMA hydrogels in varying formulation are frequently employed as scaffold materials in bone tissue engineering applications due to their biocompatibility, mechanical tuneability and biochemical properties that mimic native ECM for many cell types [32], [269]. Such custom hydrogels provide a 3D culture environment that allows a more realistic response to mechanical stimulation [270]. A fine-tuned optimal support hydrogel (10 % GelMA 1 % HAMA, 1 mm thick), identified and validated in Chapter 3, provides a suitable 3D culture environment for mechanical testing. Syringe pump-controlled fluid shear [98] [271] and centrifuge-induced cyclic compression [72] regulate osteogenesis [272] with shear and compressive forces. A combined syringe–centrifuge approach is sterile, low cost, accessible, and non-contact approach, offering multi-modal dual stimulation in BoC platforms [95].

This study examined how centrifugal cyclic loading and syringe flow shear affect metabolic activity, proliferation, and osteogenesis of MC3T3-E1 osteoblasts in GelMA/HAMA hydrogels within a BoC platform. It was hypothesised that combined flow- and centrifuge-based mechanical stimulation would enhance proliferation and osteogenesis via mechanotransduction. Individual and combined effects of each stimulation mode were compared with static controls to assess interactions and potential synergy.

4.2 Methodology

Microfluidic chips were fabricated as described in Section 3.2.1 and validated for direct cell testing as described in Section 3.2.3. GelMA/HAMA hydrogels were incorporated into these validated BoC platforms prior to conducting cell culture analysis.

4.2.1 Microfluidic Chip Preparation

The optimal hydrogel composition from Chapter 3, 10 % GelMA 1 % HAMA was fabricated as described in Section 3.2.6. During hydrogel production, MC3T3-E1 cells were suspended in the prepolymer solution at 0.5×10^6 cells/mL and pipetted into microfluidic chips wells with 100 µL of liquid gel applied per each 1 cm^2 well (to achieve a 1 mm gel thickness) within the tri-channel microfluidic chips. Hydrogels were cured and allowed to hydrate and swell overnight (Section 3.2.6). A set of four tri-channel chips were produced for centrifuge optimisation tests (to test three centrifuge levels and a static control set) prior to the main combined stimulation experiments. For the main experiment, eight tri-channels chips were produced for each combination of static, centrifuge and/or flow stimulation. The same standard incubation cell culturing methods were used as described in Section 3.2.8. Cell media in the BoC platform was replaced every 2-3 days over 7 weeks.

4.2.2 Application of Mechanical Stimuli

All BoC platforms with cell-seeded hydrogels were cultured statically for 3 days before stimulation (triplicate, n=3). Three conditions were evaluated: 1) centrifuge, 2) flow, and 3) combined centrifuge and flow. Static BoC and 2D well plates cell cultures served as controls.

Centrifuge stimulation: The BoC platform was placed in centrifuge holders and loaded into the centrifuge for required applied loading regime. Initial tests evaluated the duration for application of centrifugal loading. For this analysis, the BoC platform was centrifuged at 1 g for 0.25, 0.5, 1, 1.5, or 2 h/day and cell proliferation was assessed in triplicate at 3 weeks using the Viaflour assay. In all cases, prior to application of centrifugal loading excess media above the hydrogel was removed to prevent overflow. Then, the influence of varying the centrifugal loading on MC3T3 response was assessed. Centrifugation was applied at 0.6 g (inner well), 1.0 g (mid well), or 1.4 g (outer well) for 1 h/day. Between treatments, the BoC unite were returned to the incubator for standard incubation (37 °C, 5 % CO_2).

Flow stimulation: Intermittent shear flow was applied because it supports long-term osteogenesis [273] and is easy to implement with syringe pumps. Chips were connected to a perfusion system (KFT NE-1000 syringe pump, KFTechnology, Rome, Italy), and medium was perfused at 0 (static control), 50, 100, or 150 µL/min to repeatedly fill and empty the

cell wells bidirectionally for 1 h per day. After weekly assays, chips were rechecked the next day for changes in readings and tissue development. Volumetric flow rates and daily flow durations were selected from literature on similar flow stimulation studies [90][103][274].

Combined centrifuge and flow stimulation: Each day chips were exposed daily to both perfusion flow (50, 100, or 150 µL/min for 1 h), followed by 1 h of standard incubation for temperature and CO_2 recovery, then 1 h of 1g centrifugation applied sequentially [141]. Chips were placed in an adjacent perpendicular chip assay holder, with chip well centres placed at a median mid-well distance, with wells to the left and right having a negligible radial distance variation (of less than 5%) due to Pythagoras theorem and distance ratios of 1.5cm between well centres (opposite side) versus 6cm median distance to the radial centre.

4.2.3 Monitoring and Assays

Cell responses to stimulation were assessed at weekly timepoints after cell seeding. This was done for 5 weeks for centrifuge optimisation and up to 7 weeks for the main dual stimulation tests. BoC samples was incubated for 1 h after stimulation before measurements to allow temperature recovery. All tests were performed in triplicate (n = 3), with static BoC platform samples and 2D culture as controls. Metabolic activity (alamarBlue™), proliferation (ViaFluor 488 kit) and osteogenesis (ALP assay) were assessed as described in Section 3.2.8.

4.2.4 Data Analysis

Experimental data is archived online: https://github.com/Collib29/, with individual test files and a combined dataset (ML_FlowCentrifuge_all.csv). Flow rate and centrifugation level were treated as categorical factors. ANOVA was used for group comparisons and Tukey HSD post-hoc tests for pairwise comparisons. One-way ANOVA (GraphPad Prism 10 and Python SciPy.stats) evaluated the main effects of centrifugation (Centrifuged_(g_equiv) in dataset) or flow rate (Flow_rate_(µl/min) in dataset) alone or under single-type stimulation. Two-way ANOVA evaluated the main and interaction effects of both factors on assay output variables. These dataset output variables are labelled as follows: 560nm_alamB (alamarBlue™ absorption), 488nm_VFz_abs (ViaFluor normalised absorption), 405nm_alkP (Alkaline Phosphatase absorption), and 488nm_VF_FL (ViaFluor direct fluorescence). Data normality was assessed with distribution plots and the Shapiro–Wilk test, and homogeneity of variance with Levene's test. Statistical significance was set at p less than 0.05. Only significant differences relative to static samples and treatment sets for each week are indicated on figures. Data is given as mean plus or minus std. deviation from independent triplicate samples for each mechanical stimulation set unless stated otherwise.

4.3 Results

4.3.1 Centrifuge-Only Stimulation

Initial assessment explored application of a 1 g centrifugal load for durations of 0.25, 0.5, 1, 1.5, or 2 h/day for 3 weeks. ViaFluor amine fluorescence indicated high levels of proliferation across all groups. The highest levels of proliferation were observed in the cells subjected to centrifugal loading for a 1 h/day duration, hence this centrifuge duration was chosen as the overall optimal centrifuge duration for later experiments (Figure 4.1).

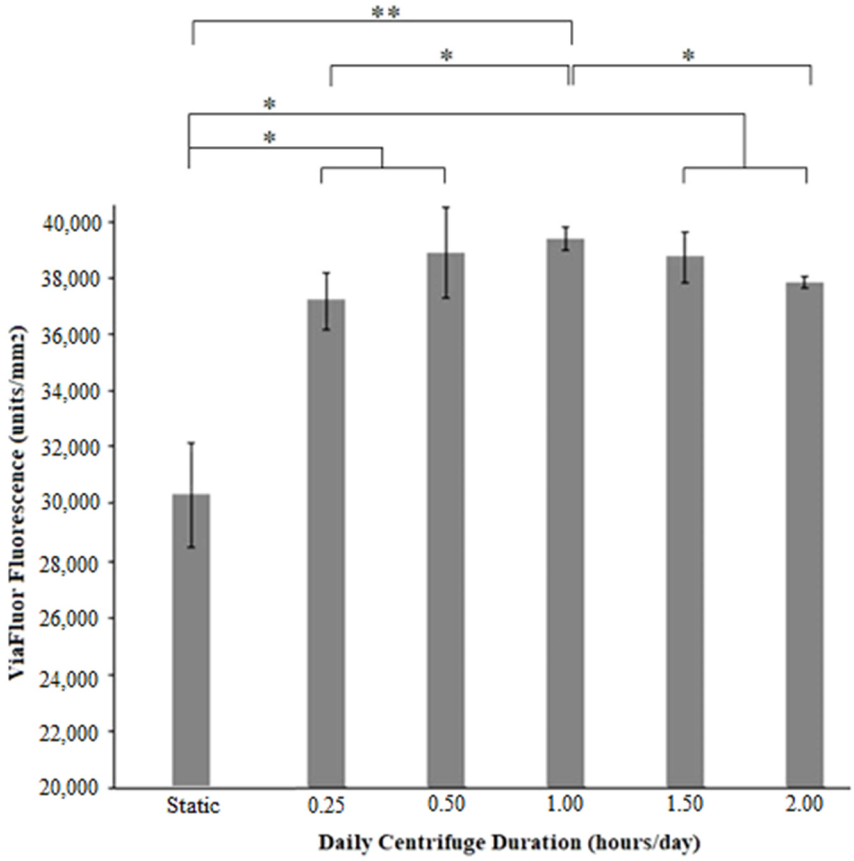


Figure 4.1 Optimisation of centrifuge duration. Comparison of assay centrifuged samples by centrifuge duration at 1 g daily over 3 weeks. Compared ViaFluor amine fluorescence on 3-week-old samples that were centrifuge stimulated for varied durations (number of hours / day) to determine an optimal centrifuge duration per day. *(*) indicates statistical significance in values difference between all duration sets and static 3D gels. * $p<0.05$ and ** $p<0.01$. All tests in triplicate (n=3).

Direct ViaFluor Fluorescence detected cell proliferation was used as the main indictor due to the larger role cell proliferation plays as part of bone cell growth at earlier stages of bone cell culturing, with osteogenesis typically not increasing significantly until about 2 weeks [160]. Later correlation results (Section 6.3.1) showed that in later weeks there is a large correlation between proliferation, metabolic activity and osteogenesis assay results.

Following identification of the optimal duration for centrifugal load application, the influence of changing the magnitude of centrifugal load was assessed. Using the Cytena Cellcyte platform, brightfield, ViaFluor amine-based fluorescence, and osteogenesis (ALP staining) images were captured and centrifuged samples (e.g., 1.4 g; Figure 4.2 A) were qualitatively compared with 2D assay-grown cell controls. Centrifuged-only stimulated samples showed clear qualitative differences between static samples and those exposed to higher g-levels, with the latter exhibiting increased proliferation, and larger clusters (Figure 4.2 A). Higher centrifugation speeds produced more interconnected, defined bone cell clusters and greater cluster density (ViaFluor image data), indicating higher levels of cellular proliferation.

Over 5 weeks, benchmarking based on ALP absorbance at 405 nm (Figure 4.2) identified 1 g as the optimal long-duration low g-force. Relative to static samples, centrifuged samples showed a 25 to 40 % increase in ALP-associated osteogenesis, with ALP peaking at 3 weeks and then moderately declining. Optimal 1g centrifugation increased ALP absorption levels by approximately 40 %, peaking at 3 weeks, while 1.4 g ALP absorption levels similarly peaked at 4 weeks, before decreasing (Figure 4.2 B).

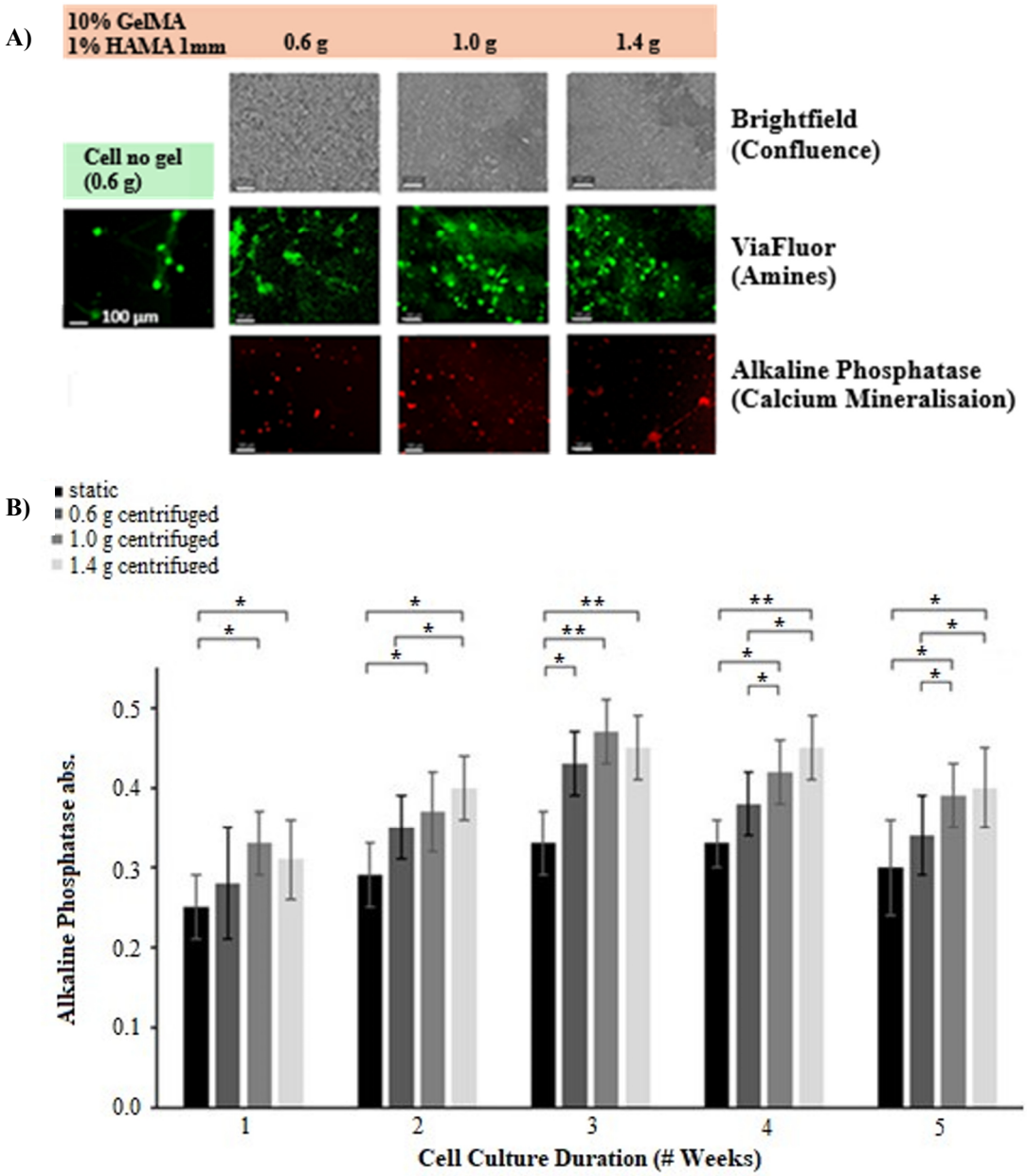


Figure 4.2 Centrifuge cyclic loading by g-level **A)** Brightfield and Multi-wavelength fluorescent images (ViaFluor 485nm & ALP 405nm) compared the response of cells within the BoC platform to various equivalent centrifuge g-force levels (0.6 g, 1.0 g and 1.4 g). Increased cell density and osteogenic activity was observed at higher g-levels. Compared at 3 weeks of cell centrifuge stimulation. Scale bar = 100 µm. **B)** Quantified Comparison of various g-force levels (0.6 g, 1.0 g, 1.4 g) vs static cell samples. Highest levels of ALP activity were observed at Week 3 – 4. Increased ALP activity was observed with increasing g's. *(*) indicates statistical significance in values difference between centrifuged, static 3D gels. * $p<0.05$ and ** $p<0.01$. All tests in triplicate (n=3).

Detailed results for significance of difference results in table-from for this test and later flow with(out) centrifuge stimulation tests by media type are given in Appendix A5 to A8. Additional assay results to Figure 4.2 from alamarBlue™ and ViaFluor testing are given in Appendix A9.

4.3.2 Flow-Only Stimulation

Across all flow rates, flow-based samples showed nearly double the cell activity, proliferation (Figures 4.3), and osteogenic mineralisation (Figure 4.4) compared to static samples at peak culture (5 weeks). Chips were typically stimulated at all flow rates but averaged at 100 µl/min. Over 4 to 5 weeks, flow-stimulated 3D gels had significantly higher metabolic activity (Figure 4.3A) and proliferation (Figure 4.3 B), with alamarBlue^{TM} activity increasing by 80 to 100 % and ViaFluor proliferation by 50 to 100 % versus static 3D gels. Static 3D gels also showed higher proliferation than 2D static cultures. Overall, all flow-shear–stimulated samples significantly outperformed static controls for cell activity or count.

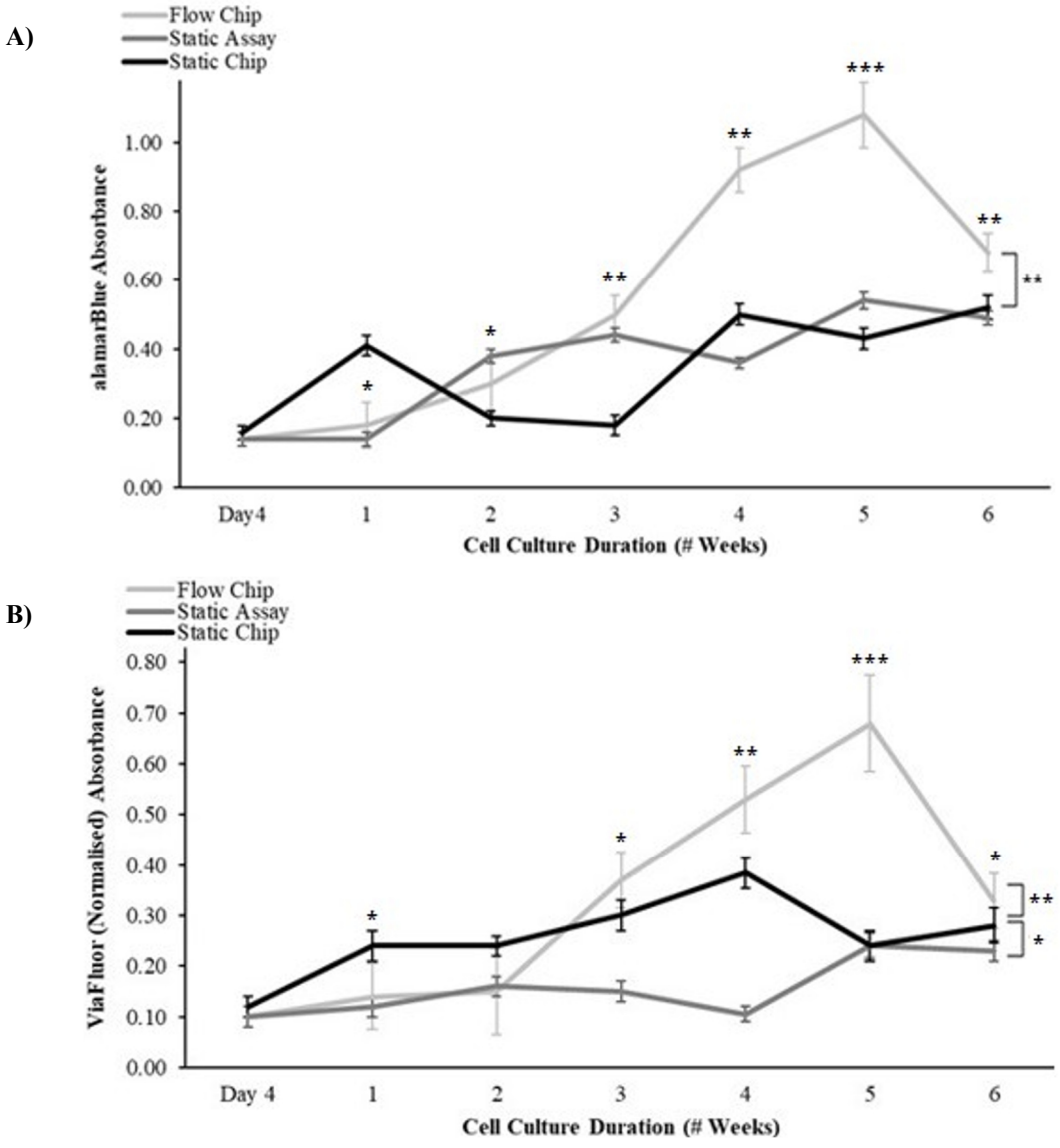


Figure 4.3 Cell metabolic activity and proliferation for flow stimulated samples vs static controls **A)** alamarBlue^{TM} cell metabolic activity (abs. 570 nm) for flow stimulated vs static cell samples. **B)** VF amine normalised absorption (488 nm) compared for cell growth for static vs flow cells. Significance compared across 3 – 6 Weeks. * (*) indicates statistical significance in values difference between flow, static 2D or 3D gels. * $p < 0.05$ and ** $p < 0.01$. All tests performed in triplicate (n=3).

Figure 4.3 A, B shows increasing divergence in cell behaviour between flow stimulated and static samples in metabolic activity and proliferation up to 5 weeks, followed by a reduction in metabolic activity and proliferation in the flow stimulated samples and convergence by 6 weeks. Quantification of ALP activity showed flow stimulated samples had significantly higher ALP activity than all variants of static samples (Figure 4.4). Flow stimulation enhanced osteogenesis. Peak levels of ALP activity are observed at 5 weeks in the flow stimulated group, with nearly a 100 % increase in ALP activity under flow shear compared to static controls. By 6 weeks, ALP activity decreases, and ALP absorption values converge as hydrogel samples begin to degrade as expected from other GelMA HAMA degradation studies [230]. The static 3D gel chip shows significantly higher ALP activity than static 2D assays, highlighting the benefit of the 3D culture environment. Across all three groups, flow-stimulated samples have the highest values.

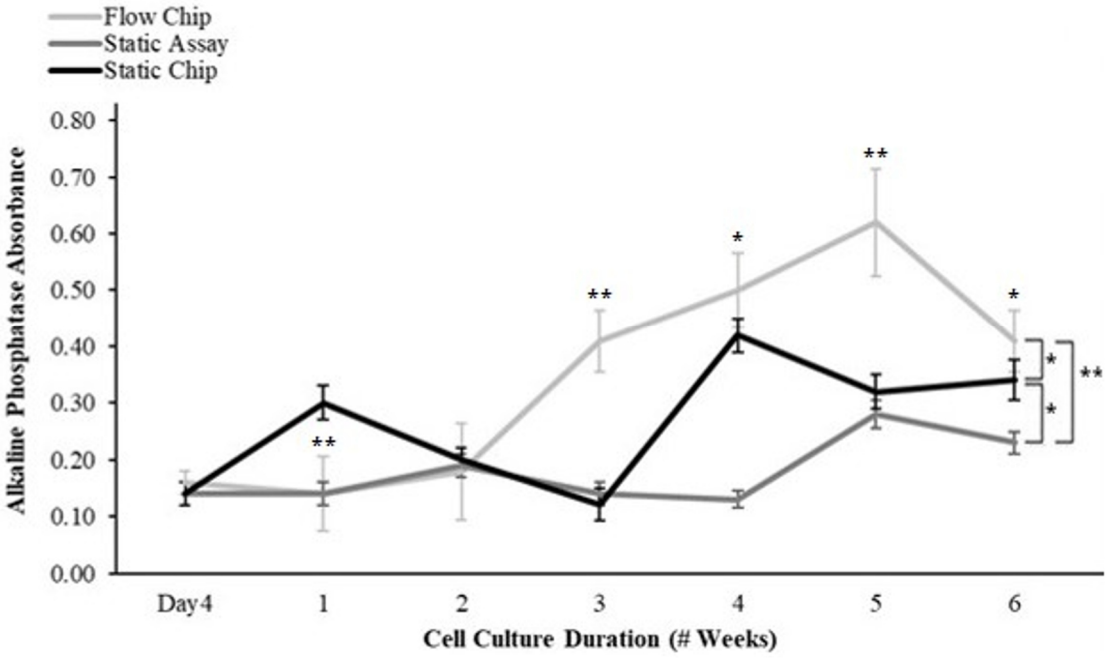


Figure 4.4 ALP absorption by flow stimulated vs static cell samples. Flow stimulated samples resulted in the highest levels of ALP activity after the 2-week timepoint. * (*) indicates statistical significance in values difference between flow, static 3D and static 2D gels. * $p<0.05$ and ** $p<0.01$. All tests performed in triplicate (n=3).

For each group, a set flow rate (50, 100, or 150 µl/min) was applied for 1h daily and compared with static controls. The results indicate that 50 µl/min flow rates resulted in the highest levels of metabolic activity and proliferation up to the 4-week timepoint (Figure. 4.5), with over a 60 % increase metabolic activity and 2-fold increase in proliferation

compared to static controls. A reduction in metabolic activity and proliferation occurred after this point, as some degradation of the hydrogel took place. The 100 µl/min group showed the highest levels of metabolic activity and proliferation at 5 weeks, with over a 70% increase in metabolic activity and 2.5-fold increase in proliferation, compared to static controls.

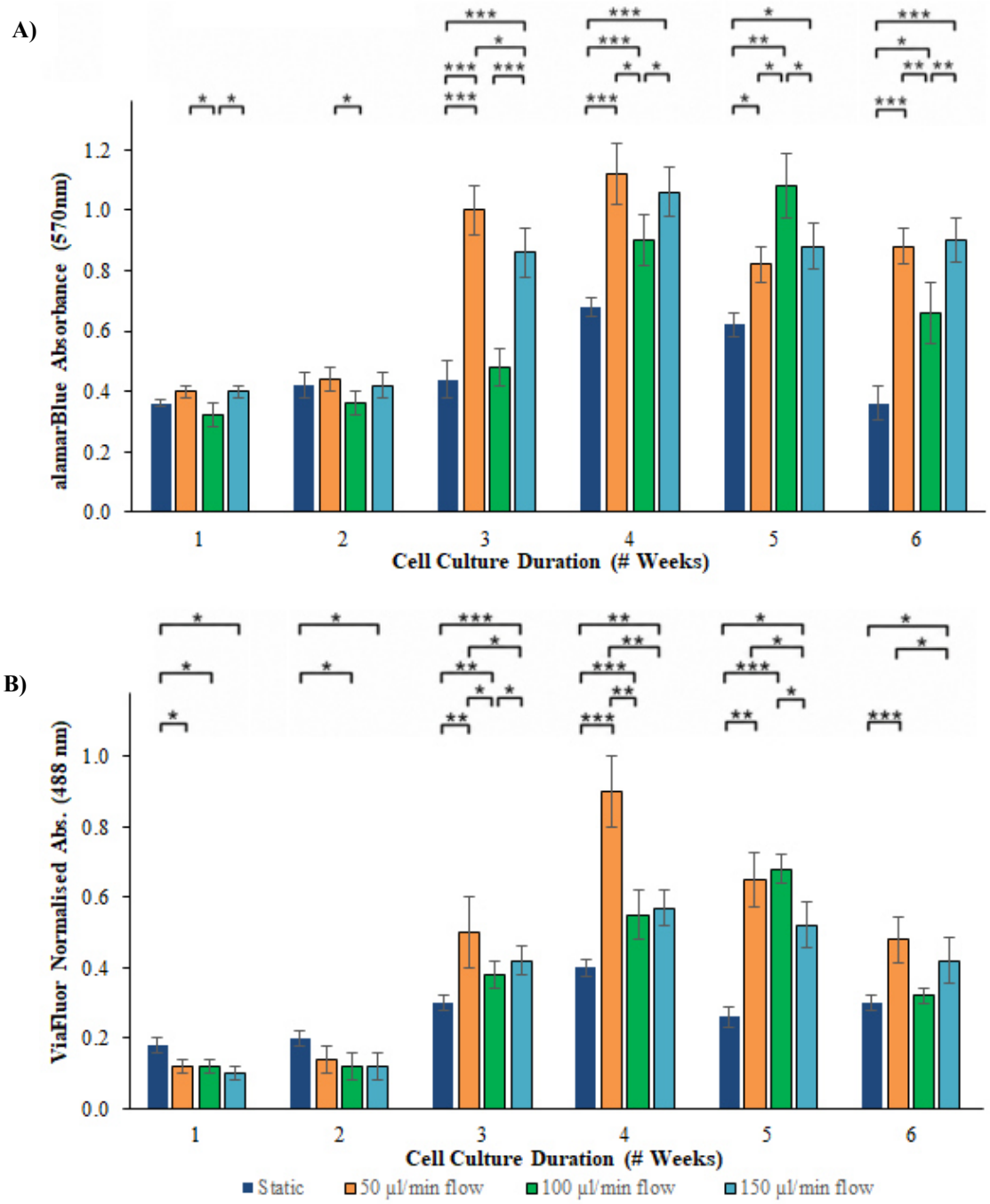


Figure 4.5 Cell metabolic activity and proliferation by flow rate treatment **A)** alamarBlue™ metabolic activity compares cell activity for 50, 100 & 150µl/min flow rates vs static samples. **B)** Amine based ViaFluor normalised absorption compares cell proliferation for 50, 100 & 150µl/min flow rates vs static samples. Statistical significance is presented between flow rate stimulated, and static controls at each timepoint. * $p<0.05$ and ** $p<0.01$, All tests performed in triplicate (n=3).

Similar trends were observed for osteogenic activity (ALP absorption) (Figure 4.6). All flow stimulation groups led to increase mineralisation compared to static controls with the highest levels of mineralisation observed in the 50 µl/min flow group at 4 weeks.

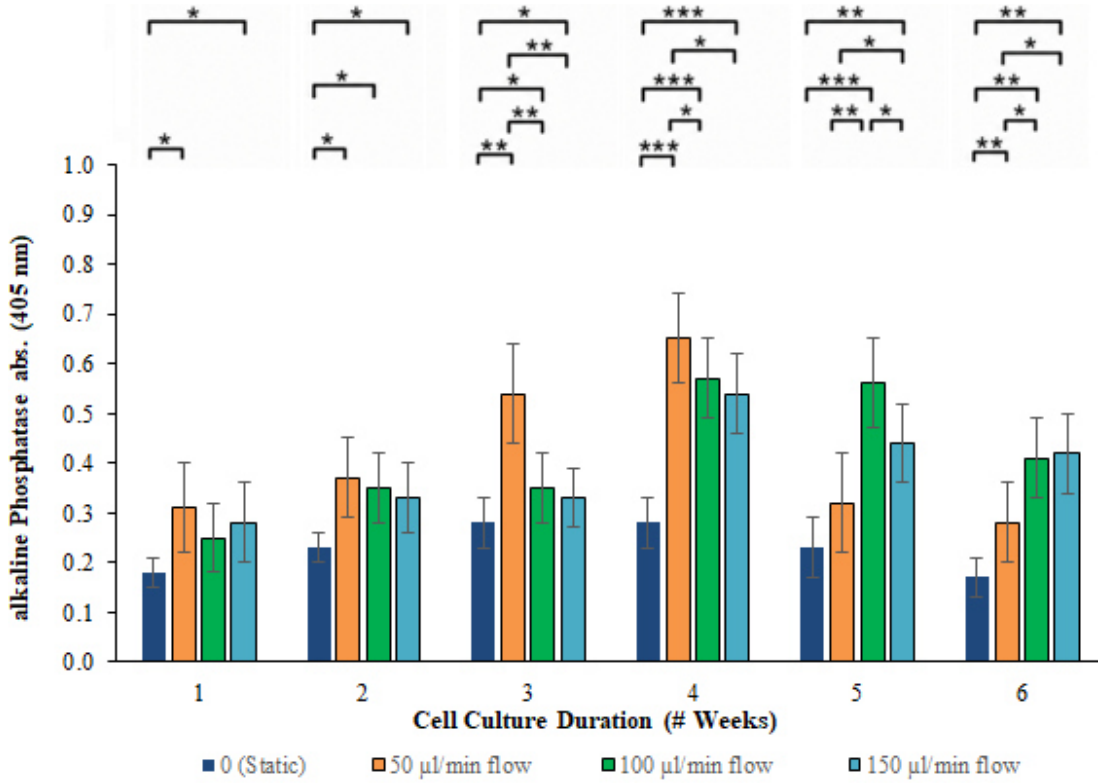


Figure 4.6 Comparison of ALP absorption (osteogenesis) by flow rate treatment. For 50, 100 & 150µl/min flow rates vs static samples. Optimal flow rate with highest osteogenesis varies over culture period. **(*) indicates statistical significance in values difference between flow rate stimulated and static 3D gels. * $p<0.05$, ** $p<0.01$ and *** $p<0.001$. All tests done in triplicate (n=3).

The optimal flow rate depended on culture stage: 50 µl/min at 4 weeks, 100 µl/min at 5 to 6 weeks. ALP absorption declined from weeks 5 to 6 due to hydrogel degradation and loss of bone cells with media changes. Higher flow rates slowed this decline, with 150 µl/min nearly stabilising ALP levels. Overall, flow stimulation at all rates delayed the culture peak and ensured less reduction of ALP absorption during later weeks more consistently and significantly than static controls. The lower mineralisation for static samples at the 5 and 6 week timepoint could be due to the lower proliferation (Figure 4.5) thus lower cell number and lower overall osteogenesis at this culture stage.

4.3.3 Combined Centrifuge and Flow Stimulation

For assay absorption data, combining centrifuge and flow stimulation increased cell metabolic activity and proliferation (ViaFluor) in 3D gels by 80 to 110 % over static 3D cultures at the 4-week peak (Figure 4.7, 4.8). Compared to flow-only, the combined stimulation showed similar proliferation levels but 20 to 25 % higher proliferation at 5 to 6 weeks and greater longevity, with less reduction of proliferated cells at this stage (Figure 4.8)

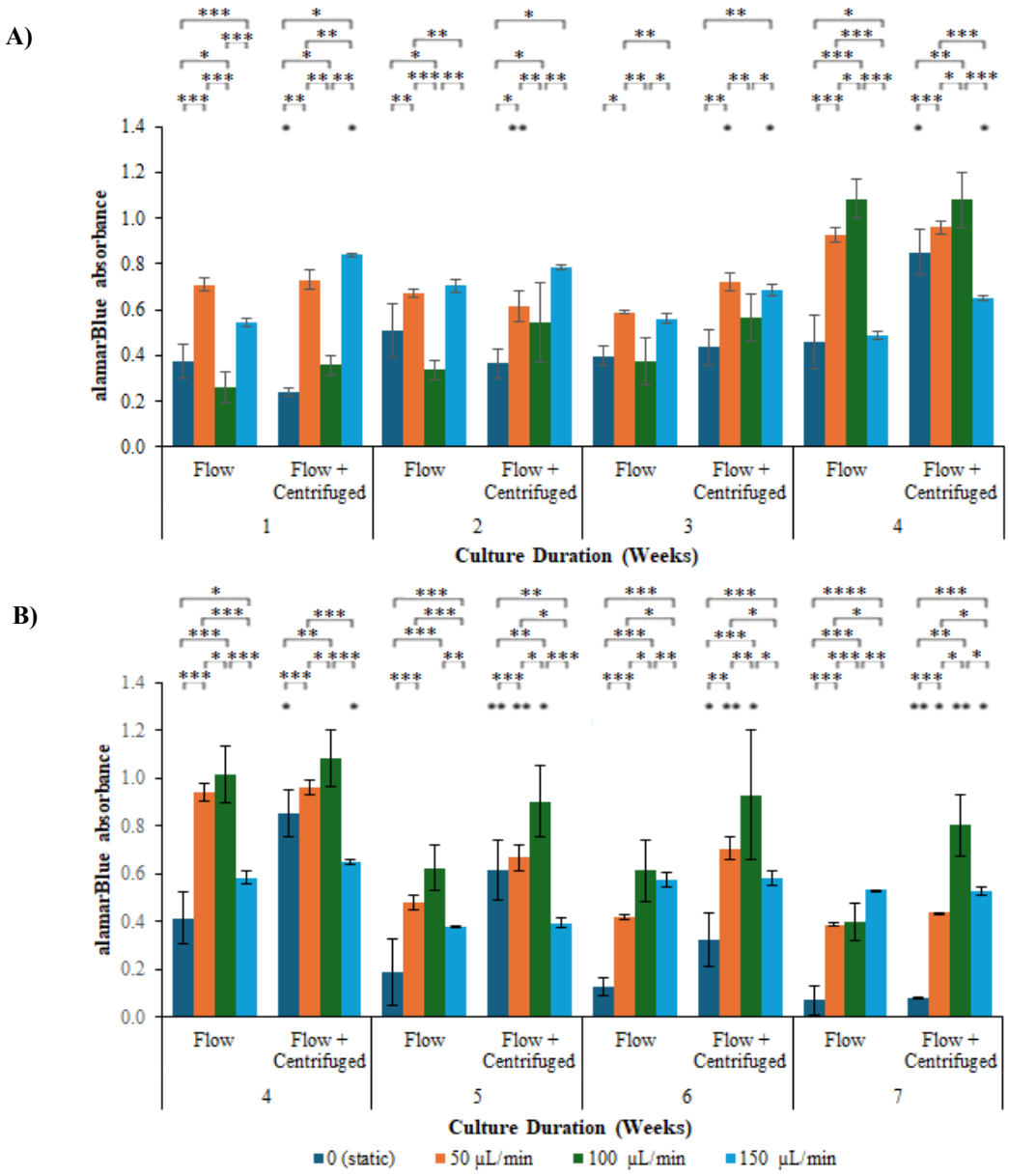


Figure 4.7 alamarBlue™ absorption by flow and centrifuge stimulation. Flow stimulated samples at flow rates of 50, 100 & 150 µl/min without centrifugation (solid bars) were compared to flow stimulated samples with centrifugation (textured hatched bars). **A)** alamarBlue™ absorption assay results for metabolic activity at Week 1 – 4 **B)** alamarBlue™ absorption assay results at Week 4 – 7. Statistical significance between samples with(out) centrifugation (with the larger, lower asterisks *) and between different flow rate sheared samples (with the smaller, higher asterisks) are indicated, * $p < 0.05$, ** $p < 0.01$ and *** $p < 0.001$. All tests were performed in triplicate (n=3).

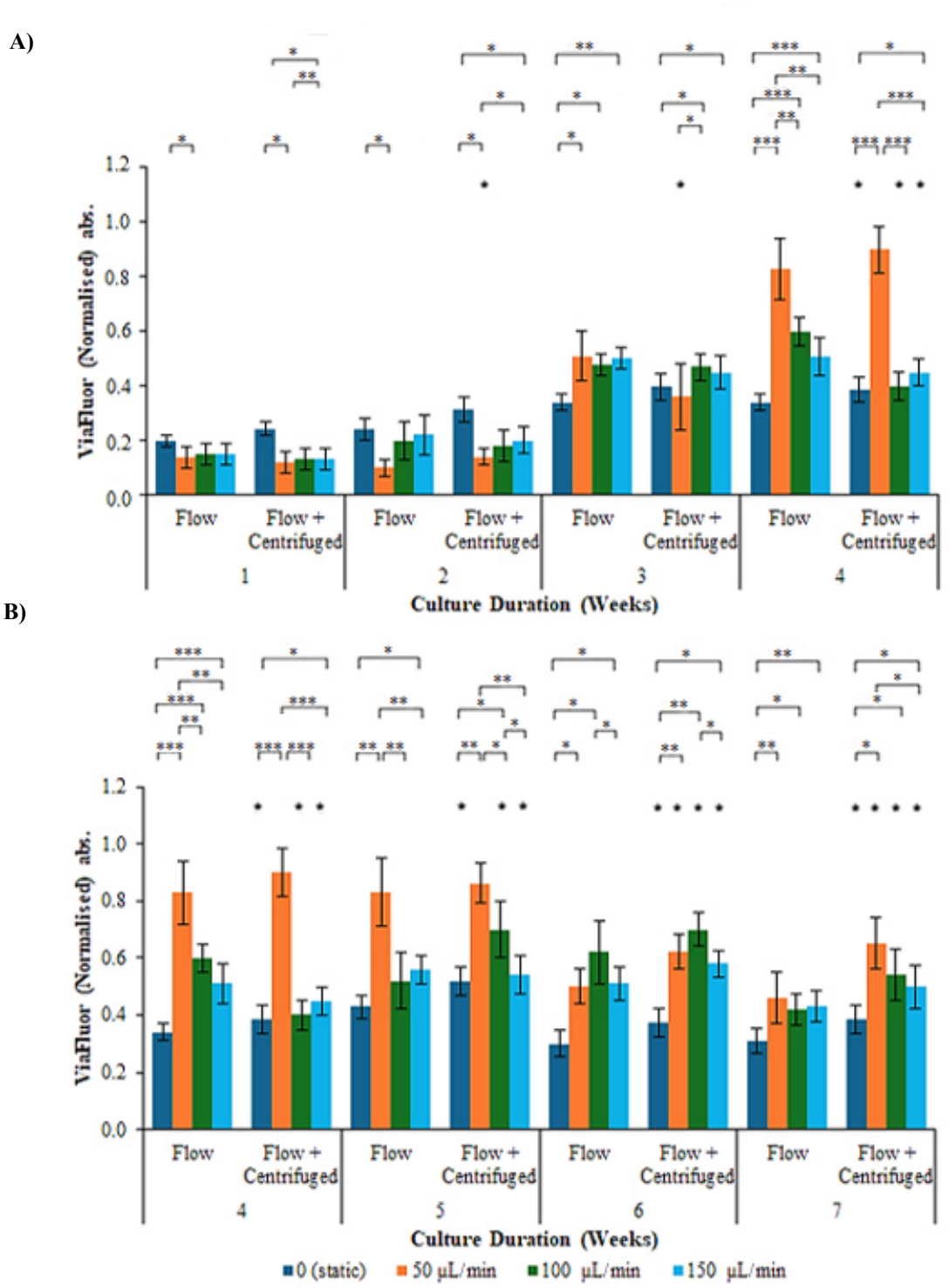


Figure 4.8 ViaFluor Fluorescence (normalised abs.) proliferation by flow and centrifuge stimulation. Flow stimulated samples at flow rates of 50, 100 & 150 µl/min without centrifugation (solid bars) were compared to flow stimulated samples with centrifugation (textured hatched bars). **A)** ViaFluor assay results at Week 1 – 4 **B)** Assay results at Week 4 – 7. Statistical significance between samples with(out) centrifugation (with larger, lower asterisks *) and between different flow rate sheared samples are indicated. * $p < 0.05$, ** $p < 0.01$ and *** $p < 0.001$. All tests done in triplicate (n=3).

Before 5 weeks, flow with centrifugation produced ViaFluor-normalised absorbance similar to flow-only stimulation. Flow alone caused larger, more significant increases in cell

proliferation than centrifugation. The combined treatment produced significantly higher proliferation at 5 to 7 weeks, especially at 50 to 100 µL/min. Flow had large, highly significant effects on ALP absorbance, while added centrifugation had only a moderate effect, significant only at 5 to 7 weeks (Figure 4.9). At peak culture, adding centrifugation to flow had minimal effect, with significance present for static and 100 µl/min samples only.

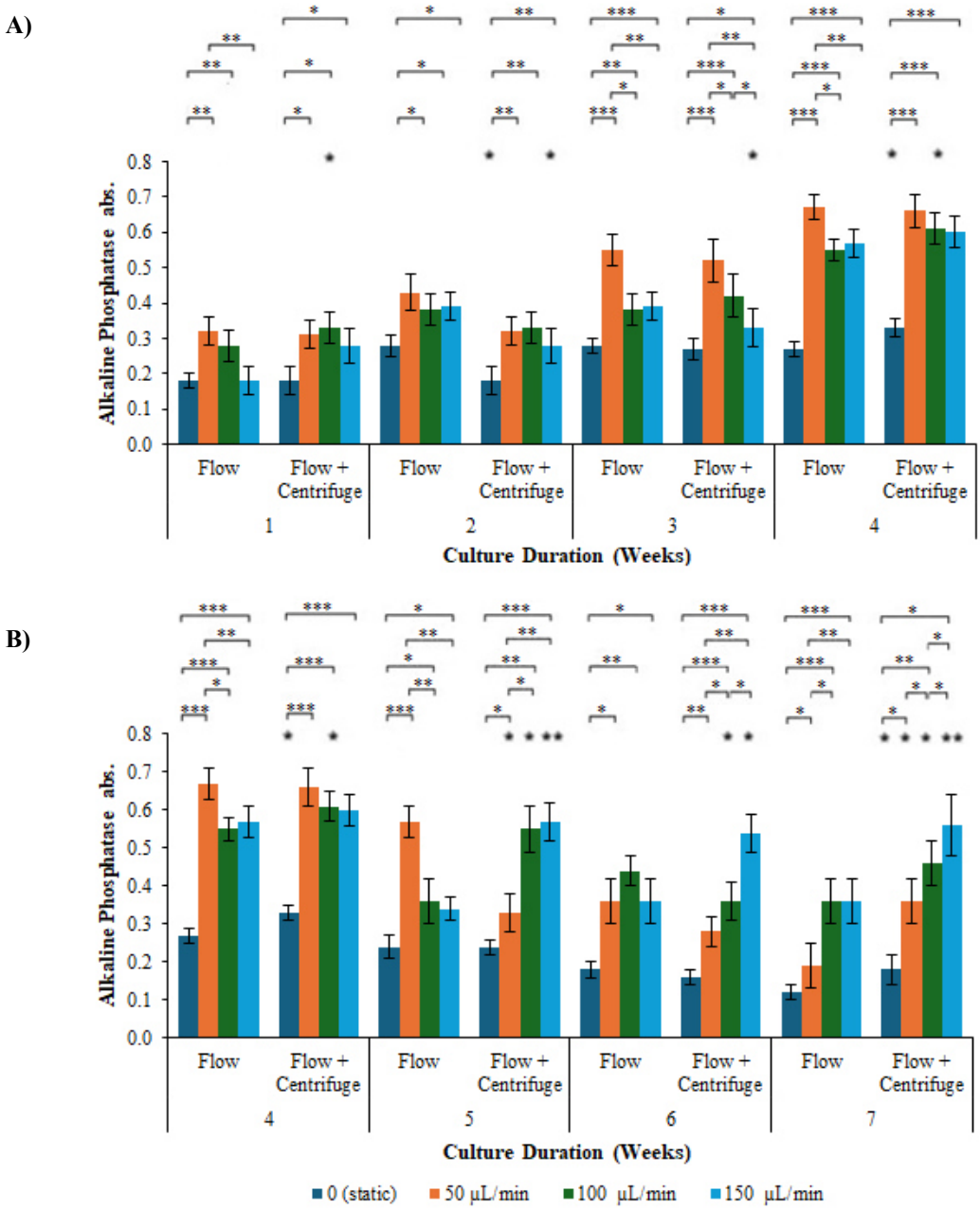


Figure 4.9 Alkaline Phosphatase absorption (osteogenesis) by flow and centrifuge stimulation. Flow stimulated samples at flow rates of 50, 100 & 150 µl/min without centrifugation (solid bars) were compared to flow stimulated samples with centrifugation (textured hatched bars). **A)** Alkaline Phosphatase abs. assay results at Week 1 – 4 **B)** Alkaline Phosphatase abs. assay results at Week 4 – 7. Statistical significance between samples with(out) centrifugation (with larger, lower asterisks *) and between different flow rate sheared vs static samples (with smaller, higher asterisks) are indicated. * $p < 0.05$, ** $p < 0.01$ and *** $p < 0.001$. All tests were done in triplicate (n=3).

For ALP absolute quantification, the flow-only chips outperformed the static chips by 50 to 80 % (Figure 4.9). The flow-only group resembled combined flow and centrifugation samples in standard media. Centrifugation produced significant increases only at 5 to 7 weeks, mainly at higher flow rates (100 to 150 µl/min). Under combined stimulation (1 g, 1 h/day), 100 µl/min generally produced the highest ALP levels, especially at later weeks, though 150 µl/min gave relatively higher values at 5 to 7 weeks in Figure 4.9. These results indicate that combined treatment affected ALP absorption and cell proliferation similarly, especially at higher flow rates in late culture (weeks 5 to 7). Broader monitoring and imaging revealed other flow-induced changes, including early alterations in surface cell morphology with greater elongation and alignment in the direction of unidirectional flow. Figures 4.10 and 4.11 indicate that the cell growth modulated by flow shear or centrifugation alter their morphology and aggregate structure, as has been shown to be the case with other similar dynamic stimulation bone tissue studies [271]. Centrifuged samples (Figure 4.11) also show increased cell proliferation and elongation but less alignment.

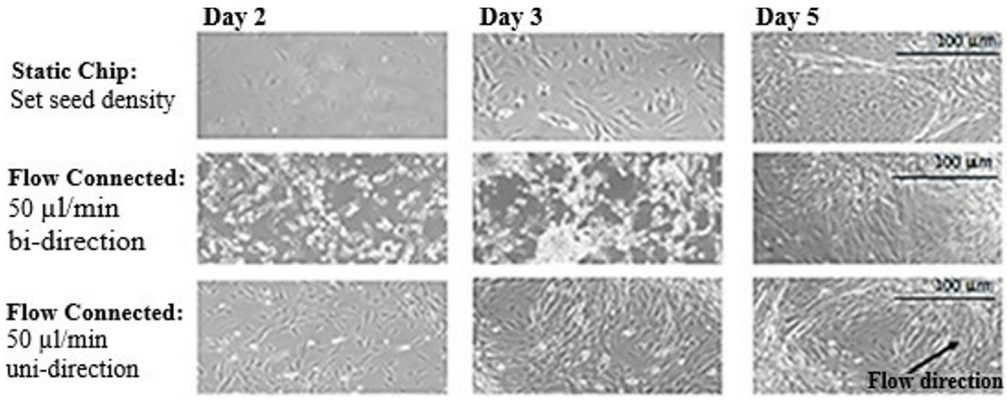


Figure 4.10 Visual Brightfield microscope flow comparison of surface bone cell/ tissue morphology under various modes of flow stimulation (further cell elongation) relative to statics.

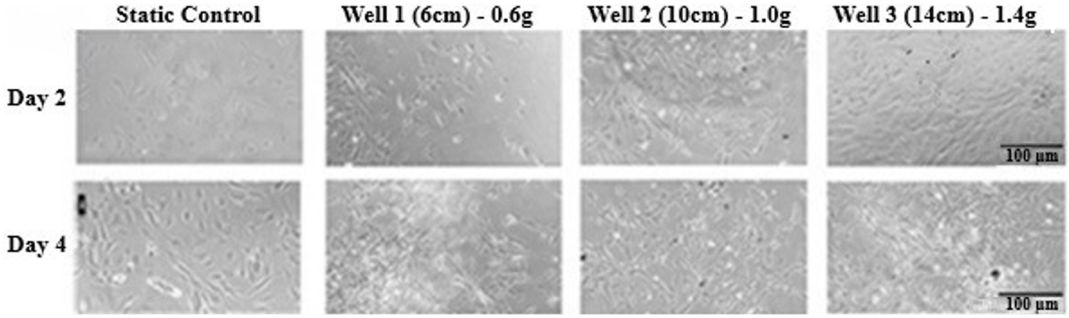


Figure 4.11 Visual Brightfield microscope comparison of bone samples centrifuged bone various radial distance / equivalent g-force levels (8cm – 14cm) showing some accelerated tissue development and more elongated cell morphology but less directional than flow stimulation.

These effects intensify with higher flow shear rates or centrifugation accelerations and increase further with longer cumulative durations of repeat stimulation (Figure 4.10, 4.11).

4.4 Discussion

This chapter investigated the influence of mechanical stimulation, centrifuge cyclic loading and flow shear, alone and combined, on cell metabolic activity, proliferation and osteogenesis. Daily centrifugation in standard media at 1 to 1.4 g was optimal. It produced a 20 to 30 % increase in proliferation and a larger 30 to 40 % increase in osteogenesis after 3 to 5 weeks (ViaFluor and ALP assays, Section 4.3.1). The effect on mineralisation was greater than on proliferation. There are a limited number of known comparable centrifuge-based bone stimulation studies to date. A similar pattern of increased cell proliferation and osteogenesis under mechanical stimulation is observed in a study by Prodanov *et al*. [275], who used 10 g centrifuge acceleration for 7 days on murine MSC bone cells, which is expected given mechanical stimulation can upregulate gene expression (such as RUN X2 and OSX) to bias these cells towards osteoblast proliferation [47]. Prodanov *et al*. observed 30 % increases in proliferation on smooth texture fibronectin substrates, comparable to this study's 1 g centrifuge results and a 1.8-fold increase in osteocalcin expression detected osteogenesis, over 2-fold more than this study's 1g osteogenesis increase over static samples [276]. This study is in contrast with the findings of Naito *et al.* [272], that applied centrifugation (600 and 4800 RPM, 20 minutes daily for 7 days) to rat bone-marrow osteoblasts. Naito *et al.* reported significantly increased ALP mRNA expression and a 2-fold rise in proliferation at 4800 RPM after 5 days [272]. In comparison, this study achieved an average 25 % proliferation increase with centrifugation alone despite using much lower speeds (120 RPM) for longer periods (1 h/day for 21 days).

Flow stimulation (Section 4.3.2) had a greater impact, increasing both proliferation and osteogenesis by 60 to 100 % at 3 to 5 weeks, depending on flow rate, 50 to 100 µL/min was optimal for proliferation and 100 to 150 µL/min for osteogenesis. Overall, flow produced the largest benefit, doubling cell growth and proliferation at 5 weeks with very high significance, more than twice the effect of centrifugation, though it is dependent on flow rate and culture stage, with 50 to 100 µL/min best in mid - late culture. Flow stimulated samples peaked later (4 to 5 vs 3 to 4 weeks for static controls) for cell activity, proliferation as well as osteogenesis (ALP activity) and these measurements reduced more slowly at 5 to 7 weeks for flow samples.

The flow shear range used in this study was 0.15 to 0.45 Pa at 50 to 150 µL/min (from Section 3.2.2, Eq. 3.4). This is consistent with Babaliari *et al.* [222], that reported 2.4-fold higher MC3T3-E1 proliferation at 50 µL/min flow versus static samples, and Tsao *et al.* [267], observed a 110 % increase in MSC osteogenesis at 3 weeks after 1 h/day stimulation at 15 µL/min (1.2 Pa shear). Vis *et al.* [109] used a similar 3D BoC with 0.2 Pa localised max

shear but with 0.01 to 0.04 Pa average bulk shear for 5 weeks. This resulted in a 1.5 to 1.8-fold increase in key osteogenic expression (RunX2 and Osteopontin expression to indicate bone differentiation and remodelling) at 21 days but cell proliferation and bone matrix mineralisation was not directly measured. Few studies use this flow shear range (0.15 to 0.45 Pa), especially for long-term 3D cultures, and focus on non-osteoblast cells, 2D cultures or short-term tests [103]. Beyond the lack of studies in this range, it was hypothesised that an intermediate flow range could simultaneously promote cell proliferation and osteogenesis with minimal trade-offs, maximising bone growth. However, flow and dual-stimulation results in Sections 4.3.2 and 4.3.3 showed that, compared with static controls, moderate shear rates mainly enhanced early cell proliferation (3 to 4 weeks), while higher shear rates mainly increased late-stage osteogenesis (ALP activity, 5 to 7 weeks), particularly in dual-stimulated samples. These results and studies by Yu *et al.* [277] or other Wittkowske *et al.* [103] reviewed studies showed that no single shear-stress range maximises both osteoblast proliferation and osteogenesis; intermediate shear promotes early proliferation, while higher shear at later stages more strongly enhances osteogenic differentiation and matrix mineralisation [103] [277]. This indicates that stage-specific modulation of flow shear is more effective than maintaining a single constant "optimal" flow throughout culture. The cell-cycle stage also influences bone cell responses. Yu *et al*. (2017) showed that higher fluid shear stress drives osteoblasts into G0/G1 arrest, suppressing proliferation while sensitising cells to osteogenic signalling and promoting differentiation over further division [277] [278]. Fundamental biological processes still enhance cell responses under various mechanical stimuli such as flow shear. Chemotransport is the movement of nutrients, signalling molecules, and waste products through the culture medium to and from cells by diffusion and fluid flow [279]. Improved cell and chemo-transport in permeable 3D flow systems ensure continuous, efficient nutrient and oxygen delivery while removing waste [279]. Combined with increased growth-related cell secretion and intercellular signalling, it can more than double cell proliferation compared with static cultures [280] [281]. Suitable flow perfusion also distributes innate cytoprotective compounds (e.g. glutathione [282]) more effectively, protecting cells from oxidative stress induced apoptosis, retaining balanced osmosis, pH, and oxidative balance [283].

Combined 1 g centrifugation and flow stimulation had a significant, moderate effect on increasing proliferation and osteo-differentiation compared with flow-only stimulation (Section.4.3.3). This dual stimulation better maintained ViaFluor proliferation (by 10 to 25 % on average) and ALP osteogenesis (by 30 to 70 % on average) than flow-only samples in late culture (5 to 7 weeks). Adding 1 g centrifugation to flow stimulation at peak culture (4

weeks) produced only marginal gains in proliferation and osteogenesis, and the interaction effect was smaller than for centrifugation alone. No known directly comparable dual-stimulation BoC studies exist. The closest work, by Kim *et al.* [87], tested flow shear and compressive strain separately on trabecular bone cells on a 3D scaffold but not in combination. This was similarly the case for another bioreactor study by McGarry *et al.* [284], where again only one type of stimulation (either mechanical stimulation or flow shear but not both) were applied to human bone MSC samples on PLL coatings. Another bioreactor study by Rindt *et al.* applied dual stimulation for 3 weeks on 3D bone samples, but used osteocytes on rigid scaffolds and did not assess mineralisation or other osteogenic features [93]. Lovecchio *et al.* [89] used dual stimulation (1 % compression at 1 Hz for 30 min twice daily plus low-shear 1 ml/min continuous perfusion) on 3D chitosan human bone MSC cultures, and increased osteogenesis 3-fold after 1 week, similar to this study's best dual-stimulated samples (2.5 to 3.3-fold vs static bone at 4 to 7 weeks). Their lower flow shear, due to channel dimensions, suggests perfusion effects were driven more by chemotransport than flow shear.

Centrifugation and high-frequency variant fluid flow both stimulate overlapping cell receptors and integrins, but with different intensities and spatiotemporal patterns than steady flow shear stimulation [90]. Detailed study of how Coriolis-induced mechanotransduction patterns act on these receptors may explain interaction effects [285] [286]. Cross-mechanical stress activates osteoblast mechanoreceptors, including ion channels (e.g. Piezo1) and primary cilia, which overlap with those stimulated by flow shear (especially ciliary receptors) [287]. This converges on common downstream activation and developmental pathways [56]. Distinct receptor sets that sense internal vs external, or tensile vs compressive stress, help distinguish cellular responses to centrifugation from those to flow shear [287], [288], leading to differences in the magnitude and timing of proliferation and differentiation.

The study showed enhanced proliferation and osteogenesis under mechanical stimulation vs static culture that is consistent with other mechanobiology studies. No other BoC studies have yet examined dual stimulation. Future work on this BoC platform could test wider flow rate and shear-stress ranges, like those reviewed by McCoy and O'Brien *et al*. [289] (0.08 to 3.0 Pa for 3D bone) and Wittkowske *et al.* [103] (under 0.01 to 3 Pa). The flow shear range can be adjusted at different cell culture stages to optimise both growth and osteogenesis, as shown in flow or dual stimulation experiments (Section 4.3) and by Yu *et al.* [277]. Adapting the Paggi *et al.* [79] chondrocyte dual-stimulation regimen (e.g. modified compression and wall shear stress magnitudes for bone) or applying the Kim *et al.* [87] regimen to BoC osteoblasts could yield informative comparisons. Other bone mechanical stimulation

methods, such as those reported by Hodgkinson et *al.* [52], could be benchmarked at similar forces and shear stresses to compare piston or hydrostatic loading with centrifugation, and viscometer with syringe-driven shear. Beyond wall flow shear stress magnitude, the effects of flow duration, profile (continuous vs intermittent or oscillatory), and frequency should also be assessed [90].

4.5 Conclusion

This study developed a dual-stimulation BoC model combining centrifuge and flow shear, extending beyond typical single-stimulation or static systems. Centrifugation alone moderately increased proliferation (1.2 to 1.4-fold) and osteogenesis (1.3 to 1.4-fold) compared to static controls by mid culture (3 to 5 weeks) but this effect largely varied by centrifuge level (with around 1g being optimal) and the culture timepoint. Flow had a greater effect (up to 2-fold during mid-culture at 3 to 5 weeks) on enhancing cell activity, proliferation, and osteogenesis compared to static controls. Cell proliferation and osteogenesis peaked around 4 weeks for stimulated samples with lower flow shear stimulated samples showing greater increases relative to static samples at early-mid stage (3 to 4 weeks) and higher flow shear stimulated samples (particularly dual stimulated) had higher retained values at later stages (5 to 7 weeks). All stimulated samples showed increased proliferation and osteogenesis compared to static controls at later times (5 to 6 weeks). Overall, centrifuge and flow stimulated samples both showed osteo-stimulatory effects. Flow stimulation showed the greatest effects. Combining centrifuge and flow for dual stimulation did not lead to higher levels of osteogenesis overall but showed increases in proliferation and osteogenesis to a greater extent at later timepoints (5 to 7 weeks) for higher flow rates (100 to 150 µl/min). Future work could examine more varied flow shear and stimulation profiles as well as optimally altered shear stimulation for various cell culture stages. Adjusting media composition, for example with cell protectants (e.g. shear buffers or thermal protectants), could further improve bone cell responses in future studies.

Chapter 5: Investigation of the Effect of Centrifuge and Flow stimulation of Osteoblast Response with Cell Protectant Media

5 Investigation of the effect of Centrifuge and Flow Stimulation on Osteoblast Response with Cell Protectant Media

5.1 Introduction

Given the potential of mechanical stimulation to modulate cell activity, proliferation and osteogenesis in BoC platforms [88], future work should expand the range and duration of applied mechanical and shear forces to test long term organoid formation [218]. Excessive shear can cause cell detachment or deformation, while minimal flow causes sub-optimal nutrient exchange [290] [291]. Adding shear and thermal-buffering cell protectant reagents to the medium can increase cell stimulation tolerance and permit longer exposure outside standard incubation conditions (e.g. temperature drops), during stimulation [292] [293].

CellShip is a new xeno-free media supplement that preserves and protects cells during refrigerated shipping, reducing shear, thermal and metabolic stress at low temperatures [138] [139]. CellShip has traits similar to Genipin, which is a natural cross-linker and membrane protectant that reduces membrane permeation under flow shear and is anti-inflammatory during cell stress [336][337]. CellShip supports cell transport and storage at 4 to 8 °C, with reversible viability officially rated for up to 5 days [138] [294]. It can sometimes replace cryopreservation by offering lower cost, quicker and convenient short-term storage (under 5 days), and can preserve 3D gelled cell samples without cell suspension [295], while also avoiding excessive DMSO exposure and ice crystallisation during suboptimal freezing of sensitive cells [296]. CellShip also has potential as a cell protectant in cell culture studies where processes such as mechanical stimulation are conducted [297] [298]. This is useful when incubator space is limited or inaccessible, or when external heating, insulated chip holders, or media HEPA buffer (for lower temperature or CO_2) are unavailable [141] [139].

Optimal CellShip concentrations vary by cell type and application, so preliminary testing for each new use is recommended [294] [295]. It was hypothesised that CellShip's cell-preserving properties would enhance cell tolerance and responses to mechanical stimulation, and that its thermal buffering would enable cells to better withstand extended periods outside standard incubation, such as during centrifugation. This study therefore compares static conditions, centrifuge cyclic loading and flow-induced shear on cell viability, metabolic activity, proliferation and osteogenesis in optimally supplemented media. Optimal CellShip concentrations were first identified, then the original mechanical stimulation study protocols (presented in Chapter 4) were repeated using the optimised CellShip supplementation (10 % w/v in Alpha-MEM and 10 % FBS).

5.2 Methodology of Centrifuge and Flow Tests with Varied Media

5.2.1 CellShip Media Optimisation and Testing Method

MC3T3-E1 cells were seeded in culture plates with CellShip:medium ratios of 1:2, 1:4, 1:6, 1:8, 1:12, 1:16, 1:20, and 1:25. Treatment groups were cultured in standard (std.) media that was composed of Alpha-MEM (10 % FBS, 1 % P/S) containing the defined CellShip concentrations. All cultures were maintained at 37 °C, 5 % CO_2. After 2 days of growth, treated samples were refrigerated (at 4 °C) for 4 days at the respective CellShip ratios, then revived from metabolic dormancy and cultured under the same incubation conditions for up to 9 days. Media were changed every 3 days with repeated composition. Cell viability after revival was assessed in triplicate (n = 3) for each CellShip/medium concentration at 5 and 9 days using Trypan Blue exclusion. All samples were compared with each other and a fresh media control at 5 and 9 days. The optimal CellShip concentration was selected on highest overall viability and used for the main tests.

5.2.2 Flow and Mechanical Experimentation

After determining the optimal CellShip concentration in standard media (Section 5.2.1 and 5.3.1), an initial centrifuge-only stimulation (0.6, 1.0, 1.4 g) was applied to three triplicate sample sets (n=3; Section 4.2) to optimise centrifuge level and duration (Section 4.2.2, 4.2.3 and 4.3.1). Another sample set was centrifuged for 3 days at 0.5, 0.75 and 1 g, starting 3 days after seeding. Subsamples were assessed by Trypan Blue viability and compared with centrifuged standard-media controls to test CellShip compatibility under mechanical stimulation (Section 5.3.2). These samples were then centrifuged daily at 0.6, 1.0 and 1.4 g for 3 weeks, with weekly assays (Section 4.2.3) and ViaFluor (at 488 nm) imaging on a Cytena CellCyte scanner at 3 weeks to visualise proliferation. At 3 weeks, proliferation and mineralisation were compared with 2D/3D static controls and centrifuged samples with and without media supplementation to validate 1 g centrifugation and CellShip for long-term mechanical stimulation with enhanced cell response (Section 5.3.2).

For the main mechanical stimulation experiment, 8 chips with triplicate gelled, cell-seeded wells (8 × 3 = 24 samples) were prepared with CellShip-supplemented and standard media, following Section 4.2.1. The main test (Section 4.2) was repeated using eight stimulation combinations (0, 50, 100, 150 μL/min flow; 0 or 1 g centrifugation) in triplicate on BoC samples with optimal CellShip-supplemented α-MEM media. Seeding and culture followed methods stated in Section 4.2.1. Metabolic activity, proliferation and osteo-differentiation were monitored as in Section 3.2.8 and 4.2.3. Centrifuge and flow stimulation followed the standard-media protocol in Section 4.2, with equivalent data collection and analysis.

5.2.3 Data Analysis

Data from the experiment are archived at https://github.com/Collib29/. One-way ANOVA (GraphPad Prism 10 and the equivalent Python SciPy.stats package) was used to test the main effect of media type (Media_type in dataset) (Alpha-Mem vs Alpha-Mem-10 %CS) as a single factor. The same analysis was run separately for volumetric flow rate (µl/min) (or Flow_rate_(µl/min) in the full dataset) and centrifuge level (Centrifuged_(g_equiv) in the full dataset) to assess their isolated effects on single-stimulation results. Two-way ANOVA was then used to test main effects of media type with flow rate or centrifuge level, and their interaction, on assay output variables: 560nm_alamB (alamarBlue^{TM} absorption), 488nm_VFz_abs (ViaFluor normalised absorption), 405nm_alkP (Alkaline Phosphatase absorption), and 488nm_VF_FL (ViaFluor direct fluorescence). A three-way ANOVA assessed the combined effects of all three variables and their interactions. Detailed ANOVA results are in Appendix A5 to A8. Significance tests on input variable categories followed the same methods as standard media centrifuge/flow testing (Section 4.2.4), with data reported as the mean plus or minus std. deviation with triplicate samples. Statistical significance was set at p less than 0.05. Only significant differences relative to static samples and between treatment sets within each week are indicated on the figures. Whole dataset statistical analysis and subsequent modelling used the full source assay dataset, including repeat measurements and both absorption and excitation/emission wavelength measurements.

5.3 Results – CellShip media supplemented stimulated BoCs

5.3.1 CellShip Concentration Optimisation

To determine the optimal CellShip (CS) concentration for improving cell viability, proliferation, and development after stress (e.g., refrigerated transport), optimisation experiments were conducted using MC3T3-E1 cells revived after 4 days of refrigeration and cultured for up to 9 days. Various culture media:CellShip volumetric ratios were tested, and cell viability was assessed by Trypan Blue exclusion at multiple time points, typically peaking 7 to10 days post-revival. This comparison is illustrated in Figure 5.1.

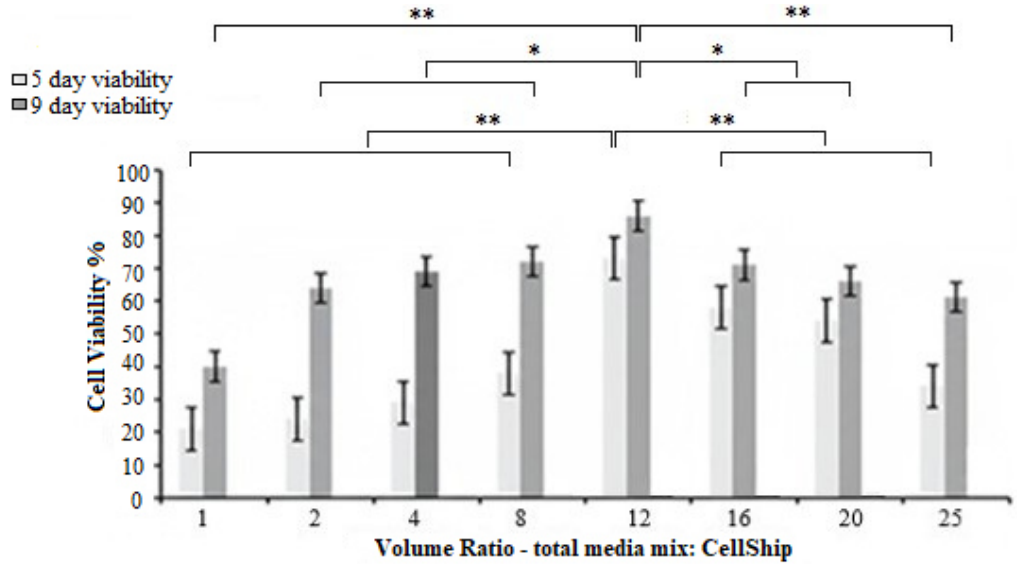


Figure 5.1 Compared varied media : CellShip ratios effect on cell viability at different 2D cell culture stages (at 5 and 9 days). Statistical significance of values difference between media ratios relative to optimal concentration ratio, given by ANOVA Tukey HSD pairwise group difference average, * =($p<0.05$), ** = ($p<0.01$), *** = ($p<0.001$). ANOVA Group comparison: series -5-day $F=5.82$ $p = 0.002$ **, series - 9-day, $F=34.7$, $p<0.001$ ***. All tests performed in triplicate (n=3).

The results showed a strong correlation between the media:CellShip ratio and cell viability after revival. CellShip supplementation increased cell viability up to the 12:1 volumetric ratio. An optimal media:CellShip ratio of 12:1 (8.3 % v/v, equivalent to 10 % w/v accounting for CellShip's density) was identified. Above this ratio, viability declined with increasing concentration, and CellShip's benefits became negligible at ratios of 25:1 and higher. These findings (Figure 5.1) were key to understanding the impact of CellShip concentration. These optimisation studies suggested that CellShip also acts as a metabolic buffer against temperature variations. One-way ANOVA showed a significant Media_type (supplement) effect on nearly all assay outputs for bone cells when comparing Alpha-Mem (control) with Alpha-Mem 10 % CS (CellShip treatment).

Figure 5.2 visually summarises the media differences for all samples (whole period, all stimulation types, averaged), comparing the two media groups across all key cellular response markers. (See Appendix A5 for full ANOVA and Tukey HSD results.)

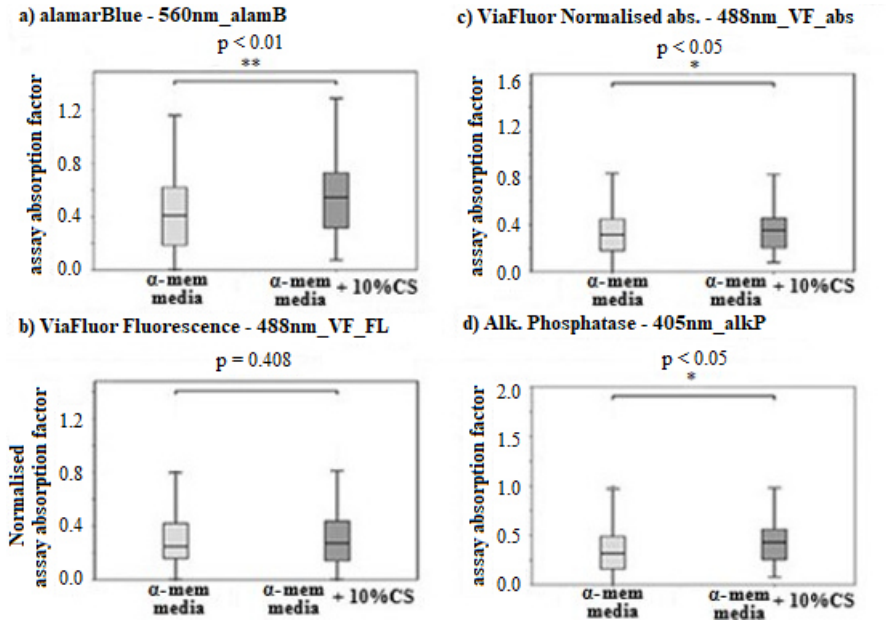


Figure 5.2 Compared distribution of Alpha-Mem media (Std. media) vs Alpha-Mem media +10 % CS (Std. media +10 % CS) media for all assay readings on key cellular outputs. Distributions of outputs – dataset variable name, **(A)** ALP absorption (405nm_alkP) **(B)** alamarBlue™ metabolic Activity (560nm_alamB), **(C)** ViaFluor absorbance (488nm_VF_abs), and **(D)** ViaFluor Fluorescence normalised absorption (488nm_VF_FL). The statistical significance (p-values from pairwise t-test) of values difference between media with(out) 10 % CellShip supplementation indicated by asterisks: * $p < 0.05$, ** $p < 0.01$, All tests performed in triplicate (n=3).

The analysis shows that 10 % CellShip supplementation very significantly increased metabolic activity (alamarBlue™) and osteogenesis (ALP absorption) by 30 % and significantly increased cell proliferation (direct Viafluor fluorescence) by 15 %, while normalised absorbance-based ViaFluor measurements remain unchanged. Overall, this 7-week dataset validates 10 % CellShip as having a significant positive effect on bone cell metabolic activity, proliferation and osteogenic development.

5.3.2 Comparative Impact of CellShip under Centrifugation Conditions

The role of CellShip was also assessed in the context of short duration centrifugation. Two-way ANOVA was used to assess the interaction between media type (Alpha-Mem vs Alpha-Mem 10 % CS) and centrifuged level (Centrifuged: 0.5 g, 0.75 g, 1 g at radial distances of 3 cm, 4.5 cm and 6 cm) on the output variables. An early indicator test first examined cell Trypan Blue viability of cells after 3 days of cell culturing (Figure 5.3).

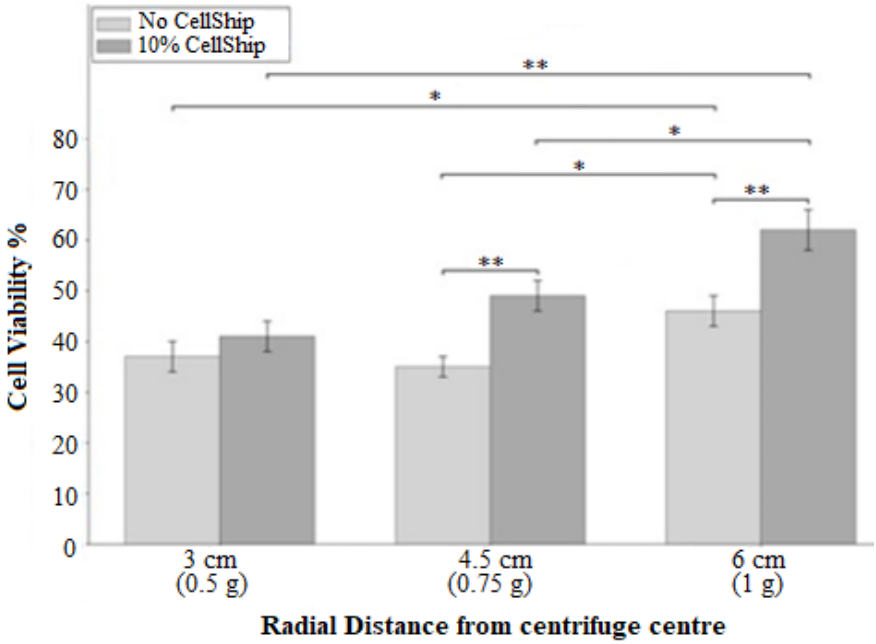


Figure 5.3 Comparative illustration of Day 3 Trypan Blue Viabilityresults for sample with(out) 10 % CellShip in subsamples placed in assay holder at increased centrifuge radial distances that induced corresponding increases in equivalent g-force. Statistical significance of values difference between centrifuged and static samples as well as between CellShip treated vs alpha-mem media only samples denoted by * $p < 0.05$, ** $p < 0.01$, *** $p<0.001$. All tests done in triplicate (n=3).

Cell viability of revived cells increased with centrifugation and increased further with CellShip supplementation indicating enhancement effects with centrifugation, showing an interaction effect. Samples were then centrifuged at 0.6 to 1.4 g for 1 h per day for three weeks to assess the initial effects of centrifugation alone and the addition of CellShip. Centrifugation-only tests over 3 weeks confirmed that 1 h per day was the optimal stimulation duration before starting the main centrifuge and flow experiments (Section 4.3.1). In parallel, gelled assay wells containing 10 % CellShip were tested with and without 1 h per day centrifugation and assessed for cell proliferation at 3 weeks (Figure 5.4), a time point chosen to follow the onset of bone nodule and matrix formation [48].

A wider range of g-forces with and without CellShip supplementation were then examined in Figure 5.4 that shows 1 g centrifugation is optimal for ViaFluor indicated cell proliferation across the ranges of g-forces tested. The centrifuged samples with 10 % CellShip very significancy increased Viafluor proliferation by 55 % on average for all these samples. CellShip enhanced cell proliferation, and higher g-forces interact positively with CellShip, increasing bone cell tolerance and proliferation under 1 h daily centrifugation for 3 weeks. Figure 5.5 shows the effects of 1 g average daily centrifugation for 3 weeks on ALP absorption, comparing gel coat, centrifugation, and CellShip.

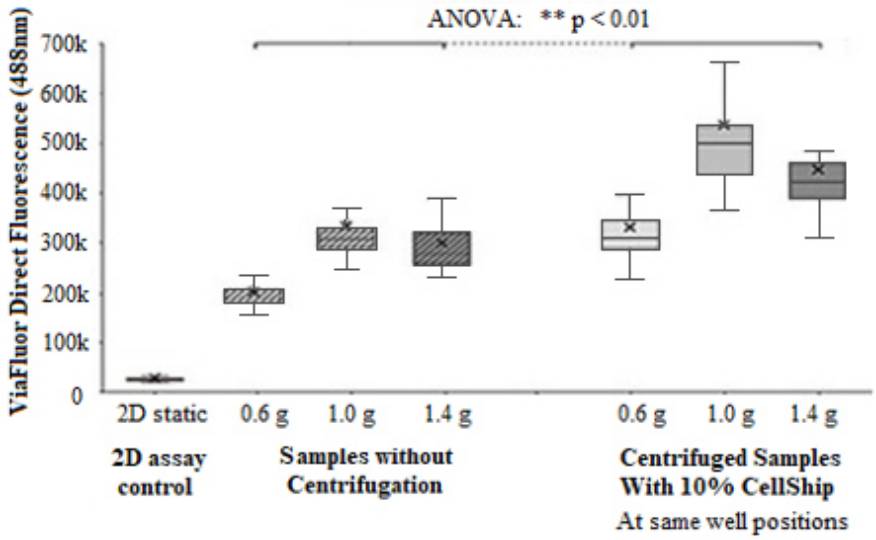


Figure 5.4 Centrifuged with 10 % CS vs Static samples **-** Comparison of ViaFluor detected cell proliferation by centrifuge stimulation level with 10 % CS media at 3 weeks, where x marks = average, mid-lines = median and boxes are interquartile range. Statistical significance of difference between centrifuged 10 % CS media group and static samples denoted by * = ($p < 0.05$), ** = ($p < 0.01$).

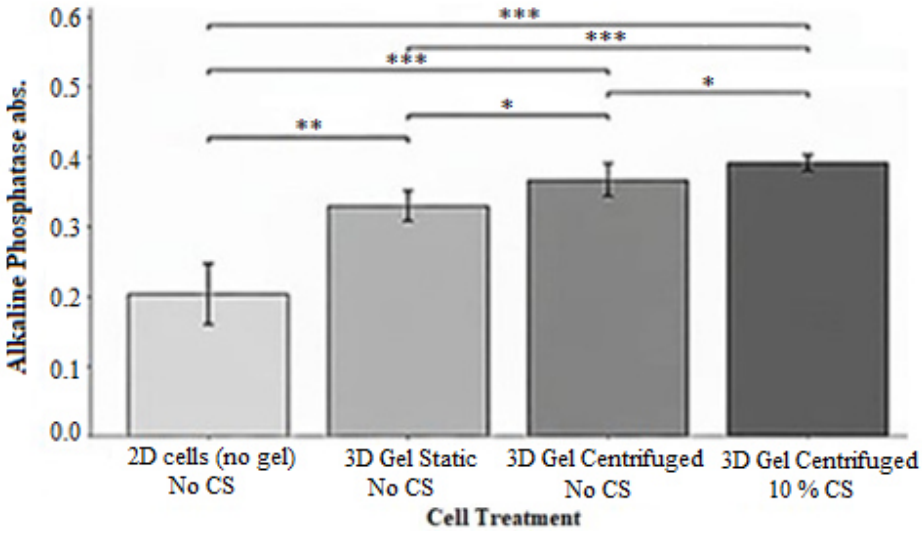


Figure 5.5 ALP absorption (osteogenesis) by BoC coating/treatment, compared effects of using 3D optimal hydrogel, centrifuging and CellShip addition in additive order. Results are means +/-SD from triplicate experiment sets. Statistical significance of values difference between coat and treatment type denoted by * = ($p < 0.05$), ** = ($p < 0.01$), *** = ($p < 0.001$). All tests performed in triplicate (n=3).

Using 3D gel had the most significant and largest effect on osteogenesis ALP activity (60 % increase), followed significantly by CellShip (25 % increase) and centrifugation (20 % increase). The benefit of CellShip depended on whether centrifugation was applied (Figure 5.4, 5.5). CellShip increased ALP absorption, ViaFluor fluorescence, and early cell viability (Figure 5.2), indicating it is beneficial compared with standard media across a wide range of centrifuge levels and durations. This validated it as a cell protectant and enhancement agent.

5.3.3 Comparative Impact of CellShip under Varying Flow Rates

The influence of CellShip supplementation was further investigated in conjunction with varying flow rates. A statistical investigation was undertaken on the interaction between media type (cell media vs cell media plus 10 % CS) and flow rates (0, 50, 100, 150 µL/min) on the output variables (Figure. 5.6), averaged for whole test period.

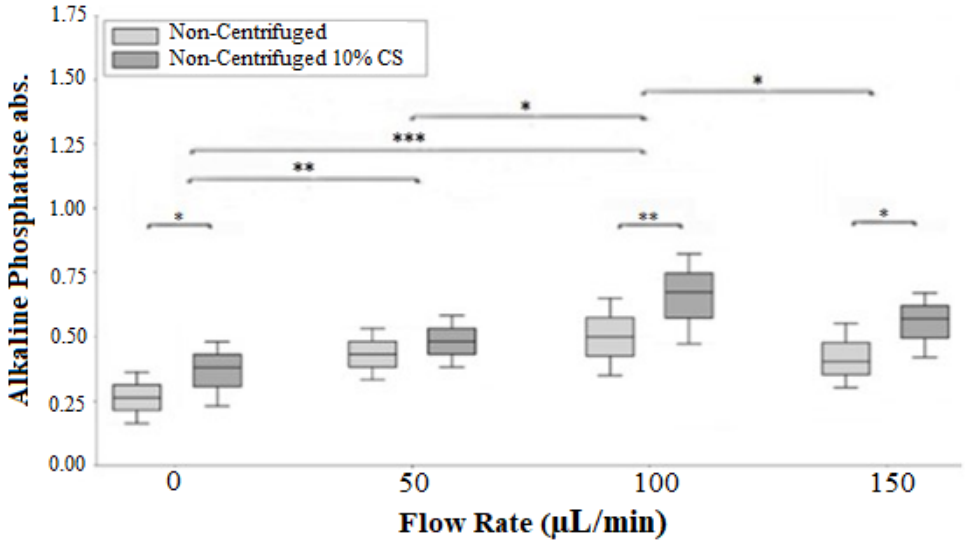


Figure 5.6 Comparison of Alpha-Mem and Alpha-Mem 10 % CS media by flow rate on ALP abs. for bone cell assay outputs. ALP absorption (abs.) distribution over full cell culture period illustrated. Statistical significance (p-values from pairwise t-test to compare media groups) is indicated by small lower asterisks: * $p < 0.05$, ** $p < 0.01$, *** $p < 0.001$. Larger * asterisks indicate statistical significance of values difference between different flow rates. All tests performed in triplicate (n=3).

Figure 5.6 shows that flow rates of 100 µL/min had the best outcome in terms of ALP absorption detected osteogenesis. This was particularly the case for samples with 10 % CellShip where significant increases of over 30 % were observed compared to standard media samples. CellShip induced increases were larger for higher flow rates (100 to 150 µL/min) showing a flow interaction effect as well. Sample sets with higher average ALP absorption reading tended to have higher variances as well. This was examined by individual weeks as well to see how flow only stimulated samples evolved over 7 weeks (Figure 5.7). Cell proliferation (ViaFluor normalised absorption) increased with flow sheared samples compared to static samples, and adding 10 % CellShip further increased this (but less significantly), especially at higher flow rates. This indicated CellShip's cell protective and shear enhancement role, its effect was on cell proliferation was most significant at 2 to 3 weeks. Individual flow rates effects with(out) 10 % CellShip are shown (Figure 5.7).

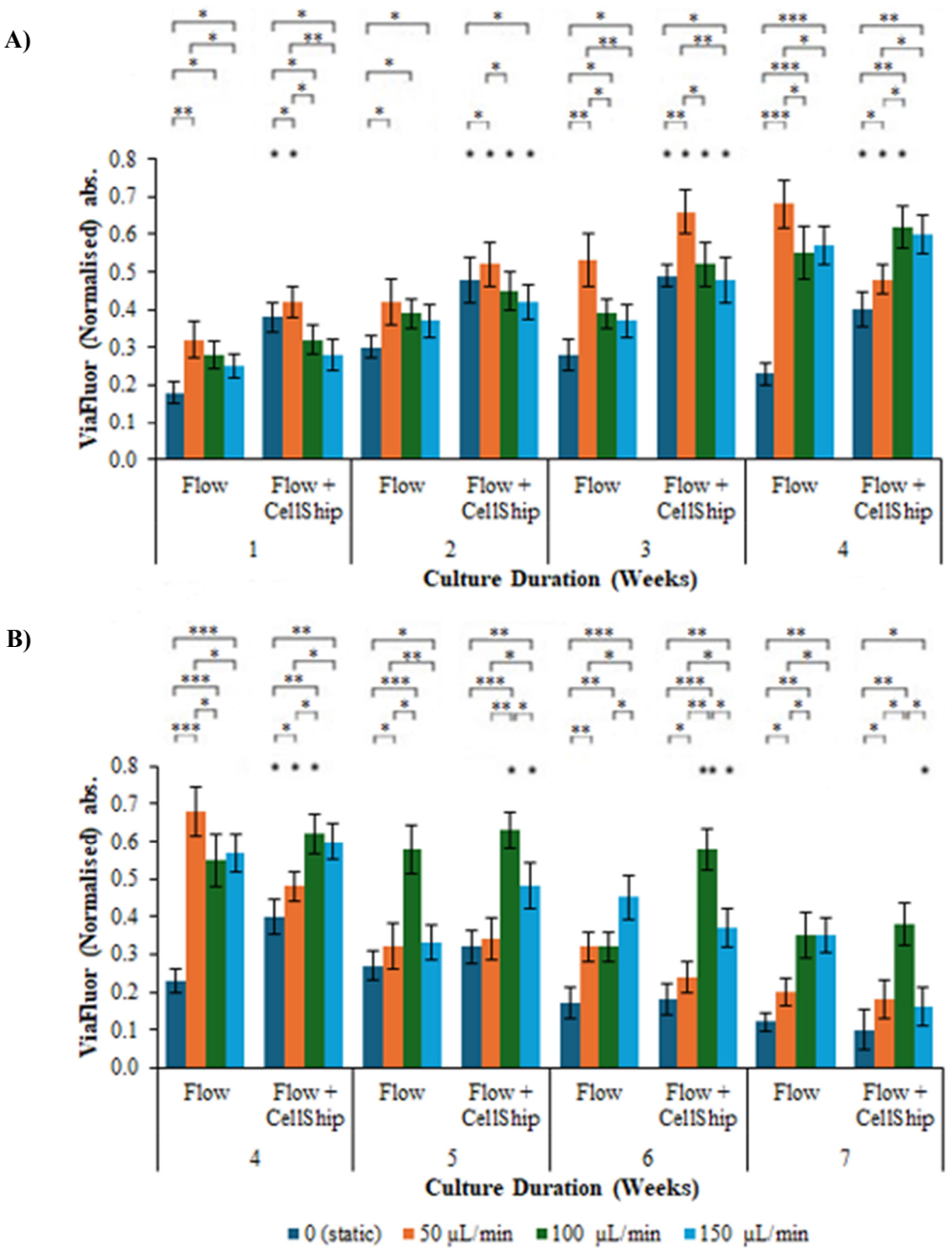


Figure 5.7 ViaFluor fluorescence compared by media type (Alpha-Mem and Alpha-Mem 10 % CS media) weekly by flow rate. **(A)** ViaFluor abs. for Flow Only stimulated samples with standard Alpha Mem media (solid bars) and with 10 %CellShip (textured hatched bars) at 1 – 4 Weeks **(B)** ViaFluor abs. for Flow Only stimulated samples with standard Alpha Mem media with(out) 10 % CellShip at 4 – 7. * $p < 0.05$, ** $p < 0.01$, *** $p < 0.001$, indicate statistical significance of difference as previous charts, with difference relative to static and flow samples. Larger * asterisks indicate statistical significance of values difference with(out) 10 % CS media. All tests done in triplicate (n=3).

The alamarBlue™ results are detailed in Appendix A9. Osteogenesis ALP activity increased with flow shear compared to static samples, and adding 10 % CellShip further increased this (but less significantly), especially at higher flow rates.

This indicated CellShip's cell protective and enhancement role, its effect was on osteogenesis was significant at 3 to 5 weeks. Individual flow rates effects with(out) 10 % CellShip are shown (Figure 5.8).

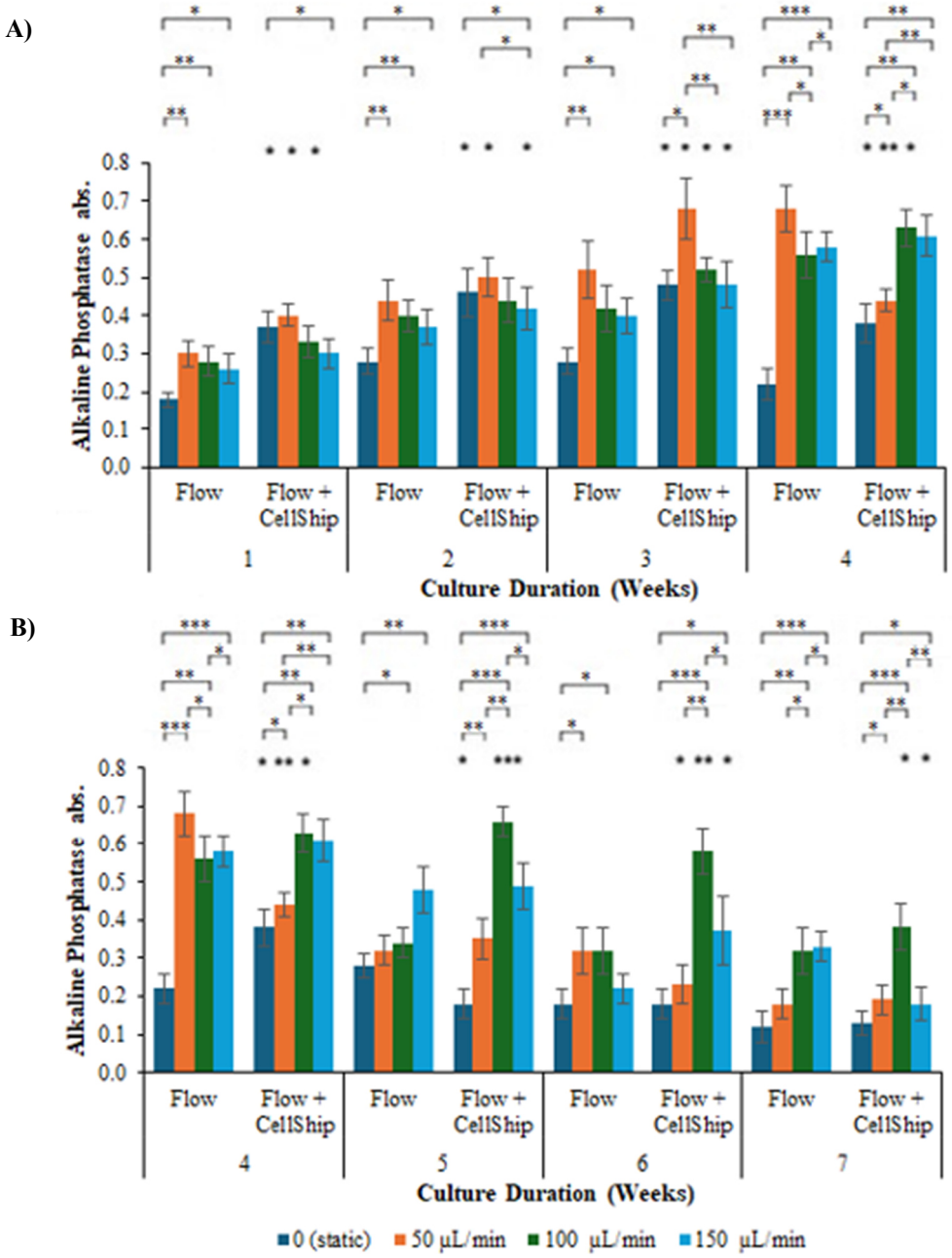


Figure 5.8 ALP absorption compared by media type (Alpha-Mem and Alpha-Mem 10 % CS media) weekly by flow rate. **(A)** –ALP abs. for Flow Only stimulated samples with standard Alpha Mem media (solid bars) and with 10 % CellShip (textured hatched bars) at 1 – 4 Weeks **(B)** ALP abs. for Flow Only stimulated samples with standard Alpha Mem media with(out) 10 % CellShip at 4 – 7. *, ** & *** indicate statistical significance of difference as previous charts, with difference relative to static and flow samples. * $p < 0.05$, ** $p < 0.01$, *** $p < 0.001$. Larger lower * asterisks indicate statistical significance of values difference with(out) 10 % CS media. All tests done in triplicate (n=3).

5.3.4 Quantitative Observations & Combined Stimuli: CellShip vs Non-CellShip

Figure 5.9 presents a statistical analysis of ALP absorption data from all experiments, combining centrifuge-only, flow-only, and dual-stimulation setups with(out) 10 % CellShip in Alpha-Mem media. It summarises results averaged over the full culture period. Flow stimulation had the largest and most significant effect on ALP absorption (with very high significance for most flow rates). Centrifugation had a moderate but significant positive effect on ALP absorption for osteogenesis. CellShip shows a moderate, highly significant positive effect that increased with higher flow and/or centrifugation, indicating a strong interaction.

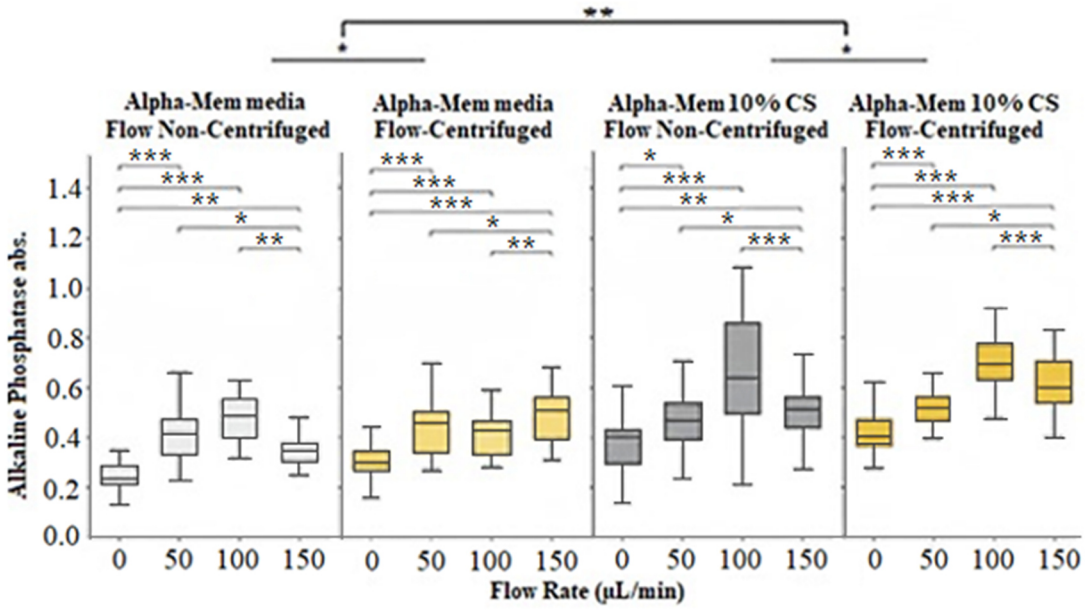


Figure 5.9 Result Summary – Full culture period (all weeks) comparative distribution analysis of Alpha-Mem and Alpha-Mem 10 % CS media on ALP abs. detected bone calcium mineralisation by flow rate and centrifugation regime. Median values with interquartile range in box plots. *(*)(*) asterisks indicate significance in difference. Lowest tier asterisks * indicate difference between flow rates and the static/zero flow rate. Larger asterisks above chart indicate significance of difference between centrifuged and non-centrifuged samples. Largest top asterisk indicates difference significance between media and this media with 10 % CellShip. Statistical significance of difference denoted by * = ($p < 0.05$), ** = ($p < 0.01$), *** = ($p < 0.001$). All tests performed in triplicate (n=3).

As with centrifugation, CellShip had a stronger effect on ALP at higher flow rates (100 or 150 µl/min), for both flow alone and flow plus centrifugation, while media-based increases were more moderate at 50 µl/min. This synergistic, potentiating effect of CellShip under higher flow or multiple stimuli needs further study on a weekly time scale. Detailed weekly flow and centrifuge with(out) CellShip results for alamarBlue^{TM} are given in Appendix A9. Cell statistics from the media comparison showed that Alpha-Mem 10 % CS with combined

stimulation samples had increased mean values for proliferation, compared with std Alpha-Mem media, particularly at 2 to 4 weeks for ViaFluor detected proliferation in Figure 5.10.

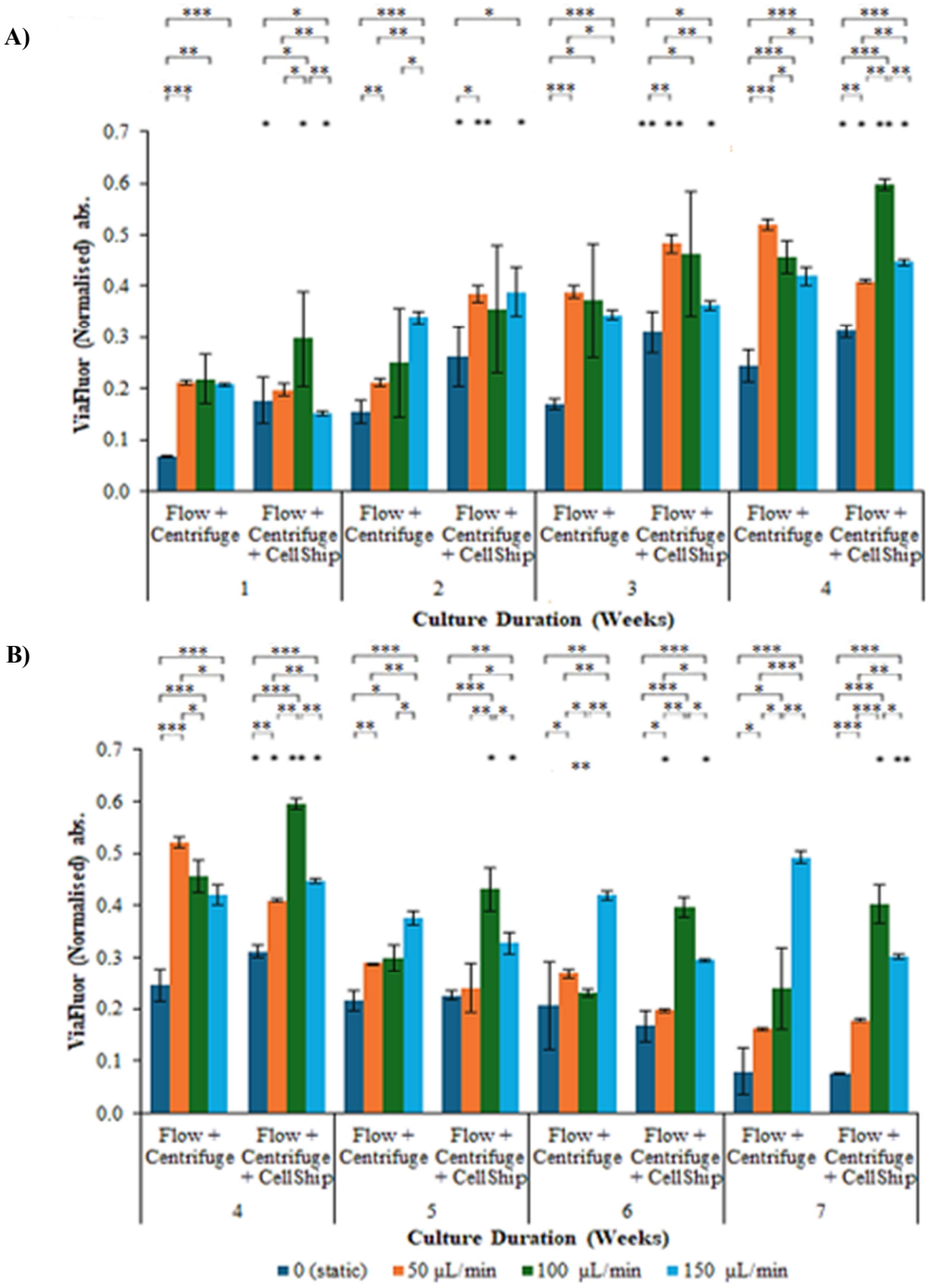


Figure 5.10 Cell proliferation (ViaFluor normalised abs.) compared by centrifuge and flow treatments, and media: Alpha-Mem media with(out) 10 % CS **(A)** ViaFluor detected cell proliferation for centrifuge and flow stimulated samples in standard Alpha Mem media (solid bars) and with 10 % CellShip (textured hatched bars) at 1 – 4 weeks **(B)** ViaFluor detected cell proliferation for centrifuge & flow stimulated samples in standard alpha Mem media with(out) 10 % CellShip at 4 – 7 weeks. *, ** & *** indicate statistical significance of difference between given flow rates and static samples. Larger low * asterisks indicate statistical significance of difference between samples with(out) 10 % CS. * $p < 0.05$, ** $p < 0.01$, *** $p < 0.001$. All tests performed in triplicate (n=3).

Cell osteogenesis statistics from the media comparison showed that Alpha-Mem 10 % CS with combined stimulation samples had increased mean osteogenesis (ALP absorption) compared with std Alpha-Mem, particularly at 5 to 7 weeks for ALP activity in Figure 5.11.

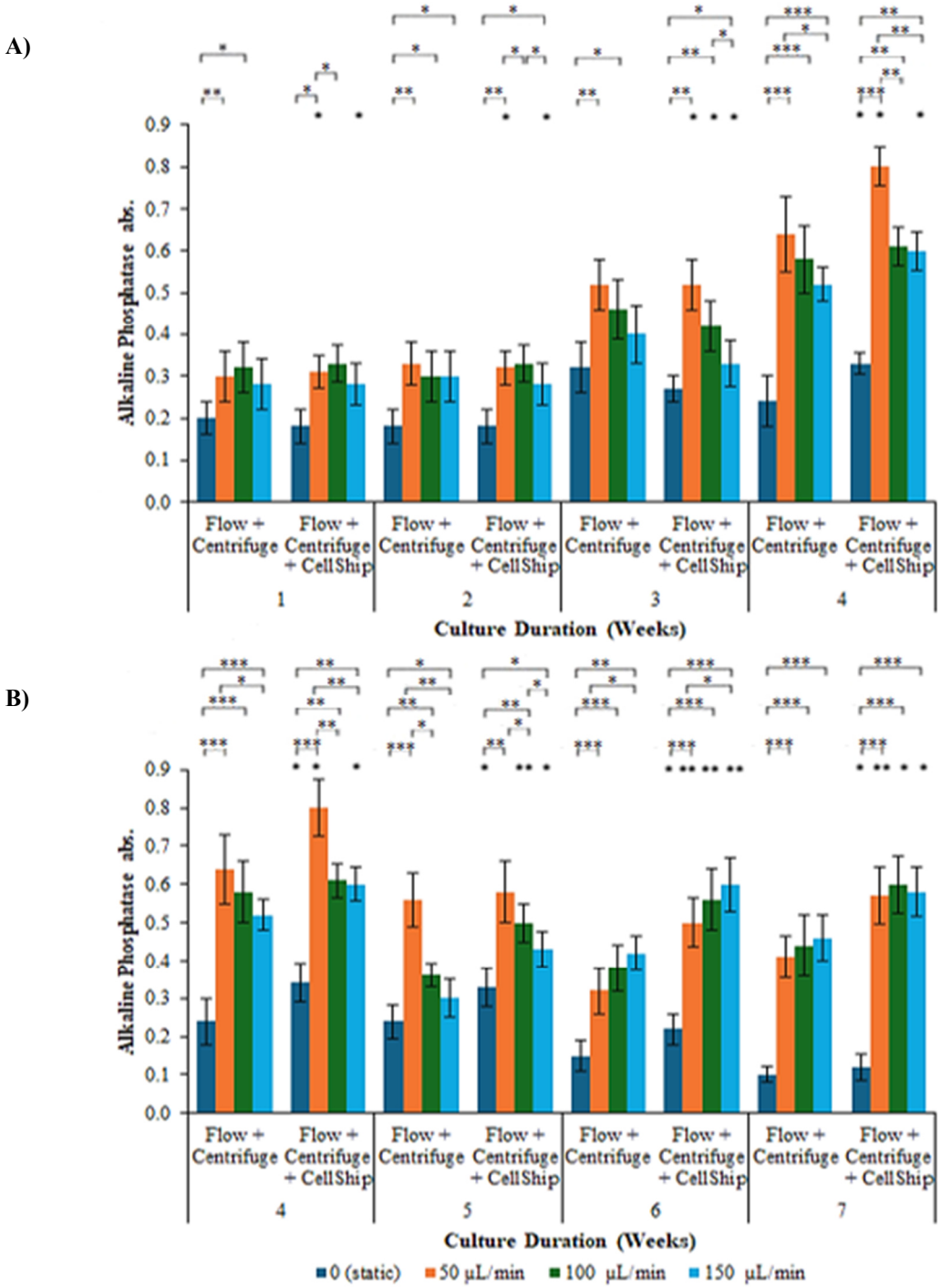


Figure 5.11 ALP abs. compared by centrifuge and flow treatments, and media: Alpha-Mem media with(out)10 % CS **(A)** ALP abs. for centrifuge and flow stimulated samples in standard Alpha Mem media (solid bars) and with 10 % CellShip (textured hatched bars) at 1 – 4 weeks **(B)** ALP abs. for centrifuge & flow stimulated samples in standard Alpha Mem media with(out) 10 % CellShip at 4 – 7 weeks. *, ** & *** indicate statistical significance of difference between given flow rates and static samples. Larger low * asterisks indicate statistical significance of difference between samples with(out) 10 % CS. * $p < 0.05$, ** $p < 0.01$, *** $p < 0.001$. All tests performed in triplicate (n=3).

Figure 5.11 shows that centrifuged samples with higher flow rates (100 to 150 µL/min) had significantly higher ALP detected osteogenesis with CellShip media versus standard media (except at 4 weeks). CellShip significantly increased ALP absorption (abs.) for all centrifuge and flow stimulated samples by 40 to 55 % at 5 to 7 weeks (except 50 µL/min at 5 weeks). In standard media, stimulated samples peaked and then ALP absorption. readings reduced sharply after 4 weeks (consistent with Figure 5.8), while samples with 10 % CellShip media also peaked at 4 weeks but retained higher ALP absorption readings at later weeks.

5.4 Discussion

These experiments examined how dual stimulation and the addition of the CellShip protectant affect cell proliferation and osteogenesis. The optimal CellShip concentration for improving viability in revived MC3T3 cells was identified as 10 % (w/v) (Section 5.3.1). At this concentration, CellShip significantly increased cell activity (alamarBlue^{TM}), proliferation (ViaFluor), and osteogenesis (ALP) versus standard media, confirming its value as a supplement (Section 5.3.1). CellShip affected bone cell growth and development, but effect size depended on the type and intensity of mechanical stimulation, indicating a modulatory role alongside the strong centrifuge and flow effects in standard media (Section 4.3), consistent with known bone cell mechanotransduction mechanisms [299] [300].

This study achieved a 20 to 25 % cell proliferation increase with centrifugation alone and 55 % with 10 % CellShip and 30 to 40 % higher osteogenic ALP activity at mid-culture (Section 4.3, 5.3), at low speeds (120 RPM for 1g equivalent, Section 3.2.2) for longer periods (1 h/day for 21 days). This study's centrifugation-only with CellShip results (Section 5.3.2) showed similar proliferation increases to Prodanov *et al*. [276] who used 10 g continuously for 7 days on MC3T3-E1 cells and observed 30 to 60 % increase in cell proliferation, despite this study's lower centrifuge acceleration (1g) with fewer total hours of stimulation.

Flow-only stimulation (Section 5.3.3) with 10 % CellShip improved shear tolerance (0.15 to 0.45 Pa) over standard media and increased ViaFluor-detected proliferation and more so osteogenic ALP activity at higher flow rates. It caused a strong effect, with 50 to 65 % higher osteogenesis at 3 to 5 weeks (mid culture) and a 95 % average increase at peak (4 weeks) versus the best standard-media static samples (Section 5.3.3, 5.3.4). This aligns with McCoy *et al.* [289] and Tsao *et al.* [267], who reported a 110 % osteogenesis increase with 1.2 Pa shear at 3 weeks. It is also consistent with Bahmaee *et al.* [115], who compared continuous (0.8 to 1.4 Pa) and intermittent (0.2 to 0.4 and 0.8 to 1.4 Pa) flow in a 3D collagen BoC over 3 weeks and found a 100 % ARS-detected osteogenesis increase for intermittent flow vs static at 2 weeks, with intermittent high–low flow outperforming a single continuous rate.

While these studies did not vary media additives, Chen *et al.* [301] increased culture medium viscosity using methylcellulose. The study showed that a 7-fold media viscosity increase in media enhanced osteogenesis by 50 % in human bone MSCs while a 70-fold increase in viscosity increased ALP activity 2.2-fold. Thus, viscosity changes from CellShip may contribute to its modulatory effects [301], [139]. However, another similar study by Lu *et al.* [302] that also increased bone cell media with methylcellulose, showed that higher medium viscosity promotes osteogenic differentiation in human MSCs by activating mechanotransduction pathways. At the same time, it reduces proliferation during osteogenesis but has little effect on proliferation during adipogenic differentiation.

Another cell-protective effect of CellShip is increased tolerance to longer flow shear duration as a shear buffer, particularly when centrifuge and flow stimulation are combined. In Section 5.3.4, CellShip supplemented, centrifuged, and flow-stimulated samples showed higher ALP based osteogenesis than standard media samples for all weeks, particularly after 5 weeks, unlike flow-only stimulated samples, that declined more. Thus, dual stimulation with CellShip may support extended longitudinal studies by acting as a long-term protectant for experiments requiring prolonged mechanical loading to capture later-stage bone organoid maturation [218] [303]. As summarised in Section 5.3.4, adding 10 % CellShip under dual stimulation increased osteogenesis significantly by about 30 to 50 % at 5 to 7 weeks.

CellShip may act as a metabolic or thermal buffer, allowing longer exposure to non-optimal temperatures and enabling 1 h, near–room temperature centrifugation with fewer adverse effects, that is useful when heated/insulated holders or incubator-based centrifugation are unavailable. This effect is distinct from shear buffering or enhancement; increased proliferation and mineralisation in CellShip-supplemented static samples kept outside incubators may reflect such buffering. CellShip may also help cells adapt more efficiently to flow or centrifugation [279] [304]. If CellShip buffers metabolism, this impact may be reduced, potentially explaining the ViaFluor and APS absorption assay values in treated samples at later stages [139] [294], with implications for improving bioreactor protocols [291]. Cell protectants used for storage induce a quiescent G0/early G1 state in cells such as MSCs to limit harmful stress responses [305]. A similar effect may occur in mechanically loaded or shear-stimulated samples with CellShip-like protectants, where studies like Yu et *al.* [277] and similar studies report enhanced mechano-sensitivity and increased osteogenic differentiation relative to proliferation compared with untreated samples [278] [306].

This study has several limitations and opportunities. Treating flow rates and centrifugation as categorical rather than continuous may mask complex relationships between these inputs and assay outputs. Larger chipsets could test more treatment combinations to expand the

dataset. Additional developmental markers such as ECM production [307], bone-related gene expression, and transcription factors could independently validate bone cell growth and development [308][309]. Although static samples were kept outside incubation for the same time as stimulated samples, more controls could compare static samples with(out) CellShip kept continuously in std. incubation to isolate the effects of out-of-incubation thermal stress.

Adding CellShip to media alters viscosity, complicating separation and quantification of mechanical stimulation and enhanced chemotransport, which is already difficult in standard media, thus requires experimental adjustment to separate these effects [310] [311]. Addressing this requires testing cell responses at fixed flow rates while varying shear stress by changing media viscosity without altering temperature or cell biochemical interactions using neutral viscosity modifiers. Sikavitsas *et al.* [310] and Li *et al.* [312] have examined this. Sikavitsas *et al.* added dextran to adjust media viscosity (and shear) at constant flow rate and temperature. Applying a similar approach first with standard media, would help distinguish viscosity, mechanical stimulation, and chemotransport effects. Then repeating this with CellShip could separate its viscosity and thermal metabolic buffer effects.

The study used only one cell line (MC3T3-E1 cells), limiting its relevance to other bone cell types or primary cells. Future work should compare primary cells with cell lines, which may respond differently to stress [128]. To develop a more comprehensive JoC platform, additional cell types such as chondrocytes, immune cells, and circulatory components should be included, along with diseased variants to model specific conditions on-chip.

5.5 Conclusion

Media optimisation showed that 10 % (w/v) CellShip in standard medium optimally preserved MC3T3-E1 viability, proliferation, and osteogenesis. In a GelMA/HAMA BoC platform, assay readings indicated higher cell activity, proliferation, and osteogenesis than in standard Alpha-MEM. As in Chapter 4, centrifugation and flow shear enhanced proliferation and osteogenesis, with flow shear having the strongest, highly significant effect and centrifugation a smaller but significant effect at specific weeks. Adding 10 % CellShip further increased proliferation and mineralisation, indicating synergy with mechanical stimulation, particularly at higher flow rates and in later culture. In late culture, CellShip's average effect size was 30 to 50 %, exceeding that of centrifugation and showing greater variability. Future work should test additional mechanical stimuli on BoC samples, adjacent cell types, or primary cells, and disentangle mechanical from thermal, metabolic, and chemo-transport effects. Modelling could also use machine or deep learning to better predict interactions between centrifugation, flow shear, and media supplements in BoC platforms.

Chapter 6: Development of Machine Learning-based Models of Cell Responses within the BoC Platform

6 Development of Machine Learning-based Models of Bone Cell Responses within the BoC Platform

6.1 Introduction

The BoC platform developed in this thesis provides a controlled environment with the capability to generate complex, multidimensional datasets that capture cellular responses to mechanical stimulation and changes to culture conditions [313]. In previous BoC sections (Section 4.3 and 5.3) the resultant data from the main mechanical stimulation and CellShip experiments generated complex multivariable non-linear time series data with considerable variation within treatment groups and between treatments throughout the testing period. This could be observed for all 8 treatment groups whether for static controls or for flow shear and/or centrifuge stimulated sets with(out) CellShip supplemented media. The traditional analytical methods employed to assess cellular response to different stimuli, have limited capability to fully interpret these heterogeneous data streams, particularly when subtle, nonlinear multi-variable relationships govern cell behaviour. ML offers a powerful solution by enabling automated pattern recognition, predictive modelling, and integration of diverse data types such as imaging and cell assays [314]. By uncovering hidden trends and correlations such as non-linear multivariable relations over time and treatment, ML can contribute to hypothesis generation, improve reproducibility, and enhance the sensitivity of BoC studies to detect early markers of osteogenesis or stress responses. Well-characterised, openly accessible datasets are essential for modelling these complex cellular responses.

This chapter examines the two resultant datasets, **ML_FlowCentrifuge.csv** and **ML_FlowCentrifuge_all.csv**, that were derived from the main *in vitro* dual stimulation experiments in Chapters 4 and 5. Methods are specified in Sections 4.2 and 5.2, with results overviewed in Sections 4.3 and 5.3. The first supports descriptive and simple ML analyses, while the expanded dataset enables deep learning models to predict bone tissue responses—cell activity, growth, and development—under varied microenvironmental conditions. These models can optimise aspects of organ-on-chip platforms, including monitoring, culture conditions, media composition, and mechanical stimulation [314], Unlike previous BoC studies with mechanical stimulation with some having ML (reviewed by Mansoorifar *et al.* [313], Hodgkinson *et al.* [52], Kong & Shin [315]), these generated datasets are openly accessible, supporting transparency, reproducibility, and benchmarking of ML models for capturing non-linear, multi-feature relationships in noisy biological data [315]. Integrating dual-stimulation BoC systems with ML enables analysis beyond conventional statistics and provides a benchmark for future multi-stimulation platforms, supporting drug testing as an

alternative to less controllable models such as animal, 2D, or static 3D *in vitro* systems (Ma *et al.*) [316] [315].

Deep learning (DL) is particularly suited for modelling complex non-linear interactions between stimuli and cellular outcomes in tissue engineering [315][317][318]. However, standard DL models often require large datasets and substantial computational resources [319] limiting their applicability in high-dimensional but data-limited biological contexts. Recent approaches using lightweight neural networks and stochastic learning mitigate overfitting and improve efficiency [320]. Motivated by these challenges, this study introduces models examined in other studies such as **Randomised Deep Neural Networks (Randomised DNN)** also known as **Randomised Deep Learning (Randomised DL** a lightweight, interpretable architecture that incorporates stochasticity in hidden layer sizes and dropout rates at runtime [199] [200]. This approach acts as an implicit regulariser, enhancing generalisation while reducing computational demands. Drawing from ensemble learning and distributional hypothesis spaces datasets [317] [321]. Randomised DL offers structural diversity, natural regularisation, and minimises the need for exhaustive hyperparameter tuning [199].

Deep neural networks (DNNs) in biomedical applications are often constrained by their black-box nature and high computational demands. These traits of the model limit trust, reproducibility, interpretability, and seamless integration into clinical workflows [322]. To enhance interpretability, two widely used Explainable AI (XAI) techniques, LIME and SHAP [323], were incorporated into the proposed Randomised DL model and evaluation pipeline. These methods offer both local (instance-level) and global (dataset-level) explanations of feature importance, supporting the biological plausibility and transparency of model predictions [323] [205]. Consistency between LIME and SHAP outputs further validated the model's predictions, providing insights into how experimental parameters influence cellular behaviour.

Considering these factors in modelling biological assay data with ML and deep learning, candidate models were compared for predictive regression of outputs from centrifuge cycling loading (centrifugation) and flow shear experiments, both with and without media variation (Chapters 4 and 5). The objective of this study was to develop, optimise, and benchmark a suite of classical and deep learning regression models, along with XAI approaches, for predicting BoC cell responses.

6.2 Classical Machine Learning Methods: Data and Processing

The data was generated through a series of controlled *in vitro* BoC mechanical stimulation experiments (Chapter 4 and 5) with methods specified in Section 4.2 and 5.2 and results analysed in Section 4.3 and 5.3. The methodology is briefly re-summarised below.

6.2.1 Experimental Design Rationale

The following input factors were examined:

1. **Media Type:** Evaluated the effects of various media and supplements, including Alpha-MEM and CellShip preservation agent, on cellular responses.
2. **Flow Stimulation:** Simulated interstitial fluid flow (a physiological mechanical shear stimulus) using syringe-connected microfluidic chips.
3. **Centrifugation:** Applied controlled mechanical loading to mimic gravitational forces or exercise-induced stimuli, assessing its impact on osteogenesis.
4. **Time:** Tracked temporal cellular dynamics and tissue development over an extended culture period for 7 weeks

The combinatorial variation of these parameters enabled the generation of a comprehensive dataset suitable for modelling both individual and interactive effects on osteoblast differentiation, ultimately supporting the development of predictive models for the bone tissue engineering outcomes.

6.2.2 Data Acquisition and Processing

Assay data from all main mechanical stimulation experiments (Chapters 4 and 5), including absorption and fluorescence readings, were collected at 1, 2, 3, 4, 5, 6, and 7 weeks. The same post-experimental analysis methods described in Section 4.2.4 were applied. This analysis period spans from before early osteogenic commitment (1 week) to advanced mineralisation (7 weeks). Summary statistics and trend analyses from Weeks 3 to 7 were used to monitor tissue development, assess dataset consistency, and curate data for downstream modelling and synthesis.

Data Cleaning and Preprocessing

The preprocessing pipeline comprised of the following steps:

1. Loading the dataset with appropriate encoding `latin1`. This is an 8-bit single-byte character encoding standard that supports 191 characters from Latin script, primarily covering Western European languages like English (ISO/IEC 8859-1).
2. Renaming columns for consistency (e.g., `Flow_Rate_(µl/min)` was renamed to `Flow_Rate`).
3. Removing any rows with missing values in the output variables.
4. Applying a column transformer for input features:
    - One-hot encoding was applied to the categorical feature `Media_type`. a preprocessing technique that converts categorical data into a binary vector format where each unique category is represented by a new column containing a 1 for the specific category and 0 for all others.
    - Standard scaling was used for all numerical input features. This is a standardization is a feature scaling technique that transforms data to have a mean of 0 and a standard deviation of 1.
5. Output variables were also standardised using `StandardScaler` to improve numerical stability and model convergence.

These steps ensured uniform formatting across all models, enabling fair comparison and reliable evaluation.

6.2.3 Dataset Detailed Description

The experimental work resulted in a core primary dataset in CSV format, **ML_FlowCentrifuge.csv.** This dataset captures experimental measurements involving microfluidic flow stimulation and centrifugation on MC3T3-E1 cells cultured in GelMA/HAMA hydrogels with each triplicate measurements entered, labelled and indexed separately. Each row represents a single experimental instance at a defined time point under specific media and stimulation conditions. The dataset includes both numeric and categorical variables, with 348 total data points (610 including parallel wavelength measurements after any rows with missing values prior to repeat measurements are filtered/removed). For each fluorescence or absorbance type, dual-wavelength readings were collected (primary/excitation and secondary/emission), enhancing measurement reliability and allowing internal cross-validation of signal consistency [324].

The Input variables (input factors) used are listed as below:

- `Week#`: Culture week (Day 1/Week 0, then weekly from Week 1, 2, 3, 4, 5, 6 and 7).
- `Media_type`: Categorical; includes Alpha-MEM, Alpha-MEM and 10 % CellShip
- `Flow_Rate_(µl/min)`: Volumetric flow rates of 0, 50, 100, or 150 µl/min applied to individual microfluidic channels within a microfluidic chip by a KFT-NE1000 syringe pump and 10ml glass syringe. This was applied on average 1 h / day.
- `Centrifuged_(g-equiv)`: Binary encoding (0 or 1 g) for equivalent motion-based g-force exposure via centrifugation (at given radial distance), applied on average 1 h / day.

The corresponding output variables (responses) used are listed as follows:

- `405nm_alkP`: ALP activity infers calcium mineralisation via assay reader absorbance at 405/415 nm (with 430 nm auxiliary measurement).
- `560nm_alamB`: alamarBlue™ metabolic activity via assay absorbance at 570/600 nm.
- `488nm_VFz_abs`: Normalised ViaFluor Fluorescence (amine-based) for cell proliferation via assay absorbance.
- `488nm_VF_FL`: Direct Fluorescent amine-based readings to detect cell proliferation via ViaFluor assay reader fluorescence at 488/495 nm.

6.3 Machine Learning Descriptive Analysis

In this section the curated dataset structure, distribution and correlation is described, followed by a Principal Component Analysis (PCA).

6.3.1 Dataset Statistical Summary, Distribution and Correlation

To better understand the characteristics of the numerical input or output variables, a statistical summary was generated. This summary includes count, mean, standard deviation, and value set/range for `Week#`, `Flow_Rate_(µl/min)` `Centrifuged_(g-equiv)`, and the four output variables `560nm_alamB`, `488nm_VFz_abs`, `488nm_VF_FL`, and `405nm_alkP`. The detailed summary of the 416 data entries when 2D control or filled repeat measurements are excluded (348 entries when `488nm_VFz_abs` zero values are removed) are presented in Table 6.1 (parallel wavelength readings were excluded).

Table 6.1 Descriptive statistics of core flow/centrifugation data

Stat	Week#	Flow_Rate (µl/min)	Centrifuged (g)	560nm_alamB	488nm_VFz_abs	488nm_VF_FL	405nm_alkP
Count	348	348	348	348	348	348	348
Mean	3.3	82.8	0.52	0.473	0.320	296813	0.372
Std-dev	2.3	53.0	0.50	0.235	0.163	191513	0.188
Value-set/range	0 to 7	0, 50, 100, 150	0, 1	0.077 to 1.176	0.089 to 1.063	7,317 to 1,128,100	0.072 to 1.450

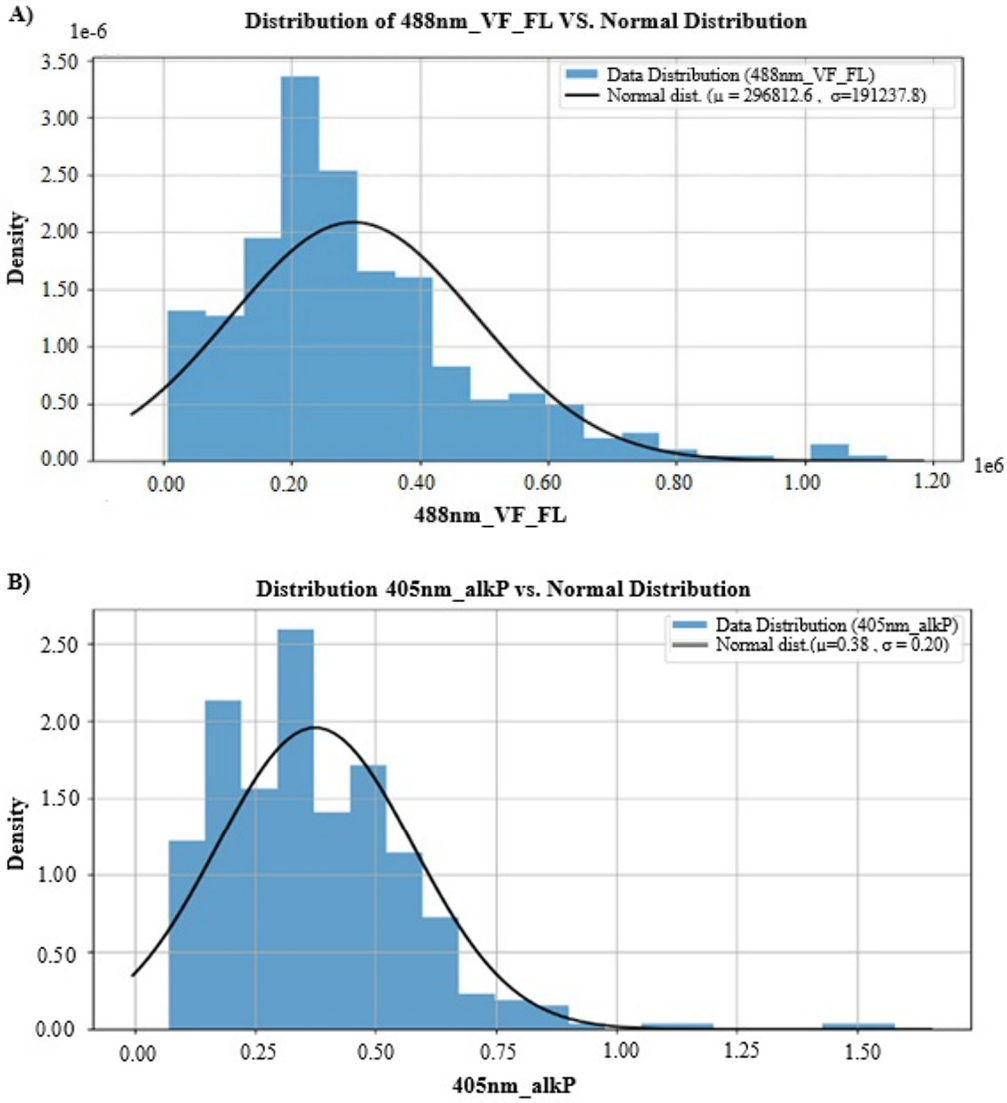


Figure 6.1 ALP, ViaFluor Output data probability density **A)** ViaFluor Fluorescence absorption distribution (488nm_VF_FL), **B)** Alkaline Phosphatase absorption distribution (405nm_alkP)

Figure. 6.1, shows the assay output distributions vs normal distribution curves. 488nm_VF_FL, representing fluorescence intensity of viable amine protein indicated cell proliferation (Figure 6.1 (a)). 405nm_alkP, representing early osteogenesis marker activity through ALP phosphatase absorbance (Figure 6.1 (b)). Output distributions are normal right skewed in distribution.

For instance, `Flow_Rate_(µl/min)` spans from 0 to 150 µl/min, with a mean of approximately 82.76 µl/min. The output variable 488nm_VF_FL shows a wide range, from approximately 7,317 to 1,128,100, with a mean around 296,813 indicating significant variability and a right-skewed distribution, which is common in biological and chemical measurements. Density plots were generated for each output variable and evaluated using the Shapiro–Wilk test. All outputs exhibited approximately right-skewed normal distributions, bounded by a lower cut-off near 0.1 due to background or baseline values from low-cell or acellular samples. These distributions were confirmed for both ViaFluor fluorescence and absorbance-based alamarBlue^{TM}, alkaline Phosphatase (ALP) readings, as illustrated in Figure 6.1 (panels a, b). The right-skewed nature of the data facilitates the use of skew- normal models or similar synthetic data augmentation methods, which preserve the proportional and correlative structure of the measured biological signals [325]. A correlation matrix (Figure 6.2) was also made for these numerical variables to explore potential linear correlative relationships between them. Strong correlations (more than 0.5) observed between the independent outputs, show an expected co-occurrence of increased metabolic, structural proliferation development, and mineralisation.

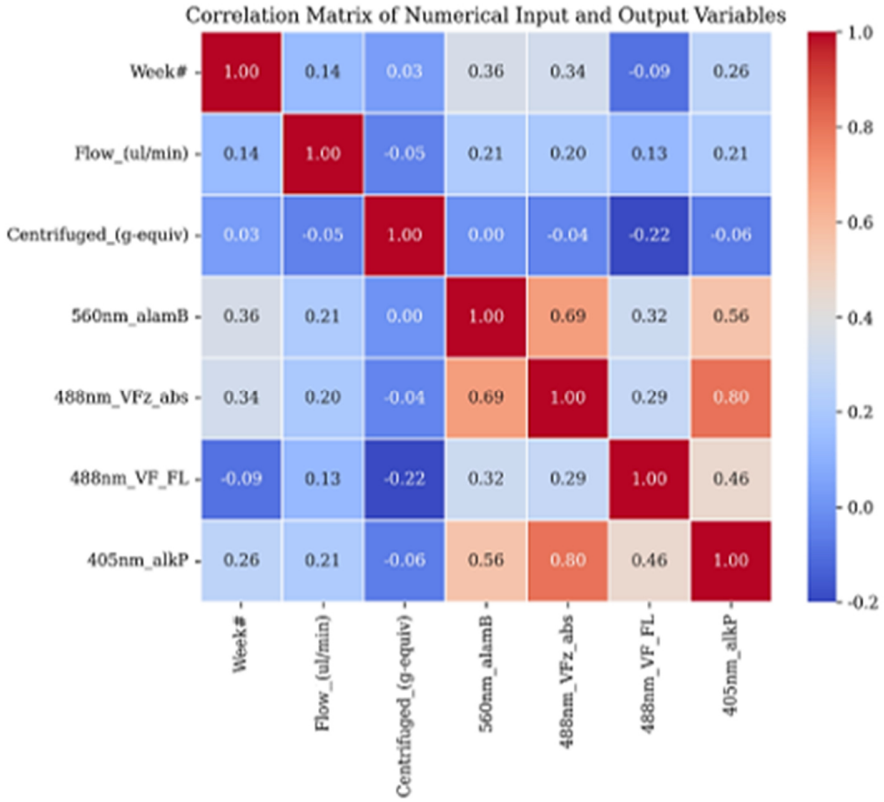


Figure 6.2 Correlation Matrix Heatmap showing simple correlation values for inputs vs outputs

An expected low to negligible correlation is observed between the inputs (Week #, Flow Rate, and Centrifugation) showing that no multi-collinearity is present, while a moderate correlation is observed between inputs and outputs although this is just a linear approximate fit and actual accurate regression fits will require more adaptive ML models that can fit non-linear relations.

6.3.2 Summary of PCA: Input Features Impact on Flow Centrifuge Outputs

The three Principal Component Analyses (PCA) conducted on the Flow Centrifuge dataset reveal distinct patterns of influence between input features and output variables. When analysing the complete feature set, media type emerged as the dominant predictor. The most revealing was the analysis that excluded the type of media, where week # and flow rate emerged as equally powerful predictors with remarkably high effect sizes ($0.73 - 0.74$) for most outputs. This indicates that in the absence of media composition information, temporal progression and flow conditions become the primary determinants of cellular responses. Centrifugation acceleration then had an effect size of 0.3 when media is removed, and this moderate centrifugation acceleration effect's remains consistently visible for all combinations of input variables included (Figure 6.3).

Figure 6.3 compares the PCA effect size for all key input inclusions.

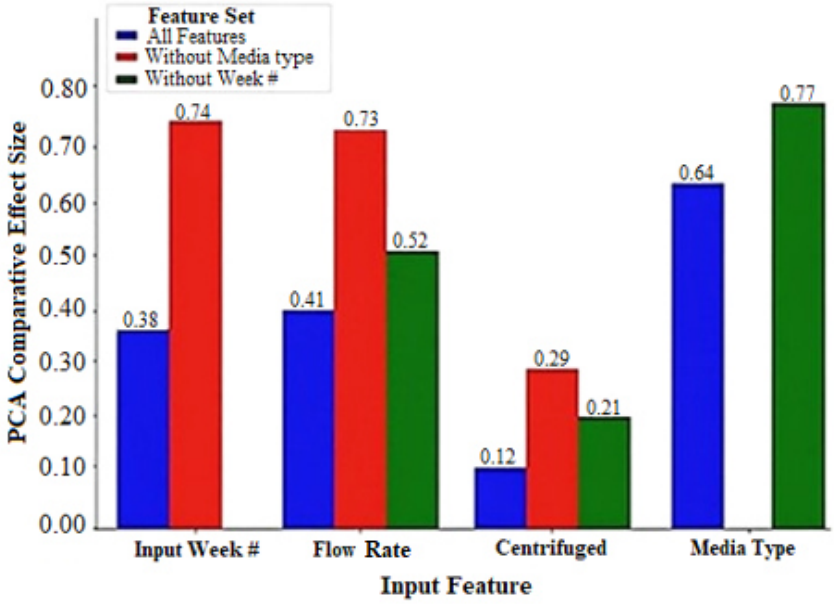


Figure 6.3 PCA comparison of different input features effect size on all assay outputs combined.

Percentages for share of the effect size are derived by dividing the factor score for a particular input/feature by the sum of the factor score of all included features/inputs combined. These findings collectively demonstrate that while media type establishes the baseline cellular response, the temporal dynamics (week#) and flow conditions work in concert to modulate specific aspects of cellular behaviour, with centrifugation force playing a specialised moderate role in influencing assay measurements.

6.3.3 Predictive Regression Model Overview

To model multiple continuous output variables, a variety of several regression algorithms commonly used for tabular data were implemented and optimised [150]:

1. **Support Vector Regression (SVR):** A non-parametric model suitable for capturing complex, non-linear relationships with suitable kernel functions in higher dimensions [326]. A variety of kernels (2^{nd} and 3^{rd} order polynomial and gaussian) were used, with the gaussian kernel being the optimisation algorithms' final choice to optimise for least loss during model training.
2. **Random Forest Regressor:** An ensemble method that averages predictions from multiple decision trees to reduce variance [327].
3. **XGBoost:** A tree-based ensemble gradient boosting optimised algorithm known for high accuracy, and speed [328].
4. **LightGBM:** A gradient boosting framework that employs leaf-wise tree growth that causes the greatest error loss reduction for faster convergence and less memory [328].

To address the multiple-output regression problem, all models were wrapped using `MultiOutputRegressor`, this enabled simultaneous prediction of multiple outputs.

Hyperparameter Optimisation - Two model hyperparameter tuning strategies were used:

1. **Random Search:** Implemented using `RandomizedSearchCV` from `scikit-learn`, this approach randomly samples from the hyperparameter space and is computationally efficient but may overlook globally optimal configurations [207] .
2. **Bayesian Optimisation:** Performed using `Optuna`, this method leverages Bayesian principles to model the performance landscape and select hyperparameters more intelligently, learning from prior evaluations, converging to optimal solutions in fewer trials [329] .

Both optimisation strategies used 30 trials per model to ensure fair comparison. Optimisation was performed using 3-fold cross-validation on the training set, with R^2 as the main metric.

6.4 Deep Learning Methodology

While previous studies demonstrated the potential of integrating mechanical loading into microfluidic systems, in addition to lacking multi-modal stimulation they lacked open-access datasets and systematic modelling benchmarks. The present study addresses this gap by publishing a structured, openly accessible dataset (ML_FlowCentrifuge_all.csv) for training of deep learning regression models, with this data derived from a 7-week experimental protocol involving MC3T3-E1 pre-osteoblasts cultured in GelMA/HAMA hydrogels. This dataset captures cell responses under varied flow types, centrifugation levels, and media formulations serving as a foundation for reproducible, and data-driven modelling in bone tissue engineering.

6.4.1. Implementation Environment

All experimental procedures were implemented in Python, selected for its robust support for numerical computing and its mature ecosystem of deep learning (DL) frameworks. Model development, training, and evaluation were executed on a high-performance computing platform equipped with an AMD Ryzen 7 5700X eight-core processor and an NVIDIA GeForce RTX 4080 GPU with 16 GB of dedicated memory. This hardware configuration ensured accelerated matrix operations, efficient parallelism, and reliable handling of computationally intensive DL workloads.

6.4.2. Dataset

The full core dataset, ML_FlowCentrifuge_all.csv, captures experimental measurements involving microfluidic flow stimulation and centrifugation on MC3T3-E1 cells cultured in GelMA/HAMA hydrogels with varied media composition with standard Alpha-Mem media (as per Chapter 4) and with 10 % CellShip (CS) cell protectant media supplement (as per Chapter 5). The ML_FlowCentrifuge_all.csv dataset includes all microplate assay wavelength measurements to generate additional data that preserves the same correlation patterns between cell culture inputs and assay outputs, as confirmed by matching output variable statistical distributions with those of the outputs of the core ML_FlowCentrifuge.csv dataset (e.g. Figure 6.1 in Section 6.3 and Figure 5.9 in Section 5.3). Flagged or missing measurements that create partial gaps for these datasets required imputation based on given feature inputs and these same output variable statistical distributions. Median based imputation was used to resolve outliers. Thus, the expanded dataset has the same features and timepoints as ML_FlowCentrifuge.csv but twice as many entries, providing more data to train deep learning models that perform better

with larger datasets. The dataset was then analysed, cleaned and processed (as detailed in Section 6.2). Statistical analysis (summary table and distribution plots) including Principal Component analysis was conducted (Section 6.3), and classical ML regression modelling (optimised variants of Random Forest, XG Boost, Light GMB and SVR models) based on the core data was carried out for output data analysis and model benchmarking (Section 6.3).
The dataset includes a mixture of both numeric and categorical variables, about 610 total data points (or 680 data points with 2D controls and over 1000 with imputed entries and repeat measurements for statistical analysis) from all wavelength assay plate readings. This is twice the volume of the classical ML models' dataset. Each row represents a single measurement-set or experimental instance at a defined time point under specific media and stimulation conditions. For each fluorescence or absorbance type, dual-wavelength readings were collected (primary/excitation and secondary/emission) creating additional data for this dataset, enhancing measurement reliability and allowing internal cross-validation of signal consistency.

Input Variables (Factors):

- Week#: Culture week (Day 1/ Week 0, then weekly from Week 1, 2, 3, 4, 5, 6 and 7).
- Media_type: Categorical; includes Alpha-MEM, AlphaMEM and 10 % CellShip (cell protectant agent)
- Flow_Rate_(μl/min): Volumetric flow rates of $0, 50, 100$, or 150 μl/min applied to individual microfluidic channels within a microfluidic chip by a KFT-NE1000 syringe pump and 10 ml glass syringe. This was applied on average 1h / day.
- Centrifuged_(g-equiv): Binary encoding (0 or 1 g) for equivalent motion-based g-force exposure via centrifugation (at given radial distance), applied on average 1 h / day.

Output Variables (Responses):

- 405nm_alkP: ALP activity to infer calcium levels via assay reader absorbance at $405/415$ nm
- 560nm_alamB: alamarBlue^{TM} metabolic activity via assay absorbance at $560/590$ nm
- 488nm_VFz_abs: Normalised absorption from amine detection of viable cell proliferation
- 488nm_VF_FL: Direct amine ViaFluor fluorescence (at $488/495$ nm) of cell proliferation.

6.4.3. Data Preprocessing

Neural network performance is fundamentally dependent on the quality, structure, and normalisation of input data. The dataset used in this study comprised categorical attributes such as Media_type and Flow_type alongside numerical features including Time_Point_(Week#) and Centrifuged. Categorical variables were encoded using a one-hot representation [330], resulting in a binary matrix $\mathbf{X}_{\text{cat}}$. This matrix was concatenated with the normalised numerical matrix to form the complete input feature matrix $\mathbf{X} \in \mathbb{R}^{n \times d}$, where n denotes the total number of samples and d the number of input features. Numerical features were standardised using z-score normalisation, which centres each feature around zero and scales it to unit variance [330]. The transformation is formally defined as

$$x_i' = \frac{x_i - \mu_i}{\sigma_i} \tag{6.1}$$

where μ_i and σ_i represent the empirical mean and standard deviation of feature dimension i, respectively. As expressed in Equation 6.1, this transformation mitigates scale-induced optimisation biases and improves convergence stability. Following normalisation and the removal of incomplete or malformed entries, the dataset was partitioned into training and testing subsets using an 80:20 stratified split to preserve representational balance across subsets. Each output variable, including $488nm_VF_FL$, was modelled independently in a supervised regression framework.

6.4.4. Randomised-Based Deep Neural Network (Randomised NN)

This work uses a Randomised-Based Deep Neural Network (Randomised NN) that embeds stochasticity directly into architectural design, departing from conventional fixed DL architectures. The key idea is that randomly sampled structural configurations, specifically hidden layer widths and dropout rates promote architectural diversity, reduce overfitting, and achieve robust approximation without manual hyperparameter tuning. Instead of treating architecture as a fixed optimisation variable, this approach models it as a distribution, aligning model instantiation with statistical learning theory and ensemble generalisation. Architectural randomness is increasingly recognised as a way to improve robustness and generalisation in NN. The Randomised NN operationalises this by sampling hidden layer sizes at runtime: the

first hidden layer width, h-1, has dimensions of $\mathcal{U}\{20,60\}$ and the second, h-2 has dimensions of $\mathcal{U}\{10,40\}$. A dropout probability range p is $\mathcal{U}(0.1,0.5)$ is also sampled and used as a stochastic regulariser during training. The functional mapping from the input vector $\mathbf{x} \in \mathbb{R}^d$ to the scalar prediction $\hat{y} \in \mathbb{R}$ is expressed as

$$\mathrm{f}_{\mathrm{rand}}(\mathbf{x}) = \mathbf{W}_3 \cdot \phi_2(\mathbf{W}_2 \cdot \phi_1(\mathbf{W}_1 \cdot \mathbf{x} + \mathbf{b}_1) + \mathbf{b}_2) + \mathbf{b}_3 \tag{6.2}$$

where ϕ_1 and ϕ_2 denote ReLU activation functions and $\mathbf{W}_i, \mathbf{b}_i$ represent the weight matrices and bias vectors, respectively [331] [332] [199]. These weights and biases are also optimised as part of the training optimisation process.

Model training is conducted using the Mean Squared Error (MSE) loss function defined as

$$\mathcal{L}_{\mathrm{MSE}} = \frac{1}{\mathrm{n}} \sum_{\mathrm{i}=1}^{\mathrm{n}} (\mathrm{y_i} - \hat{\mathrm{y}}_\mathrm{i})^2 \tag{6.3}$$

where $\mathrm{y_i}$ and $\hat{\mathrm{y}}_\mathrm{i}$ correspond to the true and predicted values of the target variable [333], Equation 6.2 encapsulates the forward computation pipeline, while Equation 6.3 governs the learning objective. Optimisation is performed using the Adam algorithm with a fixed learning rate of 0.001.

By utilising runtime architectural variability, Randomised NN introduces structural noise as a regularising factor, effectively functioning as a lightweight single-model ensemble [203]. This enables the network to achieve performance stability across varying data distributions without the overhead of explicit model ensembles or exhaustive hyperparameters search.

6.4.5. Benchmark Models

The Randomised NN was compared to three baseline neural architectures that were implemented under identical training conditions. These were artificial, deep and simple neural networks that are standard simple fundamental neural net models in ML studies that are often used to commence such modelling from [198]. Each model was trained using the MSE loss function given in Equation 6.3, optimised using Adam, and executed over 100 epochs with a batch size of 8. Metrics of interest included both predictive accuracy and computational time.

- **Artificial Neural Network (ANN)**

This baseline model comprises a single hidden layer of 32 neurons using ReLU activation. The structure reflects the canonical architecture in feedforward regression and is mathematically defined as [331] [333]:

$$\mathrm{f}_{\mathrm{ANN}}(\mathbf{x}) = \mathbf{W}_2 \cdot \phi(\mathbf{W}_1 \cdot \mathbf{x} + \mathbf{b}_1) + \mathbf{b}_2 \tag{6.4}$$

where $\phi(\cdot) = \mathrm{ReLU}(\cdot), \mathbf{W}_1 \in \mathbb{R}^{32\times d}$, and $\mathbf{W}_2 \in \mathbb{R}^{1\times 32}$. As indicated in Equation 6.4, this model captures basic nonlinear transformations and serves as a computationally efficient benchmark.

- **Deep Neural Network (DNN)**

The DNN model extends the ANN by incorporating additional representational depth and regularisation [331] [332] [334]. It includes two hidden layers, consisting of 16 and 8 neurons respectively, activated by sigmoid and ReLU functions. Dropout with a fixed rate of 0.2 follows the first activation. The overall model is expressed as

$$\mathrm{f}_{\mathrm{DNN}}(\mathbf{x}) = \mathbf{W}_3 \cdot \phi_2\big(\mathrm{Drop}(\mathbf{W}_2 \cdot \phi_1(\mathbf{W}_1 \cdot \mathbf{x} + \mathbf{b}_1) + \mathbf{b}_2)\big) + \mathbf{b}_3 \tag{6.5}$$

where $\phi_1(\cdot) = \sigma(\cdot)$ represents the sigmoid function, $\phi_2(\cdot) = \mathrm{ReLU}(\cdot)$, and Drop denotes the element-wise application of dropout. Equation 6.5 represents the hierarchical transformations performed by the network, capable of learning higher order abstractions in the data.

- **Simple Neural Network (Simple NN)**

Designed to serve as a lightweight benchmark, the Simple NN employs a single hidden layer with 16 ReLU-activated units [331] [332] [333]. Its forward mapping is given by

$$\mathrm{f}_{\mathrm{SimpleNN}}(\mathbf{x}) = \mathbf{W}_2 \cdot \phi(\mathbf{W}_1 \cdot \mathbf{x} + \mathbf{b}_1) + \mathbf{b}_2 \tag{6.6}$$

where $\phi(\cdot) = \mathrm{ReLU}(\cdot), \mathbf{W}_1 \in \mathbb{R}^{16\times d}$, and $\mathbf{W}_2 \in \mathbb{R}^{1\times 16}$. Although this architecture is structurally similar to the ANN described in Equation 6.4, it operates with reduced capacity, offering insights into performance trade-offs between model simplicity and predictive power.

6.4.6. Evaluation Metrics

Assessment of model performance was conducted using a comprehensive suite of regression evaluation metrics, encompassing both statistical fidelity and predictive precision. Specifically, the evaluation protocol utilised the Coefficient of Determination (R^2), Root Mean Squared Error (RMSE) and Mean Absolute Error (MAE). These metrics jointly quantify model fit, error magnitude, and prediction consistency across unseen test data [333].

Coefficient of Determination (R^2)

The coefficient of determination quantifies the proportion of variance in the ground truth output that is captured by the model's predictions [333]. Formally, it is defined as:

$$\mathrm{R}^2 = 1 - \frac{\sum_{\mathrm{i}=1}^{\mathrm{n}} (\mathrm{y_i} - \hat{\mathrm{y}}_\mathrm{i})^2}{\sum_{\mathrm{i}=1}^{\mathrm{n}} (\mathrm{y_i} - \bar{\mathrm{y}})^2}, \tag{6.7}$$

where $\mathrm{y_i}$ and $\hat{\mathrm{y}}_\mathrm{i}$ denote the true and predicted values for the i-th sample, and $\bar{y}$ is the empirical mean of the true target values. In Equation 6.7, an R^2 score of 1 indicates perfect prediction, while a score less than 0 implies that the model performs worse than a constant mean predictor.

Root Mean Squared Error (RMSE)

The RMSE captures the standard deviation of the residuals, thereby quantifying the average magnitude of prediction errors in the same unit as the target variable [333] . It is given by

$$\mathrm{RMSE} = \sqrt{\frac{1}{\mathrm{n}} \sum_{\mathrm{i}=1}^{\mathrm{n}} (\mathrm{y_i} - \hat{\mathrm{y}}_\mathrm{i})^2}, \tag{6.8}$$

which corresponds to the square root of the Mean Squared Error defined in Equation 6.3. RMSE penalises larger errors more severely due to the squaring operation and is sensitive to outliers in the residual distribution.

Mean Absolute Error (MAE)

MAE quantifies the average absolute deviation between predicted and actual values, offering a linear and interpretable measure of error [333]:

$$\mathrm{MAE} = \frac{1}{n}\sum_{i=1}^{n} |y_i - \hat{y}_i| \tag{6.9}$$

As shown in Equation 6.9, MAE provides a direct measure of predictive accuracy that is less sensitive to extreme errors compared to RMSE, making it a robust metric in noisy environments.

6.4.7. Training Time

In addition to predictive performance, computational efficiency was assessed via the wall-clock time required to train each model. This timing was measured from the start of the training phase until convergence, using a consistent hardware and software environment for all architectures. Recording training time facilitates a comparative analysis between model complexity and practical employability in real-time or resource constrained settings.

6.4.8. Explainable Artificial Intelligence (XAI)

In modern DL, especially in regression tasks involving high dimensional structured data, models often operate as black boxes that obscure the internal reasoning behind predictions. While architectures namely DNNs achieve high accuracy, they lack explainability, rendering them unsuitable in domains that demand transparency and accountability [335]. This issue is particularly acute in applications involving biological or clinical data, where explainability is essential for trust, validation, and domain-specific insight [336]. The present study addresses this explainability gap by integrating XAI techniques into the model evaluation pipeline. Specifically, Local Interpretable Model-Agnostic Explanations (LIME) and SHapley Additive explanations (SHAP) are employed to provide post hoc explanations for individual predictions of the trained proposed approach. These methods enable the attribution of model output to input features, thereby offering actionable insights into model behaviour across different instances.

Local Interpretable Model-Agnostic Explanations (LIME)

LIME is a perturbation-based explanation technique that constructs local surrogate models to approximate the decision boundary of a complex predictor in the neighbourhood of a given input

instance [323]. For a trained model $f: \mathbb{R}^d \rightarrow \mathbb{R}$, LIME generates a locally faithful explanation $g \in G$, where G is the set of interpretable models (e.g., linear regressors), by solving the following optimisation problem:

$$\arg\min_{g \in G} \mathcal{L}(f, g, \pi_{\mathbf{x}}) + \Omega(g), \tag{6.10}$$

where $\mathcal{L}(f, g, \pi_{\mathbf{x}})$ measures the fidelity of the explanation model g with respect to the black-box model f in a locality defined by the kernel $\pi_{\mathbf{x}}$, and $\Omega(g)$ is a regularisation term controlling the complexity of the explanation.
As expressed in Equation 6.10, LIME constructs an interpretable approximation of the model behaviour around a specific sample $\mathbf{x}$ by minimising the weighted loss between f and g. This results in a sparse, human-readable representation that highlights the most influential input features driving the model's output for that instance [335].

SHapley Additive explanations (SHAP)

SHAP is a game-theoretic framework grounded in cooperative game theory, where each input feature is interpreted as a player contributing to the model's final prediction [323]. The SHAP value ϕ_i quantifies the marginal contribution of feature i to the predicted outcome and satisfies properties such as local accuracy, consistency, and missing variance. The SHAP value for feature i is defined as:

$$\phi_i = \sum_{S \subseteq F \setminus \{i\}} \frac{|S|!\,(|F| - |S| - 1)!}{|F|!} \left[f_{S \cup \{i\}}(\mathbf{x}) - f_S(\mathbf{x}) \right], \tag{6.11}$$

where F is the full set of input features, S is a subset of features not containing i, and $f_S(\mathbf{x})$ denotes the model trained on feature subset S.
Equation 6.11 formalises SHAP as a weighted summation over all possible coalitions S, measuring the expected marginal contribution of feature i across different feature subsets. In practical implementations, exact computation of SHAP values is intractable for large $|F|$, and approximation methods such as sampling or model-specific variants (e.g., DeepSHAP) are employed.

6.5 Results

6.5.1 Classical Machine Learning Results

To compare the different classical ML regression models implemented based on the first BoC core dataset (**ML_FlowCentrifuge.csv)**, with R^2 and MAPE (Mean Absolute Percentage Error) used as evaluation metrics. Figure 6.4 compares all models with their optimiser variants for R^2 fit accuracy and Figure 6.5 is a heatmap that compares the regression models and their optimised variants, by R^2 for each assay output.

Model	Optimization	560nm_alamB	488nm_VFz_abs	488nm_VF_FL	405nm_alkP
Random Forest	Bayesian	0.775	0.752	0.935	0.791
XGBoost	Bayesian	0.745	0.712	0.901	0.783
XGBoost	Random Search	0.766	0.735	0.89	0.783
Random Forest	Random Search	0.752	0.737	0.852	0.769
LightGBM	Random Search	0.625	0.614	0.829	0.668
SVR	Random Search	0.646	0.59	0.73	0.734
SVR	Bayesian	0.643	0.584	0.726	0.763

Figure 6.4 Classical ML Regression Models R^2 fit for all outputs, with MAPE error rate

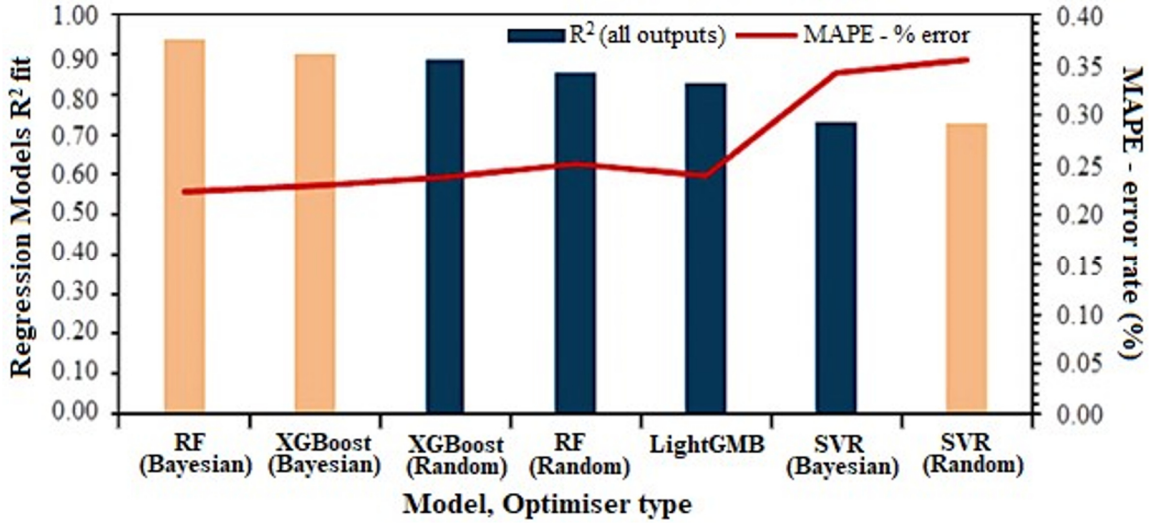


Figure 6.5 Regression Models R^2 fit for each output. Compared by models and optimisation method.

In Figure 6.4, models and their optimiser types are compared, with Bayesian optimisation shown in blue and RandomSearch in orange. Random Forest models tuned with Bayesian optimisation consistently achieved the highest predictive accuracy, followed by XGBoost.

Ensemble tree-based methods were particularly effective for this multi-output regression task. Figure 6.5 shows that the R^2 performance ranking of each model was consistent across all outputs. The direct fluorescence variable (488nm_VF_FL) was the easiest to predict, with the highest R^2 values for all models. Figure 6.6 shows that model rankings by error closely matched the R^2 (for all outputs) and MAPE rankings (Figures 6.4 and 6.5), with similar patterns across other error metrics (RMSE, MAE).

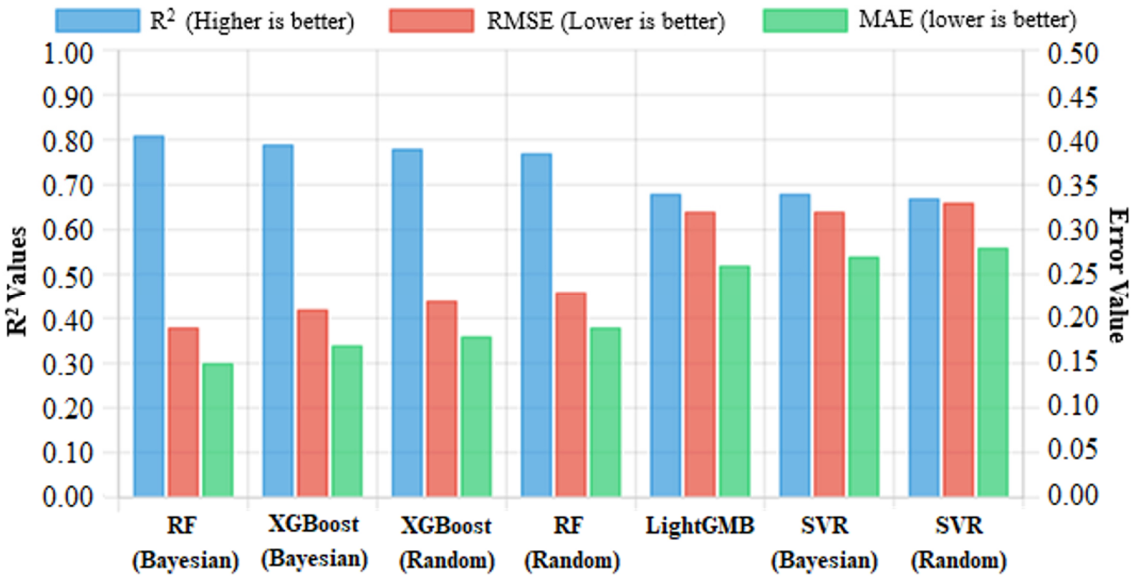


Figure 6.6 Model Performance - R^2 vs Error Metrics by regression model type. R^2 values are averaged across all outputs.

A similar inverse relationship between R^2 values and the other error types as well as MAPE is observed. The relative regression model performance remains quite consistent across the other error types as well as fitting for the various output types, demonstrating a consistency in model performance.

6.5.2 Deep Learning Results

This section presents a comparative evaluation of the proposed Randomised DL model against three benchmark architectures: ANN, DNN, and Simple NN. Four regression targets corresponding to different spectral measurements were used to assess predictive accuracy and computational efficiency. Evaluation metrics include the coefficient of determination (R^2), Root Mean Squared Error (RMSE), Mean Absolute Error (MAE), and training time in seconds. The results are summarised in Tables 6.2, 6.3, 6.4, and 6.5.

Target: 405nm_alkP: On the 405nm_alkP regression task, Randomised DL exhibited the strongest predictive capability with an R^2 value of 0.6035, outperforming all benchmark models. It achieved the lowest RMSE (0.1786) and a MAE (0.1111) marginally better than ANN. Additionally, Randomised DL required the least training time (3.32 s), indicating its computational advantage. The complete results are reported in Table 6.2.

Table 6.2 Performance comparison for target 405nm_alkP.

Model	$\boldsymbol{R^2}(\uparrow)$	**RMSE** (↓)	**MAE** (↓)	**Time** (**s**)(↓)
ANN	0.596711	0.180075	0.113934	5.421203
DNN	0.421595	0.215656	0.139475	6.336405
Simple NN	0.564739	0.187077	0.114956	5.344857
Randomised DL	**0.603474**	**0.178559**	**0.111129**	**3.321267**

Target: 488nm_VFz_abs: The 488nm_VFz_abs results highlight the consistent superiority of Randomised DL. With an R^2 of 0.7096, RMSE of 0.1391, and MAE of 0.0880, the model achieved the best performance across all metrics. It also completed training in the shortest time (3.32 seconds), underscoring its robust computational efficiency. In contrast, the DNN and Simple NN underperformed significantly, while the ANN yielded moderate results. Details are presented in Table 6.3.

Table 6.3 Performance comparison for target 488nm_VFz_abs.

Model	$R^2(\uparrow)$	RMSE (↓)	MAE (↓)	Time (s)(↓)
ANN	0.650890	0.152461	0.096337	5.441334
DNN	0.338931	0.209798	0.146893	6.434590
Simple NN	0.541252	0.174769	0.112465	5.407268
Randomised DL	**0.709608**	**0.139050**	**0.087957**	**3.317527**

Target: 560nm_alamB: For the 560nm_alamB target, Randomised DL delivered the highest R^2 value (0.4293), along with the lowest RMSE (0.1931) and MAE (0.1407). This performance demonstrates the model's resilience even under more complex scenarios. Furthermore, Randomised DL outpaced all other models in training time. ANN and DNN showed comparable but weaker performance, while Simple NN lagged notably as presented in Table 6.4.

Table 6.4 Performance comparison for target 560nm_alamB.

Model	$R^2(\uparrow)$	RMSE (↓)	MAE (↓)	Time (s)(↓)
ANN	0.332279	0.208889	0.143707	5.383228
DNN	0.338068	0.207981	0.161562	6.368834
Simple NN	0.231205	0.224142	0.159648	5.452905
Randomised DL	**0.429289**	**0.193119**	**0.140704**	**3.369693**

Target: 488nm_VF_FL: The $488nm_VF_FL$ target yielded the strongest overall performance, with Randomised DL reaching an R^2 of 0.7659 which was the highest across all experiments. It also posted the lowest RMSE (0.0744) and MAE (0.0606), along with the fastest training time (3.45 s). While ANN and Simple NN showed strong performance, neither matched the efficiency and accuracy of Randomised DL. Table 6.5 summarises the results.

Table 6.5 Performance comparison for target 488nm_VF_FL.

Model	$R^2(\uparrow)$	RMSE (↓)	MAE (↓)	Time (s)(↓)
ANN	0.716812	0.081634	0.065594	5.550810
DNN	0.613642	0.095351	0.079175	6.442259
Simple NN	0.704648	0.083368	0.068178	5.415865
Randomised DL	**0.765935**	**0.074375**	**0.060637**	**3.450576**

6.5.3 Explainable AI Results

To clarify the model's reasoning for all targets (405 nm_alkP, 488 nm_VFz_abs, 560 nm_alamB, and 488 nm_VF_FL), two post-hoc explainability methods were applied, LIME and SHAP. These methods show how each input feature affects the model's output, turning the DL model's opaque predictions into human-interpretable insights.

Target: 405nm_alkP: Figure 6.7 shows LIME explanations for one representative test instance. Flow_type_100 and Time_Point_(Week#) are the strongest positive contributors, with feature values of 2.34 and 0.79, respectively, substantially increasing their weighted contribution to prediction output. In contrast, Flow_type_50 and Media_type_Std have strong negative effects, with values of -0.67 and -1.06, lowering the predicted output. Each feature's contribution appears in a horizontal bar plot, where orange bars indicate positive and blue bars negative influence on the model output.

LIME (Local Interpretable Model-Agnostic Explanations) is interpreted by analysing a simple, local surrogate model (typically linear regression or a decision tree) that approximates the complex black-box model's behaviour around a specific prediction [335]. The explanation focuses on feature importance, where the surrogate model's coefficients or weights indicate how much each input feature contributes to the specific prediction. Positive values in the explanation signify that a feature increases the probability of the predicted class (or value), while negative values indicate that the feature decreases the likelihood of that prediction [335]. LIME results with these feature weightings are given in Fig 6.7.

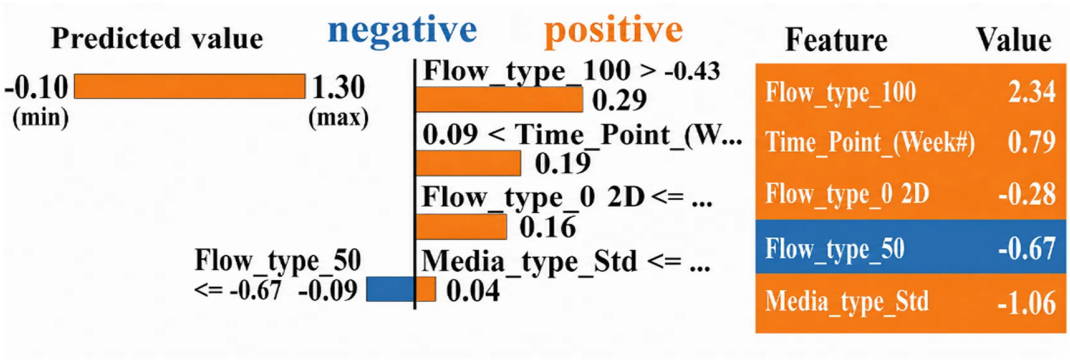


Figure 6.7 LIME explanation for $405nm_alkP$ prediction instance. Orange indicates positive and blue negative influence.

The SHAP summary plot in Figure 6.8 provides global feature importance across the dataset. Flow_type_100 is the most influential feature, adding about 0.47 SHAP units on average. Time_Point_(Week#) and Media_type_Std contribute 0.23 and 0.11, respectively, while Centrifuged contributes 0.05. The five lowest-ranked features together contribute only 0.03, indicating minor influence. The agreement between LIME and SHAP supports the reliability of the model's internal logic: both methods highlight Flow_type_100 and Time_Point_(Week#) as key predictors, showing that the model mainly relies on time dependence and experimental flow conditions to estimate the target variable.

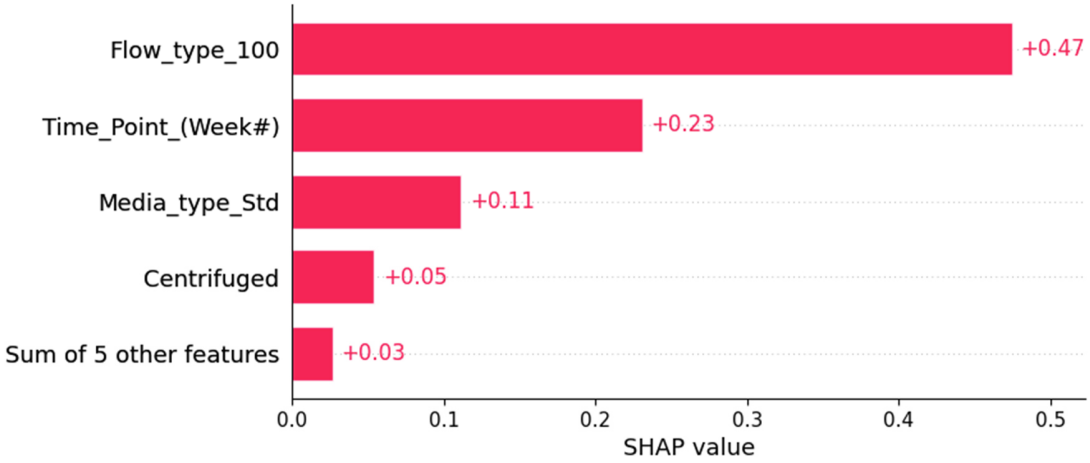


Figure 6.8 SHAP feature importance summary for 405nm_alkP.

Target: 488nm_VFz_abs: The explainability assessment for the 488nm_VFz_abs target further validates the predictive behaviour of the model by dissecting individual feature

influences using LIME and SHAP. As shown in Figure 6.9, the LIME visualisation indicates that Flow_type_100 exerts the strongest positive influence on the predicted output, supported by its high feature value of 2.34. This is followed by Time_Point_(Week#) and Flow_type_0_2D, which contribute moderately. On the other hand, Flow_type_0 and Flow_type_50 exhibit negative influence, reducing the model's prediction. The visualisation provides directional insight into how specific values of categorical and continuous variables modulate the regression output.

The SHAP summary in Figure 6.10 offers a global ranking of feature contributions across the dataset. Flow_type_100 again dominates as the most influential factor with a mean SHAP value of plus 0.58. Other important contributors include Time_Point_(Week#) and Centrifuged, adding plus 0.26 and plus 0.09 to the prediction, respectively. Interestingly, a small negative contribution is also observed from a subset of lower ranked features, collectively reducing the predicted value by minus 0.04. This highlights the balance between major and minor feature effects within the model's internal decision structure.

Overall, both explanation methods converge on identifying the dominance of flow-related variables in determining normalised fluorescence outcomes at this wavelength. The congruence between LIME and SHAP further underscores the robustness of the model's interpretability for this signal.

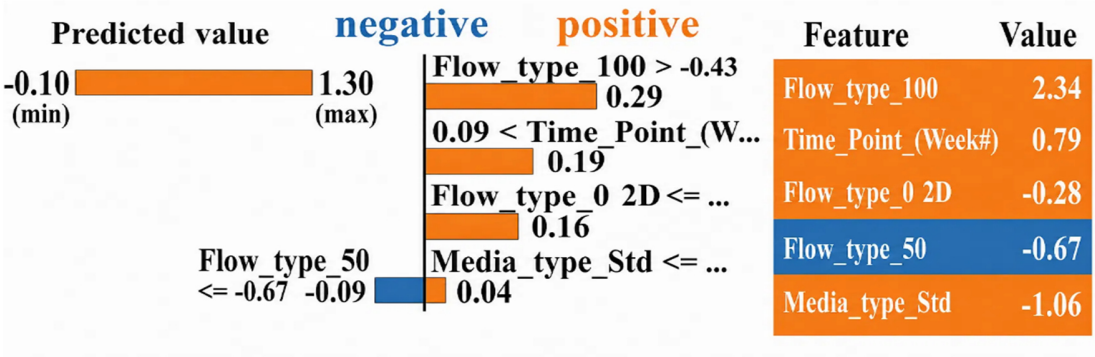


Figure 6.9 LIME explanation for 488nm_VFz_abs prediction instance

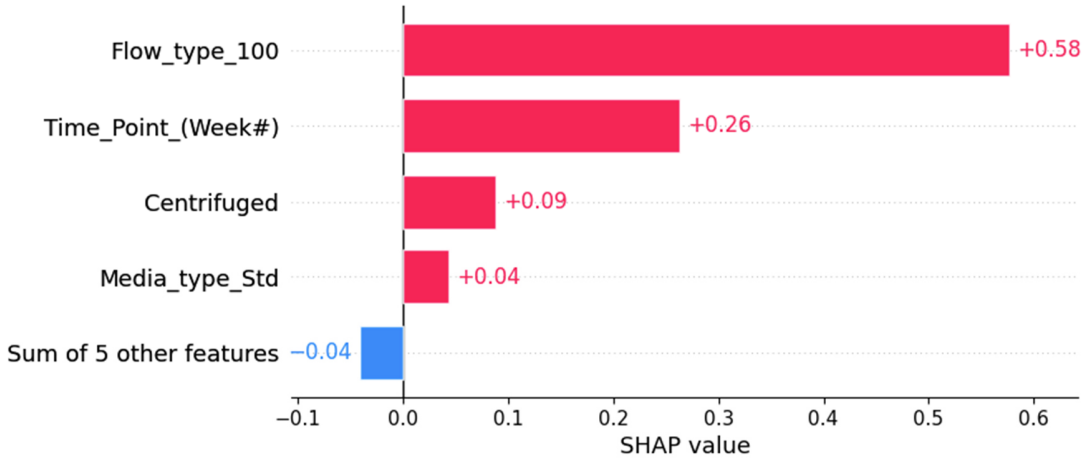


Figure 6.10 SHAP summary plot for $488nm_VFz_abs$

Target: 560nm_alamB: The explainability results for the 560nm_alamB target offer nuanced insights into how the model derives its predictions under more challenging regression conditions. Figure 6.11 illustrates the LIME explanation for a selected prediction instance. Among the positively contributing features, Flow_type_0_2D and Time_Point_(Week#) emerge with the largest local impact, with LIME weights of approximately 0.22 and 0.15, respectively. Features such as Flow_type_0 and Flow_type_100 contribute positively but with smaller weights, whereas Flow_type_50 exhibits a mild negative influence on the output.

The SHAP summary plot in Figure 6.12 provides a dataset-wide attribution profile. Flow_type_100 remains the most influential contributor globally, adding approximately plus 0.27 SHAP units, followed by Time_Point_(Week#) at plus 0.21. Interestingly, Media_type_10 % CS and Flow_type_0_2D also appear in the top five contributors, although their impacts are more subtle at plus 0.07 and plus 0.03, respectively. The aggregate contribution of lower-ranked features is again minimal, suggesting that the model relies heavily on a small subset of dominant variables.

In comparison with prior targets, the explanations here indicate a more evenly distributed importance across both experimental and contextual parameters. Although Flow_type_100 remains a dominant driver, the increased relevance of media composition and moderate SHAP weight of Time_Point_(Week#) suggest context-sensitive interactions for predicting 560nm_alamB response. Together, LIME and SHAP affirm the trustworthiness of the model by providing explainable justifications consistent with physical and experimental intuition.

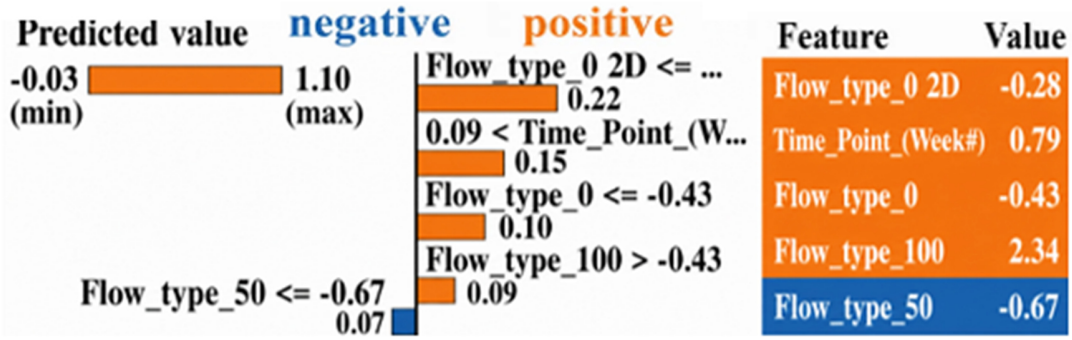


Figure 6.11 LIME explanation for 560nm_alamB prediction instance.

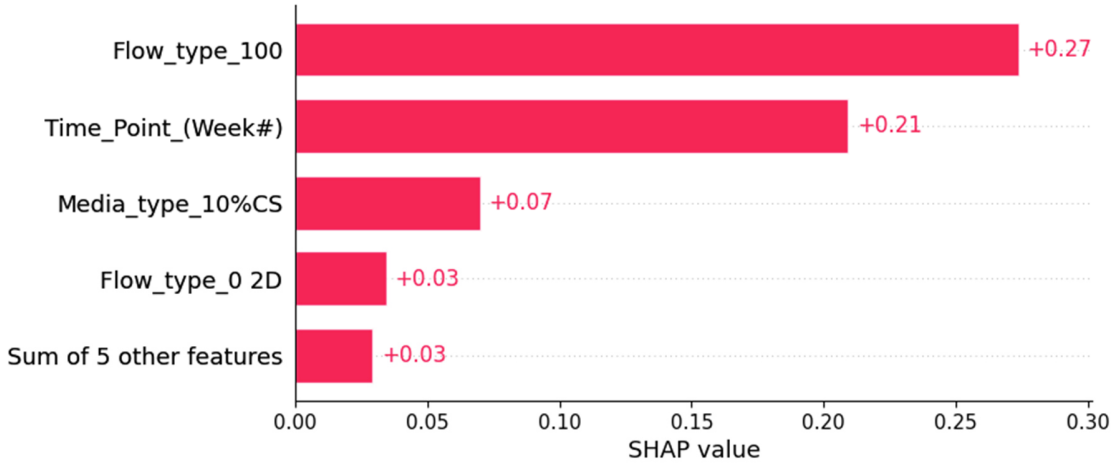


Figure 6.12 SHAP summary plot for 560nm_alamB.

Target: 488nm_VF_FL: For the $488nm_VF_FL$ regression output, the explainability analysis focused on understanding subtle feature influences in a high-performance prediction regime. The LIME result, presented in Figure 6.13 reveals that the most significant positive contributor to the predicted outcome is Flow_type_0_2D, followed by Flow_type_0, both pushing the model's prediction upward. Interestingly, Flow_type_100 appears as a suppressive factor, lowering the prediction due to its negative value (0.43). Additional contextual variables such as Flow_type_50 and Time_Point_(Week#) are present but less impactful. Dataset-wide SHAP values in Figure 6.14 clarify feature importance: Flow_type_50 contributes the most (plus 0.08), followed by smaller yet non-negligible contributions from Flow_type_0, Centrifuged, and Time_Point_(Week#). Although SHAP magnitudes are lower for this target than for others, this indicates greater model confidence and lower uncertainty due to clearer signal separation with $488nm_VF_FL$ measurements. Unlike the previous target, however, the contribution of Centrifugation gains prominence, suggesting some target-specific interaction effects.

This target is unique because its influence is distributed across many low-magnitude features, indicating the model relies on a balanced mix of inputs rather than a few dominant ones. The agreement between LIME and SHAP, identifying the same key variables with different weights, shows reliable model behaviour and coherent internal representations for fluorescence context.

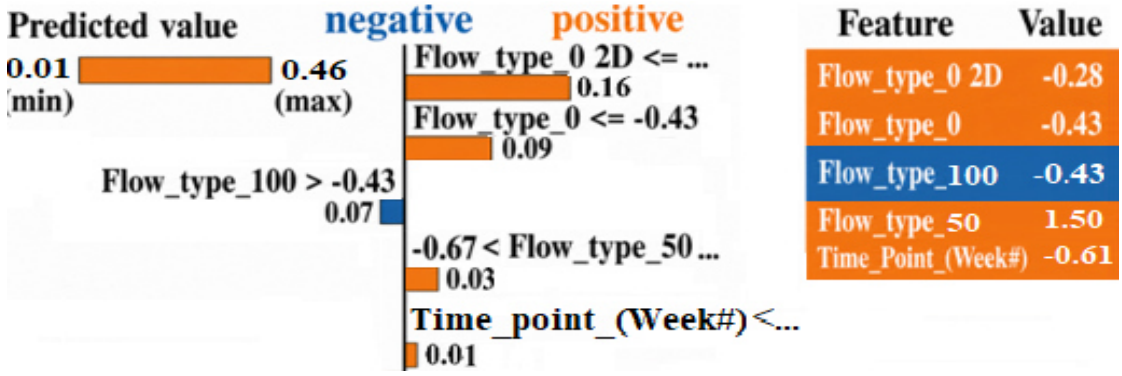


Figure 6.13 LIME explanation for $488nm_VF_FL$ prediction instance.

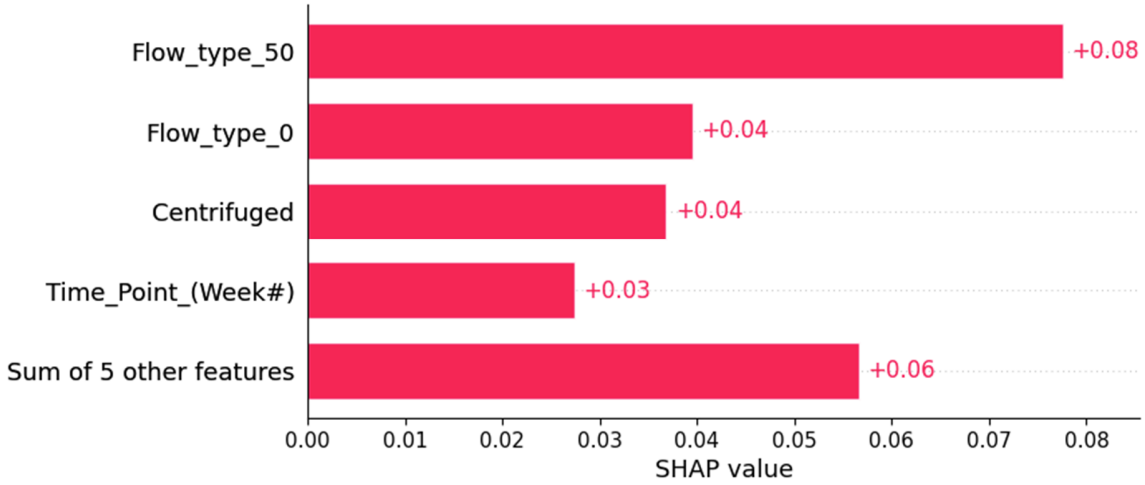


Figure 6.14 SHAP summary plot for $488nm_VF_FL$.

6.6 Discussion

6.6.1 Classical Machine Learning Discussion

Among all outputs, 488nm_VF_FL was the most predictable, with the Random Forest (Bayesian) model reaching an R^2 of 0.93. Adding MAPE exposed robustness and error trends not captured by R^2 alone. Comparing optimisation methods showed that Bayesian optimisation can markedly improve performance in high-dimensional spaces [337], although gains are model-dependent and cannot replace strong base learners. A near-inverse relationship between R^2 and error rates across models confirmed consistent evaluation, a pattern also seen for other error metrics. Figure 6.5 shows that higher-performing models (darker green, higher R^2) are moderately consistent across all bone cell growth and development outputs, particularly ViaFluor Fluorescence (488nm_VF_FL). This indicates reliable modelling of cell behaviour across independent assay outputs, supporting this experiment's reliability.

In terms of comparing model characteristics, Random Forest and XGBoost achieve better results than SVR on complex tabular data because their tree-based architecture naturally detects complex relationships (such as higher order polynomial relationships) between features and their interactions without requiring scaling of input data [192] [328] . Ensemble based models like Random Forest or XG Boost can effectively combine multiple model variants to improve overall results [192]. These types of models can directly handle mixed format tabular data with continuous as well as categorical data and allows direct interpretation of a model and its weighting on various input features without further explainability algorithms [188] [338]. The performance of SVR depends on selecting appropriate kernel types and their corresponding hyperparameters to handle non-linear relationships, noisy data and it shows sensitivity to the scale of the input data as well as data outliers [339] [340]. They performed the least effectively of all ML models and can struggle with a suitable kernel and optimisation with noisy highly variable biological cell data.

The Bayesian optimisation outperformed the Random Search due to its statistical data-based learning techniques using past results to choose hyperparameters to try on subsequent iterations [210]. This informed strategy allows it to find the optimal solution more efficiently and in fewer iterations, with less time and computation [210]. Due to these reasons ensemble models with Bayesian optimisation have the better overall performance for these regression modelling tasks.

6.6.2 Deep Learning Discussion

Across all testing, the proposed Randomised DL model outperforms conventional benchmarks (ANN, DNN, Simple NN). Evaluated on four regression targets, Randomised DL consistently achieves higher predictive accuracy, faster training, and better explainability. Model performance varied by output type, with ViaFluor fluorescence outputs yielding the best regression fits. The improvements stem from Randomised DL's stochastic architecture: unlike static-topology networks, it samples key hyperparameters—the sizes of the first and second hidden layers (h-1, h-2) and the dropout probability p (from uniform distributions).

$$\mathrm{h}_1 \sim \mathcal{U}\{20,60\}, \mathrm{h}_2 \sim \mathcal{U}\{10,40\}, \mathrm{p} \sim \mathcal{U}(0.1,0.5). \tag{6.12}$$

This introduces controlled randomness in architecture construction, effectively expanding the representational hypothesis space. The resulting stochastic model space can be expressed as:

$$\mathcal{H}_{\text{rand}} = \bigcup_{(\mathrm{h}_1,\mathrm{h}_2,\mathrm{p})} \mathcal{H}(\mathrm{h}_1, \mathrm{h}_2, \mathrm{p}), \tag{6.13}$$

where each $\mathcal{H}(\mathrm{h}_1, \mathrm{h}_2, \mathrm{p})$ represents a functional subspace defined by a sampled architectural configuration. This implicit regularisation promotes functional diversity and lowers overfitting risk. The benefits of this stochastic technique align with generalisation theory, where convergence to flatter loss minima is linked to better out-of-sample performance [341]. In contrast, conventional DNNs with fixed depths and layer sizes are more prone to sharp minima, especially in high-capacity regimes. A typical DNN forward pass is:

$$\mathrm{f}_{\mathrm{DNN}}(\mathbf{x}) = \mathbf{W}_3 \cdot \phi_2\big(\text{ Dropout }(\mathbf{W}_2 \cdot \phi_1(\mathbf{W}_1 \cdot \mathbf{x} + \mathbf{b}_1) + \mathbf{b}_2)\big) + \mathbf{b}_3, \tag{6.14}$$

where ϕ_1 and ϕ_2 denote non-linear activation functions and dropout is applied at a fixed rate. The rigidity of this formulation makes the model less adaptable to varying data complexities, and optimisation can become trapped in poor local minima if hyperparameters are suboptimal [341] [342]. From a complexity standpoint, Randomised DL provides computational advantages by dynamically selecting smaller networks when sufficient. Assuming input dimensionality d, the total number of trainable parameters in a conventional DNN is given by:

$$\theta_{\mathrm{DNN}} = \mathrm{d} \cdot \mathrm{h}_1 + \mathrm{h}_1 \cdot \mathrm{h}_2 + \mathrm{h}_2 \cdot 1 + \text{ bias terms }, \tag{6.15}$$

where h_1 and h_2 are static. In contrast, due to sampling as defined in Equation 6.12, the expected value of $\theta_{\text{RandomisedDL}}$ is lower on average, translating into reduced forward/backward pass costs and faster convergence. This theoretical reduction is supported empirically across all four regression tasks. When compared to Simple NN and ANN, Randomised DL's design offers a superior balance between expressive power and generalisation control. Simple NN lacks the architectural depth required to model higher-order interactions, while standard ANN-despite its intermediate complexity-suffers from fixed-width bottlenecks that either under-fit or over-fit the data depending on feature interactions and target variability.

Explainability assessments confirm the advantages of Randomised DL. LIME and SHAP attributions consistently match known determinants (Flow_type_100, Time_Point_(Week#), Centrifuged), and the alignment of LIME's local and SHAP's global explanations indicates internal model consistency. Lower SHAP value variance in easier tasks (e.g. $488nm_VF_FL$) suggests reduced epistemic uncertainty and more stable predictions, unlike the benchmark.

Overall, neural networks underperformed relative to classical ML regression as expected from reviews of other studies using smaller tabular datasets [191] [192]. However, it should be remembered that the neural networks were trained on a separate dataset, ML_FlowCentrifuge_all.csv that used experimental data generated from the same mechanical stimulation BoC experiments (Chapter 4, 5) only with additional parallel wavelength measurements from the assay readers. Within deep learning techniques, Randomised DL gave the best R^2, lowest errors, and highest computational efficiency, and showed the same inverse R^2–error relationship as ML models. The Randomised DL model reached R^2 of over 0.7 for some outputs but remained below the top ML ensembles (Bayesian-optimised Random Forest, XGBoost; R^2 greater than 0.9). This gap indicates that despite neural network models having a larger dataset (ML_FlowCentrifuge_all) albeit with additional measurements, there is a need for substantially more data from additional, repeated, or parallel experiments, or from statistically representative and adequate data synthesis. To improve Randomised DL, the dataset should be at least larger than 1000 entries or an order of magnitude larger than the number of model parameters [343] [344].

To date, there are no direct comparison external studies as previously discussed in Section 2.5. The most similar known study by Shaikhina *et al.* [214] employed ANN deep learning regression models for predicting age-related trabecular bone properties in OA, and specimen age given bone traits from 3D human trabecular bone specimens, achieving an R^2 of 0.96 with

low errors. This demonstrates the potential of ANNs and similar ML models and it is a large improvement from the best performing deep learning models (R^2 of 0.77) within this thesis study but comparable with marginal improvement to the performance of the best Random Forest ML model (R^2 of 0.93) of this study. This is comparing the performance on the best cell assay output (direct fluorescence detected proliferation) and the average performance of this study's best ML or deep learning models were considerably less than the ANN of Shaikhina *et al.* This study has modelled more outputs of greater variation (assay metabolic activity, proliferation and osteogenesis) in comparison to the Shaikhina *et al.* outputs such as specimen age or compressive strength which reduces comparability.

6.7 Conclusions

Two curated datasets (ML_FlowCentrifuge.csv and ML_FlowCentrifuge_all.csv) from bone cell tests under varied media, centrifuge, and flow shear on a multimodal dual stimulation BoC platform (https://github.com/Collib29/) were presented, discussed and analysed. Ensemble models (Random Forest, then XGBoost) with Bayesian optimisation performed best ($R^2 = 0.90$ to 0.93), outperforming benchmarks and all deep learning models that were trained on an expanded dataset. A stochastic deep learning model, the Randomised-Based Deep Neural Network (Randomised DL), used runtime architectural variability to improve generalisation and reduce overfitting. Across multiple regression tasks, it exceeded ANN, DNN, and simple NN baselines in R^2 and computational efficiency, but deep learning remained less effective than classical ML regression overall. The best neural model, Randomised DL, achieved $R^2 = 0.71$ to 0.77 for some outputs (e.g., ViaFluor assays) and showed increased performance variation by output type than classical models. To date, only one partially similar comparison study by Shaikhina *et al*. shows potential for greater performance. Explainable AI tools (LIME, SHAP) provided biologically meaningful insight into model decisions, enhancing interpretability and trust. This interpretable, scalable pipeline supports data-driven bone tissue engineering and could aid scaffold optimisation, drug screening, and personalised regenerative medicine strategies. PCA for the smaller ML_FlowCentrifuge dataset highlighted the flow and media effects on assay outputs combined. This was also done with the LIME and SHAP methods for the best neural net or deep learning model (Randomised DL) that highlighted flow and then centrifuge stimulation as largest factors. Further SHAP refinement on deep models, with more training data and modelling updates is recommended.

Chapter 7: Overall Discussion, Concluding Remarks and Future Perspectives

7 Overall Discussion, Concluding Remarks and Future Perspectives

7.1 Overall Discussion

This research aimed to develop a BoC platform that supports long-term bone cell culture with integrated multimodal mechanical stimulation, specifically cyclic load compression and fluid shear that can also be used for dual stimulation. The platform was used to assess bone cell behaviour under varied culture and stimulation conditions. The effects of these variables were quantified via experiment and modelled through interpretable ML, deep learning and explainable AI.

7.1.1 BoC and Gel Development

Developing biomaterials that mimic natural bone ECM is crucial for bone tissue engineering, but many BoC platforms lack this. This research integrated optimised hydrogels into BoC platforms to create a more biomimetic culture environment. Chapter 3 describes incorporating a GelMA and HAMA based gel formulation optimised for 3D BoC osteoblast culture. The study assessed how gel composition, thickness, integrity, and biocompatibility influence MC3T3-E1 osteoblast proliferation and osteogenesis, enabling in-chip bone cell culture for up to 7 weeks. Previous studies have typically focused on a single mode of mechanical stimulation. Some work, such as Kim *et al.* [87] and McGarry *et al.* [284], examined multiple modes, but not in combination on the same samples. In contrast, this study developed a chip that provides combined dual mechanical stimulation and applied it to BoC 3D cultures for both short- and long-term studies. The few known combined dual stimulation studies such as Lovecchio *et al.* [89], have looked at larger scale bioreactors rather than a BoC platform, or Paggi *et al.* [79] who developed a cartilage-on-chip for chondrocytes without bone. This makes this study a novel BoC development.

Critical Challenges in Hydrogel Stiffness and Porosity Balance

Selecting a hydrogel required balancing stiffness and porosity was needed to optimise cell behaviour and nutrient transport. Adjusting GelMA/HAMA ratios revealed trade-offs between mechanical and biological performance. El-Rashidy *et al.* [345] showed that GelMA that exceeds 14 % w/v produced stiffness of over 110 kPa, exceeded the 25 to 45 kPa range for osteogenesis identified by Engler *et al.* [144], while reduced porosity further limited nutrient diffusion and waste removal [346] . Lower GelMA concentrations (less than 10 % w/v)

preserved porosity for metabolism but compromised structural integrity under loading, where 25 kPa or more stiffness is required [144] [346]. Adding 1 % (v/v) HAMA improved degradability, compressive strength, and stiffness while maintaining porosity similar to 10 % GelMA, offering a better balance than increased GelMA alone [149] [154]. With HAMA, stiffness rose to 30 to 45 kPa (elastic modulus) and compressive strength to 17 to 28 kPa. Porosity (gel fraction %) matched values reported by Velasco-Rodriguez *et al.* [154], and swell ratios were consistent with similar gels in Cinar *et al.* [158], confirming process reproducibility.

Hydrogel and Stimulation Effects

Long-term mechanical stimulation of bone cells requires hydrogels that remain stable for at least 4 weeks. Hydrogel and flow centrifugation studies (Chapters 3, 4) showed that 10 % GelMA 1 % HAMA 1 mm gels had the highest proliferation and osteogenesis and maintained viability for 7 weeks, with stimulated samples lasting longer. In a perfusion flow-based system, this could be due to not adjusting flow rates over time with increased cell population and development. This can cause a decline in cell viability and adversely affect osteogenesis due to nutrient and oxygen gradients limiting proliferation. Hydrogel degradation over time can also cause reduced structural integrity and support for the cells. This exceeds typical *in vitro* periods up to 5 weeks [58] and exceeds longer bone cell studies such as Holy *et al.* for rat osteoblasts on biopolymer scaffolds (6 weeks) [347], enabling extended longitudinal studies. The gels preserved cell viability (Section 3.2 and 3.3) under both hypoxic and normoxic conditions, indicating they can mimic *in vivo*–like low O_2 levels in a standard incubator [231]. Incorporating inorganic ions such as Mg^{2+}, Sr^{2+}, and Zn^{2+}, important for bone growth and metabolism, may further enhance bone culture development [348].

7.1.2 Impact of Mechanical Stimulation: Centrifugation & Perfusion Flow

Bone is a dynamic tissue that constantly adapts to mechanical cues. The mechanical stimulation studies (Chapters 4, 5) examined how centrifuge cyclic loading and perfusion flow shear affect osteoblast behaviour in the developed BoC. A key innovation was creating an *in vitro* platform that integrates hydrogels with native-like mechanical stimuli to better mimic *in vivo* physiology.

Centrifuge and Flow Stimulation Effects

In standard media, osteogenesis and cell proliferation under centrifugation increased by 25 to 40 % vs static culture, comparable to the additional centrifugation effect that increased

proliferation of 30 to 60 % reported by Prodanov *et al.* [276], that applied 10g loading for 1h/daily over 1 week. Flow rates of 50 to 150 µl/min through 1 mm GelMA/HAMA produced shear stresses of 0.15 to 0.45 Pa (Equation 3.4), though it should be considered that this study investigated just a narrow range of flow shear with set applied stimulation, but this could be expanded to further investigate flow and centrifugal loading. Under these shears, the average proliferation and osteogenesis doubled compared to static samples at peak culture, similar to other studies reporting 2.2 to 2.4-fold increases at comparable flows/shears [267] [222]. Flow alone enhanced proliferation and osteogenesis by 60 to 100 % at 3 to 5 weeks, consistent with Kapur *et al.* [349] that applied a higher 0.5 to 2ml/min flow (1 to 2 Pa flow shear) and increased proliferation at least 2-fold and ALP activity 3-fold. Dual (flow and centrifuge) stimulation further increased responses beyond flow alone but with diminishing offset increases, reflecting complex interactions between modalities. Flow and flow-centrifuged samples showed similar peak proliferation/mineralisation at 4 to 5 weeks, whereas dual stimulation at 100 to 150 µl/min yielded higher values at 5 to 7 weeks (Section 4.3). Mid-late-stage culture benefited most, particularly with dual stimulation. Few dual-stimulation studies exist, but Lovecchio *et al.* [89] that applied 1 % compression at 1 Hz for 30 min twice daily plus low-shear 1 ml/min continuous perfusion over 1 week similarly reported a 3-fold increase in osteogenesis vs static controls; however, replication on BoC platforms rather than bioreactors is still needed.

Complex Flow Dynamics and Challenges

The shear stress levels in these tests exceed the mechanotransduction threshold (around 0.01 Pa) for enhanced proliferation without deformation/detachment and the around 0.1 Pa threshold for enhanced osteogenesis [103], thus providing effective stimulation. Beyond conventional mechanotransduction, media flow improves chemotransport of nutrients, signalling factors, oxygen, and waste, which may further promote proliferation and mineralisation [271] [350]. This is particularly beneficial for mature, dense cultures with higher demands for nutrient and waste exchange. Flow shear and chemotransport effects must be distinguished, as in Sikavitsas *et al.* [310], who varied shear by changing media viscosity at constant flow rate and temperature. Enhanced proliferation and development from flow or dual stimulation were partly attributed to increased IGF-I mitogenic signalling and mechanotransduction sensitivity (Kapur *et al.* [349]), alongside mechanotransduction and chemotransport effects [103] [271].

Another explanation for higher assay readings at higher flow rates or with dual stimulation in

later weeks is that ongoing cell proliferation, differentiation, and mineralisation increase bone volume. This changes gel pore size distribution, reduces flow area, and forces fluid through narrower channels, altering shear patterns and potentially increasing shear stress [119]. Higher flow or loading may further drive media through these restricted channels and pores, delaying the peak cell response. This effect was modelled and experimentally shown in 3D porous scaffold rat bone MSC cultures by Williams *et al.* [119].

A challenge with dual-stimulated samples (Section 4.3) is that centrifugal and Coriolis forces generate spiral flow patterns, causing heterogeneous shear stress and uneven cell distributions across wells [286]. This leads to non-uniform osteogenic differentiation, resembling near-surface subchondral bone [351], and requires averaging over many samples. The effect was reduced by using stiffer gels as buffers and a larger spin radius with lower spin rates (100 to 125 RPM) to maintain the same acceleration. These rates were the lowest used by Detzel *et al*., at which the effect first appears and then increases with higher spin speeds [286]. Another challenge is that there is no single optimal flow rate or shear level; the ideal treatment depends on whether proliferation, differentiation, or further mineralisation is prioritised [103][352]. Different flow rates, profiles, and regimens may be required at different culture stages, as higher or longer shear does not necessarily improve outcomes [352] [353]. Future studies could define optimal stimulation modes, magnitudes, and profiles for each culture stage to develop an integrated mechanical stimulation strategy for the entire culture lifecycle.

Enhanced Effects with CellShip Media

This study on cell responses to mechanical stimulation was extended by optimising media. CellShip, a cell preservation and protectant agent, was added at an optimal concentration to assess its effects on bone cell proliferation and osteogenesis under mechanical or flow shear stimulation and as a thermal buffer during out-of-incubator stimulation. In Section 5.3.2, 10 % (w/v) CellShip increased bone proliferation and mineralisation by 15 % alone and by 35 to 55 % with centrifugation (rising with g-level). In flow experiments (Section 5.3.3), mid-culture CellShip further enhanced proliferation and osteogenesis by 30 % beyond the 50 to 70 % increase from flow in standard media vs static controls, for a total 65 to 100 % improvement. Combined flow and centrifugation produced similar gains after mineralisation onset (2 weeks), with the strongest CellShip effects at 100 to 150 µl/min, yielding a 2 to 3-fold increase in osteogenesis vs static samples at 5 to 7 weeks, an additional 40 to 50 % over standard media

(Section 5.3.4). With this supplement, BoC samples tolerated greater stress and longer out-of-incubator times during stimulation. Using insulative holders during centrifugation or preventing chip contact with cold surfaces in culture hoods further reduced thermal stress. Out-of-incubation periods were limited to 1 h because bone cells were used without additional HEPES buffering [354]. CellShip may also have acted as a metabolic buffer in later culture (5 to 7 weeks), especially in higher-flow, dual-stimulated samples where media flow may be constricted if gel pores narrow due to excess bone growth and shear redistribution [119]. CellShip also buffers excess shear with some Genipin like properties, a natural cross-linker and membrane protectant that reduces membrane permeation under flow shear and is anti-inflammatory during cell stress [355] [356] [357]. Another possible mechanism from CellShip is that as a cell protectant it converts cells to a protective G0 quiescent cell state [277], particularly during stress or mechanical stimulation that also explains larger increases in osteogenesis versus cell proliferation for more mechanically stimulated samples when leaving this state compared to static controls [277] [278][306]. These BoC cell responses were observable for whole culture period overall but particularly during later weeks.

7.1.3 Machine Learning Applications and Modelling Opportunities

Applying ML to predict and optimise BoC cell cultures enables modelling complex links between diverse culture and mechanical stimulation conditions. Traditional models are too simplistic for high-dimensional, mixed-format, non-linear data, so classical ML and DL models were used instead. Ensemble models such as Random Forest performed best, with the highest R^2 and lowest error. These predictive models can guide further optimisation of BoC cultures.

Application of ML to BoC Platform

Evaluating ML algorithms such as SVR, Random Forests, XGBoost, LGBM, and CNNs provides key methodological insights for computational biology. This study tested their suitability for datasets of different sizes and complexity. For multivariable tabular datasets with fewer than 1,000 data points, typical in bone tissue research, classical ML models that capture linear and non-linear relationships are particularly effective, whereas CNNs are generally limited at this scale [191] [192] [343]. On the core dataset, ensemble regression models performed best, achieving R^2 scores of 0.8 to 0.9 depending on the output assay type (Section

6.5.1). Although such models can overfit and generalise poorly, repeated k-fold cross-validation was used to reduce this risk [358]. Random Forest consistently achieved the highest R^2 and lowest error, while gradient boosting ensembles (XGBoost) delivered similar accuracy, underscoring the value of ensemble ML for low-volume cell culture data [359]. XGBoost, an iteratively improving tree-based model, is suitable as it can handle missing data and includes strong regularisation [194].

Bayesian optimisation also outperformed random search for nearly all models (except SVR). Bayesian optimisation offers superior hyperparameter tuning compared with grid or random search [210]. Model performance showed a strong inverse correlation between R^2 and error metrics (Section 6.5) with higher R^2 occurring with lower MAE, MSE, and MAPE. Ensemble models like Random Forest are directly interpretable, allowing feature importance analysis without additional explainable AI methods [338] and enabling quantitative comparison of each input feature's effect on bone cell responses. This study further verified this. Designing an optimal ML model for mixed-format cell culture data that supports tissue modelling, interpretability, and culture optimisation is a novel application.

Deep learning models had lower regression R^2 than classical ML models, even with the expanded dataset (Section 6.5.2). Among ANN, DNN (single hidden layer), CNN, and Randomised NN, Randomised NN performed best. Its top model reached $R^2 \approx 0.7$ across outputs and $R^2 = 0.77$ for direct ViaFluor fluorescence (proliferation) using only 500 training instances (after train–test split). As with other models, higher R^2 corresponded to lower error. Randomised NN was also the most efficient, training about twice as fast as other deep learning models due to fewer parameters and dropped hidden nodes during training [199]. Although its R^2 remained below that of classical models (Section 6.5.1), Randomised NN may generalise better with more data (experimental or synthetic), improved architectures, and deep optimisation.

In Section 6.5.3, LIME and SHAP were evaluated for explainability. SHAP was more interpretable, explained more variance, and partially aligned with experiment results (Section 4.3 and 5.3). For flow stimulation, SHAP similarly showed around a 2.5× larger effect than centrifugation on cell proliferation and osteogenesis. It also ranked media with(out) 10 % CellShip as less influential than flow stimulation, consistent with mechanical stimulation experiments, but also ranked it less influential than centrifugation (Section 6.5.3).

7.2 Concluding Remarks

A BoC platform capable of providing combined sequential (not simultaneous) multimodal mechanical stimulation through centrifuge cyclic loading and flow shear was developed. This was the first multi-modal dual stimulation BoC that could also be used for longitudinal (over 7 weeks) 3D culture studies as well the first application of ML and deep learning regression models to microfluidic BoC platforms. An optimised GelMA/HAMA hydrogel was incorporated into the BoC platform to create a biomimetic 3D culture environment. Iterative design, fabrication, testing and cell culture produced a validated 3D BoC system suitable for longitudinal studies (over 4 weeks).

Flow or centrifuge stimulation alone increased MC3T3 bone cell activity, proliferation, and osteogenic development, consistent with prior reports. Proliferation and osteogenesis generally peaked at 4 weeks, with less variation in stimulated samples. Dual stimulation further enhanced mechanotransduction, particularly at 5 to 7 weeks, and it also delayed both the peak and decline in proliferation and osteogenesis. Across all flow shear and dual stimulation tests, no single stimulation level was optimal over the entire culture period. Lower flow shear favoured proliferation (especially for early to mid-culture), while higher flow shear or stimulation favoured osteogenesis (especially for late culture).

CellShip supplemented media improved cell responses to stimulation, extended viability outside incubation and increased experimental flexibility. Optimal outcomes were achieved using daily centrifugation (1 g, 1 h) with mid–high flow shear and 10 % CellShip supplementation, peaking at 4 to 5 weeks and yielding maximal proliferation and osteogenesis at 5 to 7 weeks compared to other treatments. For cell proliferation and osteogenesis, flow shear had a large, highly significant effect, CellShip had a moderate significant effect (more so for osteogenesis), and centrifugation had a moderate significant effect on both.

ML regression, especially ensemble methods (Random Forest, then XGBoost), accurately predicted outputs and improved with Bayesian optimisation. Simple deep learning trained on extended data had lower R^2 model fitting due to limited data, although a randomised DL model was best among DL approaches and may improve with more lab or synthetic data. SHAP analysis of this model ranked flow, then centrifugation, and then media as most influential on cell metabolic activity, proliferation and osteogenesis, differing from experiments where media interaction was the second-largest effect after flow. This work shows the value and potential of ML for bone tissue engineering applications.

7.3 Future Research Directions

Material Development: GelMA/HAMA hydrogels with further tuneable properties for different culture stages is a development opportunity. Hydrogel stiffness could be precisely adjusted for specific bone cell culture phases, and incorporating additional bone growth factors or materials into composite GelMA/HAMA hydrogels may further enhance bone growth and development. These hydrogels could be further optimised for other tissues such as cartilage.

Stimulation Patterns: Temporal aspects of combined stimulation require careful control [90] [352]. The study showed that the timing and order of centrifugal and flow stimulation strongly influence cellular responses. Selecting pulsatile, intermittent, steady, or combined loading profiles is crucial, as intermittent loading is more osteogenic than continuous loading [280]. The daily regimen - sequence, duration, and the interval between centrifugation and flow shear may affect cell signalling and tissue development [280]. A dedicated study could identify optimal load flow shear levels and regimen for each culture stage, using a multi-stage strategy that first promotes proliferation, then differentiation and mineralisation for osteogenesis. The combined effects of optimal mechanical stimulation and CellShip in extending bone cell culture viability allow longer (over 7 weeks) BoC studies on long-term outcomes. Future work could repeat BoC mechanical stimulation experiments with additional temperature variations to distinguish CellShip and thermal effects. Separate tests could vary flow shear by altering media viscosity (e.g. dextran addition) at constant flow rate
and temperature, as investigated by Sikavitsas *et al.* [310], to further separate mechanical/flow shear and chemotransport effects.

Integrated Sensing and Control: Advancing real-time monitoring and control is a key research priority. Microfluidic platforms will gain continuous cellular response monitoring by integrating optical, electrical, and mechanical sensors that enable real-time adjustment of experimental conditions. Calibrating continuous monitoring systems such as CellCyte scanners for quantified fluorescence against assay readings could support more frequent or continuous data collection. Further development of custom chip holders for direct chip readings in assay readers, CellCyte scanners, or similar devices would facilitate large-scale BoC data generation. ML algorithms

could be developed and integrated into real-time control systems (closed loop control) to adapt mechanical stimulation based on culture stage and measured growth, activity, or development.

ML Modelling: Future research should apply advanced deep learning, deep optimisation and explainable AI to expanded BoC datasets, combining them with synthesis methods based on known distributions (Section 6.2) to compare performance on real vs synthetic data and to further validate ensemble models. CNN transfer learning is promising for tissue engineering regression with high-resolution time-series data by fine-tuning pre-trained networks on small, related lab datasets as presented by Hosna *et al.* [360]. Gaussian Process Regression (GPR) can enhance experimental design and optimisation by providing predictions with uncertainty estimates [361] and supporting optimisation under constrained experimental combinations [362]. Deep temporal models (e.g., recurrent or transformer architectures for time series longitudinal biomedical data [363],[364]) could capture more dynamic osteoblast behaviour. Integrating scaled-up data from repeated experiments and multimodal data (e.g., gene expression, other osteogenic biomarkers) should improve the data's biological relevance.

Development Translation Pathways: A more realistic *in vitro* model has been developed and is a potential alternative to animal testing with further future development. Chapter 3 demonstrated basic reusability through viability testing in microfluidic BoCs (with up to three uses). These chips' microfluidic layers could be evaluated for longer-term reuse and more extended studies, reducing per-use costs in pre-clinical R&D. Future work could add cell types such as cartilage and fibroblasts to create a multicellular bilayer JoC system. The methods and concepts from this study will support developing bone and joint tissue models to improve understanding and treatment of bone or joint-related diseases.

References

[1] J. A. Kanis *et al.*, “SCOPE 2021: a new scorecard for osteoporosis in Europe”, doi: 10.1007/s11657-020-00871-9/Published.

[2] S. Subramanian, C. Anastasopoulou, and V. K. Viswanathan, “Osteogenesis Imperfecta,” *StatPearls*, Feb. 2023, Accessed: Nov. 29, 2025. [Online]. Available: https://www.ncbi.nlm.nih.gov/books/NBK536957/

[3] N. M. Appelman-Dijkstra and S. E. Papapoulos, “Paget’s disease of bone,” *Best Pract Res Clin Endocrinol Metab*, vol. 32, no. 5, pp. 657–668, Oct. 2018, doi: 10.1016/J.BEEM.2018.05.005.

[4] X. Feng and J. M. McDonald, “Disorders of Bone Remodeling,” *Annu Rev Pathol*, vol. 6, p. 121, Feb. 2011, doi: 10.1146/ANNUREV-PATHOL-011110-130203.

[5] “Osteoarthritis.” Accessed: Jul. 26, 2025. [Online]. Available: https://www.who.int/news-room/fact-sheets/detail/osteoarthritis

[6] “Rheumatoid arthritis.” Accessed: Jul. 26, 2025. [Online]. Available: https://www.who.int/news-room/fact-sheets/detail/rheumatoid-arthritis

[7] Y. Shen *et al.*, “The Global Burden of Osteoporosis, Low Bone Mass, and Its Related Fracture in 204 Countries and Territories, 1990-2019,” *Front Endocrinol (Lausanne)*, vol. 13, p. 882241, May 2022, doi: 10.3389/FENDO.2022.882241/FULL.

[8] D. M. Findlay and J. S. Kuliwaba, “Bone-cartilage crosstalk: a conversation for understanding osteoarthritis.,” *Bone Res*, vol. 4, no. 1, Sep. 2016, doi: 10.1038/boneres.2016.28.

[9] F. E. Watt and M. Gulati, “Europe PMC Funders Group New Drug Treatments for Osteoarthritis : What is on the Horizon ?,” vol. 2, no. 1, pp. 50–58, 2018.

[10] K. Duval *et al.*, “Modeling Physiological Events in 2D vs. 3D Cell Culture,” *Physiology*, vol. 32, no. 4, pp. 266–277, 2017, doi: 10.1152/physiol.00036.2016.

[11] D. Huh, G. A. Hamilton, and D. E. Ingber, “From 3D cell culture to organs-on-chips,” *Trends Cell Biol*, vol. 21, no. 12, pp. 745–754, 2011, doi: 10.1016/j.tcb.2011.09.005.

[12] O. Curtis, “Animal testing alternatives via OoC,” *Lab Chip*, 2020, doi: 10.1039/D0LC01124J.

[13] L. Breitwieser and S. Huber, “Joint-on-chip (JoC) modelling,” *Nat Protoc*, 2022, doi: 10.1038/s41596-022-00705-7.

[14] E. A. Galan, H. Zhao, X. Wang, Q. Dai, W. T. S. Huck, and S. Ma, “Intelligent Microfluidics: The Convergence of Machine Learning and Microfluidics in Materials Science and Biomedicine,” *Matter*, vol. 3, no. 6, pp. 1893–1922, 2020, doi: 10.1016/j.matt.2020.08.034.

[15] C. Xu and S. A. Jackson, “Machine learning and complex biological data The revolution of biological techniques and demands for new data mining methods,” *Genome Biol*, vol. 20, no. 76, pp. 1–4, 2019, [Online]. Available: https://doi.org/10.1186/s13059-019-1689-0

[16] V. Šromová, D. Sobola, and P. Kaspar, “A Brief Review of Bone Cell Function and Importance,” *Cells*, vol. 12, no. 21, p. 2576, Nov. 2023, doi: 10.3390/CELLS12212576.

[17] T. Takano-Yamamoto, “Osteocyte function under compressive mechanical force,” *Japanese Dental Science Review*, vol. 50, no. 2, pp. 29–39, May 2014, doi: 10.1016/J.JDSR.2013.10.004.

[18] O. Verborgt, G. J. Gibson, and M. B. Schaffler, “Loss of osteocyte integrity in association with microdamage and bone remodeling after fatigue in vivo,” *Journal of Bone and Mineral Research*, vol. 15, no. 1, pp. 60–67, 2000, doi: 10.1359/JBMR.2000.15.1.60.

[19] R. Zhou *et al.*, “Endocrine role of bone in the regulation of energy metabolism,” *Bone Research 2021 9:1*, vol. 9, no. 1, pp. 25-, May 2021, doi: 10.1038/s41413-021-00142-4.

[20] R. Florencio-Silva, G. R. D. S. Sasso, E. Sasso-Cerri, M. J. Simões, and P. S. Cerri, “Biology of Bone Tissue: Structure, Function, and Factors That Influence Bone Cells,” *Biomed Res Int*, vol. 2015, p. 421746, 2015, doi: 10.1155/2015/421746.

[21] N. H. Hart *et al.*, “Biological basis of bone strength: anatomy, physiology and measurement,” *J Musculoskelet Neuronal Interact*, vol. 20, no. 3, p. 347, Sep. 2020,

Accessed: Nov. 29, 2025. [Online]. Available: https://pmc.ncbi.nlm.nih.gov/articles/PMC7493450/

[22] S. Sieber, R. Lauster, and M. Koenigsmark, “Bone marrow - on - a - chip : Long - term culture of human haematopoietic stem cells in a three - dimensional microfluidic environment”, doi: 10.1002/term.2507.

[23] S. A. Höger, T. Cong, A. J. Hall, J. Lane, and A. Runer, “Subchondral bone contribution to osteochondral health and injury,” *Ann Jt*, vol. 10, no. 0, Jul. 2025, doi: 10.21037/AOJ-25-12/COIF.

[24] G. Liu *et al.*, “3D printed osteochondral scaffolds: design strategies, present applications and future perspectives,” *Front Bioeng Biotechnol*, vol. 12, p. 1339916, Feb. 2024, doi: 10.3389/FBIOE.2024.1339916/FULL.

[25] H. Madry, C. N. van Dijk, and M. Mueller-Gerbl, “The basic science of the subchondral bone,” *Knee Surgery, Sports Traumatology, Arthroscopy*, vol. 18, no. 4, pp. 419–433, Apr. 2010, doi: 10.1007/S00167-010-1054-Z/METRICS.

[26] Y. Wang, L. Wei, L. Zeng, D. He, and X. Wei, “Nutrition and degeneration of articular cartilage,” *Knee Surgery, Sports Traumatology, Arthroscopy*, vol. 21, no. 8, p. 1751, Aug. 2012, doi: 10.1007/S00167-012-1977-7.

[27] N. Mathavan and O. D. Kennedy, “Skeletal Changes Associated with Osteoarthritis,” *Clin Rev Bone Miner Metab*, vol. 17, no. 3–4, pp. 123–137, Dec. 2019, doi: 10.1007/S12018-019-09264-0/METRICS.

[28] M. Rauner, H. Taipaleenmäki, E. Tsourdi, and E. M. Winter, “Osteoporosis Treatment with Anti-Sclerostin Antibodies-Mechanisms of Action and Clinical Application.,” *J Clin Med*, vol. 10, no. 4, p. 787, Feb. 2021, doi: 10.3390/jcm10040787.

[29] D. C. Bury, T. S. Rogers, and M. M. Dickman, “Osteomyelitis: Diagnosis and Treatment,” *Am Fam Physician*, vol. 104, no. 4, pp. 395–402, Oct. 2021, Accessed: Nov. 29, 2025. [Online]. Available: https://www.aafp.org/pubs/afp/issues/2021/1000/p395.html

[30] B. S. Komm *et al.*, “Estrogen binding, receptor mRNA, and biologic response in osteoblast-like osteosarcoma cells,” *Science (1979)*, vol. 241, no. 4861, pp. 81–84, 1988, doi: 10.1126/SCIENCE.3164526.

[31] X. Zhu, Y. T. Chan, R. S. Tuan, P. S. H. Yung, and Y. Jiang, “Subchondral Bone Remodeling: A Therapeutic Target for Osteoarthritis.,” *Front Cell Dev Biol*, vol. 8, Jan. 2021, doi: 10.3389/fcell.2020.607764.

[32] W. Hu, Y. Chen, C. Dou, and S. Dong, “Microenvironment in subchondral bone: predominant regulator for the treatment of osteoarthritis,” *Ann Rheum Dis*, vol. 80, no. 4, pp. 413–422, Nov. 2020, doi: 10.1136/annrheumdis-2020-218089.

[33] T. Adachi, M. Hojo, and Y. Kameo, “Trabecular bone remodelling simulation considering osteocytic response to fluid-induced shear stress,” *Philosophical Transactions of the Royal Society A: Mathematical, Physical and Engineering Sciences*, vol. 368, no. 1920, pp. 2669–2682, Jun. 2010, doi: 10.1098/rsta.2010.0073.

[34] S. R. Goldring and M. B. Goldring, “Changes in the osteochondral unit during osteoarthritis: structure, function and cartilage-bone crosstalk,” *Nat Rev Rheumatol*, vol. 12, no. 11, pp. 632–644, 2016, doi: 10.1038/nrrheum.2016.148.

[35] N. Sahin and H. Yesil, “Regenerative methods in osteoarthritis,” *Best Pract Res Clin Rheumatol*, no. xxxx, p. 101824, 2023, doi: 10.1016/j.berh.2023.101824.

[36] K. S. Upchurch and J. Kay, “Evolution of treatment for rheumatoid arthritis,” *Rheumatology (United Kingdom)*, vol. 51, no. SUPPL. 6, Dec. 2012, doi: 10.1093/rheumatology/kes278.

[37] S. Ryan, A. Baird, G. Vaz, and A. Urquhart, “Drug Discovery Approaches Utilizing Three-Dimensional Cell Culture,” pp. 1–11, 2016, doi: 10.1089/adt.2015.670.

[38] M. Kapałczyńska *et al.*, “2D and 3D cell cultures – a comparison of different types of cancer cell cultures,” *Archives of Medical Science*, vol. 14, no. 4, pp. 910–919, 2018, doi: 10.5114/aoms.2016.63743.

[39] S. Knecht, B. Vanwanseele, and E. Stu, “A review on the mechanical quality of articular cartilage – Implications for the diagnosis of osteoarthritis,” vol. 21, pp. 999–1012, 2006, doi: 10.1016/j.clinbiomech.2006.07.001.

[40] A. Cacciamali, R. Villa, and S. Dotti, “3D Cell Cultures: Evolution of an Ancient Tool for New Applications,” *Front Physiol*, vol. 13, p. 836480, Jul. 2022, doi: 10.3389/FPHYS.2022.836480.

[41] J. Kim and B. Koo, “Human organoids: model systems for human biology and medicine,” *Nat Rev Mol Cell Biol*, doi: 10.1038/s41580-020-0259-3.

[42] S. Campuzano and A. E. Pelling, “Scaffolds for 3D Cell Culture and Cellular Agriculture Applications Derived From Non-animal Sources,” *Front Sustain Food Syst*, vol. 3, no. May, pp. 1–9, 2019, doi: 10.3389/fsufs.2019.00038.

[43] M. Hofer and M. P. Lutolf, “Engineering organoids,” *Nat Rev Mater*, vol. 6, no. 5, pp. 402–420, 2021, doi: 10.1038/s41578-021-00279-y.

[44] R. M. Owens, “Advanced tissue engineering for in vitro drug safety testing,” *MRS Communications 2023 13:5*, vol. 13, no. 5, pp. 685–694, Aug. 2023, doi: 10.1557/S43579-023-00421-7.

[45] C. Arrigoni, S. Lopa, C. Candrian, and M. Moretti, “Organs-on-a-chip as model systems for multifactorial musculoskeletal diseases,” *Curr Opin Biotechnol*, vol. 63, pp. 79–88, Jun. 2020, doi: 10.1016/j.copbio.2019.12.006.

[46] W. J. Polacheck, R. Li, S. G. M. Uzel, and R. D. Kamm, “Microfluidic platforms for mechanobiology,” *Lab Chip*, vol. 13, no. 12, pp. 2252–2267, May 2013, doi: 10.1039/C3LC41393D.

[47] Z. Liu, Q. Wang, J. Zhang, S. Qi, Y. Duan, and C. Li, “The Mechanotransduction Signaling Pathways in the Regulation of Osteogenesis,” *International Journal of Molecular Sciences 2023, Vol. 24, Page 14326*, vol. 24, no. 18, p. 14326, Sep. 2023, doi: 10.3390/IJMS241814326.

[48] E. E. Golub and K. Boesze-Battaglia, “The role of alkaline phosphatase in mineralization,” *Curr Opin Orthop*, vol. 18, no. 5, pp. 444–448, 2007.

[49] J. White and E. Brown, “Alkaline phosphatase as a bone formation marker,” *Arch Biochem Biophys*, 2018, doi: 10.1016/j.abb.2018.04.002.

[50] J. U. A. Choi, A. W. Kijas, J. Lauko, and A. E. Rowan, “The Mechanosensory Role of Osteocytes and Implications for Bone Health and Disease States,” *Front Cell Dev Biol*, vol. 9, p. 770143, Feb. 2022, doi: 10.3389/FCELL.2021.770143/XML/NLM.

[51] N. Zuela-Sopilniak and J. Lammerding, “Can’t handle the stress? Mechanobiology and disease,” *Trends Mol Med*, vol. 28, no. 9, pp. 710–725, Sep. 2022, doi: 10.1016/J.MOLMED.2022.05.010.

[52] T. Hodgkinson, I. N. Amado, F. J. O’Brien, and O. D. Kennedy, “The role of mechanobiology in bone and cartilage model systems in characterizing initiation and progression of osteoarthritis,” *APL Bioeng*, vol. 6, no. 1, Mar. 2022, doi: 10.1063/5.0068277/2820313.

[53] F. Martino, A. R. Perestrelo, V. Vinarský, S. Pagliari, and G. Forte, “Cellular Mechanotransduction: From Tension to Function,” *Front Physiol*, vol. 9, no. JUL, p. 824, Jul. 2018, doi: 10.3389/FPHYS.2018.00824.

[54] F. Padilla, R. Puts, L. Vico, and K. Raum, “Stimulation of bone repair with ultrasound: A review of the possible mechanic effects,” *Ultrasonics*, vol. 54, no. 5, pp. 1125–1145, Jul. 2014, doi: 10.1016/J.ULTRAS.2014.01.004.

[55] C. H. Lohmann *et al.*, “Pulsed electromagnetic field stimulation of MG63 osteoblast-like cells affects differentiation and local factor production,” *Journal of Orthopaedic Research*, vol. 18, no. 4, pp. 637–646, Jul. 2000, doi: 10.1002/JOR.1100180417.

[56] T. Stuart, “Cell membrane mechanoreceptors in bone,” *Biomaterials*, 2019, doi: 10.1016/j.biomaterials.2019.119547.

[57] Y. Hu *et al.*, “Bone/cartilage organoid on-chip: Construction strategy and application,” *Bioact Mater*, vol. 25, no. January, pp. 29–41, 2023, doi: 10.1016/j.bioactmat.2023.01.016.

[58] D. Mitra, J. Whitehead, O. W. Yasui, and J. K. Leach, “Bioreactor Culture Duration of Engineered Constructs Influences Bone Formation by Mesenchymal Stem Cells,”

Biomaterials, vol. 146, p. 29, Nov. 2017, doi: 10.1016/J.BIOMATERIALS.2017.08.044.

[59] C. M. Leung *et al.*, "A guide to the organ-on-a-chip," *Nature Reviews Methods Primers*, vol. 2, no. 1, 2022, doi: 10.1038/s43586-022-00118-6.

[60] Elveflow, "A review about organ-on-chips." Accessed: Jan. 02, 2022. [Online]. Available: https://www.elveflow.com/microfluidic-reviews/organs-on-chip-3d-cell-culture/a-review-about-organ-on-chip/

[61] Catapult Medical Discovery, "Organ-On-A-Chip Technologies (OOAC): Current status and translatability of data," Liverpool, Manchester, 2018.

[62] A. Delaquilla, "History of Microfluidics," *Elveflow*, Elvesys, Feb. 05, 2021. Accessed: Nov. 29, 2025. [Online]. Available: https://elveflow.com/microfluidic-reviews/history-of-microfluidics/

[63] T. C. Cameron *et al.*, "PDMS Organ-On-Chip Design and Fabrication: Strategies for Improving Fluidic Integration and Chip Robustness of Rapidly Prototyped Microfluidic In Vitro Models," *Micromachines (Basel)*, vol. 13, no. 10, p. 1573, Oct. 2022, doi: 10.3390/MI13101573/S1.

[64] F. Yu, W. Hunziker, and D. Choudhury, "Engineering microfluidic organoid-on-a-chip platforms," *Micromachines (Basel)*, vol. 10, no. 3, pp. 1–12, 2019, doi: 10.3390/mi10030165.

[65] Y. Huang, S. Liu, W. Yang, and C. Yu, "Surface roughness analysis and improvement of PMMA-based microfluidic chip chambers by CO 2 laser cutting," *Appl Surf Sci*, vol. 256, no. 6, pp. 1675–1678, Jan. 2010, doi: 10.1016/J.APSUSC.2009.09.092.

[66] M. A. M. Ahmed, K. M. Jurczak, N. S. Lynn, J. P. S. H. Mulder, E. M. J. Verpoorte, and A. Nagelkerke, "Rapid prototyping of PMMA-based microfluidic spheroid-on-a-chip models using micromilling and vapour-assisted thermal bonding," *Sci Rep*, vol. 14, no. 1, pp. 1–14, Dec. 2024, doi: 10.1038/S41598-024-53266-Y;SUBJMETA=166,631,639,67,70,985;KWRD=BIOMEDICAL+ENGINEERING,CANCER+MODELS.

[67] L. Osborne, “Soft lithography alternatives for OoC,” *Lab Chip*, 2019, doi: 10.1039/C9LC00608D.

[68] “Choosing the Right Microfluidic Chip: Materials, Fabrication, and Cost - Conduct Science.” Accessed: Dec. 06, 2025. [Online]. Available: https://conductscience.com/choosing-the-right-microfluidic-chip-materials-fabrication-and-cost-copy/

[69] L. Banh, K. K. Cheung, M. W. Y. Chan, E. W. K. Young, and S. Viswanathan, “Advances in organ-on-a-chip systems for modelling joint tissue and osteoarthritic diseases,” *Osteoarthritis Cartilage*, vol. 30, no. 8, pp. 1050–1061, Aug. 2022, doi: 10.1016/j.joca.2022.03.012.

[70] M. Culebras, C. J. Grande, F. G. Torres, O. P. Troncoso, C. M. Gomez, and M. C. Bañó, “Optimization of Cell Growth on Bacterial Cellulose by Adsorption of Collagen and Poly-L-Lysine,” *International Journal of Polymeric Materials and Polymeric Biomaterials*, vol. 64, no. 8, pp. 411–415, Jan. 2015, doi: 10.1080/00914037.2014.958829.

[71] C. Jensen and Y. Teng, “Is It Time to Start Transitioning From 2D to 3D Cell Culture?,” *Front Mol Biosci*, vol. 7, p. 33, 2020, doi: 10.3389/fmolb.2020.00033.

[72] S. Schneider, F. Erdemann, O. Schneider, T. Hutschalik, and P. Loskill, “Organ-on-a-disc: A platform technology for the centrifugal generation and culture of microphysiological 3D cell constructs amenable for automation and parallelization,” *APL Bioeng*, vol. 4, no. 4, p. 046101, Dec. 2020, doi: 10.1063/5.0019766.

[73] M. Tang, G. Wang, S. K. Kong, and H. P. Ho, “A review of biomedical centrifugal microfluidic platforms,” *Micromachines (Basel)*, vol. 7, no. 2, 2016, doi: 10.3390/MI7020026.

[74] M. Aliabouzar, S. J. Lee, X. Zhou, G. L. Zhang, and K. Sarkar, “Effects of scaffold microstructure and low intensity pulsed ultrasound on chondrogenic differentiation of human mesenchymal stem cells,” *Biotechnol Bioeng*, vol. 115, no. 2, pp. 495–506, Feb. 2018, doi: 10.1002/BIT.26480;ISSUE:ISSUE:DOI.

[75] A. K. Gupta, K. P. Srivastava, and S. Avasthi, “Pulsed electromagnetic stimulation in nonunion of tibial diaphyseal fractures.,” *Indian J Orthop*, vol. 43, no. 2, p. 156, Jan. 2009, doi: 10.4103/0019-5413.50850.

[76] H. Y. Lin and Y. J. Lin, “In vitro effects of low frequency electromagnetic fields on osteoblast proliferation and maturation in an inflammatory environment,” *Bioelectromagnetics*, vol. 32, no. 7, pp. 552–560, Oct. 2011, doi: 10.1002/BEM.20668;WGROUP:STRING:PUBLICATION.

[77] D. H. Shin and J. H. Cho, “Piezoelectric Actuator with Frequency Characteristics for a Middle-Ear Implant,” *Sensors 2018, Vol. 18, Page 1694*, vol. 18, no. 6, p. 1694, May 2018, doi: 10.3390/S18061694.

[78] S. R. Shahmoradi *et al.*, “Induction of Chondrogenic Differentiation in Human Mesenchymal Stem Cells Cultured on Human Demineralized Bone Matrix Scaffold under Hydrostatic Pressure,” *Tissue Eng Regen Med*, vol. 16, no. 1, p. 69, Feb. 2018, doi: 10.1007/S13770-018-0164-4.

[79] C. Paggi, B. Venzac, J. Leijten, L. M. Teixeira Leijten, S. Le gac, and M. Karperien, “Cartilage-on-chip: a multi-modal platform to study human chondrocyte’s response to mechanical stimuli,” *Osteoarthritis Cartilage*, vol. 28, no. 2020, pp. S176–S177, 2020, doi: 10.1016/j.joca.2020.02.287.

[80] L. Banh # †, K. K. Cheung, M. W. Y. Chan # †, E. W. K. Young, S. Viswanathan # †, and M. W. Y. Chan, “Corrigendum to ‘Advances in organ-on-a-chip systems for modelling joint tissue and osteoarthritic diseases’ Osteoarthritis Cartilage 30 (2022) 1050-1061,” *Osteoarthritis Cartilage*, vol. 32, pp. 966–967, 2024, doi: 10.1016/j.joca.2024.04.005.

[81] D. Lee, A. Erickson, T. You, A. T. Dudley, and S. Ryu, “Pneumatic microfluidic cell compression device for high-throughput study of chondrocyte mechanobiology,” *Lab Chip*, vol. 18, no. 14, pp. 2077–2086, Jul. 2018, doi: 10.1039/C8LC00320C.

[82] P. Occhetta *et al.*, “Hyperphysiological compression of articular cartilage induces an osteoarthritic phenotype in a cartilage-on-a-chip model,” *Nat Biomed Eng*, vol. 3, no. 7, pp. 545–557, 2019, doi: 10.1038/s41551-019-0406-3.

[83] H. Lin, T. P. Lozito, P. G. Alexander, R. Gottardi, and R. S. Tuan, “Stem Cell-Based Microphysiological Osteochondral System to Model Tissue Response to Interleukin-1β,” *Mol Pharm*, vol. 11, no. 7, pp. 2203–2212, Jul. 2014, doi: 10.1021/MP500136B.

[84] Z. Lin *et al.*, “Osteochondral Tissue Chip Derived From iPSCs: Modeling OA Pathologies and Testing Drugs,” *Front Bioeng Biotechnol*, vol. 7, p. 493543, Dec. 2019, doi: 10.3389/FBIOE.2019.00411/BIBTEX.

[85] “ORGAN CHIP TO MODEL MAMMALIAN JOINT - University of Pittsburgh - Of the Commonwealth System of Higher Education.” Accessed: Dec. 06, 2025. [Online]. Available: https://www.freepatentsonline.com/y2019/0276784.html

[86] C. Mondadori *et al.*, “Recapitulating monocyte extravasation to the synovium in an organotypic microfluidic model of the articular joint,” *Biofabrication*, vol. 13, no. 4, 2021, doi: 10.1088/1758-5090/ac0c5e.

[87] B. G. Kim, J. H. Kwag, H. S. Kim, K. H. Kim, and C. H. Kim, “Bone cell response to fluid shear stress and cyclic compressive strain in 3D trabecular bone,” *Tissue Eng Regen Med*, vol. 6, no. 4–11, pp. 540–548, 2009, Accessed: Dec. 08, 2025. [Online]. Available: https://yonsei.elsevierpure.com/en/publications/bone-cell-response-to-fluid-shear-stress-and-cyclic-compressive-s/

[88] K. A. J. Middleton, Y. H. Vivian Ma, and L. You, “Measuring Bone Cell Response to Fluid Shear Stress and Hydrostatic/Dynamic Pressure,” *Experimental Methods in Orthopaedic Biomechanics*, pp. 217–232, Jan. 2017, doi: 10.1016/B978-0-12-803802-4.00014-7.

[89] J. Lovecchio, P. Gargiulo, J. L. Vargas Luna, E. Giordano, and Ó. E. Sigurjónsson, “A standalone bioreactor system to deliver compressive load under perfusion flow to hBMSC-seeded 3D chitosan-graphene templates,” *Scientific Reports 2019 9:1*, vol. 9, no. 1, pp. 16854-, Nov. 2019, doi: 10.1038/s41598-019-53319-7.

[90] E. Stavenschi, M. N. Labour, and D. A. Hoey, “Oscillatory fluid flow induces the osteogenic lineage commitment of mesenchymal stem cells: The effect of shear stress magnitude, frequency, and duration,” *J Biomech*, vol. 55, pp. 99–106, Apr. 2017, doi: 10.1016/J.JBIOMECH.2017.02.002.

[91] A. Carriero, I. Jonkers, and S. J. Shefelbine, “Mechanobiological prediction of proximal femoral deformities in children with cerebral palsy,” *Comput Methods Biomech Biomed Engin*, vol. 14, no. 3, pp. 253–262, 2011, doi: 10.1080/10255841003682505.

[92] P. Crowell, A. Boynton, and M. Mungiole, “Exoskeleton Power and Torque Requirements Based on Human Biomechanics”.

[93] W. D. Rindt *et al.*, “A 3D bioreactor model to study osteocyte differentiation and mechanobiology under perfusion and compressive mechanical loading,” *Acta Biomater*, vol. 184, pp. 210–225, Aug. 2024, doi: 10.1016/J.ACTBIO.2024.06.041.

[94] D. Harris and M. Brown, “Centrifuge-based force application in microfluidics,” *Lab Chip*, 2022, doi: 10.1039/D1LC00876K.

[95] J. J. Franco, T. Nagata, T. Okamoto, and S. Mukai, “An ultralow-cost portable centrifuge from discarded materials for medical applications,” *Scientific Reports 2023 13:1*, vol. 13, no. 1, pp. 3081-, Feb. 2023, doi: 10.1038/s41598-023-30327-2.

[96] G. Green, “Microfluidic pumping systems for organ-on-chip applications,” *Lab Chip*, 2018, doi: 10.1039/C8LC00934H.

[97] Fluigent, “Microfluidics definitions and advantages.” Accessed: Nov. 02, 2021. [Online]. Available: https://www.fluigent.com/resources-support/expertise/expertise-reviews/what-is-microfluidics/microfluidics-definitions-and-advantages/

[98] S. Morgan, “Syringe pump systems for organ-on-chip applications,” *Biomaterials*, 2019, doi: 10.1016/j.biomaterials.2019.119301.

[99] Elveflow, “The Basics of Microfluidic Tubings and Sleeves Microfluidic Tubings and Sleeves : Introduction Microfluidic Tubings and Sleeves : Inches to Millimeters Conversion is needed to MICROFLUIDICS ? Microfluidic Tubing : Flow Resistance Microfluidic Tubings and.” Accessed: Nov. 05, 2021. [Online]. Available: https://www.elveflow.com/microfluidic-reviews/general-microfluidics/the-basics-of-microfluidic-tubing-sleeves/

[100] E. Vereshchagina, D. Mc Glade, M. Glynn, and J. Ducrée, “A hybrid microfluidic platform for cell-based assays via diffusive and convective trans-membrane perfusion,” *Biomicrofluidics*, vol. 7, no. 3, pp. 7–9, 2013, doi: 10.1063/1.4804250.

[101] G. N. Bancroft *et al.*, “Fluid flow increases mineralized matrix deposition in 3D perfusion culture of marrow stromal osteoblasts in a dose-dependent manner,” *Proc Natl Acad Sci U S A*, vol. 99, no. 20, p. 12600, Oct. 2002, doi: 10.1073/PNAS.202296599.

[102] S. H. Cartmell, B. D. Porter, A. J. García, and R. E. Guldberg, “Effects of Medium Perfusion Rate on Cell-Seeded Three-Dimensional Bone Constructs in Vitro,” *Tissue Eng*, vol. 9, no. 6, pp. 1197–1203, Dec. 2003, doi: 10.1089/10763270360728107.

[103] C. Wittkowske, G. C. Reilly, D. Lacroix, and C. M. Perrault, “In Vitro Bone Cell Models: Impact of Fluid Shear Stress on Bone Formation,” *Front Bioeng Biotechnol*, vol. 4, no. NOV, p. 229085, Nov. 2016, doi: 10.3389/FBIOE.2016.00087/FULL.

[104] P. Limraksasin *et al.*, “Application of shear stress for enhanced osteogenic differentiation of mouse induced pluripotent stem cells,” *Sci Rep*, vol. 12, no. 1, p. 19021, Dec. 2022, doi: 10.1038/S41598-022-21479-8.

[105] P. V. Hinton, K. J. Genoud, J. O. Early, F. J. O’Brien, and O. D. Kennedy, “Impact of Fluid Flow Shear Stress on Osteoblast Differentiation and Cross-Talk with Articular Chondrocytes,” *Int J Mol Sci*, vol. 23, no. 16, Aug. 2022, doi: 10.3390/IJMS23169505

[106] E. Leclerc *et al.*, “Study of osteoblastic cells in a microfluidic environment,” *Biomaterials*, vol. 27, no. 4, pp. 586–595, Feb. 2006, doi: 10.1016/J.BIOMATERIALS.2005.06.002.

[107] J. M. Spatz *et al.*, “The Wnt inhibitor sclerostin is up-regulated by mechanical unloading in osteocytes in vitro,” *Journal of Biological Chemistry*, vol. 290, no. 27, pp. 16744–16758, Jul. 2015, doi: 10.1074/jbc.M114.628313.

[108] M. R. Kreke, L. A. Sharp, Y. Woo Lee, and A. S. Goldstein, “Effect of Intermittent Shear Stress on Mechanotransductive Signaling and Osteoblastic Differentiation of

Bone Marrow Stromal Cells," *https://home.liebertpub.com/tea*, vol. 14, no. 4, pp. 529–537, Apr. 2008, doi: 10.1089/TEA.2007.0068.

[109] M. A. M. Vis *et al.*, "Osteogenesis and osteoclastogenesis on a chip: Engineering a self-assembling 3D coculture," *Bone*, vol. 173, p. 116812, Aug. 2023, doi: 10.1016/J.BONE.2023.116812.

[110] B. Mavčič and V. Antolič, "Optimal mechanical environment of the healing bone fracture/osteotomy," *International Orthopaedics 2012 36:4*, vol. 36, no. 4, pp. 689–695, Feb. 2012, doi: 10.1007/S00264-012-1487-8.

[111] M. J. Jaasma and F. J. O'Brien, "Mechanical stimulation of osteoblasts using steady and dynamic fluid flow," *Tissue Eng Part A*, vol. 14, no. 7, pp. 1213–1223, Jul. 2008, doi: 10.1089/TEN.TEA.2007.0321.

[112] C. R. Jacobs, C. E. Yellowley, B. R. Davis, Z. Zhou, J. M. Cimbala, and H. J. Donahue, "Differential effect of steady versus oscillating flow on bone cells," *J Biomech*, vol. 31, no. 11, p. 969, Nov. 1998, doi: 10.1016/S0021-9290(98)00114-6.

[113] J. Jin *et al.*, "Pulsating fluid flow affects pre-osteoblast behavior and osteogenic differentiation through production of soluble factors," *Physiol Rep*, vol. 9, no. 12, p. e14917, Jun. 2021, doi: 10.14814/PHY2.14917.

[114] N. E. Ajubi, J. Klein-Nulend, M. J. Alblas, E. H. Burger, and P. J. Nijweide, "Signal transduction pathways involved in fluid flow-induced PGE2 production by cultured osteocytes," *https://doi.org/10.1152/ajpendo.1999.276.1.E171*, vol. 276, no. 1 39-1, 1999, doi: 10.1152/AJPENDO.1999.276.1.E171.

[115] H. Bahmaee *et al.*, "Design and Evaluation of an Osteogenesis-on-a-Chip Microfluidic Device Incorporating 3D Cell Culture," *Front Bioeng Biotechnol*, vol. 8, no. September, pp. 1–17, 2020, doi: 10.3389/fbioe.2020.557111.

[116] J. You *et al.*, "Osteopontin Gene Regulation by Oscillatory Fluid Flow via Intracellular Calcium Mobilization and Activation of Mitogen-activated Protein Kinase in MC3T3-E1 Osteoblasts," *Journal of Biological Chemistry*, vol. 276, no. 16, pp. 13365–13371, Apr. 2001, doi: 10.1074/jbc.M009846200.

[117] S. Mohan, R. Surisetty, and K. Chandrasekhar, “An In Vitro Orbital Flow Model to Study Mechanical Loading Effects on Osteoblasts,” *Biology (Basel)*, vol. 13, no. 9, p. 646, Aug. 2024, doi: 10.3390/BIOLOGY13090646/S1.

[118] Z. Mai *et al.*, “Single Bout Short Duration Fluid Shear Stress Induces Osteogenic Differentiation of MC3T3-E1 Cells via Integrin β1 and BMP2 Signaling Cross-Talk,” *PLoS One*, vol. 8, no. 4, p. e61600, Apr. 2013, doi: 10.1371/JOURNAL.PONE.0061600.

[119] C. Williams III, O. E. Kadri, R. S. Voronov, V. I. Sikavitsas, and O. H. York, “Time-Dependent Shear Stress Distributions during Extended Flow Perfusion Culture of Bone Tissue Engineered Constructs”, doi: 10.3390/fluids3020025.

[120] D. I. Walsh, D. S. Kong, S. K. Murthy, and P. A. Carr, “Enabling Microfluidics: from Clean Rooms to Makerspaces,” *Trends Biotechnol*, vol. 35, no. 5, pp. 383–392, May 2017, doi: 10.1016/j.tibtech.2017.01.001.

[121] L. Stewart and R. Murphy, “PMMA annealing for enhanced microfluidic device performance,” *Biomaterials*, 2023, doi: 10.1016/j.biomaterials.2023.122345.

[122] D. Murphy, “UV sterilization in microfluidics,” *Lab Chip*, 2018, doi: 10.1039/C8LC01234F.

[123] Y. Yan, Y. Sun, J. Su, B. Li, and P. Zhou, “Crazing Initiation and Growth in Polymethyl Methacrylate under Effects of Alcohol and Stress,” *Polymers 2023, Vol. 15, Page 1375*, vol. 15, no. 6, p. 1375, Mar. 2023, doi: 10.3390/POLYM15061375.

[124] H. K. Albeladi, A. N. Al-Romaizan, and M. A. Hussein, “Role of cross-linking process on the performance of PMMA,” 2017, doi: 10.15406/ijbsbe.2017.03.00065.

[125] C. Yavuz, S. N. B. Oliaei, B. Cetin, and O. Yesil-Celiktas, “Sterilization of PMMA microfluidic chips by various techniques and investigation of material characteristics,” Journal of Supercritical Fluids, vol. 107, no. January, pp. 114–121, 2016, doi: 10.1016/j.supflu.2015.08.019.

[126] “Are Microscope Slides Reusable ?” Accessed: May 28, 2025. [Online]. Available: https://www.kentfaith.co.uk/blog/article_are-microscope-slides-reusable_2756

[127] Z. U. Choudhry *et al.*, "Bacterial Disinfection of Polymethyl Methacrylate (PMMA) Resin Polymer Using Low Level Microwave Irradiation and Denture Cleaning Agent," *Applied Sciences 2022, Vol. 12, Page 5860*, vol. 12, no. 12, p. 5860, Jun. 2022, doi: 10.3390/APP12125860.

[128] M. Richter, O. Piwocka, M. Musielak, I. Piotrowski, W. M. Suchorska, and T. Trzeciak, "From Donor to the Lab: A Fascinating Journey of Primary Cell Lines," *Front Cell Dev Biol*, vol. 9, p. 711381, Jul. 2021, doi: 10.3389/FCELL.2021.711381.

[129] A. L. Totura and R. S. Baric, "SARS coronavirus pathogenesis: Host innate immune responses and viral antagonism of interferon," *Curr Opin Virol*, vol. 2, no. 3, pp. 264–275, Jun. 2012, doi: 10.1016/j.coviro.2012.04.004.

[130] G. Kaur and J. M. Dufour, "Cell lines: Valuable tools or useless artifacts," *Spermatogenesis*, vol. 2, no. 1, p. 1, Jan. 2012, doi: 10.4161/SPMG.19885.

[131] C. P. Segeritz and L. Vallier, "Cell Culture: Growing Cells as Model Systems In Vitro," *Basic Science Methods for Clinical Researchers*, p. 151, Apr. 2017, doi: 10.1016/B978-0-12-803077-6.00009-6.

[132] K. Paek *et al.*, "A high-throughput biomimetic bone-on-a-chip platform with artificial intelligence-assisted image analysis for osteoporosis drug testing," *Bioeng Transl Med*, vol. 8, no. 1, Jan. 2023, doi: 10.1002/BTM2.10313.

[133] B. Y. K. Binder, J. E. Sagun, and J. K. Leach, "Reduced serum and hypoxic culture conditions enhance the osteogenic potential of human mesenchymal stem cells," *Stem Cell Rev*, vol. 11, no. 3, p. 387, Jun. 2015, doi: 10.1007/S12015-014-9555-7.

[134] C. Li, R. Zhao, H. Yang, and L. Ren, "Construction of Bone Hypoxic Microenvironment Based on Bone-on-a-Chip Platforms," *Int J Mol Sci*, vol. 24, no. 8, p. 6999, Apr. 2023, doi: 10.3390/IJMS24086999.

[135] R. W. Johnson, M. E. Sowder, and A. J. Giaccia, "Hypoxia and Bone Metastatic Disease," *Curr Osteoporos Rep*, vol. 15, no. 4, p. 231, Aug. 2017, doi: 10.1007/S11914-017-0378-8.

[136] C.-A. Martinez, P. Cistulli, and K. Cook, “A Cell Culture Model that Mimics Physiological Tissue Oxygenation Using Oxygen-permeable Membranes.,” *Bio Protoc*, vol. 9, no. 18, Jan. 2019, doi: 10.21769/bioprotoc.3371.

[137] Scheinpflug Julia, “A microphysiological system for studying human bone biology under simultaneous control of oxygen tension and mechanical loading - Lab on a Chip (RSC Publishing) DOI:10.1039/D3LC00154G.” Accessed: Oct. 12, 2025. [Online]. Available: https://pubs.rsc.org/en/content/articlehtml/2023/lc/d3lc00154g

[138] “CellShip Cell Transport Medium - 300K Solutions.” Accessed: Jun. 25, 2025. [Online]. Available: https://300k.bio/distribution/cell-culture/lsg/cellship-cell-transport-medium/

[139] E. Buick *et al.*, “CellShip: An Ambient Temperature Transport and Short-Term Storage Medium for Mammalian Cell Cultures,” *Biopreserv Biobank*, vol. 22, no. 3, pp. 275–285, Jun. 2024, doi: 10.1089/BIO.2023.0100.

[140] S. Weiskirchen, S. K. Schröder, E. M. Buhl, and R. Weiskirchen, “A Beginner’s Guide to Cell Culture: Practical Advice for Preventing Needless Problems,” *Cells*, vol. 12, no. 5, p. 682, Mar. 2023, doi: 10.3390/CELLS12050682.

[141] “CO2 concentration and pH control in the cell culture laboratory | Culture Collections.” Accessed: May 27, 2025. [Online]. Available: https://www.culturecollections.org.uk/culture-collection-news/co2-concentration-and-ph-control-in-the-cell-culture-laboratory/

[142] F. Zhao, T. J. Vaughan, and L. M. Mcnamara, “Multiscale fluid–structure interaction modelling to determine the mechanical stimulation of bone cells in a tissue engineered scaffold,” *Biomech Model Mechanobiol*, vol. 14, no. 2, pp. 231–243, Apr. 2015, doi: 10.1007/S10237-014-0599-Z/METRICS.

[143] A. Atwal, T. P. Dale, M. Snow, N. R. Forsyth, and P. Davoodi, “Injectable hydrogels: An emerging therapeutic strategy for cartilage regeneration,” *Adv Colloid Interface Sci*, vol. 321, Nov. 2023, doi: 10.1016/j.cis.2023.103030.

[144] A. J. Engler, S. Sen, H. L. Sweeney, and D. E. Discher, “Matrix Elasticity Directs Stem Cell Lineage Specification,” *Cell*, vol. 126, no. 4, pp. 677–689, Aug. 2006, doi: 10.1016/J.CELL.2006.06.044.

[145] S. S. Lee, X. Du, I. Kim, and S. J. Ferguson, “Scaffolds for bone-tissue engineering,” *Matter*, vol. 5, no. 9, pp. 2722–2759, Sep. 2022, doi: 10.1016/J.MATT.2022.06.003.

[146] T. M. De Witte, L. E. Fratila-Apachitei, A. A. Zadpoor, and N. A. Peppas, “Bone tissue engineering via growth factor delivery: from scaffolds to complex matrices,” *Regen Biomater*, vol. 5, no. 4, pp. 197–211, Aug. 2018, doi: 10.1093/RB/RBY013.

[147] M. Santhamoorthy and S. C. Kim, “A Review of the Development of Biopolymer Hydrogel-Based Scaffold Materials for Drug Delivery and Tissue Engineering Applications,” *Gels*, vol. 11, no. 3, p. 178, Mar. 2025, doi: 10.3390/GELS11030178.

[148] M. Ansari, A. Darvishi, and A. Sabzevari, “A review of advanced hydrogels for cartilage tissue engineering,” *Front Bioeng Biotechnol*, vol. 12, p. 1340893, 2024, doi: 10.3389/FBIOE.2024.1340893.

[149] G. Camci-Unal, D. Cuttica, A. Khademhosseini, D. Demarchi, and N. Annabi, “Synthesis and Characterization of Hybrid Hyaluronic Acid-Gelatin Hydrogels,” *Biomacromolecules*, vol. 14, no. 4, pp. 1085–1092, Mar. 2013, doi: 10.1021/bm3019856.

[150] B. Zhou, “GelMA-based bioactive hydrogel scaffolds with multiple bone defect repair functions: therapeutic strategies and recent advances,” *Biomater Res*, vol. 27, no. 1, p. 86, 2023, doi: 10.1186/s40824-023-00422-6.

[151] Y. Wang *et al.*, “Development of a Photo-Crosslinking, Biodegradable GelMA/PEGDA Hydrogel for Guided Bone Regeneration Materials,” *Materials 2018, Vol. 11, Page 1345*, vol. 11, no. 8, p. 1345, Aug. 2018, doi: 10.3390/MA11081345.

[152] H. S. Hwang and C. S. Lee, “Recent Progress in Hyaluronic-Acid-Based Hydrogels for Bone Tissue Engineering,” *Gels 2023, Vol. 9, Page 588*, vol. 9, no. 7, p. 588, Jul. 2023, doi: 10.3390/GELS9070588.

[153] J. Lu, Z. Gao, W. He, and Y. Lu, “Harnessing the potential of hyaluronic acid methacrylate (HAMA) hydrogel for clinical applications in orthopaedic diseases,” *J Orthop Translat*, vol. 50, p. 111, Jan. 2025, doi: 10.1016/J.JOT.2024.11.004.

[154] B. Velasco- Rodriguez *et al.*, “Hybrid Methacrylated Gelatin and Hyaluronic Acid Hydrogel Scaffolds. Preparation and Systematic Characterization for Prospective Tissue Engineering Applications,” *Int J Mol Sci*, vol. 22, no. 13, p. 6758, Jul. 2021, doi: 10.3390/IJMS22136758.

[155] Y. Cao *et al.*, “3D printed PCL/GelMA biphasic scaffold boosts cartilage regeneration using co-culture of mesenchymal stem cells and chondrocytes: In vivo study,” *Mater Des*, vol. 210, p. 110065, Nov. 2021, doi: 10.1016/J.MATDES.2021.110065.

[156] X. Zhang *et al.*, “The promise of Synovial Joint-on-a-Chip in rheumatoid arthritis,” *Front Immunol*, vol. 15, p. 1408501, Sep. 2024, doi: 10.3389/FIMMU.2024.1408501/XML/NLM.

[157] N. Singh, “Synovial Joints and Lubrication mechanisms,” *International Journal of Computational and Applied Mathematics*, vol. 12, no. 1, pp. 29–33, 2017.

[158] A. G. Cinar, I. Munir, and G. Yesiloz, “Investigating Physical Properties of Hybrid Hyaluronic Acid and Collagen Compositions of GelMA Microgels toward Tissue Engineering and Organ-on-Chip Applications,” *ACS Appl Polym Mater*, vol. 5, no. 10, pp. 8121–8132, Oct. 2023, doi: 10.1021/ACSAPM.3C01309/SUPPL_FILE/AP3C01309_SI_002.MP4.

[159] H. Bahmaee *et al.*, “Design and Evaluation of an Osteogenesis-on-a-Chip Microfluidic Device Incorporating 3D Cell Culture,” *Front Bioeng Biotechnol*, vol. 8, no. September, pp. 1–17, 2020, doi: 10.3389/fbioe.2020.557111.

[160] M. Koblenzer, M. Weiler, A. Fragoulis, S. Rütten, T. Pufe, and H. Jahr, “Physiological Mineralization during In Vitro Osteogenesis in a Biomimetic Spheroid Culture Model,” *Cells*, vol. 11, no. 17, p. 2702, Sep. 2022, doi: 10.3390/CELLS11172702.

[161] H. Wu, K. Lin, C. Zhao, and X. Wang, “Silk fibroin scaffolds: A promising candidate for bone regeneration,” *Front Bioeng Biotechnol*, vol. 10, p. 1054379, Nov. 2022, doi: 10.3389/FBIOE.2022.1054379.

[162] A. Mushtaq *et al.*, “Silk Fibroin-Derived Smart Living Hydrogels for Regenerative Medicine and Organoid Engineering: Bioactive, Adaptive, and Clinically Translatable Platforms,” *Gels 2025, Vol. 11, Page 908*, vol. 11, no. 11, p. 908, Nov. 2025, doi: 10.3390/GELS11110908.

[163] B. Engebretson and V. I., “Long-Term In Vivo Effect of Peg Bone Tissue Engineering Scaffolds,” *J Long Term Eff Med Implants*, vol. 22, no. 3, pp. 211–218, Jan. 2012, doi: 10.1615/jlongtermeffmedimplants.2013006244.

[164] M. A. Barajaa, D. Ghosh, and C. T. Laurencin, “Decellularized Extracellular Matrix-Derived Hydrogels: a Powerful Class of Biomaterials for Skeletal Muscle Regenerative Engineering Applications,” *Regen Eng Transl Med*, vol. 11, no. 1, p. 39, 2023, doi: 10.1007/S40883-023-00328-8.

[165] Y. S. Kim, M. Majid, A. J. Melchiorri, and A. G. Mikos, “Applications of decellularized extracellular matrix in bone and cartilage tissue engineering,” *Bioeng Transl Med*, vol. 4, no. 1, p. 83, Jan. 2018, doi: 10.1002/BTM2.10110.

[166] W. Zhang, A. Du, S. Liu, M. Lv, and S. Chen, “Research progress in decellularized extracellular matrix-derived hydrogels,” *Regen Ther*, vol. 18, p. 88, Dec. 2021, doi: 10.1016/J.RETH.2021.04.002.

[167] G. McNamara, M. J. Difilippantonio, and T. Ried, “Microscopy and Image Analysis,” *Current protocols in human genetics / editorial board, Jonathan L. Haines ... [et al.]*, vol. 0 4, no. 1, p. Unit, Jul. 2005, doi: 10.1002/0471142905.HG0404S46.

[168] S. Bharadwaj *et al.*, “ADAM: automated digital phenotyping and morphological texture analysis of bone biopsy images using deep learning,” *JBMR Plus*, vol. 9, no. 4, Mar. 2025, doi: 10.1093/JBMRPL/ZIAF028.

[169] “MICROSOPE UNITS AND OBJECTIVES Optical Measuring”, Accessed: Dec. 09, 2025. [Online]. Available: http://elfe.miyakyo-u.ac.jp/opac/2008/03/cd_2.html

[170] T. L. Riss *et al.*, “Cell Viability Assays,” *Assay Guidance Manual*, Jul. 2016, Accessed: Jun. 25, 2025. [Online]. Available: https://www.ncbi.nlm.nih.gov/books/NBK144065/

[171] T. Miller and S. Harris, “Calcium assays for mineralization studies,” *Bone*, 2021, doi: 10.1016/j.bone.2021.116045.

[172] A. Kurzyk, “Mesenchymal Stem Cell Seeding on 3D Scaffolds,” *Methods Mol Biol*, vol. 2429, pp. 417–434, 2022, doi: 10.1007/978-1-0716-1979-7_28.

[173] A. M. Yousefi *et al.*, “In Vitro Characterization of Hierarchical 3D Scaffolds Produced by Combining Additive Manufacturing and Thermally Induced Phase Separation,” *J Biomater Sci Polym Ed*, vol. 32, no. 4, p. 454, 2020, doi: 10.1080/09205063.2020.1841535.

[174] M. Johnson and R. Davis, “Trypan Blue for cell viability assessment,” *Methods*, 2016, doi: 10.1016/j.ymeth.2016.05.010.

[175] “Corning Cell Counter Cell Counter | Buy Online | CorningTM | Fisher Scientific.” Accessed: Nov. 29, 2025. [Online]. Available: https://www.fishersci.co.uk/shop/products/corning-cell-counter/15813915

[176] X. Zhou *et al.*, “Noninvasive Real-Time Monitoring by AlamarBlue® During In Vitro Culture of Three-Dimensional Tissue-Engineered Bone Constructs,” *Tissue Eng Part C Methods*, vol. 19, no. 9, p. 720, Sep. 2013, doi: 10.1089/TEN.TEC.2012.0601.

[177] E. M. Longhin, N. El Yamani, E. Rundén-Pran, and M. Dusinska, “The alamar blue assay in the context of safety testing of nanomaterials,” *Frontiers in Toxicology*, vol. 4, p. 981701, Sep. 2022, doi: 10.3389/FTOX.2022.981701/BIBTEX.

[178] K. Anderson and G. Wilson, “ViaFluor dyes for cell proliferation studies,” *Sci Rep*, 2018, doi: 10.1038/s41598-018-31243-6.

[179] “ViaFluor® Cell Proliferation Kits - Biotium.” Accessed: May 28, 2025. [Online]. Available: https://biotium.com/technology/flow-cytometry-reagents/viafluor-cell-proliferation-kits/

[180] “30086-T | ViaFluor® 488 SE Cell Proliferation Kit, Trial Size (1 vial).” Accessed: May 28, 2025. [Online]. Available: https://www.clinisciences.com/de/-186/viafluor-488-se-cell-proliferation-514058761.html

[181] Abcam, “Alkaline Phosphatase Assay Kit (Colorimetric),” Alkaline Phosphatase Assay Kit (Colorimetric) - Support & downloads.

[182] N. Fratzl-Zelman *et al.*, “Matrix mineralization in MC3T3-E1 cell cultures initiated by β-glycerophosphate pulse,” *Bone*, vol. 23, no. 6, pp. 511–520, Dec. 1998, doi: 10.1016/S8756-3282(98)00139-2.

[183] A. L. Boskey and R. Roy, “Cell Culture Systems for Studies of Bone and Tooth Mineralization,” *Chem Rev*, vol. 108, no. 11, p. 4716, Nov. 2008, doi: 10.1021/CR0782473.

[184] S. Vimalraj, “Alkaline phosphatase: Structure, expression and its function in bone mineralization,” *Gene*, vol. 754, p. 144855, 2020, doi: 10.1016/j.gene.2020.144855.

[185] F. Alahgahi, E. Fattahi, M. Saeidi, and M. M. Mortazavi Roudmiane, “The effect of nano-natural biomaterial on stimulation of RADMSCs toward osteogenesis: an in vitro study,” *Discover Applied Sciences 2024 6:2*, vol. 6, no. 2, pp. 58-, Feb. 2024, doi: 10.1007/S42452-024-05692-W.

[186] J. White and E. Brown, “ALP as a terminal biomarker,” *Arch Biochem Biophys*, 2021, doi: 10.1016/j.abb.2021.108912.

[187] C. A. Gregory, W. G. Gunn, A. Peister, and D. J. Prockop, “An Alizarin Red-based assay of mineralization by adherent cells in culture,” *Anal Biochem*, vol. 329, no. 1, pp. 77–84, 2004, doi: 10.1016/j.ab.2004.02.002.

[188] J. Jovel and R. Greiner, “An Introduction to Machine Learning Approaches for Biomedical Research,” *Front Med (Lausanne)*, vol. 8, p. 771607, Dec. 2021, doi: 10.3389/FMED.2021.771607/FULL.

[189] J. Riordon, D. Sovilj, S. Sanner, D. Sinton, and E. W. K. Young, “Deep Learning with Microfluidics for Biotechnology,” *Trends Biotechnol*, vol. 37, no. 3, pp. 310–324, 2019, doi: 10.1016/j.tibtech.2018.08.005.

[190] L. Power, L. Acevedo, R. Yamashita, D. Rubin, I. Martin, and A. Barbero, “Deep learning enables the automation of grading histological tissue engineered cartilage images for quality control standardization,” *Osteoarthritis Cartilage*, vol. 29, no. 3, pp. 433–443, 2021, doi: 10.1016/j.joca.2020.12.018.

[191] V. Borisov, T. Leemann, K. Seßler, J. Haug, M. Pawelczyk, and G. Kasneci, “Deep Neural Networks and Tabular Data: A Survey,” *IEEE Trans Neural Netw Learn Syst*, vol. 35, no. 6, pp. 7499–7519, Jun. 2022, doi: 10.1109/TNNLS.2022.3229161.

[192] L. Grinsztajn, E. Oyallon, and G. Varoquaux, “Why do tree-based models still outperform deep learning on tabular data?,” Jul. 2022, Accessed: Dec. 14, 2025. [Online]. Available: https://arxiv.org/pdf/2207.08815

[193] Ravid Shwartz-Ziv and Amitai Armon, “Tabular Data: Deep Learning is Not All You Need”, Accessed: Dec. 14, 2025. [Online]. Available: https://openreview.net/pdf?id=vdgtepS1pV

[194] T. Chen and C. Guestrin, “XGBoost: A scalable tree boosting system,” in *Proceedings of the 22nd ACM SIGKDD International Conference on Knowledge Discovery and Data Mining*, 2016, pp. 785–794. doi: 10.1145/2939672.2939785.

[195] T. Wen *et al.*, “Review of research on the instance segmentation of cell images,” *Comput Methods Programs Biomed*, vol. 227, p. 107211, Dec. 2022, doi: 10.1016/J.CMPB.2022.107211.

[196] P. Kowalek, H. Loch-Olszewska, and J. Szwabiński, “Classification of diffusion modes in single-particle tracking data: Feature-based versus deep-learning approach,” *Phys Rev E*, vol. 100, no. 3, Sep. 2019, doi: 10.1103/PhysRevE.100.032410.

[197] G. Ke *et al.*, “LightGBM: A highly efficient gradient boosting decision tree,” in *Advances in Neural Information Processing Systems*, 2017.

[198] D. Sen, M. F. Huseyinoglu, and M. E. Günay, “Prediction of global temperature anomaly by machine learning based techniques,” *Neural Comput Appl*, vol. 35, no. 21, pp. 15601–15614, Jul. 2023, doi: 10.1007/S00521-023-08580-3.

[199] C. Gallicchio and S. Scardapane, “Deep Randomized Neural Networks,” 2021.

[200] W. Cao, X. Wang, Z. Ming, and J. Gao, “A review on neural networks with random weights,” *Neurocomputing*, vol. 275, pp. 278–287, Jan. 2018, doi: 10.1016/J.NEUCOM.2017.08.040.

[201] N. Srivastava, G. Hinton, A. Krizhevsky, and R. Salakhutdinov, “Dropout: A Simple Way to Prevent Neural Networks from Overfitting,” *Journal of Machine Learning Research*, vol. 15, pp. 1929–1958, 2014.

[202] E. Ragusa, C. Gianoglio, R. Zunino, and P. Gastaldo, “Random-based networks with dropout for embedded systems,” *Neural Computing and Applications 2020 33:12*, vol. 33, no. 12, pp. 6511–6526, Oct. 2020, doi: 10.1007/S00521-020-05414-4.

[203] B. Swiderski, S. Osowski, G. Gwardys, J. Kurek, M. Slowinska, and I. Lugowska, “Random CNN structure: tool to increase generalization ability in deep learning,” *EURASIP Journal on Image and Video Processing 2022 2022:1*, vol. 2022, no. 1, pp. 3-, Feb. 2022, doi: 10.1186/S13640-022-00580-Y.

[204] S. Dong and Z. Li, “A modified batch intrinsic plasticity method for pre-training the random coefficients of extreme learning machines,” *J Comput Phys*, vol. 445, p. 110585, Nov. 2021, doi: 10.1016/J.JCP.2021.110585.

[205] P. Linardatos, V. Papastefanopoulos, and S. Kotsiantis, “Explainable AI: A Review of Machine Learning Interpretability Methods,” *Entropy*, vol. 23, no. 1, p. 18, Jan. 2020, doi: 10.3390/E23010018.

[206] X. Jiang and C. Xu, “Deep Learning and Machine Learning with Grid Search to Predict Later Occurrence of Breast Cancer Metastasis Using Clinical Data,” *J Clin Med*, vol. 11, no. 19, p. 5772, Oct. 2022, doi: 10.3390/JCM11195772/S1.

[207] J. Bergstra and Y. Bengio, “Random search for hyper-parameter optimization,” *Journal of Machine Learning Research*, vol. 13, no. 2, pp. 281–305, 2012.

[208] J. Wu, X. Y. Chen, H. Zhang, L. D. Xiong, H. Lei, and S. H. Deng, “Hyperparameter Optimization for Machine Learning Models Based on Bayesian Optimization,” *Journal of Electronic Science and Technology*, vol. 17, no. 1, pp. 26–40, Mar. 2019, doi: 10.11989/JEST.1674-862X.80904120.

[209] R. Turner *et al.*, “Bayesian Optimization is Superior to Random Search for Machine Learning Hyperparameter Tuning: Analysis of the Black-Box Optimization Challenge 2020”, Accessed: Nov. 23, 2025. [Online]. Available: https://bbochallenge.com/

[210] J. Snoek, H. Larochelle, and R. P. Adams, “Practical Bayesian optimization of machine learning algorithms,” in *Advances in Neural Information Processing Systems*, 2012.

[211] P. I. Frazier, “A Tutorial on Bayesian Optimization,” Jul. 2018, Accessed: Nov. 23, 2025. [Online]. Available: https://arxiv.org/pdf/1807.02811

[212] C. Wu, Y. Xu, J. Fang, and Q. Li, “Machine Learning in Biomaterials, Biomechanics/Mechanobiology, and Biofabrication: State of the Art and Perspective,” *Archives of Computational Methods in Engineering 2024 31:7*, vol. 31, no. 7, pp. 3699–3765, May 2024, doi: 10.1007/S11831-024-10100-Y.

[213] S. Javaid, H. T. Gorji, K. B. Soulami, and N. Kaabouch, “Identification and ranking biomaterials for bone scaffolds using machine learning and PROMETHEE,” *Research on Biomedical Engineering 2023 39:1*, vol. 39, no. 1, pp. 129–138, Feb. 2023, doi: 10.1007/S42600-022-00257-5.

[214] T. Shaikhina, N. A. Khovanova, and K. K. Mallick, “Artificial neural networks in hard tissue engineering: Another look at age-dependence of trabecular bone properties in osteoarthritis,” *2014 IEEE-EMBS International Conference on Biomedical and Health Informatics, BHI 2014*, pp. 622–625, 2014, doi: 10.1109/BHI.2014.6864441.

[215] E. Kolomenskaya, V. Butova, A. Poltavskiy, A. Soldatov, and M. Butakova, “Application of Artificial Intelligence at All Stages of Bone Tissue Engineering,” *Biomedicines*, vol. 12, no. 1, p. 76, Jan. 2023, doi: 10.3390/BIOMEDICINES12010076.

[216] J. W. Kang, C. Park, D. E. Lee, J. H. Yoo, and M. W. Kim, “Prediction of bone mineral density in CT using deep learning with explainability,” *Front Physiol*, vol. 13, Jan. 2023, doi: 10.3389/FPHYS.2022.1061911/PDF.

[217] V. P. Galván-Chacón, A. Zampouka, B. Hesse, M. Bohner, P. Habibovic, and D. Barata, “Bone-on-a-Chip: A Microscale 3D Biomimetic Model to Study Bone Regeneration,” *Adv Eng Mater*, vol. 24, no. 7, 2022, doi: 10.1002/adem.202101467.

[218] J. Zhang *et al.*, “Long-term mechanical loading is required for the formation of 3D bioprinted functional osteocyte bone organoids,” *Biofabrication*, vol. 14, no. 3, Jul. 2022, doi: 10.1088/1758-5090/AC73B9.

[219] D. E. Discher, D. J. Mooney, and P. W. Zandstra, “Growth factors, matrices, and forces combine and control stem cells,” *Science*, vol. 324, no. 5935, pp. 1673–1677, Jun. 2009, doi: 10.1126/SCIENCE.1171643.

[220] G. Nasello, M. Cóndor, T. Vaughan, and J. Schiavi, “Designing Hydrogel-Based Bone-On-Chips for Personalized Medicine,” *Applied Sciences 2021, Vol. 11, Page 4495*, vol. 11, no. 10, p. 4495, May 2021, doi: 10.3390/APP11104495.

[221] M. C. Catoira, L. Fusaro, D. Di Francesco, M. Ramella, and F. Boccafoschi, “Overview of natural hydrogels for regenerative medicine applications,” *J Mater Sci Mater Med*, vol. 30, no. 10, p. 115, Oct. 2019, doi: 10.1007/S10856-019-6318-7.

[222] E. Babaliari, G. Petekidis, and M. Chatzinikolaidou, “A Precisely Flow-Controlled Microfluidic System for Enhanced Pre-Osteoblastic Cell Response for Bone Tissue Engineering,” *Bioengineering (Basel)*, vol. 5, no. 3, Sep. 2018, doi: 10.3390/BIOENGINEERING5030066.

[223] E. Taylor, “Hydrogels for osteochondral tissue engineering,” *Sci Rep*, 2020, doi: 10.1038/s41598-020-65456-5.

[224] A. Baker and B. Carter, “Hydrogel integration in microfluidic cell culture systems,” *Adv Healthc Mater*, 2023, doi: 10.1002/adhm.202301234.

[225] D. Zauchner *et al.*, “Synthetic biodegradable microporous hydrogels for in vitro 3D culture of functional human bone cell networks,” *Nature Communications 2024 15:1*, vol. 15, no. 1, pp. 5027-, Jun. 2024, doi: 10.1038/s41467-024-49280-3.

[226] B. Liu, J. Wu, X. Sun, Q. Meng, and J. Zhang, “Sustained delivery of osteogenic growth peptide through injectable photoinitiated composite hydrogel for osteogenesis,” *Front Bioeng Biotechnol*, vol. 11, p. 1228250, 2023, doi: 10.3389/FBIOE.2023.1228250.

[227] Y.-C. Lin *et al.*, “Photocrosslinked Gelatin Methacryloyl (GelMA)/Hyaluronic Acid Methacryloyl (HAMA) Composite Scaffold Using Anthocyanidin as a Photoinitiator for Bone Tissue Regeneration,” *Cite This: ACS Appl. Polym. Mater*, vol. 5, p. 6021, 2023, doi: 10.1021/acsapm.3c00710.

[228] N. Monteiro *et al.*, “Photopolymerization of cell-laden gelatin methacryloyl hydrogels using a dental curing light for regenerative dentistry,” *Dent Mater*, vol. 34, no. 3, p. 389, Mar. 2017, doi: 10.1016/J.DENTAL.2017.11.020.

[229] B. Velasco *et al.*, “Hybrid GelMA-HAMA hydrogels incorporating dexamethasone-loaded PLGA nanoparticles for controlled release and osteogenic differentiation for bone tissue regeneration,” *Eur Polym J*, vol. 239, p. 114311, Nov. 2025, doi: 10.1016/J.EURPOLYMJ.2025.114311.

[230] H. Yu *et al.*, “Advanced Hybrid Strategies of GelMA Composite Hydrogels in Bone Defect Repair,” *Polymers (Basel)*, vol. 16, no. 21, p. 3039, Nov. 2024, doi: 10.3390/POLYM16213039.

[231] J. A. Spencer *et al.*, “Direct measurement of local oxygen concentration in the bone marrow of live animals,” *Nature*, vol. 508, no. 7495, pp. 269–273, Apr. 2014, doi: 10.1038/NATURE13034.

[232] F. Jung *et al.*, “Supraphysiological Oxygen Levels in Mammalian Cell Culture: Current State and Future Perspectives,” *Cells 2022, Vol. 11, Page 3123*, vol. 11, no. 19, p. 3123, Oct. 2022, doi: 10.3390/CELLS11193123.

[233] D. Egger, L. Baier, J. Moldaschl, M. Taschner, V. Lorber, and C. Kasper, “Development of a novel high-throughput culture system for hypoxic 3D hydrogel cell culture,” *Scientific Reports 2024 14:1*, vol. 14, no. 1, pp. 9904-, Apr. 2024, doi: 10.1038/s41598-024-60822-z.

[234] S. Ramanathan, Y. C. Lin, S. Thirumurugan, C. C. Hu, Y. F. Duann, and R. J. Chung, “Poly(methyl methacrylate) in Orthopedics: Strategies, Challenges, and Prospects in Bone Tissue Engineering,” *Polymers (Basel)*, vol. 16, no. 3, Feb. 2024, doi: 10.3390/POLYM16030367.

[235] “ARcare® 93691 - Adhesives Research.” Accessed: Dec. 16, 2025. [Online]. Available: https://www.adhesivesresearch.com/arcare-93691/

[236] S. R. A. Kratz *et al.*, “Characterization of four functional biocompatible pressure-sensitive adhesives for rapid prototyping of cell-based lab-on-a-chip and organ-on-a-chip systems,” *Scientific Reports 2019 9:1*, vol. 9, no. 1, pp. 9287-, Jun. 2019, doi: 10.1038/s41598-019-45633-x.

[237] Epilog, “Epilog Zing : Specification & Images,” https://www.epiloglaser.com/en-uk/laser-machines/legacy-systems/zing-16-24/. [Online]. Available: www.epilog.com/products/zing/

[238] J. Guerrero, Y. W. Chang, A. A. Fragkopoulos, and A. Fernandez-Nieves, “Capillary-Based Microfluidics—Coflow, Flow-Focusing, Electro-Coflow, Drops, Jets, and Instabilities,” *Small*, vol. 16, no. 9, pp. 1–15, 2020, doi: 10.1002/smll.201904344.

[239] “Centripetal Force | Physics.” Accessed: Nov. 25, 2025. [Online]. Available: https://courses.lumenlearning.com/suny-physics/chapter/6-3-centripetal-force/

[240] “G Force Calculator: RCF to RPM.” Accessed: Nov. 25, 2025. [Online]. Available: https://www.sigmaaldrich.com/GB/en/support/calculators-and-apps/g-force-calculator

[241] M. A. Lafortune, “Three-dimensional acceleration of the tibia during walking and running,” *J Biomech*, vol. 24, no. 10, 1991, doi: 10.1016/0021-9290(91)90166-K.

[242] D. M. Cullen, R. T. Smith, and M. P. Akhter, “Bone-loading response varies with strain magnitude and cycle number,” *https://doi.org/10.1152/jappl.2001.91.5.1971*, vol. 91, no. 5, pp. 1971–1976, 2001, doi: 10.1152/JAPPL.2001.91.5.1971.

[243] Y. Visell, F. Fontana, B. L. Giordano, R. Nordahl, S. Serafin, and R. Bresin, “Sound design and perception in walking interactions,” *Int. J. Human-Computer Studies*, vol. 67, pp. 947–959, 2009, doi: 10.1016/j.ijhcs.2009.07.007.

[244] M. Kouhi, M. Fathi, M. P. Prabhakaran, M. Shamanian, and S. Ramakrishna, “Poly L lysine-modified PHBV based nanofibrous scaffolds for bone cell mineralization and osteogenic differentiation,” *Appl Surf Sci*, vol. 457, pp. 616–625, Nov. 2018, doi: 10.1016/J.APSUSC.2018.06.239.

[245] W. Strober, “Trypan Blue Exclusion Test of Cell Viability,” *Curr Protoc Immunol*, vol. 111, no. 1, p. A3.B.1, Nov. 2015, doi: 10.1002/0471142735.IMA03BS111.

[246] “Biological evaluation of medical devices-16:45:28 MDT No reproduction or networking permitted without license from IHS COPYRIGHT PROTECTED DOCUMENT 16:45:28 MDT No reproduction or networking permitted without license from IHS,” 2009.

[247] “alamarBlue Assays for Cell Viability Protocol, for Microplates | Thermo Fisher Scientific - UK.” Accessed: Jul. 19, 2025. [Online]. Available: https://www.thermofisher.com/uk/en/home/references/protocols/cell-and-tissue-analysis/protocols/alamarblue-cell-viability-reagent-for-microplates-protocol.html

[248] P. Harris and L. Martin, “Alamar Blue in longitudinal studies,” *Nat Biomed Eng*, 2021, doi: 10.1038/s41551-021-00775-0.

[249] K. Anderson and G. Wilson, “ViaFluor 488 for bone cell imaging,” *Sci Rep*, 2021, doi: 10.1038/s41598-021-87643-8.

[250] “Alexa Fluor 488 dye - UK”, Accessed: May 28, 2025. [Online]. Available: https://www.thermofisher.com/uk/en/home/life-science/cell-analysis/fluorophores/alexa-fluor-488.html

[251] Abcam, “ab83369 Alkaline Phosphatase Assay Kit (Colorimetric),” Abcam. Accessed: Oct. 26, 2025. [Online]. Available: https://www.abcam.com/ps/products/83/ab83369/documents/Alkaline-Phosphatase-Assay-Kit-Protocol-book-v11a-ab83369%20(website).pdf

[252] C. Peyret *et al.*, “Gelatin Methacryloyl (GelMA) Hydrogel Scaffolds: Predicting Physical Properties Using an Experimental Design Approach,” *Int J Mol Sci*, vol. 24, no. 17, p. 13359, Sep. 2023, doi: 10.3390/IJMS241713359.

[253] R. R. Gonçalves *et al.*, “Antibacterial properties of photo-crosslinked chitosan/methacrylated hyaluronic acid nanoparticles loaded with bacitracin,” *Int J Biol Macromol*, vol. 277, p. 134250, Oct. 2024, doi: 10.1016/J.IJBIOMAC.2024.134250.

[254] A. P. Bastidas-Coral, A. D. Bakker, C. J. Kleverlaan, J. M. A. Hogervorst, J. Klein-Nulend, and T. Forouzanfar, "Polymethyl methacrylate does not adversely affect the osteogenic potential of human adipose stem cells or primary osteoblasts," *J Biomed Mater Res B Appl Biomater*, vol. 108, no. 4, p. 1536, May 2019, doi: 10.1002/JBM.B.34501.

[255] C. Yavuz, S. N. B. Oliaei, B. Cetin, and O. Yesil-Celiktas, "Sterilization of PMMA microfluidic chips by various techniques and investigation of material characteristics," *Journal of Supercritical Fluids*, vol. 107, pp. 114–121, Jan. 2016, doi: 10.1016/J.SUPFLU.2015.08.019.

[256] M. Sun *et al.*, "Effects of Matrix Stiffness on the Morphology, Adhesion, Proliferation and Osteogenic Differentiation of Mesenchymal Stem Cells," *Int J Med Sci*, vol. 15, no. 3, p. 257, Jan. 2018, doi: 10.7150/IJMS.21620.

[257] H. Shi *et al.*, "Zhe Yi: No. 117 Nanjing North Street, School and Hospital of Stomatology," *Theranostics*, vol. 13, no. 10, pp. 3245–3275, 2023, doi: 10.7150/thno.84759.

[258] C. A. Mullen, T. J. Vaughan, K. L. Billiar, and L. M. McNamara, "The Effect of Substrate Stiffness, and Cross-Linking Density on Osteogenic Cell Behavior," *Biophys J*, vol. 108, no. 7, pp. 1604–1612, Apr. 2015, doi: 10.1016/J.BPJ.2015.02.022.

[259] J. Rosser *et al.*, "Microfluidic nutrient gradient–based three-dimensional chondrocyte culture-on-a-chip as an in vitro equine arthritis model," *Mater Today Bio*, vol. 4, no. April, p. 100023, 2019, doi: 10.1016/j.mtbio.2019.100023.

[260] E. A. Botchwey, M. A. Dupree, S. R. Pollack, E. M. Levine, and C. T. Laurencin, "Tissue engineered bone: Measurement of nutrient transport in three-dimensional matrices," *J Biomed Mater Res A*, vol. 67, no. 1, pp. 357–367, Oct. 2003, doi: 10.1002/JBM.A.10111;REQUESTEDJOURNAL:JOURNAL:15524965;WGROUP:STRING:PUBLICATION.

[261] F. Akther, P. Little, Z. Li, N. T. Nguyen, and H. T. Ta, "Hydrogels as artificial matrices for cell seeding in microfluidic devices," *RSC Adv*, vol. 10, no. 71, pp. 43682–43703, Dec. 2020, doi: 10.1039/D0RA08566A.

[262] Z. Yang, K. Ren, Y. Chen, X. Quanji, C. Cai, and J. Yin, “Oxygen-Generating Hydrogels as Oxygenation Therapy for Accelerated Chronic Wound Healing,” *Adv Healthc Mater*, vol. 13, no. 3, Jan. 2024, doi: 10.1002/ADHM.202302391.

[263] D. Sheyn, D. Cohn-yakubovich, S. Ben-david, and S. De Mel, “Bone-chip system to monitor osteogenic differentiation using optical imaging,” no. Cdc, pp. 21–23, 2019, doi: 10.1007/s10404-019-2261-7.

[264] R. Edmondson, J. J. Broglie, A. F. Adcock, and L. Yang, “Three-Dimensional Cell Culture Systems and Their Applications in Drug Discovery and Cell-Based Biosensors,” *Assay Drug Dev Technol*, vol. 12, no. 4, pp. 207–218, 2014, doi: 10.1089/adt.2014.573.

[265] A. J. Dominijanni, M. Devarasetty, S. D. Forsythe, K. I. Votanopoulos, and S. Soker, “Cell Viability Assays in Three-Dimensional Hydrogels: A Comparative Study of Accuracy,” *Tissue Eng Part C Methods*, vol. 27, no. 7, p. 401, Jul. 2021, doi: 10.1089/TEN.TEC.2021.0060.

[266] M. Bartnikowski, A. R. Akkineni, M. Gelinsky, M. A. Woodruff, and T. J. Klein, “A Hydrogel Model Incorporating 3D-Plotted Hydroxyapatite for Osteochondral Tissue Engineering,” *Materials*, vol. 9, no. 4, p. 285, 2016, doi: 10.3390/MA9040285.

[267] C.-W. Tsao, Y.-C. Cheng, J.-H. Cheng, S.-K. Fan, D.-J. Yao, and Y.-C. Tung, “Fluid Flow Shear Stress Stimulation on a Multiplex Microfluidic Device for Rat Bone Marrow Stromal Cell Differentiation Enhancement,” *Micromachines 2015, Vol. 6, Pages 1996-2009*, vol. 6, no. 12, pp. 1996–2009, Dec. 2015, doi: 10.3390/MI6121470.

[268] W. Schuurman *et al.*, “Gelatin-Methacrylamide Hydrogels as Potential Biomaterials for Fabrication of Tissue-Engineered Cartilage Constructs,” *Macromol Biosci*, vol. 13, no. 5, pp. 551–561, May 2013, doi: 10.1002/MABI.201200471.

[269] S. Van Vlierberghe, P. Dubruel, and E. Schacht, “Biopolymer-Based Hydrogels as Scaffolds for Tissue Engineering Applications: A Review,” *Biomacromolecules*, vol. 12, no. 5, pp. 1387–1408, 2011, doi: 10.1021/bm200083n.

[270] A. L. Hillberg, C. A. Holmes, and M. Tabrizian, “Effect of genipin cross-linking on the cellular adhesion properties of layer-by-layer assembled polyelectrolyte films,” *Biomaterials*, vol. 30, no. 27, pp. 4463–4470, Sep. 2009, doi: 10.1016/J.BIOMATERIALS.2009.05.026.

[271] T. L. Donahue, T. R. Haut, C. E. Yellowley, H. J. Donahue, and C. R. Jacobs, “Mechanosensitivity of bone cells to oscillating fluid flow induced shear stress may be modulated by chemotransport,” *J Biomech*, vol. 36, no. 9, pp. 1363–1371, 2003, doi: 10.1016/S0021-9290(03)00118-0.

[272] K. Naito, K. Matsuzaka, K. Ishigami, and T. Inoue, “Mechanical force promotes proliferation and early differentiation of bone marrow derived osteoblast-like cells in vitro,” *Oral Medicine & Pathology*, vol. 13, no. 4, pp. 143–149, 2009, doi: 10.3353/OMP.13.143.

[273] H. Bahmaee *et al.*, “Design and Evaluation of an Osteogenesis-on-a-Chip Microfluidic Device Incorporating 3D Cell Culture,” *Front Bioeng Biotechnol*, vol. 8, p. 557111, Sep. 2020, doi: 10.3389/FBIOE.2020.557111/BIBTEX.

[274] Y. Xi, “Flow duration and cell culture optimization,” *Sci Rep*, 2021, doi: 10.1038/s41598-021-87645-6.

[275] D. H. Lee, J. C. Park, and H. Suh, “Effect of centrifugal force on cellular activity of osteoblastic MC3T3-E1 cells in vitro,” *Yonsei Med J*, vol. 42, no. 4, pp. 405–410, 2001, doi: 10.3349/YMJ.2001.42.4.405.

[276] L. Prodanov, J. J. W. A. Van Loon, J. Te Riet, J. A. Jansen, and X. F. Walboomers, “Substrate nanotexture and hypergravity through centrifugation enhance initial osteoblastogenesis,” *Tissue Eng Part A*, vol. 19, no. 1–2, pp. 114–124, Jan. 2013, doi: 10.1089/TEN.TEA.2012.0267.

[277] L. Yu *et al.*, “Fluid shear stress induces osteoblast differentiation and arrests the cell cycle at the G0 phase via the ERK1/2 pathway,” *Mol Med Rep*, vol. 16, no. 6, pp. 8699–8708, Dec. 2017, doi: 10.3892/MMR.2017.7720.

[278] W. Luo *et al.*, “Laminar shear stress delivers cell cycle arrest and anti-apoptosis to mesenchymal stem cells,” *Acta Biochim Biophys Sin (Shanghai)*, vol. 43, no. 3, pp. 210–216, Mar. 2011, doi: 10.1093/ABBS/GMR004.

[279] S. M. Warren, A. M. Sailon, A. C. Allori, E. H. Davidson, D. D. Reformat, and R. J. Allen, “A Novel Flow-Perfusion Bioreactor Supports 3D Dynamic Cell Culture,” *J Biomed Biotechnol*, vol. 2009, p. 873816, 2009, doi: 10.1155/2009/873816.

[280] P. Erickson, T. Houwayek, A. Burr, M. Teryek, and B. Parekkadan, “A continuous flow cell culture system for precision cell stimulation and time-resolved profiling of cell secretion,” *Anal Biochem*, vol. 625, p. 114213, Jul. 2021, doi: 10.1016/J.AB.2021.114213.

[281] S. El Hajj *et al.*, “Bone Spheroid Development Under Flow Conditions with Mesenchymal Stem Cells and Human Umbilical Vein Endothelial Cells in a 3D Porous Hydrogel Supplemented with Hydroxyapatite,” *Gels*, vol. 10, no. 10, p. 666, Oct. 2024, doi: 10.3390/GELS10100666/S1.

[282] G. Hu *et al.*, “Glutathione limits RUNX2 oxidation and degradation to regulate bone formation,” *JCI Insight*, vol. 8, no. 16, 2023, doi: 10.1172/JCI.INSIGHT.166888.

[283] B. David *et al.*, “A Perfusion Bioreactor for Engineering Bone Constructs: An In Vitro and In Vivo Study,” *https://home.liebertpub.com/tec*, vol. 17, no. 5, pp. 505–516, Feb. 2011, doi: 10.1089/TEN.TEC.2010.0468.

[284] J. G. Mcgarry, J. Klein-Nulend, M. G. Mullender, and P. J. Prendergast, “A comparison of strain and fluid shear stress in stimulating bone cell responses--a computational and experimental study,” *FASEB J*, vol. 19, no. 3, pp. 1–22, Mar. 2005, doi: 10.1096/FJ.04-2210FJE.

[285] M. Banh, “Centrifuge-based force modulation for OoC,” *Biomaterials*, 2020, doi: 10.1016/j.biomaterials.2020.120876.

[286] J. Detzel, M. Thorson, and C. Ivory, “A Study of the Coriolis Effect on the Fluid Flow Profile in a Centrifugal Bioreactor,” *Biotechnol Prog*, no. 1, pp. 705–723, 2009, doi: 10.1002/btpr.183.

[287] H. Choi, “Bone cell mechanosensory systems,” *Sci Rep*, 2020, doi: 10.1038/s41598-020-68902-6.

[288] B. L. Ricca, G. Venugopalan, and D. A. Fletcher, “To pull or be pulled: parsing the multiple modes of mechanotransduction,” *Curr Opin Cell Biol*, vol. 25, no. 5, pp. 558–564, Oct. 2013, doi: 10.1016/J.CEB.2013.06.002.

[289] R. J. McCoy and F. J. O’Brien, “Influence of shear stress in perfusion bioreactor cultures for the development of three-dimensional bone tissue constructs: A review,” *Tissue Eng Part B Rev*, vol. 16, no. 6, pp. 587–601, Dec. 2010, doi: 10.1089/TEN.TEB.2010.0370.

[290] R. J. Mccoy, C. Jungreuthmayer, and F. J. O’Brien, “Influence of flow rate and scaffold pore size on cell behavior during mechanical stimulation in a flow perfusion bioreactor,” *Biotechnol Bioeng*, vol. 109, no. 6, pp. 1583–1594, Jun. 2012, doi: 10.1002/BIT.24424.

[291] A. B. Yeatts and J. P. Fisher, “Bone tissue engineering bioreactors: Dynamic culture and the influence of shear stress,” *Bone*, vol. 48, no. 2, pp. 171–181, Feb. 2011, doi: 10.1016/J.BONE.2010.09.138.

[292] D. Liu, D. Fang, W. Li, X. Wan, L. Lang, and Z. Wang, “Whole serum as cell protection reagent in cell shipment at low or room temperature,” *Tissue Cell*, vol. 80, p. 101994, Feb. 2023, doi: 10.1016/J.TICE.2022.101994.

[293] I. Horiguchi *et al.*, “Protection of human induced pluripotent stem cells against shear stress in suspension culture by Bingham plastic fluid,” *Biotechnol Prog*, vol. 37, no. 2, Mar. 2021, doi: 10.1002/BTPR.3100.

[294] E. Buick *et al.*, “Cell shipment without a cold chain,” *Biopreserv Biobank*, vol. 22, no. 3, pp. 179–180, Sep. 2020, doi: 10.1089/BIO.2023.0100.

[295] X. Chen and S. Thibeault, “Effect of DMSO Concentration, Cell Density and Needle Gauge on the Viability of Cryopreserved Cells in Three Dimensional Hyaluronan Hydrogel,” *Conference proceedings : Annual International Conference of the IEEE Engineering in Medicine and Biology Society. IEEE Engineering in Medicine and*

Biology Society. Conference, vol. 2013, p. 6228, 2013, doi: 10.1109/EMBC.2013.6610976.

[296] J. Galvao, B. Davis, M. Tilley, E. Normando, M. R. Duchen, and M. F. Cordeiro, "Unexpected low-dose toxicity of the universal solvent DMSO," *FASEB Journal*, vol. 28, no. 3, pp. 1317–1330, 2014, doi: 10.1096/FJ.13-235440,.

[297] B. Rothammer *et al.*, "Rheological behavior of an artificial synovial fluid – influence of temperature, shear rate and pressure," *J Mech Behav Biomed Mater*, vol. 115, no. October 2020, p. 104278, 2021, doi: 10.1016/j.jmbbm.2020.104278.

[298] C. Poon, "Measuring the density and viscosity of culture media for optimized computational fluid dynamics analysis of in vitro devices," *J Mech Behav Biomed Mater*, vol. 126, p. 105024, Feb. 2022, doi: 10.1016/J.JMBBM.2021.105024.

[299] P. V. Hinton, S. M. Rackard, and O. D. Kennedy, "In Vivo Osteocyte Mechanotransduction: Recent Developments and Future Directions," *Curr Osteoporos Rep*, vol. 16, no. 6, pp. 746–753, Dec. 2018, doi: 10.1007/S11914-018-0485-1.

[300] S. Weinbaum, S. C. Cowin, and Y. Zeng, "Mechanotransduction and flow sensation in bone," *Annu Rev Biomed Eng*, vol. 13, pp. 119–147, 2011, doi: 10.1146/annurev-bioeng-071910-124701.

[301] Y. Q. Chen, M. C. Wu, M. T. Wei, J. C. Kuo, H. W. Yu, and A. Chiou, "High-viscosity driven modulation of biomechanical properties of human mesenchymal stem cells promotes osteogenic lineage," *Mater Today Bio*, vol. 26, p. 101058, Jun. 2024, doi: 10.1016/J.MTBIO.2024.101058.

[302] C. Lu *et al.*, "Influence of viscosity on adipogenic and osteogenic differentiation of mesenchymal stem cells during 2D culture," *Biomater Sci*, vol. 12, no. 21, pp. 5598–5609, Oct. 2024, doi: 10.1039/D4BM00710G.

[303] G. Fletcher, "Long-term force actuation in bone OoC," *Biomaterials*, 2020, doi: 10.1016/j.biomaterials.2020.120112.

[304] F. Zhao, D. Lacroix, K. Ito, B. van Rietbergen, and S. Hofmann, "Changes in scaffold porosity during bone tissue engineering in perfusion bioreactors considerably affect

cellular mechanical stimulation for mineralization," *Bone Rep*, vol. 12, p. 100265, Jun. 2020, doi: 10.1016/J.BONR.2020.100265.

[305] B. H. Johnstone, D. Gu, C.-H. Lin, J. Du, and E. J. Woods, "Identification of a fundamental cryoinjury mechanism in MSCs and its mitigation through cell-cycle synchronization prior to freezing," *Cryobiology*, vol. 113, 2023, doi: 10.1016/j.cryobiol.2023.104592.

[306] W. Lee, S. R. Eo, J. H. Choi, Y. M. Kim, M. H. Nam, and Y. K. Seo, "The Osteogenic Differentiation of Human Dental Pulp Stem Cells through G0/G1 Arrest and the p-ERK/Runx-2 Pathway by Sonic Vibration," *Int J Mol Sci*, vol. 22, no. 18, p. 10167, Sep. 2021, doi: 10.3390/IJMS221810167.

[307] H. Simmons, "ECM-mimicking support materials for bone tissue," *Biomaterials*, 2021, doi: 10.1016/j.biomaterials.2021.120987.

[308] A. M. F. S. Mohamed, "An overview of bone cells and their regulating factors of differentiation," *Malaysian Journal of Medical Sciences*, vol. 15, no. 1, pp. 4–12, 2008.

[309] F. Papadogiannis *et al.*, "Osteogenic differentiation of bone marrow mesenchymal stem cells on chitosan/gelatin scaffolds: gene expression profile and mechanical analysis," *Biomed Mater*, vol. 15, no. 6, Nov. 2020, doi: 10.1088/1748-605X/ABA325.

[310] V. I. Sikavitsas, G. N. Bancroft, J. J. Lemoine, M. A. K. Liebschner, M. Dauner, and A. G. Mikos, "Mineralized matrix deposition by marrow stromal osteoblasts in 3D perfusion culture increases with increasing fluid shear forces," Proceedings of the National Academy of Sciences of the United States of America (2003) 100(25) 14683-14688, doi: 10.1073/pnas.2434367100

[311] Y. Ban *et al.*, "Response of osteoblasts to low fluid shear stress is time dependent," *Tissue Cell*, vol. 43, no. 5, pp. 311–317, Oct. 2011, doi: 10.1016/J.TICE.2011.06.003.

[312] D. Li, T. Tang, J. Lu, and K. Dai, "Effects of flow shear stress and mass transport on the construction of a large-scale tissue-engineered bone in a perfusion bioreactor," *Tissue Eng Part A*, vol. 15, no. 10, pp. 2773–2783, Oct. 2009, doi: 10.1089/TEN.TEA.2008.0540.

[313] A. Mansoorifar, R. Gordon, R. C. Bergan, and L. E. Bertassoni, “Bone-on-a-chip: microfluidic technologies and microphysiologic models of bone tissue,” *Adv Funct Mater*, vol. 31, no. 6, p. 2006796, Feb. 2020, doi: 10.1002/ADFM.202006796.

[314] J. Li *et al.*, “An Overview of Organs-on-Chips Based on Deep Learning,” *Research*, vol. 2022, p. 9869518, Jan. 2022, doi: 10.34133/2022/9869518.

[315] S. H. Kong and C. S. Shin, “Applications of Machine Learning in Bone and Mineral Research,” Endocrinol. Metab. (Seoul), vol. 36, no. 5, pp. 928–937, Oct. 2021, doi: 10.3803/ENM.2021.1111.

[316] P. Ma, A. Qin, T. Winkler, and J. Zhao, “Harnessing mechanobiology to enhance cell therapy,” *Mechanobiology in Medicine*, vol. 2, no. 4, p. 100102, Dec. 2024, doi: 10.1016/J.MBM.2024.100102.

[317] D. K. Nguyen, C. H. Lan, and C. L. Chan, “Deep ensemble learning approaches in healthcare to enhance the prediction and diagnosing performance: the workflows, deployments, and surveys on the statistical, image-based, and sequential datasets,” *Int J Environ Res Public Health*, vol. 18, no. 20, Oct. 2021, doi: 10.3390/IJERPH182010811.

[318] R. Wilson and J. Lee, “Deep learning for tissue classification,” *Comput Biol Med*, 2019, doi: 10.1016/j.compbiomed.2019.103348.

[319] T. Han, S. A. Ponduru, R. Cook, J. Huang, G. Sant, and A. Kumar, “A Deep Learning Approach to Design and Discover Sustainable Cementitious Binders: Strategies to Learn From Small Databases and Develop Closed-form Analytical Models,” *Front Mater*, vol. 8, no. January, pp. 1–15, 2022, doi: 10.3389/fmats.2021.796476.

[320] J. Lever, M. Krzywinski, and N. Altman, “Points of Significance: Model selection and overfitting,” Aug. 2016, *Nature Publishing Group*. doi: 10.1038/nmeth.3968.

[321] H. Il Suk, S. W. Lee, and D. Shen, “Deep ensemble learning of sparse regression models for brain disease diagnosis,” *Med Image Anal*, vol. 37, pp. 101–113, Apr. 2017, doi: 10.1016/J.MEDIA.2017.01.008.

[322] B. Dickson, “A new technique called ‘concept whitening’ promises to provide neural network interpretability | VentureBeat,” 2021, [Online]. Available:

https://venturebeat.com/2021/01/12/a-new-technique-called-concept-whitening-promises-to-provide-neural-network-interpretability/

[323] A. M. Salih *et al.*, "A Perspective on Explainable Artificial Intelligence Methods: SHAP and LIME," Jun. 2024, doi: 10.1002/aisy.202400304.

[324] S. N. Rampersad, "Multiple applications of Alamar Blue as an indicator of metabolic function and cellular health," *Sensors*, vol. 12, no. 9, pp. 12347–12360, 2012, doi: 10.3390/s120912347.

[325] G. G. Hamedani *et al.*, "A New Right-Skewed One-Parameter Distribution with Mathematical Characterizations, Distributional Validation, and Actuarial Risk Analysis, with Applications," *Symmetry (Basel)*, vol. 15, no. 7, p. 1297, 2023, doi: 10.3390/sym15071297.

[326] G. Taylor and L. Anderson, "SVM for microfluidic applications," *MethodsX*, 2018, doi: 10.1016/j.mex.2018.12.010.

[327] L. Breiman, "Random forests," *Mach Learn*, vol. 45, no. 1, pp. 5–32, 2001, doi: 10.1023/A:1010933404324.

[328] "Popular Machine Learning Algorithms: CART, Random Forest, GBM, XGBoost, LightGBM, and CatBoost | by Merve Yavuz | Medium." Accessed: Jun. 08, 2025. [Online]. Available: https://medium.com/@arcyalcin/popular-machine-learning-algorithms-cart-random-forest-gbm-xgboost-lightgbm-and-catboost-2c22018cadef

[329] T. Akiba, S. Sano, T. Yanase, T. Ohta, and M. Koyama, "Optuna: A next-generation hyperparameter optimization framework," in *Proceedings of the 25th ACM SIGKDD International Conference on Knowledge Discovery & Data Mining*, 2019, pp. 2623–2631. doi: 10.1145/3292500.3330701.

[330] A. Demircioğlu, "The effect of feature normalization methods in radiomics," *Insights into Imaging 2023 15:1*, vol. 15, no. 1, pp. 2-, Jan. 2024, doi: 10.1186/S13244-023-01575-7.

[331] S. Walczak and N. Cerpa, "Artificial Neural Networks," *Encyclopedia of Physical Science & Technology*, pp. 631–645, Jan. 2003, doi: 10.1016/B0-12-227410-5/00837-1.

[332] T. T. Dufera, “Deep neural network for system of ordinary differential equations: Vectorized algorithm and simulation,” *Machine Learning with Applications*, vol. 5, p. 100058, Sep. 2021, doi: 10.1016/J.MLWA.2021.100058.

[333] J. R. Terven, D. M. Cordova-Esparza, A. Ramirez-Pedraza, E. A. Chavez-Urbiola, and J. A. Romero-Gonzalez, “LOSS FUNCTIONS AND METRICS IN DEEP LEARNING PUBLISHED IN SPRINGER ARTIFICIAL INTELLIGENCE REVIEW AS: A COMPREHENSIVE SURVEY OF LOSS FUNCTIONS AND METRICS IN DEEP LEARNING,” 2025, doi: 10.1007/s10462-025-11198-7.

[334] F. Nazari and W. Yan, “Convolutional versus Dense Neural Networks: Comparing the Two Neural Networks’ Performance in Predicting Building Operational Energy Use Based on the Building Shape”.

[335] D. Muhammad and M. Bendechache, “Unveiling the black box: A systematic review of Explainable Artificial Intelligence in medical image analysis,” *Comput Struct Biotechnol J*, vol. 24, pp. 542–560, Dec. 2024, doi: 10.1016/j.csbj.2024.08.005.

[336] A. Singh, S. Sengupta, and V. Lakshminarayanan, “Explainable Deep Learning Models in Medical Image Analysis,” *J Imaging*, vol. 6, no. 6, p. 52, Jun. 2020, doi: 10.3390/JIMAGING6060052.

[337] M. L. Santoni, E. Raponi, R. De Leone, and C. Doerr, “Comparison of High-Dimensional Bayesian Optimization Algorithms on BBOB,” *ACM Transactions on Evolutionary Learning and Optimization*, vol. 4, no. 3, Mar. 2023, doi: 10.1145/3670683.

[338] R. L. Marchese Robinson, A. Palczewska, J. Palczewski, and N. Kidley, “Comparison of the Predictive Performance and Interpretability of Random Forest and Linear Models on Benchmark Data Sets,” *J Chem Inf Model*, vol. 57, no. 8, pp. 1773–1792, Aug. 2017, doi: 10.1021/ACS.JCIM.6B00753.

[339] M. Sabzekar and S. M. H. Hasheminejad, “Robust regression using support vector regressions,” *Chaos Solitons Fractals*, vol. 144, p. 110738, Mar. 2021, doi: 10.1016/J.CHAOS.2021.110738.

[340] E. Raczko and B. Zagajewski, “Comparison of support vector machine, random forest and neural network classifiers for tree species classification on airborne hyperspectral APEX images,” *Eur J Remote Sens*, vol. 50, no. 1, pp. 144–154, 2017, doi: 10.1080/22797254.2017.1299557.

[341] N. Shirish Keskar, D. Mudigere, J. Nocedal, M. Smelyanskiy, P. Tak, and P. Tang, “On Large-Batch Training for Deep Learning: Generalization Gap & Sharp Minima,” 2017.

[342] S. Park and N. Kwak, “Analysis on the dropout effect in convolutional neural networks,” *Lecture Notes in Computer Science (including subseries Lecture Notes in Artificial Intelligence and Lecture Notes in Bioinformatics)*, vol. 10112 LNCS, pp. 189–204, 2017, doi: 10.1007/978-3-319-54184-6_12.

[343] W. Wydmanski, O. Bulenok, and M. Smieja, “HyperTab: Hypernetwork Approach for Deep Learning on Small Tabular Datasets,” *2023 IEEE 10th International Conference on Data Science and Advanced Analytics, DSAA 2023 - Proceedings*, Apr. 2023, doi: 10.1109/DSAA60987.2023.10302504.

[344] A. Alwosheel, S. van Cranenburgh, and C. G. Chorus, “Is your dataset big enough? Sample size requirements when using artificial neural networks for discrete choice analysis,” *Journal of Choice Modelling*, vol. 28, pp. 167–182, Sep. 2018, doi: 10.1016/J.JOCM.2018.07.002.

[345] A. A. El-Rashidy *et al.*, “Effect of Polymeric Matrix Stiffness on Osteogenic Differentiation of Mesenchymal Stem/Progenitor Cells: Concise Review,” *Polymers 2021, Vol. 13, Page 2950*, vol. 13, no. 17, p. 2950, Aug. 2021, doi: 10.3390/POLYM13172950.

[346] A. Talaei *et al.*, “Optimizing the composition of gelatin methacryloyl and hyaluronic acid methacryloyl hydrogels to maximize mechanical and transport properties using response surface methodology,” *J Biomed Mater Res B Appl Biomater*, vol. 111, no. 3, pp. 526–537, Mar. 2023, doi: 10.1002/JBM.B.35169.

[347] C. E. Holy, Soichet M. S ., and Davies J. E., “Three-dimensional culture of rat calvarial osteoblasts in porous biodegradable polymers,” *J Biomed Mater Res*, vol. 2000 Sep 5 51(3), no. 15, pp. 376–382, Sep. 2000, doi: 10.1002/1097-4636(20000905)51:3

[348] Y. Tao *et al.*, “Enhanced functionalities of biomaterials through metal ion surface modification,” *Front Bioeng Biotechnol*, vol. 13, p. 1522442, Apr. 2025, doi: 10.3389/FBIOE.2025.1522442/FULL.

[349] S. Kapur, S. Mohan, D. J. Baylink, and K. H. W. Lau, “Fluid shear stress synergizes with insulin-like growth factor-I (IGF-I) on osteoblast proliferation through integrin-dependent activation of IGF-I mitogenic signaling pathway,” *Journal of Biological Chemistry*, vol. 280, no. 20, pp. 20163–20170, May 2005, doi: 10.1074/jbc.M501460200.

[350] K. Zha *et al.*, “Heterogeneity of mesenchymal stem cells in cartilage regeneration : from characterization to application,” 2021, doi: 10.1038/s41536-021-00122-6.

[351] B. P. Hung, D. L. Hutton, and W. L. Grayson, “Mechanical control of tissue-engineered bone,” *Stem Cell Research & Therapy 2013 4:1*, vol. 4, no. 1, pp. 10-, Jan. 2013, doi: https://doi.org/10.1186/scrt158.

[352] S. Yamada, M. A. Yassin, T. Schwarz, J. Hansmann, and K. Mustafa, “Induction of osteogenic differentiation of bone marrow stromal cells on 3D polyester-based scaffolds solely by subphysiological fluidic stimulation in a laminar flow bioreactor,” *J Tissue Eng*, vol. 12, p. 20417314211019376, 2021, doi: 10.1177/20417314211019375.

[353] Thermo Fisher Scientific, “Cell Culture Environment | Thermo Fisher Scientific - UK,” Thermo Fisher Scientific. Accessed: Oct. 09, 2025. [Online]. Available: https://www.thermofisher.com/uk/en/home/references/gibco-cell-culture-basics/cell-culture-environment.html

[354] Y. Yu, S. Xu, S. Li, and H. Pan, “Genipin-cross-linked hydrogels based on biomaterials for drug delivery: a review,” *Biomater Sci*, vol. 9, no. 5, pp. 1583–1597, Mar. 2021, doi: 10.1039/D0BM01403F.

[355] R. A. A. Muzzarelli, M. El Mehtedi, C. Bottegoni, A. Aquili, and A. Gigante, “Genipin-Crosslinked Chitosan Gels and Scaffolds for Tissue Engineering and Regeneration of Cartilage and Bone,” *Mar Drugs*, vol. 13, no. 12, p. 7314, Dec. 2015, doi: https://doi.org/10.3390/md13127068.

[356] Q. S. Wang, G. F. Wang, H. Y. Zhang, F. Q. Zhao, and Y. L. Cui, “Development of genipin crosslinked gelatin matrices on surface interaction: Enhancing the biocompatibility by attenuating sterile inflammation,” *Chin J Chem Eng*, vol. 38, pp. 205–215, Oct. 2021, doi: 10.1016/J.CJCHE.2021.03.022.

[357] B. P. Evans, B. Xue, and M. Zhang, “Improving generalisation of AutoML systems with dynamic fitness evaluations,” *GECCO 2020 - Proceedings of the 2020 Genetic and Evolutionary Computation Conference*, pp. 324–332, Jan. 2020, doi: 10.1145/3377930.3389805.

[358] “Gradient Boosting Frameworks (XGBoost, LightGBM, CatBoost) – Innovative Data Science & AI Consulting – David Gramling, Ph.D.” Accessed: Jun. 08, 2025. [Online]. Available: https://sawdatascience.com/gradient-boosting-frameworks-xgboost-lightgbm-catboost/

[359] “Ensemble Learning: How Combining Multiple Models Can Improve Your Machine Learning Results | by Data Overload | Medium.” Accessed: Jun. 08, 2025. [Online]. Available: https://medium.com/@data-overload/ensemble-learning-how-combining-multiple-models-can-improve-your-machine-learning-results-7683e4ea6bef

[360] A. Hosna, E. Merry, J. Gyalmo, Z. Alom, Z. Aung, and M. A. Azim, “Transfer learning: a friendly introduction,” *J Big Data*, vol. 9, no. 1, pp. 1–19, Dec. 2022, doi: 10.1186/S40537-022-00652-W.

[361] A. Moore and E. Johnson, “Gaussian process regression for microfluidics,” *J Theor Biol*, 2017, doi: 10.1016/j.jtbi.2017.11.022.

[362] A. Moore and E. Johnson, “Gaussian process for OoC optimization,” *J Theor Biol*, 2021, doi: 10.1016/j.jtbi.2021.110876.

[363] A. Cascarano *et al.*, “Machine and deep learning for longitudinal biomedical data: a review of methods and applications,” *Artif Intell Rev*, vol. 56, pp. 1711–1771, Nov. 2023, doi: 10.1007/S10462-023-10561-W.

[364] C. A. Siebra, M. Kurpicz-Briki, and K. Wac, “Transformers in health: a systematic review on architectures for longitudinal data analysis,” *Artificial Intelligence Review 2024 57:2*, vol. 57, no. 2, pp. 32-, Feb. 2024, doi: 10.1007/S10462-023-10677-Z.

[365] R. Mohapatra, M. Leist, S. von Aulock, and T. Hartung, “Guidance for Good In Vitro Reporting Standards (GIVReSt) - A draft for stakeholder discussion and background documentation,” *ALTEX*, vol. 42, no. 3, pp. 376–396, 2025, doi: 10.14573/ALTEX.2507041.

[366] E. Huizingh, “The Use of SPSS in Statistical Research,” *Applied Statistics with SPSS*, pp. 6–23, Apr. 2007, doi: 10.4135/9781446249390.

[367] “Comparison of New Era InfusionONE and SyringeONE.” Accessed: Jun. 24, 2026. [Online]. Available: https://blog.darwin-microfluidics.com/comparison-of-new-era-infusionone-and-syringeone/

Appendices

Appendix A1: All Design Revisions

The design of the BoC platform and microfluidic unit evolved over several design revisions to ensure the required developed flow of media would occur within the BoC channels and wells as part of the later validation, optimisation and main dual stimulation testing. The comparison of previous versions of the JoC or BoC unit, from 2nd to 5th revision, prior to the creation of mini-chip are shown in Fig A1.1. The final Mini-chip design chosen for production and experiments uses version 5 parallel cell-well (well parallel to channel) flow channel configuration depicted in the final image sequence at the bottom of Fig A1.1:

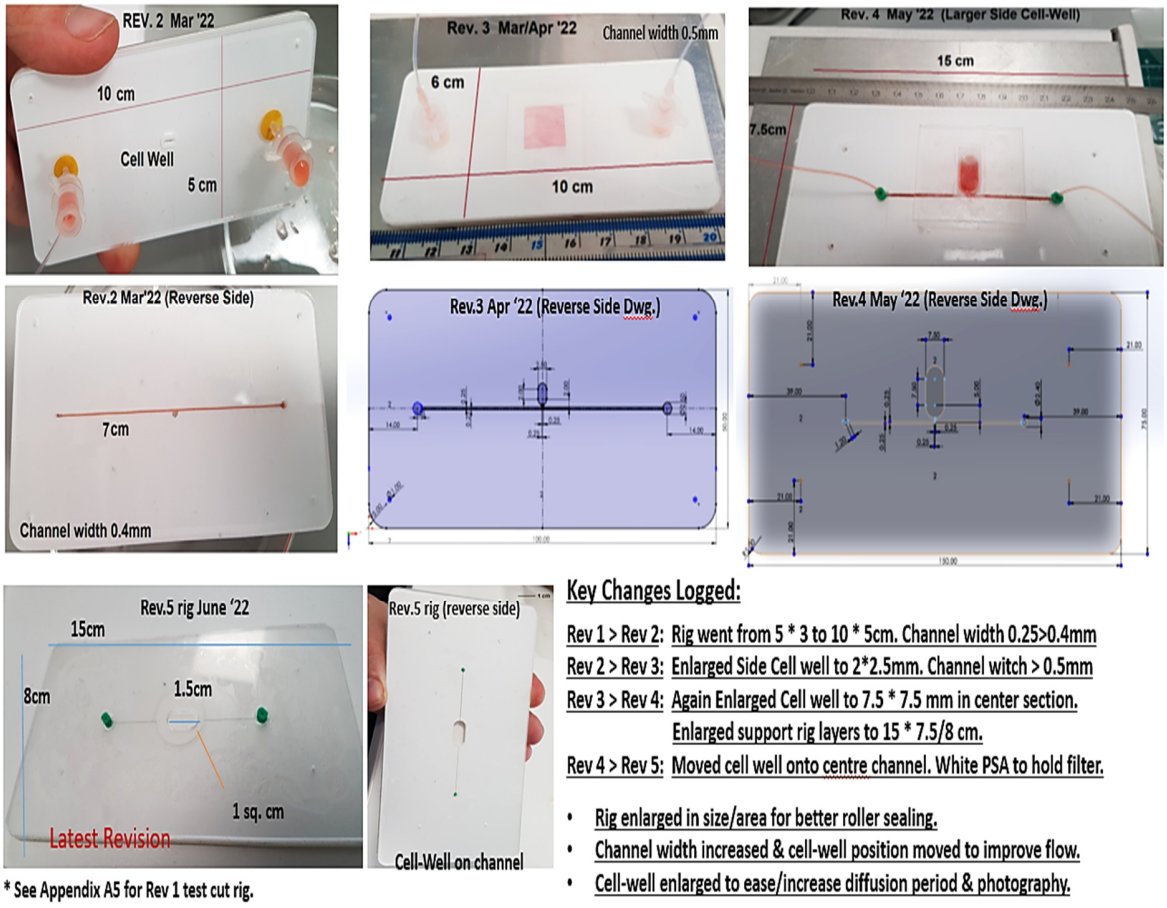


Fig A1.1 Montage of Microfluidic BoC revisions

The latest version of BoC units and platform used, with parallel cell-well configurations for single and tri-channel chips and double chip holder centrifuge disk to test up to two JBoCs simultaneously or test a single BoC while holding a similar weight dummy chip as a counter-weight during centrifuge tests:

A) **B)**

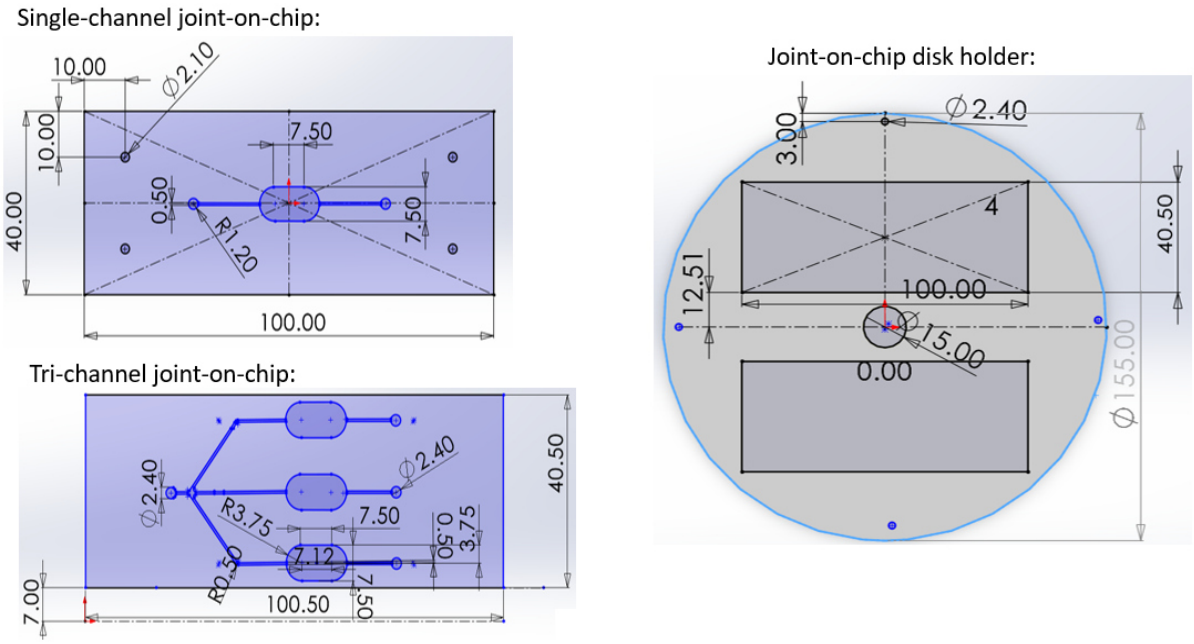


Fig A1.2 AutoCAD design with measurements. **A)** Design for single channel and tri-channel BoC **B)** Design for Centrifuge disk holder (platform holder) for up to two BoC units

An alternative configuration rectangular assay holder was also created to hold the long side of chips along the radial axis. This would allow chip samples in each chip well to be spun at similar radial distance from the centrifuge spin centre. The difference in chip well radial distance was negligible given chip length or width and corresponding angles (with distance variation remaining within 5 %).

Appendix A2: Raw Metrology Width & Roughness Data

The following raw channel width data to measure and compare individual BoC microfluidic channel widths was derived from the Keyence high-resolution digital microscope that was used to measure BoC channel widths. Some sample channels widths were also independently verified on the Bruker surface profilers, with this repeated for a sample sheet with 250-micron-wide channels to verify required quality performance at 500 microns or below:

Comparison of three separate single channel BoCs, dimension (µm):

Location:	Location #	Chip 1	Chip 2	Chip 3
Point Inlet	1	480	468	489
Inlet mid	2	465	470	486
Inlet near end	3	491	490	496
Inlet well	4	505	502	510
Outlet start	5	495	483	495
Outlet mid	6	463	473	487
Outlet end	7	472	464	489
	Channel Avg.	481.6	478.6	493.1
	Chip Std. Dev	14.8	12.7	7.7
	cv %	3.07%	2.65%	1.57%
	Avg dev from 500	-18.4	-21.4	-6.9
	Avg dev from 500 %	**-3.7%**	**-4.3%**	**-1.4%**

All chips avg	484.43
All chips std dev.	13.64
cv %	2.8%
avg dev. 500	-15.57
avg dev. 500 %	-3.1%

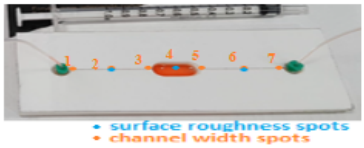


Fig A2.1 Comparison of three separate single channel BoCs, dimension (µm)

Comparison of channels within tri-channel BoC, dimension (μm):

Joint-on-chip Location:	Tri-channel chip Location #	Channel 1 Width (um)	Channel 2 Width (um)	Channel 3 Width (um)
Point Inlet	1	480		
Inlet mid	2	470	458	481
Inlet near end	3	493	490	481
Inlet well	4	512	505	502
Outlet start	5	497	487	493
Outlet mid	6	489	470	466
Outlet end	7	487	470	472
	Channel Avg.	489.7	480.0	482.5
	Chip Std. Dev	12.3	15.6	12.1
	cv %	2.50%	3.25%	2.51%
	Avg dev from 500	-10.3	-20.0	-17.5
	Avg dev from 500 %	**-2.06%**	**-4.00%**	**-3.50%**

All chips avg	484.37
All chips std dev.	14.00
cv %	2.9%
avg dev. 500	-15.63
avg dev. 500 %	-3.1%



Fig A2.2 Comparison of channels within tri-channel BoC, dimension (μm)

Comparison of surface roughness along single channel chip (μm):

Location:	Location #	Chip 1	Chip 2	Chip 3
Inlet floor	1	20.2	20.3	21.2
Cell Well floor	2	18.8	19.1	19.6
Outlet floor	3	21.4	22.3	22.8
	Channel Avg.	20.1	20.6	21.2
	Chip Std. Dev	1.1	1.3	1.3
	cv %	5.28%	6.42%	6.16%
	avg dev. 1mm depth	0.02	0.02	0.02
	avg dev. 1mm depth %	**2.0%**	**2.1%**	**2.1%**

All chips avg	20.63
All chips std dev.	1.31
cv %	6.4%
avg dev. 1mm depth %	2.1%

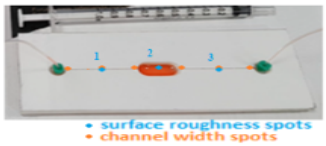


Fig A2.3 Comparison of surface roughness along single channel chip (μm)

Comparison of surface roughness along tri-channel chip (µm):

Location:	Location #	Channel 1	Channel 2	Channel 3
Inlet floor	1	23.2	21.3	24.2
Cell Well floor	2	20.8	22.1	25.6
Outlet floor	3	21.2	22.7	22.1
	Channel Avg.	21.7	22.0	24.0
	Chip Std. Dev	1.0	0.6	1.4
	cv %	4.83%	2.60%	6.00%
	avg dev. 1mm depth	0.02	0.02	0.02
	avg dev. 1mm depth %	**2.2%**	**2.2%**	**2.4%**

All chips avg	22.58
All chips std dev.	1.46
cv %	6.5%
avg dev. 1mm depth %	2.3%

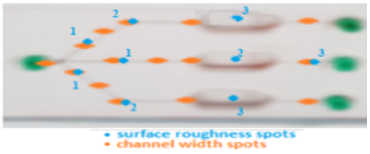


Fig A2.4 Comparison of surface roughness along tri-channel chip (µm)

Surface roughness sampled as in X or Y profiles – plots below to compose surface roughness (previous tables) as part of the chip validation process in Section 3.2.2. Sample surface roughness profiling on PMMA sheets with 250-micron channels (outer limit testing) also verified channel widths independent of optimal microscopy.

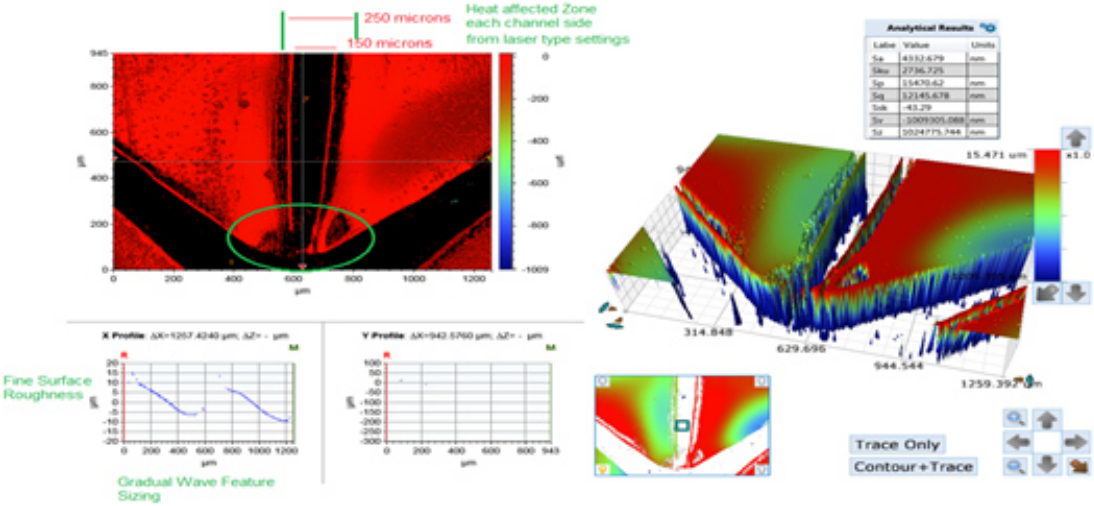


Fig A2.5 Quality inspection of chip tri-channel junction (width and height profiling)

Appendix A3: Detailed Flow Testing RGB Data

Various snapshots were taken during the experimental set up during the fill/empty variation tests. Fig A3.1 illustrates the lab setup for flow testing with a parallel cell-well chip during a fill test. A KFTechnology NE-1000 syringe pump is used to fill a parallel cell-well chip fill.

A)

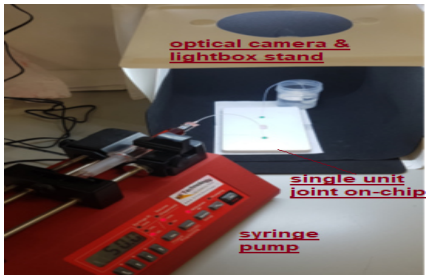
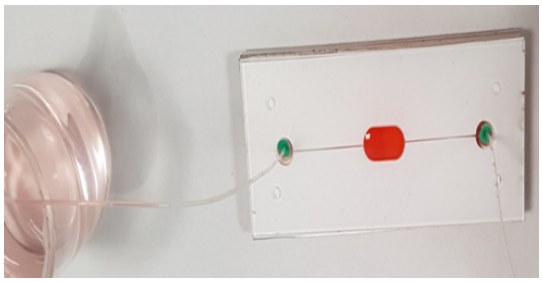


Fig A3.1 A) Lightbox used to control Background

B)



B) Mini-chip (right) has fluid-filled outlet to avoid capillary back-flow

Timing for gels to ooze media and for cell wells to fill/empty were recorded, and a detailed time-series set of image snapshots were taken for filling and emptying. An example cell-well fill/emptying test with thixotropic dye by a sample flow rate (50µL/min) is given below, this was repeated for all flow rates with results given in Section 3.3.1, with a sample shown in Fig A3.2.

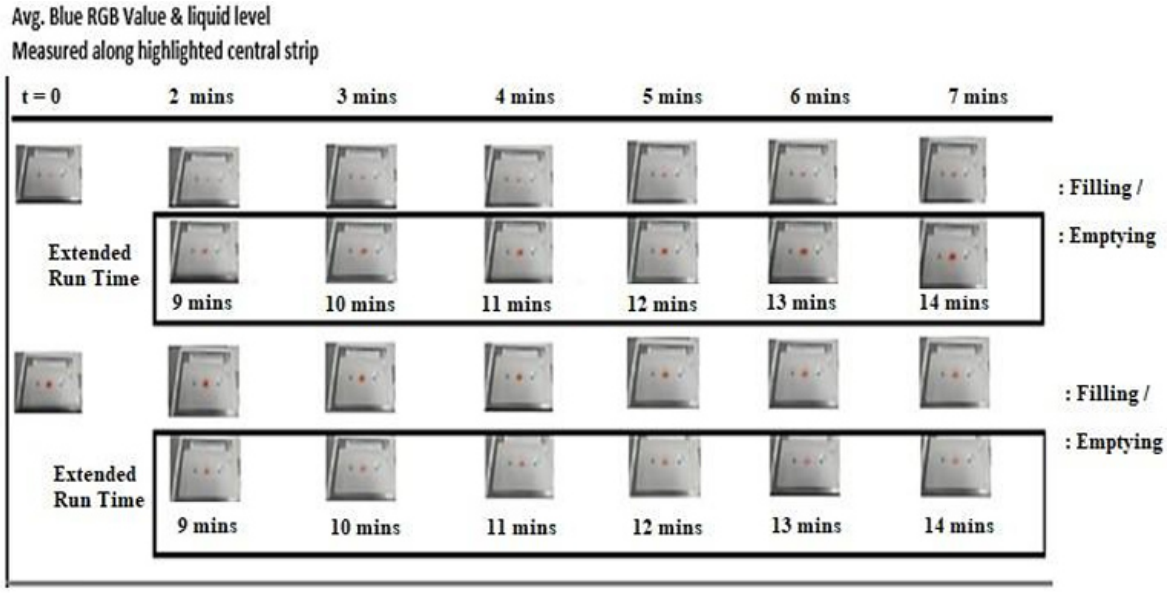


Fig A3.2 Recorded Timings of Filling and Emptying of a single channel BoC at 50 µL/min

This time series of image data could be taken and processed by ImageJ to take image Red, Geen and Blue (RGB) colour components and split and analyse their change in values in the regions of interest within the cell well. Upon media or test fluid entry, flow shear was observed to start occurring when a 0.5 mm wide rim of media formed around the perimeter rim of the cell well gels and diffusion of media into the gels then commenced until saturation was reached as excess media crossed the well with a gradual and upward filling of the cell well.

In the Fig A3.3 top-image below, sample result data below of gradient change dyed fluid fill level altering RGB (particular G, B) colour intensity as a function of mid cell –well x distance (horizontal distance), demonstrating the presence of progressively increasing diffusion with spatial gradient fill/emptying above filter membranes within the cell wells. Expected mirror-image behaviour between filling and emptying is observed. This was used to verify when complete filling and emptying of wells had occurred with corresponding fill, empty times, measured repeatedly (in triplicate) to determine the fill/empty fill rate variance and hence flow time variance.

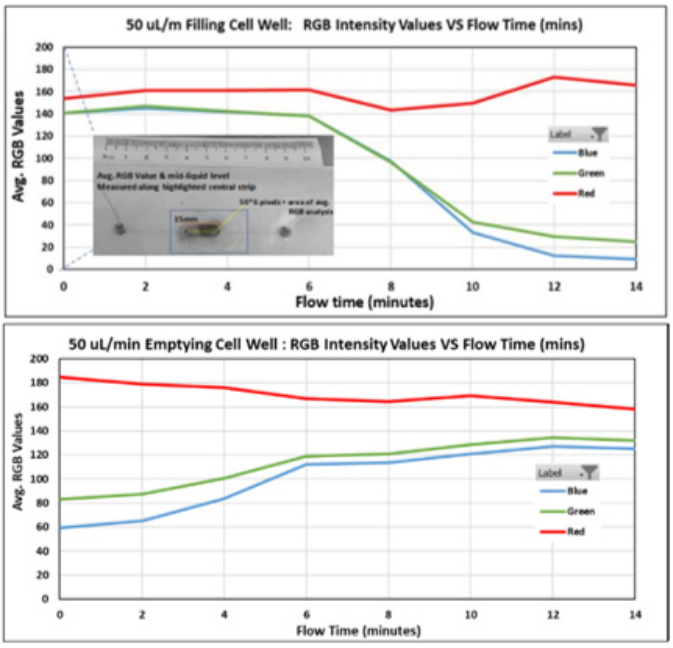


Fig A3.3 Recorded Fill level, and timings of filling/emptying of a single channel BoC at 50 µL/min

Fig A3.4 also shows similar mirror-image R G D value alteration behaviour between dye fluid filling and emptying within cell-wells. This observed dyed fluid level and RGD level (hence RGB colour intensities) are shown for various flow rates and over flow time as well as cell-well x-length:

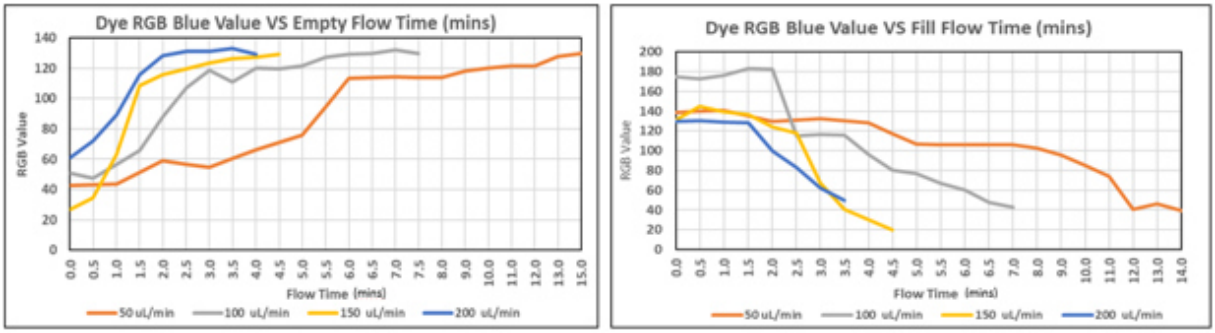


Fig A3.4 Recorded timings of filling/emptying of a single channel BoC by different flow rates

Binary non-steady state diffusion was taken as the approximate closest model that most closely explained this observed behaviour over time in Fig A3.4. Variable diffusion rates over time were observed as a function of flow rates. Diffusion as a function cell-well x-distance was also observed in figure A3.3. This further demonstrates variable diffusion occurring, as a function of cell well dyed fluid fill/empty level. This is consistent or generally congruent across different flow rates demonstrating variable diffusion at varied flow rates with variation across all flow rates, that is seen as part of flow verification in Fig A3.5 where a variety of syringe types were tested on syringe pump flow rates of 5 – 1000 µL/min. The flow rate was measured by the volume of a BoC cell well divided by the volume's fill time and then measured by this well volume divided by its empty time, with both measurements made three times to give six flow rate measurements. The variation between the six of these measurements gave the flow rate variation. Testing showed a flow rate variation of ± 5 – 10 % from 10 µL/min or higher, indicating consistent and leak-free flow.

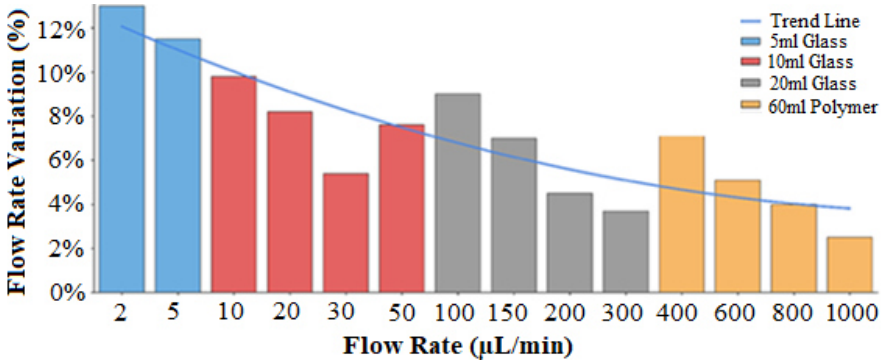


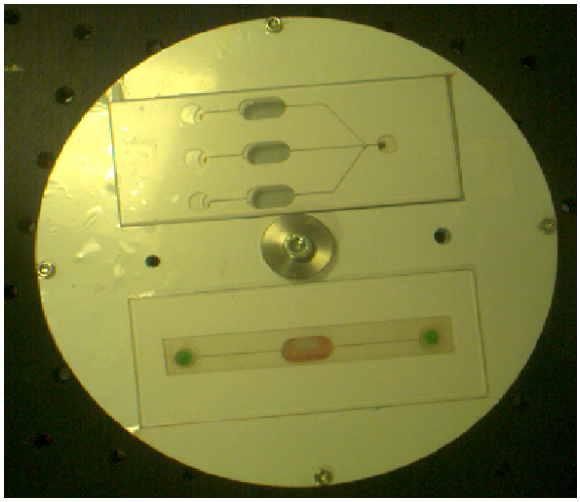
Fig A3.5 Recorded timings of filling/emptying of a single channel BoC by different flow rates

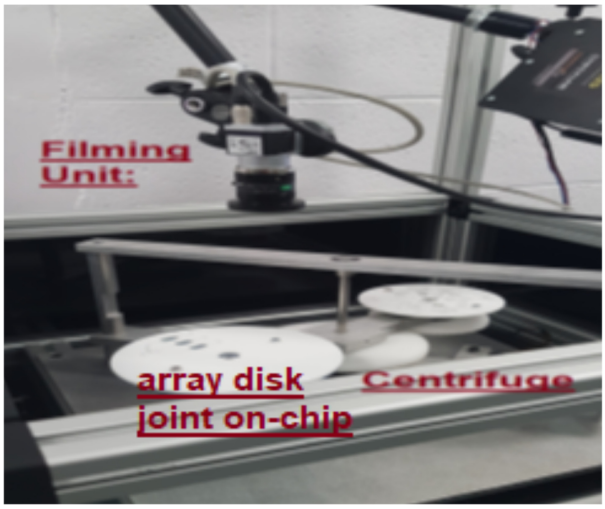
This flow verification testing showed a flow variation of 7 to 9 % (a plus or minus 3.5 to 4.5% deviation) at 50 – 150 µL/min using a 10ml glass syringe (at 50 µL/min) and a 20ml glass syringe (at 100 - 150 µL/min). This was similar to findings by independent vendor testing [367].

Appendix A4: Centrifuge Disk Setup & Testing

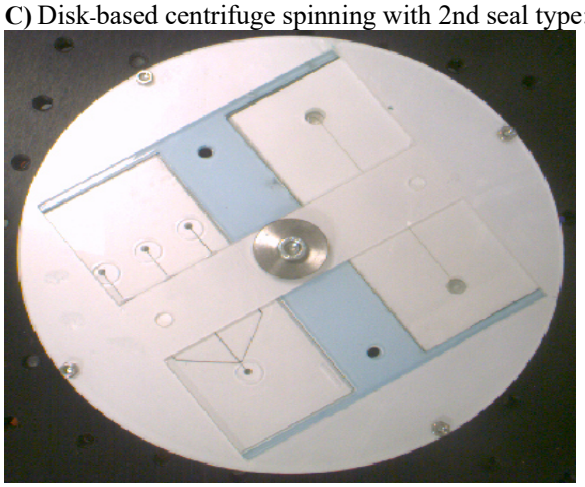
The centrifuge set-up was completed and successfully tested on the arm and disk spin-based centrifuge, with results of the disk spin system present in Section 4.2.3. Microfluidic flow testing was done due to the disk spin system applying higher angular velocity-based stresses on the chip test fluid and induced further mechanical integrity challenges for BoC in-disk platform. Three seal methods were tested. Method 1 (top-left image) comprised of clear PSA seal that was overlayed on the chip to prevent leakage. Method 2 (bottom-left image) had the same outer seal as Method 1 but also possessed an inner PSA seal over the cell wells and under the outer PSA seal. Method 3 (top-left image) used clear adhesion layers and clear PMMA cover plus addition PSA overlayed for the luer port sealings. This consistently prevented BoC seal leaks and damage with both arm and disk centrifuge methods. Method 3 was the chosen method in Section 4.2.2.

Fig A4.1 A Disk-based centrifuge with 1st seal time (top), that is clear PSA seal, and 3rd/final seal type (bottom): **B)** Arm-based centrifuge spun (larger radius lower speed)

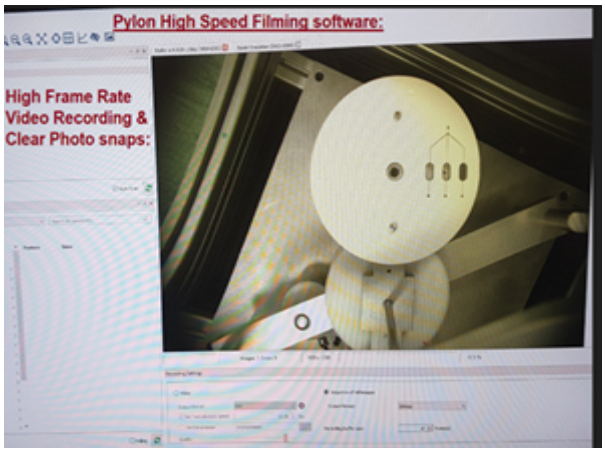




C) Disk-based centrifuge spinning with 2nd seal type:



D) Pylon automated video & image data



Images in this section are of demonstrated passed integrity and leak testing for the chips, taken at the end of centrifuge tests. Depending on support materials, the arm-based centrifuge (if available) may hold an advantage with lower spin velocities at a given applied centrifuge force with less probability of disrupting cell support materials. Alternatively, a smaller spin radius with higher angular velocity increased the Coriolis effect on cells. Stiffer gels and adhesion coatings with increased attachment/binding properties on studied cell types may further counteract this.

Appendix A5: SPSS T-Test Compare Alpha-Mem 10 % CellShip vs Alpha-Mem

This section compares the significance of difference between all samples with(out) CellShip for all individual assay outputs. A Python Graph-pad library derived statistical analysis was carried out on mid stage cell culture data (Week 3 to 6) to determine the most statistically significant relationships between input features and outputs as well as effect sizes. This comprehensive statistical analysis in Appendix A5 to A8 (with Section 3.3, 4.3 and 5.3 results analysis) used recommended GIVReSt as guidance for *in vitro* cell analysis reporting [365] and presents a detailed comparison between Alpha-Mem control media and Alpha-Mem 10 % CS (CellShip-enhanced) media across multiple biomarker measurements in a controlled experimental setting. The analysis follows SPSS statistical reporting conventions [366] , and includes descriptive statistics, independent samples t-tests, variance equality assessments, and detailed subgroup analyses by experimental conditions.

Dataset Overview

Total Sample Size: 417 observations
Control Group (Alpha-Mem): n = 225
Treatment Group (Alpha-Mem 10 % CS): n = 192

Measured Variables:
• 560nm_alamB - Alamar Blue viability assay
• 488nm_VFz_abs - ViaFluor absorbance
• 405nm_alkP - Alkaline phosphatase activity
• 488nm_VF_FL - ViaFluor fluorescence

Descriptive Statistics

Table A5.1: Descriptive Statistics Summary

Variable	Group	N	Mean	Std Dev	Std Error
560nm_alamB (alamarBlue™)	CtL	225	0.4119	0.2217	0.0148
	CS	192	0.5067	0.2602	0.0188
488nm_VFz_abs (ViaFluor Abs)	CtL	223	0.2910	0.1470	0.0098
	CS	192	0.3419	0.2075	0.0150
405nm_alkP (Alk Phosphatase)	CtL	223	0.3220	0.1654	0.0111
	CS	192	0.4108	0.2359	0.0170
488nm_VF_FL (ViaFluor FL)	CtL	204	272,069.36	193,116.02	13,520.83
	CS	144	331,865.43	184,249.62	15,354.14

Note: CtL = Alpha-Mem Control, CS = Alpha-Mem 10 % CS CellShip

Key Observations:

• CellShip group shows 23.0 % increase in alamarBlue™ signal (metabolic activity)

• ViaFluor absorbance elevated by 17.5 % (membrane integrity)

• Alkaline phosphatase activity increased by 27.6 % (osteogenic differentiation)

• ViaFluor fluorescence demonstrates 22.0 % enhancement (cellular activity)

Appendix A6: Compared effects of Centrifugation vs Non-Centrifugation on biomarker outputs

In this section the statistical significance of difference between Centrifuged and non Cenrifuged samples that also had various flow shear treatments was compared. A Python Graph-pad library derived statistical analysis was carried out on mid stage cell culture data (Week 3 to 6) to determine the most statistically significant relationships between input features and outputs as well as effect sizes. This comprehensive statistical analysis presents a detailed comparison between non-centrifuged (0 g-equiv) and centrifuged (1 g-equiv) samples across multiple biomarker measurements in a controlled experimental setting. The analysis follows SPSS statistical reporting conventions [366], and includes descriptive statistics, independent samples t-tests, variance equality assessments, and detailed subgroup analyses by flow rate and media type conditions.

Dataset Overview

Total Sample Size: 417 observations
Non-Centrifuged Group (0 g-equiv): n = 207
Centrifuged Group (1 g-equiv): n = 210

Measured Variables:

- 560nm_alamB - alamarBlue™ viability assay
- 488nm_VFz_abs - ViaFluor absorbance
- 405nm_alkP - Alkaline phosphatase activity
- 488nm_VF_FL - ViaFluor fluorescence

Descriptive Statistics

Table A6.1: Descriptive Statistics Summary

Variable	Group	N	Mean	Std Dev	Std Error
560nm_alamB (alamarBlue™)	C	207	0.4468	0.2443	0.0170
	NC	210	0.4642	0.2450	0.0169
488nm_VFz_abs (ViaFluor Abs)	C	207	0.3710	0.1902	0.0132
	NC	208	0.3082	0.1676	0.0116
405nm_alkP (Alk Phosphatase)	C	206	0.3705	0.2047	0.0143
	NC	209	0.3058	0.2069	0.0143
488nm_VF_FL (ViaFluor FL)	C	168	341,241.68	213,502.31	16,472.06
	NC	180	255,345.38	158,087.07	11,783.11

Note: NC = Non-Centrifuged (0 g-equiv), C = Centrifuged (1 g-equiv)

Key Observations:

• Centrifugation shows minimal effect on alamarBlue™ signal (minus 3.9 % decrease)

• ViaFluor normalised absorbance moderately increased with centrifugation (plus 23.0 %)

• Alkaline phosphatase activity moderately increased by centrifugation (plus 24.0 %)

• ViaFluor fluorescence significantly increased with centrifugation (plus 25.2 %)

Independent Samples T-Test Results

Table A6.2: Statistical Significance Testing

Variable	t-statistic	df	Significance	Mean Diff	Cohen's d
560nm_alamB (alamarBlue™)	-0.728	415	0.0467 *	0.0174	0.171 (Small)
488nm_VFz_abs (ViaFluor Abs)	0.723	413	0.0470 *	0.0127	0.211 (Small)
405nm_alkP (Alk Phosphatase)	0.726	413	0.0468 *	0.0147	0.271 (Small)
488nm_VF_FL (ViaFluor FL)	4.284	346	< 0.001***	85,896.30	0.460 (Medium)

Significance: *** p less than 0.001, ** p less than 0.01, * p less than 0.05

Effect Size: Small (0.2), Medium (0.5), Large (0.8)

Positive Cohen's d indicates higher values in non-centrifuged group

Variance Equality Assessment

Table A6.3: Levene's Test for Equality of Variances

Variable	F-statistic	Significance	Interpretation
560nm_alamB (alamarBlue™)	0.009	0.924	Equal variances assumed
488nm_VFz_abs (ViaFluor Abs)	0.075	0.785	Equal variances assumed
405nm_alkP (Alk Phosphatase)	0.227	0.634	Equal variances assumed
488nm_VF_FL (ViaFluor FL)	12.016	< 0.001***	Unequal variances

Interpretation: Most variables show equal variances between centrifuged and non-centrifuged groups, except for ViaFluor fluorescence which exhibits significantly unequal variances, indicating that centrifugation may affect the consistency of fluorescence measurements.

Subgroup Analysis by Flow Rate and Media Type

Table A6.4: Subgroup Analysis Summary

Flow Rate	Media Type	Variable	Non-Cent Mean	Cent Mean	p-value
50 µl/min	Alpha-Mem	560nm_alamB	0.694	0.554	0.033*
		488nm_VF_FL	508,340	345,212	0.014*
50 µl/min	Alpha-Mem 10 % CS	560nm_alamB	0.414	0.663	0.001**
100 µl/min	Alpha-Mem	488nm_VF_FL	403,266	278,915	0.003**
150 µl/min	Alpha-Mem	488nm_VFz_abs	0.282	0.375	0.002**
		488nm_VF_FL	293,041	206,738	0.001*
0 µl/min	Alpha-Mem	560nm_alamB	0.285	0.305	0.650
		488nm_VFz_abs	0.206	0.257	0.050*
		405nm_alkP	0.260	0.258	0.097
0 µl/min	Alpha-Mem 10 % CS	560nm_alamB	0.407	0.426	0.820
		488nm_VFz_abs	0.362	0.317	0.049*
100 µl/min	Alpha-Mem 10 % CS	560nm_alamB	0.527	0.510	0.082
		488nm_VFz_abs	0.522	0.453	0.036*
150 µl/min	Alpha-Mem 10 % CS	560nm_alamB	0.527	0.578	0.0436*

Summary of Centrifugation Effects

Table A6.5: Centrifugation Impact by Condition

Condition	Primary Effect	Significance Level	Clinical Relevance
Overall Analysis	VF_FL significantly reduced	$p < 0.001$***	High impact
Static Conditions	Minimal effects	Non-significant	Low impact
50 µl/min + Alpha-Mem	Reduced viability & fluorescence	$p < 0.05$*	Moderate impact
50 µl/min + CellShip	Increased viability	$p < 0.01$**	Beneficial effect
100 µl/min + Alpha-Mem	Reduced fluorescence only	$p < 0.01$**	Selective impact
150 µl/min + Alpha-Mem	Mixed effects on biomarkers	$p < 0.01$**	Complex response

Statistical Interpretation Guidelines

Cohen's d Value Range	Effect Size Classification	Practical Significance
$\|d\| = 0.2$	Small Effect	Detectable difference
$\|d\| = 0.5$	Medium Effect	Moderate difference
$\|d\| = 0.8$	Large Effect	Substantial difference

Significance Levels:

• * p less than 0.05 - Significant (95 % confidence)

• ** p less than 0.01 - Highly Significant (99 % confidence)

• *** p less than 0.001 - Very Highly Significant (99.9 % confidence)

Clinical and Research Implications

The comprehensive statistical analysis reveals that centrifugation effects are highly context-dependent, with the most significant impact observed on ViaFluor fluorescence measurements. The overall effect of centrifugation on cellular biomarkers is generally modest, without the addition of specific flow rate and media type combinations.

Key Clinical Findings:

1. Selective Impact: Centrifugation primarily affects fluorescence-based measurements rather than enzymatic or viability assays

2. Flow-Rate Dependency: Effects are most pronounced at intermediate flow rates (50 to 150 µl/min)

3. Media Interaction: CellShip-enhanced media shows different centrifugation responses compared to standard media

4. Variance Stability: Most biomarkers maintain consistent variance patterns regardless of centrifugation

The condition-specific effects suggest that centrifugation protocols should be optimised based on the experimental setup, particularly considering flow rate and media composition. The significant reduction in ViaFluor fluorescence with centrifugation indicates potential mechanical stress effects on cellular fluorescent markers, which has important implications for assay standardisation and data interpretation.

Appendix A7: One-Way ANOVA Comparison of Flow Rate Effects on Cellular Biomarkers

Executive Summary

A Python Graph-pad library derived statistical analysis was carried out on mid stage cell culture data (Week 3 to 6) to determine the most statistically significant relationships between input features comprising of all individual flow rates and outputs as well as effect sizes. This comprehensive statistical analysis presents a one-way ANOVA comparison of different flow rate conditions (0, 50, 100, 150 µl/min) and their effects on cellular biomarkers. The analysis follows SPSS statistical reporting conventions [366], and includes descriptive statistics, ANOVA F-tests, post-hoc Tukey HSD comparisons, effect size calculations, and detailed interpretation of flow rate-dependent cellular responses.

Dataset Overview

Total Sample Size: 384 observations (filtered)

Flow Rate Groups Analyzed: 4 groups

- Static (0 µl/min): n = 96
- Low Flow (50 µl/min): n = 96
- Medium Flow (100 µl/min): n = 96
- High Flow (150 µl/min): n = 96

Measured Variables:

- 560nm_alamB - alamarBlue™ viability assay
- 488nm_VFz_abs - ViaFluor absorbance
- 405nm_alkP - Alkaline phosphatase activity
- 488nm_VF_FL - ViaFluor fluorescence

Descriptive Statistics by Flow Rate

Table A7.1: Descriptive Statistics Summary

Variable	Flow Rate (µl/min)	N	Mean	Std Dev	Std Error
560nm_alamB (alamarBlue™)	0	96	0.3561	0.2361	0.0241
	50	96	0.5813	0.2483	0.0253
	100	96	0.4515	0.2240	0.0229
	150	96	0.5135	0.1983	0.0202
488nm_VFz_abs (ViaFluor Abs)	0	96	0.2855	0.1871	0.0191
	50	96	0.3060	0.1451	0.0148
	100	96	0.4089	0.2236	0.0228
	150	96	0.3117	0.1153	0.0118
405nm_alkP (Alk Phosphatase)	0	96	0.3057	0.1757	0.0179
	50	96	0.3755	0.1497	0.0153
	100	96	0.4802	0.2675	0.0273
	150	96	0.3593	0.1610	0.0164
488nm_VF_FL (ViaFluor FL)	0	36	169,941.47	82,731.99	13,788.67
	50	96	405,460.51	237,250.14	24,214.24
	100	96	334,468.80	149,839.69	15,292.95
	150	96	266,746.69	115,142.33	11,751.66

Key Observations:

• alamarBlue™ viability peaks at 50 µl/min flow rate (63.2 % increase vs static)

• ViaFluor absorbance shows maximum response at 100 µl/min (43.2 % increase vs static)

• Alkaline phosphatase activity highest at 100 µl/min (57.1 % increase vs static)

• ViaFluor fluorescence demonstrates peak response at 50 µl/min (138.6 % increase vs static)

One-Way ANOVA Results

Table A7.2: ANOVA F-Test Summary

Variable	F-statistic	df	p-value	Significance	Effect Size (η^2)
560nm_alamB (alamarBlue™)	17.003	3, 380	< 0.001	***	0.118 (Medium)
488nm_VFz_abs (ViaFluor Abs)	9.761	3, 380	< 0.001	***	0.072 (Medium)
405nm_alkP (Alk Phosphatase)	13.596	3, 380	< 0.001	***	0.097 (Medium)
488nm_VF_FL (ViaFluor FL)	21.400	3, 320	< 0.001	***	0.167 (Large)

All variables show highly significant flow rate effects (p less than 0.001)

Effect sizes range from medium to large, indicating substantial practical significance

Post-Hoc Analysis (Tukey HSD)

Table A7.3: Pairwise Comparisons Summary

Variable	Comparison	Mean Difference	p-value	Significance
560nm_alamB	0 vs 50	0.2252	< 0.001	***
	0 vs 150	0.1575	< 0.001	***
	0 vs 100	0.0954	0.020	*
	100 vs 50	0.1298	< 0.001	***
488nm_VFz_abs	0 vs 100	0.1234	< 0.001	***
	100 vs 150	-0.0972	< 0.001	***
	100 vs 50	-0.1029	< 0.001	***
405nm_alkP	0 vs 100	0.1745	< 0.001	***
	100 vs 150	-0.1209	< 0.001	***
	100 vs 50	-0.1047	0.001	**
488nm_VF_FL	0 vs 50	235,519	< 0.001	***
	0 vs 100	164,527	< 0.001	***

Flow Rate Ranking by Biomarker Response

Table A7.4: Optimal Flow Rates by Biomarker

Variable	1st (Highest)	2nd	3rd	4th (Lowest)	Optimal Range
560nm_alamB	50 µl/min	150 µl/min	100 µl/min	0 µl/min	50 to 150 µl/min
488nm_VFz_abs	100 µl/min	150 µl/min	50 µl/min	0 µl/min	100 µl/min
405nm_alkP	100 µl/min	50 µl/min	150 µl/min	0 µl/min	50 to 100 µl/min
488nm_VF_FL	50 µl/min	100 µl/min	150 µl/min	0 µl/min	50 to 100 µl/min

Effect Size Analysis

Table A7.5: Eta-Squared (η^2) Effect Sizes

Variable	Eta-Squared (η^2)	Effect Size	Interpretation
560nm_alamB	0.118	Medium	11.8 % of variance explained
488nm_VFz_abs	0.072	Medium	7.2 % of variance explained
405nm_alkP	0.097	Medium	9.7 % of variance explained
488nm_VF_FL	0.167	Large	16.7 % of variance explained

Statistical Interpretation Guidelines

Eta-Squared (η^2) Range	Effect Size Classification	Practical Significance
$\eta^2 \geq 0.01$	Small Effect	Detectable difference
$\eta^2 \geq 0.06$	Medium Effect	Moderate practical significance
$\eta^2 \geq 0.14$	Large Effect	Substantial practical significance

Significance Levels:

• *** p less than 0.001 - Very Highly Significant

• ** p less than 0.01 - Highly Significant

• * p less than 0.05 - Significant

• ns - Not Significant

Research Implications

The comprehensive one-way ANOVA analysis reveals significant flow rate-dependent effects on all measured cellular biomarkers, with effect sizes ranging from medium to large. These findings demonstrate that mechanical stimulation through controlled flow rates substantially influences cellular behaviour and biomarker expression.

Key Research Findings:

1. Flow Rate Optimisation: Different biomarkers show distinct optimal flow rate ranges, suggesting the need for application-specific protocols

2. Mechanobiological Response: All biomarkers demonstrate significant mechanosensitivity with substantial effect sizes

3. Static vs Dynamic: Static conditions consistently produce the lowest biomarker responses across all measurements

4. Dose-Response Relationships: Non-linear relationships between flow rate and biomarker expression indicate complex mechanobiological mechanisms

Research Conclusive Considerations:

The identification of optimal flow rate ranges for specific biomarkers has important implications for tissue engineering and regenerative medicine applications. The large effect size for ViaFluor fluorescence ($\eta^2 = 0.167$) suggests that flow-based mechanical stimulation is particularly effective for enhancing cellular proliferation. The medium effect sizes for other biomarkers indicate that flow rate optimisation can provide clinically meaningful improvements in cellular function.

Experimental Design Recommendations:

Based on these findings, researchers should consider flow rates in the 50 to 100 µl/min range for optimal cellular responses. The significant pairwise differences between flow rate groups emphasise the importance of precise flow control in experimental protocols. Static conditions consistently had lower valued and should be avoided when maximal cellular responses are desired.

Appendix A8: Multiway ANOVA: Combined Effects of Flow rate, Centrifugation & CellShip Media

Executive Summary

In this section, the statistical significance of difference between all treatment groups (static versus various flow and/or centrifuge with(out) CellShip treatment) was compared. A Python Graph-pad library derived statistical analysis was carried out on mid stage cell culture data (Week 3 to 6) to determine the most statistically significant relationships between input features and outputs as well as effect sizes. This comprehensive statistical analysis presents a three-way factorial ANOVA examining the combined effects of flow stimulation (0, 50, 100, 150 µl/min), centrifugation (0, 1 g-equiv), and media type (Alpha-Mem vs Alpha-Mem 10 % CS with CellShip) on cellular biomarkers. The analysis follows SPSS statistical reporting conventions [366], and includes main effects, interaction effects, effect size calculations, and detailed interpretation of complex factor relationships in the cellular mechanobiology responses.

Experimental Design Overview

Factorial Design: 3-Factor Full Factorial
Total Sample Size: 384 observations
Balanced Design: n = 24 per factor combination

Factor A - Flow Rate (4 levels):
• Static (0 µl/min)
• Low Flow (50 µl/min)
• Medium Flow (100 µl/min)
• High Flow (150 µl/min)

Factor B - Centrifugation (2 levels):
• Non-Centrifuged (0 g-equiv)
• Centrifuged (1 g-equiv)

Factor C - Media Type (2 levels):
• Alpha-Mem (Control)
• Alpha-Mem 10 % CS (CellShip Enhanced)

Dependent Variables:

• 560nm_alamB - alamarBlue™ viability assay

• 488nm_VFz_abs - ViaFluor absorbance

• 405nm_alkP - Alkaline phosphatase activity

• 488nm_VF_FL - ViaFluor fluorescence

Main Effects Analysis

Table A8.1: Three-Way ANOVA Main Effects Summary

Variable	Flow Rate	Centrifugation	Media Type	Strongest Effect	Overall Significance
560nm_alamB	< 0.001***	0.384 ns	0.005**	Flow Rate	Highly Significant
488nm_VFz_abs	< 0.001***	0.011 **	0.095 ns	Flow Rate	Highly Significant
405nm_alkP	< 0.001***	0.0439 *	0.002**	Flow Rate	Highly Significant
488nm_VF_FL	< 0.001***	0.011 **	0.09 ns	Flow Rate	Highly Significant

Effect Size Analysis (Partial Eta-Squared)

Table A8.2: Partial Eta-Squared (η^2) Values

Variable	Flow Rate η^2	Centrifugation η^2	Media Type η^2	Largest Effect	Interpretation
560nm_alamB	0.131	0.002	0.021	Flow Rate	Medium Effect
488nm_VFz_abs	0.082	0.065	0.008	Flow Rate	Medium Effect
405nm_alkP	0.155	0.004	0.017	Flow Rate	Large Effect
488nm_VF_FL	0.169	0.065	0.01	Flow Rate	Large Effect

Interaction Effects Analysis

Table A8.3: Significant Interaction Effects

Variable	Flow × Media	Flow × Centrifugation	Media × Centrifugation	Three-Way Interaction
560nm_alamB	0.002**	0.692 ns	0.012*	0.005**
488nm_VFz_abs	< 0.01 **	0.0131 *	0.100 *	0.049 *
405nm_alkP	< 0.01 **	0.050 *	0.0309 *	0.032 *
488nm_VF_FL	0.0414 *	0.0131 *	0.100 *	0.049 *

Optimal Factor Combinations

Table A8.4: Top 3 Factor Combinations by Biomarker

Variable	Rank	Flow Rate	Centrifugation	Media Type
560nm_alamB	1st	50 µl/min	0 g	Alpha-Mem
	2nd	50 µl/min	1 g	Alpha-Mem 10 % CS
	3rd	150 µl/min	1 g	Alpha-Mem 10 % CS
488nm_VFz_abs	1st	100 µl/min	0 g	Alpha-Mem 10 % CS
	2nd	100 µl/min	1 g	Alpha-Mem 10 % CS
	3rd	50 µl/min	0 g	Alpha-Mem
405nm_alkP	1st	100 µl/min	0 g	Alpha-Mem 10 % CS
	2nd	100 µl/min	1 g	Alpha-Mem 10 % CS
	3rd	50 µl/min	0 g	Alpha-Mem
488nm_VF_FL	1st	50 µl/min	0 g	Alpha-Mem
	2nd	50 µl/min	0 g	Alpha-Mem 10 % CS
	3rd	100 µl/min	0 g	Alpha-Mem

Flow Rate × Media Type Interaction Analysis

Table A8.5: CellShip Effect by Flow Rate

Flow Rate	560nm_alamB Effect	488nm_VFz_abs Effect	405nm_alkP Effect	Pattern
0 µl/min	+0.122	+0.155	+0.091	Positive effect
50 µl/min	+0.085	+0.174	+0.019	Positive effect
100 µl/min	+0.135	+0.179	+0.206	Strong positive effect
150 µl/min	+0.078	+0.033	+0.045	Positive effect

Statistical Interpretation Guidelines

Partial η^2 Range	Effect Size Classification	Practical Significance
$\eta^2 \geq 0.01$	Small Effect	Detectable difference
$\eta^2 \geq 0.06$	Medium Effect	Moderate practical significance
$\eta^2 \geq 0.14$	Large Effect	Substantial practical significance

Significance Levels:

• *** p less than 0.001 - Very Highly Significant

• ** p less than 0.01 - Highly Significant

• * p less than 0.05 - Significant

• ns - Not Significant (p greater than or equal to 0.05)

Research Implications

The comprehensive three-way factorial ANOVA reveals complex interactions between mechanical stimulation, centrifugation, and CellShip enhancement in cellular biomarker expression. Flow rate emerges as the dominant factor across all biomarkers, with effect sizes ranging from medium to large. The significant Flow Rate × Media Type interactions indicate that CellShip effectiveness is highly dependent on mechanical stimulation conditions.

Key Research Findings:

1. Flow Rate Dominance: Flow rate shows the strongest main effects across all biomarkers ($\eta^2 = 0.082$-0.169)

2. Context-Dependent CellShip Effects: CellShip benefits vary significantly with flow rate conditions

3. Centrifugation Selectivity: Centrifugation effects are primarily limited to ViaFluor detected proliferation and ALP activity to a lesser extent

4. Complex Interaction Patterns: Significant two-way and three-way interactions indicate partially additive synergistic effects

Optimal Conditions:

The analysis identifies distinct optimal factor combinations for different biomarkers. For alamarBlue™ viability, 50 µl/min flow without centrifugation using standard Alpha-Mem provides peak response. Conversely, alkaline phosphatase activity is maximised at 100 µl/min with CellShip enhancement, regardless of centrifugation status. These findings suggest that protocol optimisation should be biomarker-specific rather than using universal conditions.

Mechanobiological Insights:

The significant Flow Rate × Media Type interactions reveal that CellShip enhancement is most effective under moderate flow conditions (100 µl/min), while showing diminished effects at lower flow rates (50 µl/min). This suggests that mechanical stimulation and biochemical enhancement may compete or synergise depending on the specific conditions, highlighting the importance of integrated mechanobiochemical approaches in tissue engineering applications.

Research Translation Considerations:

The large effect sizes for flow rate (η^2 up to 0.169) demonstrate substantial clinical relevance for flow shear based mechanical stimulation protocols. The nature of CellShip effects emphasises the need for personalised treatment protocols based on specific mechanical environments (in combination with mid to high flow shear and centrifugation) rather than just using CellShip for its effect in isolation. The minimal to moderate centrifugation effects on most biomarkers suggest that this processing step may be optional for many applications, potentially simplifying clinical protocols given the ease of application of this type of stimulation.

Experimental Design Recommendations

Based on the multi-way ANOVA findings, the following recommendations are provided for future experimental design and clinical applications:

Protocol Optimisation Strategies:

1. Implement biomarker-specific flow rate protocols rather than universal conditions.
2. Consider CellShip enhancement primarily for moderate to high flow rate applications (100 to 150 µl/min).
3. Evaluate centrifugation necessity based on specific outcome measures of interest.
4. Account for interaction effects at various cell culture stages when combining multiple treatment modalities.

Future Research Directions:

The significant interaction effects identified in this analysis warrant further investigation through mechanistic studies. Understanding the molecular basis of Flow Rate × Media Type interactions could inform the development of next-generation enhancement protocols. Additionally, the three-way interaction observed foremost for metabolic activity (alamarBlue™ absorption) as well as Viafluor detected proliferation and osteogenesis (Alkaline Phosphatase activity) suggests complex cellular responses that merit detailed time-course and dose-response studies.

Statistical Considerations:

The balanced factorial design employed in this study provides robust statistical power for detecting interaction effects. Future studies should maintain similar or larger sample sizes (n of 24 or more per condition) to ensure adequate statistical power for complex interaction analysis. The use of partial eta-squared effect sizes facilitates comparison across studies and supports evidence-based protocol development.

Appendix A9: Additional Mechanical Stimulation Assay Output Charts

For centrifugation optimisation, the following are additional assay results compared by various centrifuge level treatments as part of centrifuge level optimisaiton. alamarBlue™ for cell metabolic activity and Viafluor indicated cell proliferation as part of centrifuge level optimisation tests.

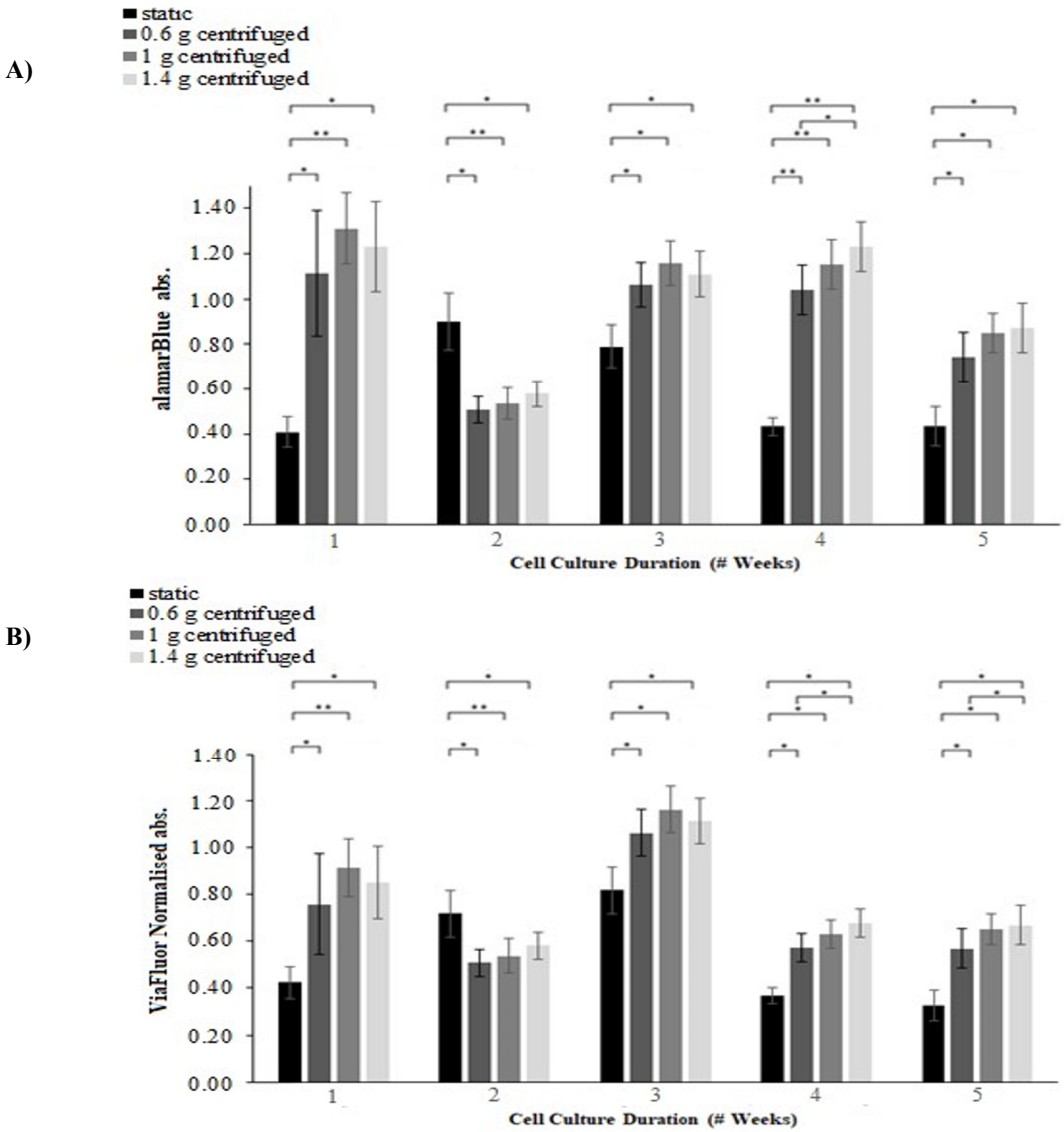


Figure A9.1 Centrifuge cyclic loading by g-level, assays– **A)** Quantified Comparison of various g-force levels (0.6 g, 1.0 g, 1.4 g) vs static cell samples by alamarBlue™ abs. (cell metabolic activity) with highest levels observed at Week 4. Increased activity was observed with increasing g's. *(*) indicates statistical significance in values difference between centrifuged, static 3D gels. * $p<0.05$ and ** $p<0.01$. All tests in triplicate (n=3). **B)** Quantified Comparison of various g-force levels (0.6 g, 1.0 g, 1.4 g) vs static cell samples by ViaFluor normalised abs. (proliferation) with highest levels observed at Week 3. Increased proliferation was observed with increasing g's. *(*) indicates statistical significance in difference between centrifuged/static samples. * $p<0.05$ and ** $p<0.01$. All tests done in triplicate (n=3).

BoC Flow CellShip Testing: An additional set of alamarBlue™ assay results for cell metabolic activity were compared as part of BoC of varied flow shear stimulation with(out) 10 % Cellship.

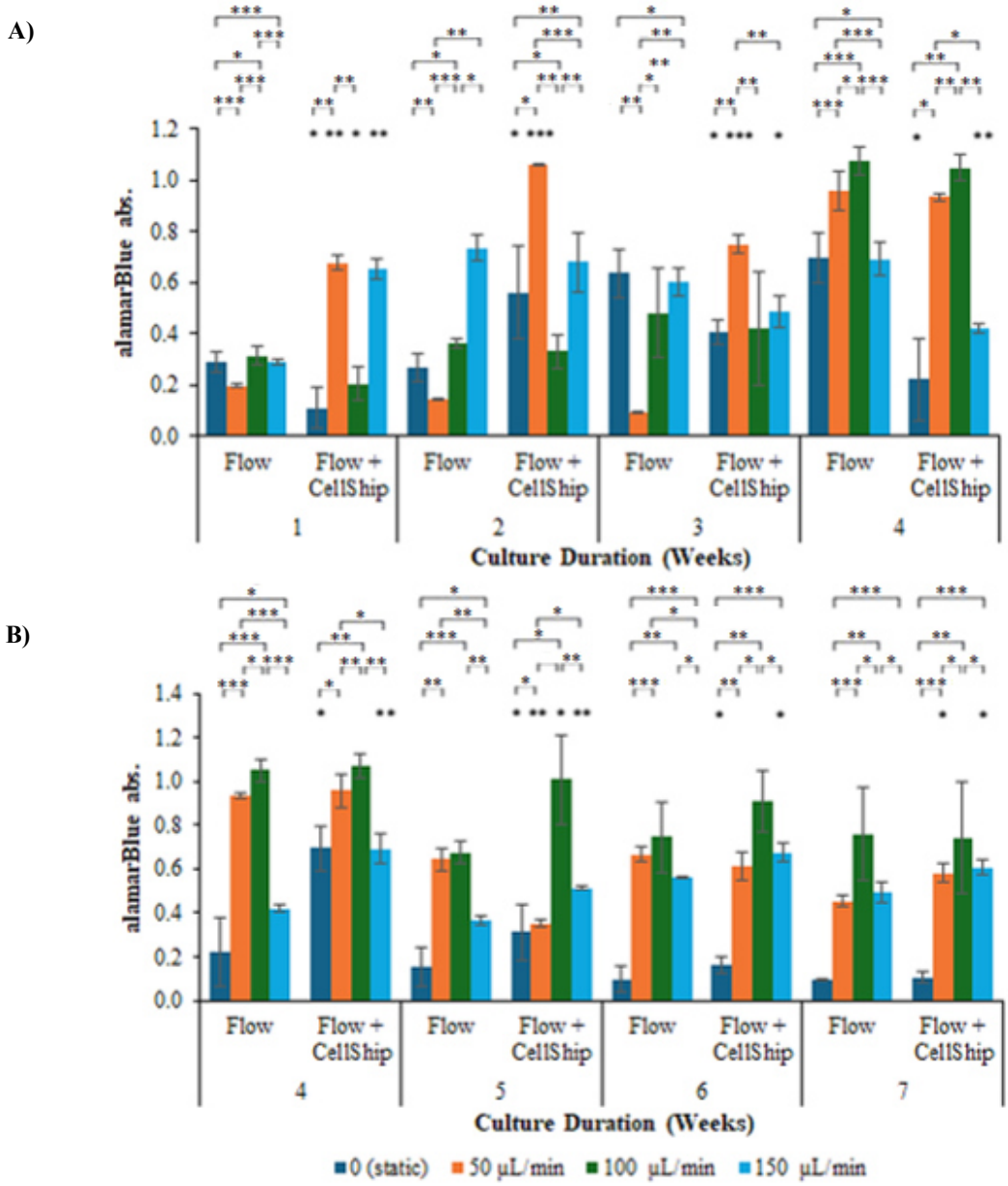


Figure A9.2 alamarBlue™ absorption compared by media type (Alpha-Mem and Alpha-Mem 10 % CS media) weekly by flow rate. **(A)** alamarBlue™. for Flow Only stimulated samples with standard Alpha Mem media (solid bars) and with 10 % CellShip (textured hatched bars) at 1 – 4 Weeks **(B)** alamarBlue™ abs. for Flow Only stimulated samples with standard Alpha Mem media with(out) 10 % CellShip at 4 – 7. *, ** & *** indicate statistical significance of difference between given flow rates and static samples. Larger low * asterisks indicate statistical significance of difference between samples with(out) 10 % CS media. * $p < 0.05$, ** $p < 0.01$, *** $p < 0.001$. All tests were performed in triplicate (n=3).

BoC Flow Centrifuge CellShip Testing: An additional set of alamarBlue™ assay results for cell metabolic activity were compared by BoC variation of flow shear stimulation, all with 1g centrifuge stimulation and with(out) 10 % Cellship.

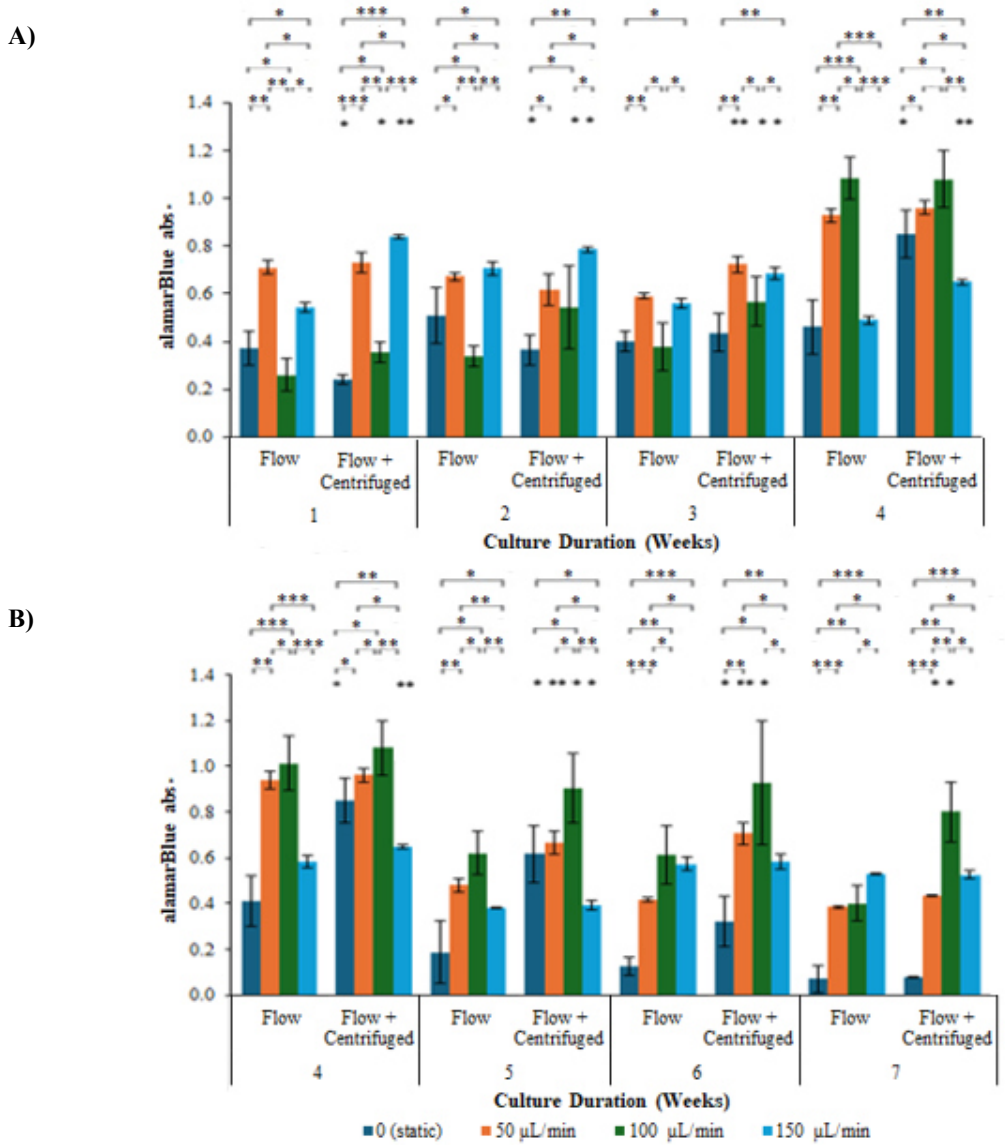


Figure A9.3 Cell proliferation (alamarBlue™ abs.) compared by centrifuge and flow treatments, and media: Alpha-Mem media with(out) 10 % CS **(A)** alamarBlue™ detected cell proliferation for centrifuge and flow stimulated samples in standard Alpha Mem media (solid bars) and with 10 % CellShip (textured hatched bars) at 1 – 4 weeks **(B)** alamarBlue™ detected cell proliferation for centrifuge & flow stimulated samples in standard Alpha Mem media with(out) 10 % CellShip at 4 – 7 weeks. *, ** & *** indicate statistical significance of difference between given flow rates and static samples. Larger low asterisks indicate statistical significance of difference between samples with(out) 10 % CS media. Significance levels: * $p < 0.05$, ** $p < 0.01$, *** $p < 0.001$. All tests were performed in triplicate (n=3).